Synthesis and Characterization of Block Copolymers Containing Metal Nanoclusters

by
RUSSELL CLAY

Bachelor of Science, Chemical Engineering
Cornell University, Ithaca, New York, 1991

Master of Science of Chemical Engineering Practice
Massachusetts Institute of Technology, Cambridge, Masasachusetts, 1994

Submitted to the Department of Chemical Engineering in partial fulfillment of the requirements for the degree of

DOCTOR OF PHILOSOPHY
in Chemical Engineering

at the
MASSACHUSETTS INSTITUTE OF TECHNOLOGY
June, 1997

Signature of Author______________________________
Department of Chemical Engineering
May 8, 1997

Certified by____________________
Robert E. Cohen, St. Laurent Professor of Chemical Engineering
Thesis Advisor

Accepted by____________________
Robert E. Cohen
Chairman, Committee for Graduate Students

Synthesis and Characterization of Block Copolymers Containing Metal Nanoclusters

by
RUSSELL CLAY

Submitted to the Department of Chemical Engineering on May 8, 1997,
in partial fulfillment of the requirements for the degree of
Doctor of Philosophy in Chemical Engineering

Abstract

A general methodology has been established for the synthesis of transition metal nanoclusters within the carboxylic acid functionalized domains of microphase-separated block copolymer films. In this technique the films are soaked in aqueous metal salt solutions prior to reduction of the sequestered metal ions with hydrogen or aqueous sodium borohydride. Our metal nanoclusters are more evenly distributed and more uniformly sized than those made by depositing metal vapor into liquid monomer. Furthermore, our technique does not require the expensive and complicated synthesis of organometallic monomers.

The rate and extent of aqueous metal ion transport (Ag^+, Au^{+3}, Co^{+2}, Cu^{+2}, Eu^{+2}, Eu^{+3}, Fe^{+2}, Fe^{+3}, Gd^{+3}, Ni^{+2}, Pt^{+4}, $[PdCl_4]^{-2}$, $[PtCl_4]^{-2}$, and $[PtCl_6]^{-2}$) into $[MTD]_{400}[NORCOOH]_{50}$ (MTD = methyltetracyclododecene and NORCOOH = 2-norbornene-5,6,-dicarboxylic acid) was monitored using inductively coupled plasma atomic emission spectroscopy. Continuous interconnected polyNORCOOH domains were found to be necessary for metal ion uptake from aqueous solutions. Ion exchange between acid protons and metal ions was found to be the primary binding mechanism. The metal-bound carboxylate ions in the polyNORCOOH domains are re-protonated by hydrogen reduction, rendering them active for further participation in metal binding. UV-visible spectroscopy showed that 10 micron thick Ag, Au, and Cu cluster containing films were brightly colored due to the surface plasmon absorptions of the embedded clusters. Both UV-visible spectra and the theory of Clippe et al. indicated our silver nanoclusters were electronically isolated within the 10 micron thick films following a single loading and reduction sequence (LARS).

Cluster size (ca. 30 Å) was relatively independent of the extent of Ag^+ loading during a single LARS, indicating that nucleation is fast relative to growth. A 10 micron thick film was subjected to a series of four Ag^+ LARS, corresponding to a cumulative Ag^+ loading of 26 wt. % Ag in the overall polymer/Ag composite. The mean cluster size increased from 37 Å, after the first LARS, to 65 Å, after the fourth LARS. Therefore, pre-existing Ag clusters appear to act as nucleation sites for additional cluster growth during subsequent LARS. However, some smaller clusters were also observed following multiple LARS, indicating that the nucleation of new clusters also occurs, leading to a broadening of the cluster size distribution.

Conversion of carboxylic acid groups, within $[MTD]_{400}[NORCOOH]_{50}$, to the sodium carboxylate form, $[MTD]_{400}[NORCOONa]_{50}$, results in large increases in both the rate and extent of loading. The improvement in loading is due largely to the acetate ion's much lower stability constant with Na^+, $K_1 \sim 0.7\ (mole/l\ )^{-1}$, than with H^+, $K_1 \sim 6.3 \times 10^4\ (mole/l\ )^{-1}$, which allows transition metal and rare earth ions, $K_1 \sim 3\text{-}1600\ (mole/l\ )^{-1}$, to more easily exchange with the weakly bound Na^+ ions than with the much more strongly bound H^+ ions.

Thesis Supervisor: Robert E. Cohen, Professor of Chemical Engineering

Acknowledgments

I would like to take this opportunity to thank everyone who contributed to the successful completion of this thesis, as well as those who gave $100,000 or more to the Democratic National Party. I am about to recite a rather long list of people to whom I am indebted. Therefore, I first wish to express my appreciation to those whose names I should have included, but didn't due to my imperfect memory. I wish to thank my advisor Professor Robert E. Cohen, for his patience, encouragement, insight, and enthusiasm for my research. I consider myself extremely fortunate to have worked in his group.

I also wish to thank (contingent upon their final approval of this document) my thesis committee members, Professors: Edward Merrill, Greg Rutledge, Richard Schrock, and Jackie Ying, for their valuable recommendations and insightful questions.

Thanks to all past and present members of the Cohen Group® for your moral support, advice, and attendance at my seminars. I won't even attempt to name all of you! I'll just mention one, my good friend Yot Long.

I wish to express my great appreciation to those who provided the technical help without which I couldn't have completed this project: David Bell (metal coating), Mike Frongillo (TEM), Anthony Garratt-Reed and David Hull (STEM), Tim McClure and Libby Shaw (DSC and UV-VIS), Aaron Moment (IR), Tony Modestino and Steve Wetzel (NMR and ICP), Fangcheng Chou (SQUID), Peter Kloumann and Joe Adario (WAXS), Rich Perilli (DEKTAK), and Bob Digiacomo (glass blowing).

I also wish to acknowledge members of the support staff for helping me find food when I was hungry. Without your assistance, I might have missed out on my share of the leftovers. Thanks Janet, for making sure I got paid before my creditors could ruin my credit rating.

I must also thank the Department of Defense, the National Science Foundation, and NASA for helping to fund this research. I also wish to thank Dr. Mary Ann Meador, my NASA advisor, for her interest in my research.

Thanks also to those special friends who helped me through the last five years: T.A., D.L., K.L., H.H., A.P., and S.B.. Thanks also to the members of the MIT Scuba Club and Metrowest Dive Club. I will miss all of you.

Last, but not least, I wish to thank my mother, sister, Dave, and other members of my family, for their steady supply of support, encouragement, and concern for my well-being.

Table of Contents

Abstract 2

Acknowledgments 3

Table of Contents 5

List of Figures 10

List of Tables 15

Chapter 1 General Introduction 16

- 1.1. Block Copolymers 16
- 1.2. Ring Opening Metathesis Polymerization 19
  - 1.2.1. Mechanism 20
  - 1.2.2. Modern Initiators 21
- 1.3. Metal Nanoclusters 22
  - 1.3.1. Properties and Applications 25
  - 1.3.2. Synthesis of Metal Nanoclusters 26
  - 1.3.3. Synthesis of Metal Nanocluster/Polymer Composites 27
  - 1.3.4. Previous Nanocluster/Polymer Composite Work by Cohen and Schrock Groups 28
- 1.4. "Universal" Metal Nanocluster Synthesis Method 31
  - 1.4.1. Objective 31
  - 1.4.2. Method of Approach 31

Chapter 2 Synthesis and Characterization of Monomers and Polymers 34

- 2.1. Monomers 34
  - 2.1.1. MTD 34
  - 2.1.2. NORCOOH and NORCOOTMS 35

2.1.3. NORCOH and NORCOTMS 36

2.2. Polymers 37

2.2.1. Synthesis 37

2.2.2. PolyMTD 41

2.2.3. PolyNORCOOTMS and PolyNORCOOH 41

2.2.4. PolyNORCOTMS and PolyNORCOH 45

2.3. References for Chapters 1 & 2 46

Chapter 3 Synthesis of Metal Nanoclusters within Microphase-Separated Diblock Copolymers: A "Universal" Approach 50

3.1 Summary 50

3.2 Experimental 50

3.2.1. Immobilization of Metal Ions and Complexes 51

3.2.2. Reduction of Metal Ions and Complexes 52

3.3. Results and Discussion 54

3.3.1. Microtomed Films 54

3.3.2. Bulk Films 62

3.4. Conclusions 72

3.5. References for Chapter 3 73

Chapter 4 Synthesis of Metal Nanoclusters within Microphase-Separated Diblock Copolymers: ICP-AES Analysis of Metal Ion Uptake 74

4.1. Summary 74

4.2. Experimental 75

4.2.1. Metal Ion Uptake in Carboxylic Acid Functionalized Films 75

4.2.2. Reduction of Metal Ions and Complexes 78

4.3. Results and Discussion 78

4.3.1. Metal Ion Uptake in Carboxylic Acid Functionalized Films 78

4.3.2. IR Spectroscopy 85

4.3.3. WAXS Characterization 85

4.3.4. UV-Visible Spectroscopy 89

4.4. Conclusions 102

4.5. References for Chapter 4 103

Chapter 5 Synthesis of Metal Nanoclusters within Microphase-Separated Diblock Copolymers: Sodium Carboxylate vs. Carboxylic Acid Functionalization 105

5.1. Summary 105

5.2. Experimental 107

5.2.1. Metal Ion Uptake in Sodium Carboxylate Functionalized Films 108

5.2.2. Analysis of Ag^+ Loading Capacity (Multiple LARS) 108

5.2.3. Extent of Ag^+ Loading vs. Cluster Size (Single LARS) 109

5.3. Results and Discussion 109

5.3.1. Metal Ion Uptake in Sodium Carboxylate Functionalized Films 109

5.3.2. Analysis of Ag^+ Loading Capacity (Multiple LARS) 114

5.3.3. Extent of Ag^+ Loading vs. Cluster Size (Single LARS) 119

5.4. Conclusions 129

5.5. References for Chapter 5 130

Chapter 6 Oxidation of Silver Nanoclusters by Palladium or Platinum Ions 131

6.1. Summary 131

6.2. Experimental 132

6.2.1. Oxidation of Ag Nanoclusters in 10 μm Thick Films 132

6.2.2. Oxidation of Ag Nanoclusters in Microtomed Films 133

6.3. Results and Discussion 134

6.3.1. Oxidation of Ag Nanoclusters in 10 μm Thick Films 134

6.3.2. Oxidation of Ag Nanoclusters in Microtomed Films 142

6.4. Conclusions 146

6.5. References for Chapter 6 144

Chapter 7 Synthesis of Cobalt and Nickel Containing Nanoclusters within Microphase-Separated Diblock Copolymers 149

7.1. Summary 149

7.2. Experimental 149

7.2.1. Reduction of Co^{+2} and Ni^{+2} Loaded $[MTD]_{400}[NORCOOH]_{50}$ in Aqueous Sodium Borohydride Solutions 150

7.2.2. Reduction of Co^{+2} and Ni^{+2} Loaded $[MTD]_{400}[NORCOOH]_{50}$ in Organic Sodium Borohydride Solutions 152

7.2.3. Thermal Decomposition of Dicobalt Octacarbonyl within $[MTD]_{400}[NORCOOH]_{50}$ 152

7.3. Results and Discussion 153

7.3.1. Reduction of Co^{+2} and Ni^{+2} Loaded $[MTD]_{400}[NORCOOH]_{50}$ in Aqueous Sodium Borohydride Solutions 153

7.3.2. Reduction of Co^{+2} and Ni^{+2} Loaded $[MTD]_{400}[NORCOOH]_{50}$ in Organic Sodium Borohydride Solutions 155

7.3.3. Thermal Decomposition of Dicobalt Octacarbonyl within $[MTD]_{400}[NORCOOH]_{50}$ 159

7.4. Conclusions 170

7.5. References for Chapter 7 173

Chapter 8 Synthesis of Palladium Nanoclusters within Microphase-Separated Diblock Copolymers: Alternative Methods 175

8.1. Summary 175

8.2. Experimental 175

8.2.1. Synthesis of Palladium Nanoclusters within $[MTD]_{400}[NORCOH]_{50}$ 176

8.2.2. Palladium Uptake from Tetrahydrofuran Solutions 176

8.3. Results and Discussion 178
    8.3.1. Synthesis of Palladium Nanoclusters within $[MTD]_{400}[NORCOH]_{50}$ 178
    8.3.2. Palladium Uptake from Tetrahydrofuran Solutions 180
8.4. Conclusions 187
8.5. References for Chapter 8 188

Chapter 9 Conclusions and Future Work 190
9.1. Conclusions 190
9.2. Future Work 193
9.3. References for Chapter 9 194

Appendices 195
A. Materials 195
B. Equipment 196
C. Monomer Synthesis 198
    C.1. Dicyclopentadiene "cracking" 198
    C.2. NORCOOH 198
    C.3. NORCOOTMS 199
    C.4. NORCOTMS 200
D. Film Casting 201
    D.1. 1000 Å Thick Films 201
    D.2. 10 μm Thick Films 202
    D.3. > 0.1 mm Thick Films 203

List of Figures

Figure 1.1: Linear block copolymer nomenclature 16

Figure 1.2: Common equilibrium diblock copolymer morphologies 18

Figure 1.3: ROMP of cyclic olefins via mechanism proposed by Herrison and Chauvin 20

Figure 1.4: Chemical structure of Schrock initiator 21

Figure 1.5: Examples of ROMP monomers 23

Figure 1.6: ROMP polymerization of norbornene with the Schrock initiator 24

Figure 1.7: Chemical structure of Grubb's initiators 24

Figure 1.8: Incorporation of Ag and Au into $[MTD]_{300}[NORPHOS]_{20}$ 29

Figure 1.9: "Universal" metal cluster synthesis method 32

Figure 2.1: Chemical structure of MTD 34

Figure 2.2: Chemical structures of NORCOOH and NORCOOTMS 35

Figure 2.3: Chemical structures of NORCOH and NORCOTMS 36

Figure 2.4: Block copolymer synthesis 38

Figure 2.5: PolyNORCOOTMS acidification 39

Figure 2.6: Infrared spectra of $[MTD]_{200}$ 42

Figure 2.7: Infrared spectra of $[NORCOOH]_{200}$ 44

Figure 3.1: Electron micrograph of Ag^+ stained $[MTD]_{400}[NORCOOH]_{40}$ 51

Figure 3.2: Electron micrograph of microtomed Ag^+ loaded film 57

Figure 3.3: Electron micrograph of microtomed $[PtCl_6]^{-2}$ loaded film 57

Figure 3.4: Electron micrograph of microtomed Ag^+ loaded and reduced film 58

Figure 3.5: Electron micrograph of microtomed $[PtCl_6]^{-2}$ loaded and reduced film 58

Figure 3.6: Electron micrograph of microtomed Au^{+3} loaded and reduced film 59

Figure 3.7: Electron micrograph of microtomed $[PdCl_4]^{-2}$ loaded and reduced film 59

Figure 3.8: Electron micrograph of microtomed Cu^{+2} loaded and reduced film 60

Figure 3.9: Electron micrograph of microtomed Ni^{+2} loaded and reduced film 60

Figure 3.10: Electron micrograph of Ag^{+} loaded $[MTD]_{400}[NORCOOH]_{40}$ film following reduction in 1 wt. % aqueous $NaBH_4$ 61

Figure 3.11: Electron micrograph of bulk Ag^{+} loaded film 64

Figure 3.12: Electron micrograph of bulk silver containing film after 1st LARS 64

Figure 3.13: Electron micrograph of bulk silver containing film after 2nd loading and prior to 2nd reduction 65

Figure 3.14: Electron micrograph of bulk silver containing film after 2nd LARS 65

Figure 3.15: Electron micrograph of bulk gold containing film after 1st LARS 67

Figure 3.16: Electron micrograph of bulk palladium containing film after 2nd LARS 67

Figure 3.17: WAXS data from bulk silver containing film: (a) unloaded film; (b) Ag^{+} loaded film; (c) film after 1st LARS; (d) film after 2nd LARS 68

Figure 3.18: WAXS data from bulk palladium containing film after 2nd LARS 70

Figure 3.19: WAXS data from bulk gold containing film: (a) unloaded film; (b) Au^{+3} loaded film; (c) film after 1st LARS; (d) film after 2nd LARS 71

Figure 4.1: Loading capacity of $[MTD]_{400}[NORCOOH]_{50}$ as a function of time: Au^{+3} (AuCl3), Ag^{+} ($Ag(OOCCH_3)$, Pd^{+2} ($Na_2PdCl_4x3H_2O$), Cu^{+2} ($Cu(OOCCH_3)_2$, Fe^{+2} ($Fe(OOCCH_3)_2$ 79

Figure 4.2: Loading capacity of $[MTD]_{400}[NORCOOH]_{50}$ for Ag^{+} as a function of time: (a) unloaded film; (b) previously loaded with Ag^{+} and reduced; (c) previously loaded with Ag^{+} but not reduced 83

Figure 4.3: IR spectra of $[MTD]_{400}[NORCOOH]_{50}$: (a) unloaded film; (b) previously loaded with Ag^{+} but not reduced; (c) previously loaded with Ag^{+} and reduced 86

Figure 4.4: WAXS data from silver nanocluster containing $[MTD]_{400}[NORCOOH]_{50}$ film: (a) after 1st loading/reduction sequence; (b) after 2nd loading/reduction sequence 87

Figure 4.5: WAXS data from gold nanocluster containing $[MTD]_{400}[NORCOOH]_{50}$ film 88

Figure 4.6: Electron micrograph of 10 μm thick silver nanocluster containing film 90

Figure 4.7: Electron micrograph of 10 μm thick oxidized copper nanocluster containing film 90

Figure 4.8: UV-Visible spectra of 10 μm thick gold nanocluster containing $[MTD]_{400}[NORCOOH]_{50}$ film 91

Figure 4.9: UV-Visible spectra of 10 μm thick silver nanocluster containing $[MTD]_{400}[NORCOOH]_{50}$ film 92

Figure 4.10: UV-Visible spectra of 10 μm thick oxidized copper nanocluster containing $[MTD]_{400}[NORCOOH]_{50}$ film 93

Figure 4.11: 10 μm thick $[MTD]_{400}[NORCOOH]_{50}$ films after aqueous metal loading and hydrogen reduction: (a) $AuCl_3$; (b) $Ag(OOCCH_3)$; (c) $Cu(OOCCH_3)_2$ 94

Figure 4.12: Eigenfrequency spectra of various Ag particle clusters as computed from the theory of Clippe et al. 98

Figure 4.13: 2-D projection of silver nanoclusters homogeneously dispersed on a hypothetical simple cubic lattice 101

Figure 5.1: Metal cluster synthesis scheme 106

Figure 5.2: Loading capacity of $[MTD]_{400}[NORCOONa]_{50}$ vs. $[MTD]_{400}[NORCOOH]_{50}$ for Cu^{+2} ($Cu(OOCCH_3)_2$): (a) Cu^{+2} into $[MTD]_{400}[NORCOONa]_{50}$; (b) Na^{+} out of $[MTD]_{400}[NORCOONa]_{50}$; (c) Cu^{+2} into $[MTD]_{400}[NORCOOH]_{50}$ 110

Figure 5.3: Loading capacity of $[MTD]_{400}[NORCOONa]_{50}$ for Ag^{+} (multiple LARS): (a) first loading; (b) third loading; (c) second loading; (d) fourth loading 115

Figure 5.4: IR spectra of block copolymer film following each step of the first two LARS: (a) unloaded film; (b) first Na^{+} loading; (c) first Ag^{+} loading; (d) first reduction; (e) second Na^{+} loading; (f) second Ag^{+} loading; (g) second reduction 118

Figure 5.5: WAXS data from silver nanocluster containing $[MTD]_{400}[NORCOOH]_{50}$ film (multiple LARS): (a) first LARS; (b) second LARS; (c) third LARS; (d) fourth LARS 120

Figure 5.6: Electron micrograph of silver nanocluster containing $[MTD]_{400}[NORCOOH]_{50}$ film after first LARS 121

Figure 5.7: Electron micrograph of silver nanocluster containing $[MTD]_{400}[NORCOOH]_{50}$ film after third LARS 121

Figure 5.8: Electron micrograph of silver nanocluster containing $[MTD]_{400}[NORCOOH]_{50}$ film after 2 weeks of loading and reduction 123

Figure 5.9: Electron micrograph of silver nanocluster containing $[MTD]_{400}[NORCOOH]_{50}$ film after 7 weeks of loading and reduction 123

Figure 5.10: Cluster growth within a volume element contributing to single cluster 126

Figure 5.11: Gibbs free energy of formation (ΔG) as a function of critical nuclei radius (r^*) 127

Figure 6.1: UV-visible absorption spectrum of 10 μm thick Pd nanocluster containing $[MTD]_{400}[NORCOOH]_{50}$ film 136

Figure 6.2: WAXS data from 10 μm thick Ag cluster containing film after soaking in 0.005 M aqueous $Na_2PdCl_4x3H_2O$ 137

Figure 6.3: WAXS data from 10 μm thick Ag cluster containing film after soaking in 0.005 M aqueous $Na_2PdCl_4x3H_2O$: (a) 0 hr; (b) 845 hr 138

Figure 6.4: WAXS data from 10 μm thick Ag cluster containing film after soaking in 0.005 M aqueous $Na_2PtCl_4xH_2O$ 141

Figure 6.5: Electron micrograph of a Ag cluster containing film 143

Figure 6.6: Electron micrograph of a Ag cluster containing film after 3 hr on 0.005 M aqueous $Na_2PdCl_4x3H_2O$ 143

Figure 6.7: Electron micrograph of a Ag cluster containing film after 15 hr on 0.005 M aqueous $Na_2PdCl_4x3H_2O$ 145

Figure 6.8: Electron micrograph of a Ag cluster containing film after 103 hr on 0.005 M aqueous $Na_2PdCl_4x3H_2O$ 145

Figure 7.1: WAXS data from Co^{+2} loaded $[MTD]_{400}[NORCOOH]_{50}$ film after soaking in aqueous $NaBH_4$ 154

Figure 7.2: Electron micrograph of Ni^{+2} loaded $[MTD]_{400}[NORCOOH]_{50}$ film 156

Figure 7.3: Electron micrograph of Co^{+2} loaded $[MTD]_{400}[NORCOOH]_{50}$ film 156

Figure 7.4: Electron micrograph of Ni^{+2} loaded $[MTD]_{400}[NORCOOH]_{50}$ film after soaking in THF/$NaBH_4$ solution 158

Figure 7.5: Electron micrograph of Co^{+2} loaded $[MTD]_{400}[NORCOOH]_{50}$ film after soaking in THF/$NaBH_4$ solution 158

Figure 7.6: UV-visible spectra of air stored $Co_2(CO)_8$ loaded films: (a) unheated; (b) heated 160

Figure 7.7: Electron micrograph of $Co_2(CO)_8$ loaded $[MTD]_{400}[NORCOOH]_{50}$ film 162

Figure 7.8: Electron micrograph of $Co_2(CO)_8$ loaded $[MTD]_{400}[NORCOOH]_{50}$ film after heating under vacuum 162

Figure 7.9: Typical M vs. H hysteresis loop for a bulk ferromagnetic or ferrimagnetic material: M_s = saturation magnetization, M_r = remanent magnetization, and H_c = coercivity 163

Figure 7.10: Variation of coercivity with particle diameter 164

Figure 7.11: Temperature dependence of the critical diameter, D_p, for spherical cobalt particles 167

Figure 7.12: M vs. H plot for $Co_2(CO)_8$ loaded $[MTD]_{400}[NORCOOH]_{50}$ film after heating and 20 days in air (300 K) 168

Figure 7.13: M vs. H plot for $Co_2(CO)_8$ loaded $[MTD]_{400}[NORCOOH]_{50}$ film after heating and 20 days in air (10 K) 169

Figure 7.14: M vs. H plot for $Co_2(CO)_8$ loaded $[MTD]_{400}[NORCOOH]_{50}$ film after heating and 30 days in air (300 K) 171

Figure 7.15: M vs. H plot for unheated $Co_2(CO)_8$ loaded $[MTD]_{400}[NORCOOH]_{50}$ film after 90 days in air (300 K) 172

Figure 8.1: Electron micrograph of $[MTD]_{400}[NORCOH]_{50}$ film after floating on 0.005 M aqueous $Na_2PdCl_4x3H_2O$ 179

Figure 8.2: Electron micrograph of $[MTD]_{400}[NORCOH]_{50}$ film after floating on 0.005 M aqueous $Na_2PdCl_4x3H_2O$ and reduction under hydrogen 179

Figure 8.3: Electron micrograph of $[MTD]_{400}[NORCOOH]_{50}$ film after soaking in 0.1 M $Na_2PdCl_4x3H_2O$ (water/THF) solution 181

Figure 8.4: WAXS data from $[MTD]_{400}[NORCOOH]_{50}$ film after soaking in 0.1 M $Na_2PdCl_4x3H_2O$ (water/THF) solution: (a) prior to hydrogen reduction; (b) after hydrogen reduction 182

Figure 8.5: Electron micrograph of solution phase loaded $[MTD]_{400}[NORCOOH]_{50}$ (0.05 moles $Na_2PdCl_4x3H_2O$/mole COOH) after hydrogen reduction 184

Figure 8.6: Electron micrograph of solution phase loaded $[MTD]_{400}[NORCOOH]_{50}$ (0.5 moles $Na_2PdCl_4x3H_2O$/mole COOH) after hydrogen reduction 184

Figure 8.7: WAXS data from solution phase loaded $[MTD]_{400}[NORCOOH]_{50}$ prior to hydrogen reduction: (a) 0.05 moles $Na_2PdCl_4x3H_2O$/mole COOH; (b) 0.25 moles $Na_2PdCl_4x3H_2O$/mole COOH; (c) 1.0 moles $Na_2PdCl_4x3H_2O$/mole COOH 185

Figure 8.8: WAXS data from solution phase loaded $[MTD]_{400}[NORCOOH]_{50}$ after hydrogen reduction: (a) 0.05 moles $Na_2PdCl_4x3H_2O$/mole COOH; (b) 0.25 moles $Na_2PdCl_4x3H_2O$/mole COOH; (c) 0.50 moles $Na_2PdCl_4x3H_2O$/mole COOH; (d) 1.0 moles $Na_2PdCl_4x3H_2O$/mole COOH 186

List of Tables

Table 3.1 Metal loading of microtomed films 52

Table 3.2 Metal loading of bulk films 52

Table 3.3 Standard electrochemical reduction potentials 53

Table 3.4 Reduction of metal loaded microtomed films 54

Table 3.5 Reduction of metal loaded bulk films 54

Table 3.6 TEM results of metal loading and reduction in microtomed films 55

Table 3.7 TEM results of metal loading and reduction in bulk films 62

Table 4.1 Aqueous ICP-AES metal loading experiments 77

Table 4.2 ICP-AES metal loading experiments in methanol 78

Table 4.3 Loading capacity of polyNORCOOH from aqueous solutions 81

Table 4.4 Loading capacity of polyNORCOOH from methanol 84

Table 5.1 Loading capacity: $[MTD]_{400}[NORCOOH]_{50}$ vs. $[MTD]_{400}[NORCOONa]_{50}$ 112

Table 5.2 Stability constants between selected metal ions and the acetate ion 114

Table 5.3 Mean silver crystal diameter vs. extent of loading 122

Table 5.4 Density of Ag clusters within polyNORCOOH domain vs. loading 124

Table 6.1 Soaking schedule for 10 μm thick Ag nanocluster containing films 133

Table 6.2 EPMA measurements of cluster composition 146

Table 7.1 D-spacings: Calculated vs. NiB 157

Table 8.1 Mass of 0.125 M Na2PdCl4x3H2O solution added to 2 g of 2 wt. % polymer soluion 177

Chapter 1

General Introduction

1.1. Block Copolymers

Block copolymers are long molecules composed of sequences (blocks) of chemically distinct repeat units (monomers).[1] In linear block copolymers, different sequences are covalently bonded, end-to-end, forming a single chain. As shown in Figure 1.1, linear block copolymers are classified by the number sequences present in each polymer chain. Copolymers with two sequences are referred to as diblocks, copolymers with three sequences are referred to as triblocks, and polymers with more than three sequences are referred to as multiblocks.

AAAAAAAA--BBBBBBBB	diblock
AAAAA--BBBBB--CCCCCC	triblock
$-(\mathrm{AAAAA{-}{-}BBBBB})_n-$	multiblock

Figure 1.1: Linear block copolymer nomenclature

Shown in equations (1-1) through (1-3) are the thermodynamic relations which govern the mixing of homopolymers A (AAA....AAA) and B (BBB...BBB).[2]

$$\Delta G_{mix} = \Delta H_{mix} - T\Delta S_{mix} \qquad (1\text{-}1)$$

where

$$\Delta H_{mix} = \chi_{AB} n_A \phi_B kT \qquad (1\text{-}2)$$

$$\Delta S_{mix} = -k(n_A \ln\phi_A + n_B \ln\phi_B) \qquad (1\text{-}3)$$

ΔG_{mix}, ΔH_{mix}, and ΔS_{mix}, represent the Gibbs free energy, enthalpy, and configurational entropy of mixing, respectively, T is the absolute temperature, n_i and ϕ_i represent the number of chains and volume fraction of polymer i (A or B) in the system, respectively, k is Boltzmann's constant, and χ_{AB} is the Flory-Huggins polymer-polymer interaction parameter. The Flory-Huggins polymer-polymer interaction parameter is defined is equation (1-4),[2]

$$\chi_{AB} = z\Delta w_{AB}x_A/kT \qquad (1\text{-}4)$$

where z is the number of contacts between a monomer unit and its neighbors, Δw_{AB} is the energy of interaction caused by contact between monomer units -A- and -B-, and x_A is the number of monomer units in polymer chain A.

In general, χ_{AB} is very large due to the large number of monomer units in the chain, x_A. In contrast, there will usually be relatively few (compared to nonpolymeric systems) polymer molecules of any given type, n_i. In the case of ΔH_{mix}, the large and small values of χ_{AB} and n_i offset each other, so ΔH_{mix} has a magnitude comparable to nonpolymeric systems. ΔS_{mix}, however, is much smaller for polymeric systems than for nonpolymeric systems. Since ΔH_{mix} is usually positive, ΔG_{mix} will be positive for most polymeric systems at temperatures of interest; therefore, most homopolymer blends are immiscible.

Similar reasoning leads us to conclude that disparate blocks within linear diblock copolymers will often be immiscible; however, macroscopic phase separation cannot occur due to covalent bonds between the dissimilar blocks. Instead, dissimilar blocks form locally segregated microdomains of the minority fraction in a matrix of the major component. The phenomenon of local segregation between disparate blocks, in block copolymers, is commonly referred to as microphase separation.[1,3] In the case of (A-B) diblock copolymers, microphase separation is controlled by three variables: the volume fraction of component A (f_A), the overall degree of polymerization (N), and the Flory-Huggins interaction parameter (χ_{AB}).

The product $\chi_{AB}N$ is crucial in determining the phase state of (A-B) diblock copolymers, since the enthalpic and entropic contributions to ΔG_{mix} scale as χ_{AB} and N^{-1} respectively.[4-6] For low values of $\chi_{AB}N$, the entropic term dominates, and the diblock copolymer will exist as a single disordered (homogeneous) phase. However, as $\chi_{AB}N$ increases, the system will pass through an order-disorder transition, and form a locally ordered (inhomogeneous) morphology.

As shown in Figure 1.2, the most common equilibrium diblock copolymer morphologies are spherical, cylindrical, and lamellar. Spherical morphologies are usually seen within diblock copolymers containing up to 15 volume percent A. Cylindrical (hexagonally packed) morphologies usually occur from 15 to 30 volume percent A, and lamellar morphologies are generally observed from 30 to 70 volume percent A. Occasionally, an equilibrium, ordered bicontinuous double diamond morphology is observed between the cylindrical and lamellar regions.[7] In many cases, such as during rapid casting from solution, diblock copolymers become kinetically locked in nonequilibrium

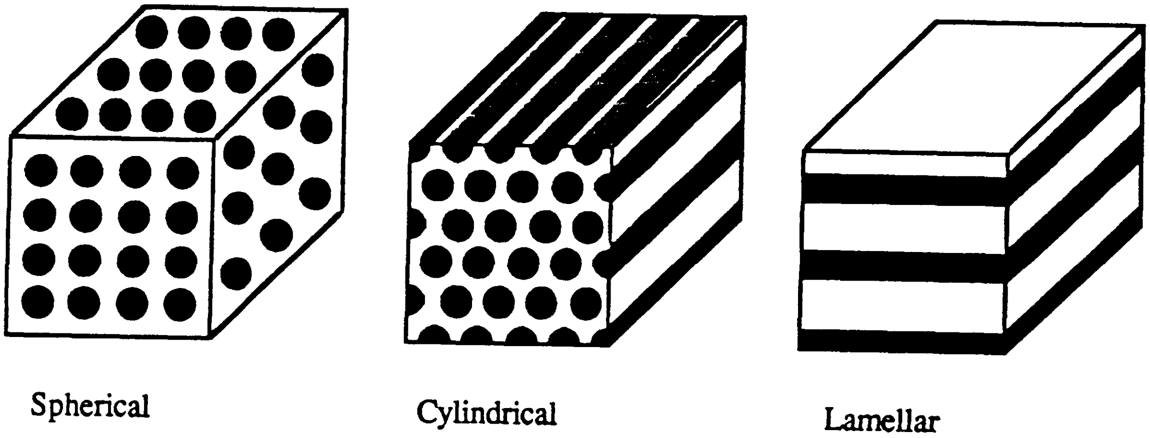

Figure 1.2: Common equilibrium diblock copolymer morphologies

morphologies. In these instances, microphase separation into one of the previously mentioned equilibrium morphologies is thermodynamically favored, but will not occur at an observable rate due to limited chain mobility below a polymers glass transition temperature.

Block copolymers are interesting because properties such as gas permeability and electrical conductivity, which are isotropic (directionally independent) in homogeneous systems, often become anisotropic (directionally dependent) in microphase-separated systems.[8]

1.2. Ring Opening Metathesis Polymerization

Anionic polymerization and ring opening metathesis polymerization (ROMP) are two of the most commonly used methods for synthesizing block copolymers. Anionic polymerizations have been extensively studied during the last several decades,[9] but their industrial use is limited because they often require solvents. Anionic polymerizations, however, are of great interest because they allow very good control over molecular weight and molecular weight distribution. Anionic polymerizations occur at metal-organic sites consisting of a carbanion and a metallic counterion. Anionic polymerizations can be initiated by metal organics such as butyl lithium or radical ionics such as sodium naphthalene. Anionic growth takes place by nucleophilic attack of a carbanion onto a monomer, where the carbanionic site is restored at the chain end. In aprotic solvents, with no electrophilic functionality, termination and transfer reactions are unlikely to occur . Therefore, the carbanionic sites remain active for durations long compared to the polymerization process. In these cases, the polymerization is often referred to as "living", because a second monomer can be polymerized after the first, allowing the formation of block copolymers.

Ring opening metathesis polymerizations also involve sites which remain active for durations long compared to the polymerization process and allow the formation of numerous block copolymers. However, ROMP may be considered more versatile than anionic polymerization, because several ROMP initiators allow for "living" polymerizations in the presence of protic solvents.

1.2.1. Mechanism

During ROMP reactions, cyclic olefins are ring opened to form polymers with unsaturation in their backbones, rather than the typical 1,2-addition products observed with Ziegler-Natta catalysts.[10,11] The mechanism of ROMP reactions was studied extensively during the late 1960's and early 1970's. Calderon et al.[12] and Dall'Asta et al.[13] demonstrated via nuclear magnetic resonance studies that the double bond itself is cleaved. Herrison and Chauvin[14] proposed the currently accepted metathesis (ligand switching)[15] mechanism shown in Figure 1.3. This mechanism involves the formation of a metal carbene that reacts with a cyclic olefin, forming a metallacycloalkane intermediate, which then rearranges to form a new metal carbene.

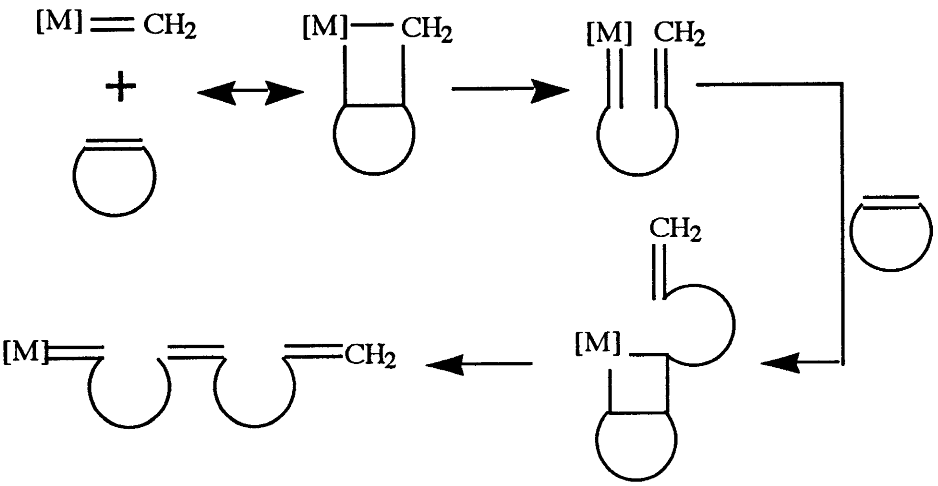

Figure 1.3: ROMP of cyclic olefins via mechanism proposed by Herrison and Chauvin [M] represents transition metal center with attached ligands.

$WCl_6/EtAlCl_2/EtOH$, the Calderon catalyst,[16,17] is capable of initiating cycloalkene metathesis polymerizations. However, a major disadvantage of ROMP is that double bonds remain in the final product. These remaining double bonds can be nearly as reactive as the double bonds in the monomer for many early ROMP catalysts such as the Calderon catalyst.

Therefore, chain scission and cyclic oligomer formation often occur, leading to polymers with very high polydispersity indices.[16]

1.2.2. Modern Initiators

The development of organometallic initiators such as the Schrock initiator[18,19] made it possible to synthesize low polydispersity (PDI < 1.1) polymers via ROMP. As shown in Figure 1.4, the Schrock initiator can have either Mo or W as its active center, and various alkoxide ligands can be used to tune its reactivity.

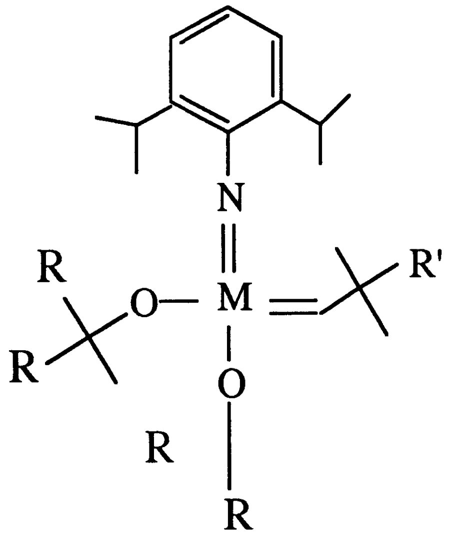

M = Mo or W
R = CH_3 or CF_3
R' = CH_3 or Ph

Figure 1.4: Chemical structure of the Schrock initiator

Schrock initiators react only with strained cyclic olefins and are sterically unable to react with the acyclic olefins found within ROMP polymers. Both the W and Mo containing initiators can polymerize strained cyclic olefins functionalized with metals, halides, ethers, secondary amines, and tertiary amines. In addition, the Mo containing initiator can tolerate esters, nitriles, and amides.[20] It was proposed that molybdenum's smaller electron shell causes the attached ligands to be closer together, which sterically inhibits the functionalities from attacking the metal center. Shown in Figure 1.5 is a partial list of strained cyclic olefins which have been polymerized using Schrock initiators. Shown in Figure 1.6 is the ROMP polymerization of norbornene.

Despite the Schrock initiators ability to produce living polymers of very narrow molecular weight, they do have several disadvantages. They are difficult and expensive to produce; although they are now commercially available from Strem Chemicals, Inc. (Newburyport, MA). Schrock initiators are also intolerant to oxygen, moisture, and protic solvents. Therefore, polymerizations must be conducted in an inert atmosphere drybox.

In recent years, Professor R. Grubbs et al. have made significant contributions to ROMP chemistry by developing a class of ruthenium containing initiators capable of polymerizing many functionalized, strained cyclic olefins.[21,22] These Ru based initiators, shown in Figure 1.7, are moderately stable to air. In addition, they are stable in organic solvents in the presence of water, alcohol, and acetic acid. However, although the Grubb's initiators tend to be more robust than the Schrock initiators, they also form polymers with slightly higher polydispersity indices (PDI 1.1-1.3). Furthermore, although Grubb's initiators are tolerant to protic species in solution, they are not always tolerant of the same species when attached to monomers. Grubb's initiators are commercially available from Boulder Chemical, Inc. (Boulder, CO).

1.3. Metal Nanoclusters

Metal nanoclusters are small aggregates of metal atoms (~10-100 Å in diameter) with agglomeration numbers from O(10) to O(10,000). The diminutive size of metal nanoclusters results in a large surface area to volume ratio. Nanoclusters are interesting because they can exhibit properties characteristic of neither metal atoms nor bulk metal.[23,24] Metal nanoclusters offer considerable potential for applications in both advanced materials and heterogeneous catalysis.

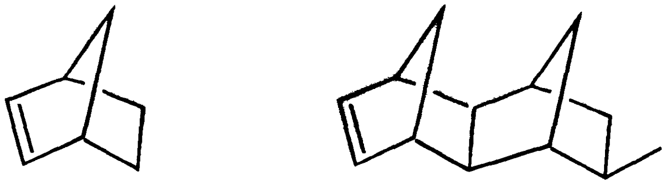

norbornene methyltetracyclododecene (MTD)

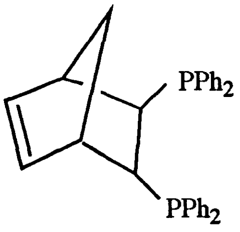

2-exo-3-endo-bis(diphenylphosphino)bicyclo[2.2.1]heptene (NORPHOS)

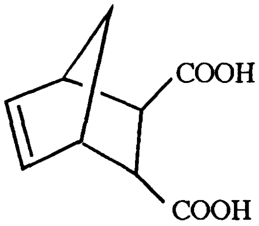

2-norbornene-5,6,-dicarboxylic acid (NORCOOH)

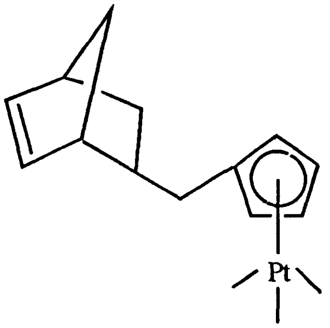

endo-2-cyclopentadienylmethylnorborn-5-enyl trimethyl platinum ([Pt])

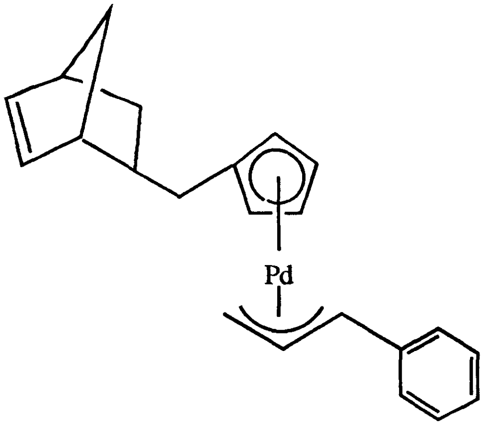

endo-2-cyclopentadienylmethylnorborn-5-enyl 1-phenylallyl palladium ([Pd])

Figure 1.5: Examples of ROMP monomers

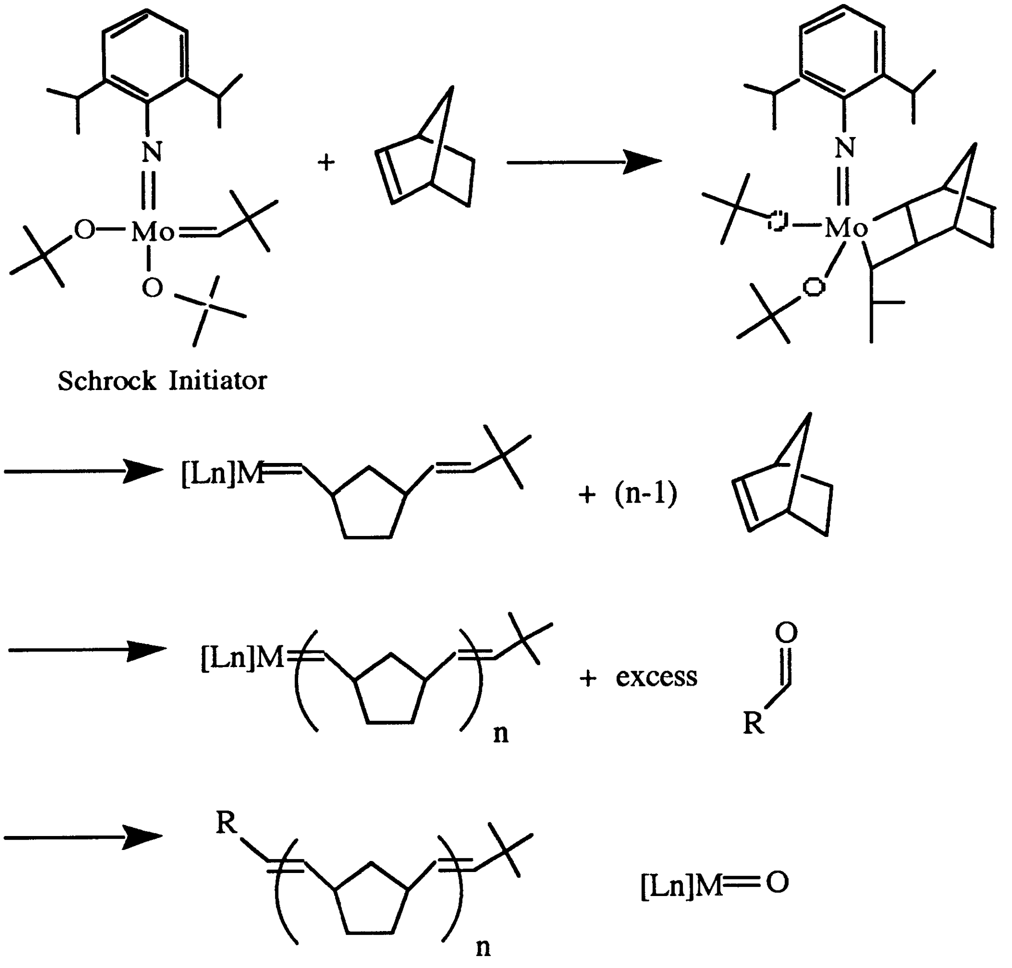

Figure 1.6: ROMP polymerization of norbornene with the Schrock initiator The ligands and the metal atom are abbreviated [Ln]M.

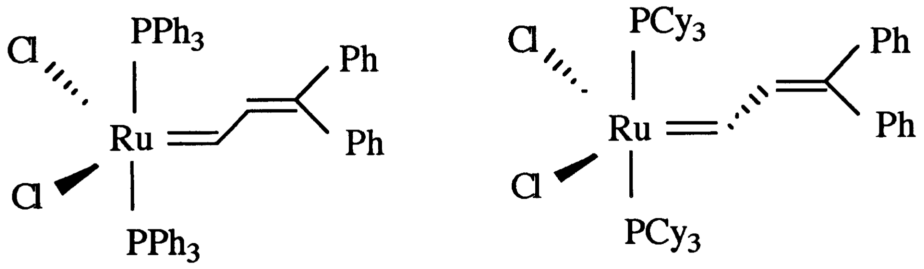

Figure 1.7: Chemical structure of Grubb's initiators

1.3.1. Properties and Applications

The small number of atoms, large surface area to volume ratio, and diminutive size of nanoclusters results in unusual properties including quantum size effects, nonlinear optical behavior, and high catalytic activity. Quantum size effects are unusual size-dependent properties which can occur in nanoclusters as a result of their discrete, incompletely developed molecular orbital band structure. Examples of quantum size effects include the reduction of melting point[25,26] and increase in absorption band width, with decreasing cluster diameter.[27] Nonlinear optics (NLO) refer to unique optical phenomena which occur when laser light passes through a material.[28] NLO effects have potential applications in a number of fields including telecommunications and digital computing. The high conductivity and small size of metal nanoclusters makes them good candidates for the conductive domains in high-dielectric composites. These composites which contain conductive spheres dispersed in a nonconducting matrix can have large dielectric constants and have applications in capacitors.[29,30]

The most significant current use of metal nanoclusters is in catalysis. Several metals are used industrially as catalysts including: Pt, Rh, Sn, Pd, Ni, Ag, Co, Cu, and Zn. Pt and Pt-Rh or Pt-Sn combinations, supported on acidified γ-alumina, are widely used in catalytic reforming.[31] Both Pd and Ni are commonly used as hydrogenation catalysts, and ethylene can be oxidized to ethylene oxide over Ag supported on α-alumina.[32] In addition, both alumina supported Ni and Co catalyze carbon monoxide methanation, a reaction important in the purification of hydrogen gas.[33,34] Combinations of alumina supported Cu and Zn are used by ICI and Lurgi to produce methanol from synthesis gas.[31]

Recent research has shown bimetallic catalysts consisting of a Group VIII and a Group IB metal can yield higher selectivities and/or activities than pure metals.[35] Examples of such combinations include Ni-Cu and Pd-Au. It has been shown that the presence of a Group IB metal with a Group VIII metal inhibits hydrogenalysis on the Group VIII metal.[35] Therefore, selectivity for isomerization of n-alkanes to branched alkanes is higher with Group VIII/Group IB bimetallic catalysts than with Group VIII metals alone. Sinfelt et al.[35] have demonstrated that incorporation of 5 to 85 mole % Cu in Ni leads to increases in activity for cyclohexane dehydrogenation. Toshima et al.[36] have shown that alloys of Pd and Au respectively in a 4 to 1 ratio were more active than pure Pd for cyclooctadiene reduction. It has been hypothesized that the unusual selectivities and activities of bimetallic catalysts are due to electronic interactions which modify the local bonding properties of the metal.

Polymers are rarely used commercially as catalyst supports because of their low thermal stability (T_m polyethylene ~137 °C, T_g polystyrene ~100 °C).[37] However, recent studies have shown polymer supported catalysts offer potential as artificial enzymes which can catalyze highly selective reactions under mild conditions. This unusual selectivity is a result of size/shape and polar/electronic interactions between the polymer and the reactants or products. Homogeneous hydrogenations of organic compounds containing both cyclic and side-chain double bonds, catalyzed by $RhCl(PPh_3)_3$, have been compared with hydrogenations by the polymer bound analog (styrene 2% DVB resins).[38] The ratio of side-chain to cyclic double bonds hydrogenated was found to be several times greater for the polymer bound catalyst than for the homogeneous catalyst, presumably due to steric crowding at the active sites experienced by cyclic moieties. It is reasonable to believe polymer supported metal nanoclusters may also lead to very selective catalysis.

1.3.2. Synthesis of Metal Nanoclusters

Metal nanoclusters can be prepared through a variety of techniques including metal acid or salt reduction, metal evaporation, and sputtering. Boutonnet et al.[39] have synthesized monodisperse particles (30-50 Å) of Pt, Pd, and Rh by reduction of metal salts with hydrogen or hydrazine. The colloidal metal clusters were stabilized within surfactant micelles, and both the standard deviation and reproducibility of the diameter were found to be 10%. Yatsuya and Mihama[40] developed a technique where metal is evaporated in vacuum onto the surface of an oil. This method produced well dispersed uniform clusters with a mean diameter below 100 Å. Metal nanoclusters have also been successfully prepared by sputtering, in which high energy ions are fired at bulk metals causing the ejection of metal atoms and metal ions. Sputtering, however, results in low metal cluster yields.[41]

1.3.3. Synthesis of Metal Nanocluster/Polymer Composites

The study and use of metal cluster properties often requires that they be uniformly sized and homogeneously dispersed on a dielectric (non-conducting) support. A narrow size distribution is necessary to study size-dependent cluster properties, and the dielectric support will prevent interactions between metal cluster electrons and other conductive materials. In addition, the support must be transparent to access cluster optical properties. Similarly, permeable supports are required for catalytic applications.

Polymers are often used as support materials because they can be transparent, permeable, and easily processed. Klabunde et al.[42] have prepared films of polystyrene and poly(methyl methacrylate) containing Ag, Au, and Pd clusters (10-150 Å). The films were synthesized by deposition of metal vapor into liquid monomer which was subsequently polymerized; however, it was found that the metal clusters agglomerated within both polymers. Heilmann and Hamann[43] prepared polymer/metal composite films by simultaneous metal evaporation and plasma polymerization of benzene or hexamethyldisilazan. Homogeneous films containing Ag, Au, Cu, In, Ge, Co, and Sn were synthesized; however, the clusters were irregularly shaped and had a large size distribution.

Metal cluster/polymer composites have many potential applications including: non-fading dyes, nano-wire arrays, high frequency antennae, and "smart" materials, where the conductivity varies with temperature or applied stress. However, there are few viable techniques for the synthesis of such materials containing uniformly sized, homogeneously dispersed, polymer supported metal nanoclusters. Thin films (< 1 μm) can be produced by sequestration of metal salts within block copolymer micelles followed by reduction and solution casting;[44-46] however, it is not clear whether this approach can also produce thicker composite films containing evenly dispersed metal clusters. McCarthy et al. developed a method of synthesizing bulk polymer/metal composites containing evenly dispersed and relatively uniformly sized metal clusters, in which metal salts are diffused into polymer films from supercritical CO_2 followed by reduction.[47]

Another promising technique was recently developed by the Cohen (chemical engineering) and Schrock (chemistry) groups at MIT. This technique involves ring opening metathesis polymerization of block copolymers, of which one block either contains a metal atom or can be coordinated with a metal atom via phosphine centers.[48] The block copolymers exhibit microphase separation, and reduction of metal atoms in the films produces relatively uniformly sized clusters of less than 100 Å in diameter. These clusters are largely restricted to the original metal complex containing microdomains.

1.3.4. Previous Nanocluster/Polymer Composite Work by Cohen and Schrock Groups

Synthesis of metal nanoclusters within the microdomains of block copolymers has been a subject of interest within the Cohen and Schrock groups for the past several years. Y. Ng Cheong Chan[49], a postdoctoral researcher in the Schrock group, first demonstrated the feasibility of metal cluster synthesis via ROMP by preparing Ag and Au clusters within $[MTD]_{300}[NORPHOS]_{20}$ block copolymers. The polymers were synthesized on a 0.5 g scale by first polymerizing 300 equivalents of MTD followed by the addition of 20 equivalents of NORPHOS to the living polyMTD. Polymerization was initiated by the Mo containing Schrock initiator and was terminated with excess pivaldehyde.

As shown in Figure 1.8, Ag and Au were incorporated into the polymer by adding Ag(COD)(Hfacac)[50] or $Au(PMe_3)Me$[51] respectively to a solution of polymer in benzene. Films of $[MTD]_{300}[Ag_2(Hfacac)_2(NORPHOS)]_{20}$ (Ag-1) and $[MTD]_{300}[Au_2(Me)_2(NORPHOS)]_{20}$ (Au-1) were examined by transmission electron microscopy (TEM) and found to have lamellar and cylindrical morphologies respectively. Thin sections (200-300 Å) of both films were heated in air at 150 °C for 15 and 48 hours

$$[\mathrm{NORPHOS}]_{20}[\mathrm{MTD}]_{300} \xrightarrow[-40\ \mathrm{COD}]{40\ \mathrm{Ag(Hfacac)(COD)}} [\mathrm{Ag_2(Hfacac)_2(NORPHOS)}]_{20}[\mathrm{MTD}]_{300}$$

$$[\mathrm{NORPHOS}]_{20}[\mathrm{MTD}]_{300} \xrightarrow[-40\ \mathrm{PMe_3}]{40\ \mathrm{Au(PMe_3)(Me)}} [\mathrm{Au_2(Me)_2(NORPHOS)}]_{20}[\mathrm{MTD}]_{300}$$

Figure 1.8: Incorporation of Ag and Au into $[\mathrm{MTD}]_{300}[\mathrm{NORPHOS}]_{20}$

respectively. Subsequent TEM analysis revealed the formation of Ag (20-100 Å) and Au (15-40 Å) clusters, which resided primarily within the original polyNORPHOS microdomains.

In addition to work with Ag and Au clusters, Dr. Chan[52] developed the organometallic monomers [Pd] and [Pt] shown in Figure 1.5. Gordon Craig[53] then prepared nanoclusters of Pd and Pt using [Pd] and [Pt] respectively. The polymers $[\mathrm{MTD}]_{113}[\mathrm{Pd}]_{50}$, $[\mathrm{MTD}]_{163}[\mathrm{Pd}]_{10}$, and $[\mathrm{MTD}]_{200}[\mathrm{Pt}]_{40}$ were synthesized in toluene. The Pd containing films were reduced under a hydrogen pressure of 5 bars at 100 °C for several days. The Pt containing films were reduced by exposure to UV light for 24 hours followed by the previously described hydrogen treatment.

TEM micrographs of $[\mathrm{MTD}]_{113}[\mathrm{Pd}]_{50}$, $[\mathrm{MTD}]_{163}[\mathrm{Pd}]_{10}$, and $[\mathrm{MTD}]_{200}[\mathrm{Pt}]_{40}$ before reduction, showed the films had lamellar, spherical, and cylindrical morphologies respectively. Both TEM and SAXS were used to determine the interdomain spacings in the films. In all cases, reduction resulted in the formation of metal clusters (20-50 Å) which were homogeneously dispersed, largely within the original organometallic microdomains. Characteristic WAXS patterns confirmed the films contained f.c.c. Pd and Pt crystals.

In addition to work with pure metals, the synthesis of metal compounds within microphase separated block copolymers has been extensively studied. Vishak Sankaran[54] successfully prepared films containing ZnS, $\mathrm{ZnF_2}$, PbS, and CdS clusters. It was demonstrated that ZnS clusters could be converted to $\mathrm{ZnF_2}$ clusters at room temperature by treatment with a HF-pyridine complex. Furthermore, X-ray photoelectron spectroscopy studies, with ZnS clusters, showed the band-edge separation increased from 3.5 eV for bulk ZnS to 5.7 eV for 30 Å diameter clusters.

Jiang Yue, a postdoctoral researcher in the Cohen group, studied $[MTD]_{800}[NORCOOH]_{30}$, $[MTD]_{600}[NORCOOH]_{40}$, and $[MTD]_{600}[NORCOOH]_{30}$ block copolymers, and developed a "universal" technique for metal sulfide nanocluster synthesis.[55] It was found that several different metal ions including Cd^{+2}, Co^{+2}, Cu^{+2}, Fe^{+2}, Pb^{+2}, and Zn^{+2}, from aqueous metal chloride solutions, could be substituted for hydrogen ions within the polyNORCOOH domains. Subsequent treatment of the films with H_2S yielded metal sulfide clusters and was thought to restore the carboxylic acid functionality. Experiments were conducted in which ZnS was formed first, followed by CdS. Scanning transmission electron microscopy (X-ray microprobe analysis) maps showed that the Zn, Cd, and S were essentially restricted to the polyNORCOOH microdomains. It was hypothesized that CdS nucleated on the surface of existing ZnS clusters forming shell & core type structures.

Researchers in the Cohen and Schrock groups have demonstrated the synthesis of metal and semiconductor nanoclusters confined within the microdomains of block copolymers. Metal cluster synthesis is possible using organometallic monomers, and semiconductor cluster synthesis may be achieved through chemical treatment of organometallic or purely organic block copolymers. Spherical, cylindrical, and lamellar morphologies have been observed, and it was shown that morphology can be controlled by varying copolymer block lengths. Semiconductor clusters have been synthesized, and the band-edge separation was shown to increase with decreasing ZnS cluster size. Furthermore, it was shown that the copolymer microdomains could serve as nanoscale reactors.

The work described above clearly demonstrates the feasibility of synthesizing metal and semiconductor nanoclusters in-situ within the domains of microphase separated block copolymers. However, electric and catalytic cluster properties remain largely unexplored, and several questions remain to be answered. Furthermore, the "universal" synthesis technique for metal sulfide clusters has yet to be extended to pure metals.

1.4. "Universal" Metal Nanocluster Synthesis Method

1.4.1. Objective

The purpose of this project is to develop a general and simple method for the synthesis of several types of uniformly sized and homogeneously dispersed transition metal nanoclusters, stabilized within microphase-separated diblock copolymers. Organometallic block copolymers containing [Pd] or [Pt] blocks offer one method for the synthesis of uniformly sized and evenly dispersed metal nanoclusters. In these materials the nanoscale distribution of metal clusters within the film can be precisely controlled by varying the ratio of the organic to organometallic block lengths to produce spherical, cylindrical, or lamellar morphologies. However, this technique is neither general nor simple. A different organometallic monomer must be synthesized for each metal one wishes to incorporate into the polymer. In addition, even after synthesis routes to organometallic monomers are discovered, manufacture generally requires several complicated reaction and separation steps. We propose to eliminate the need for organometallic monomers by expanding Dr. Yue's "universal" semiconductor cluster method[55] to the synthesis of pure metal clusters.

1.4.2. Method of Approach

In our strategy, shown in Figure 1.9, metal ions or complexes are coordinated to carboxylic acid groups within the water soluble polyNORCOOH domains of a $[MTD]_{400}[NORCOOH]_{50}$ block copolymer by immersion of the polymer in aqueous metal salt solutions. The metal ions and complexes are subsequently reduced by heating the metal loaded polymer under hydrogen (ions with positive electrochemical reduction potentials) or by immersion in aqueous sodium borohydride (ions with negative electrochemical reduction potentials). For several transition metals, the resulting nanoclusters are uniformly sized and

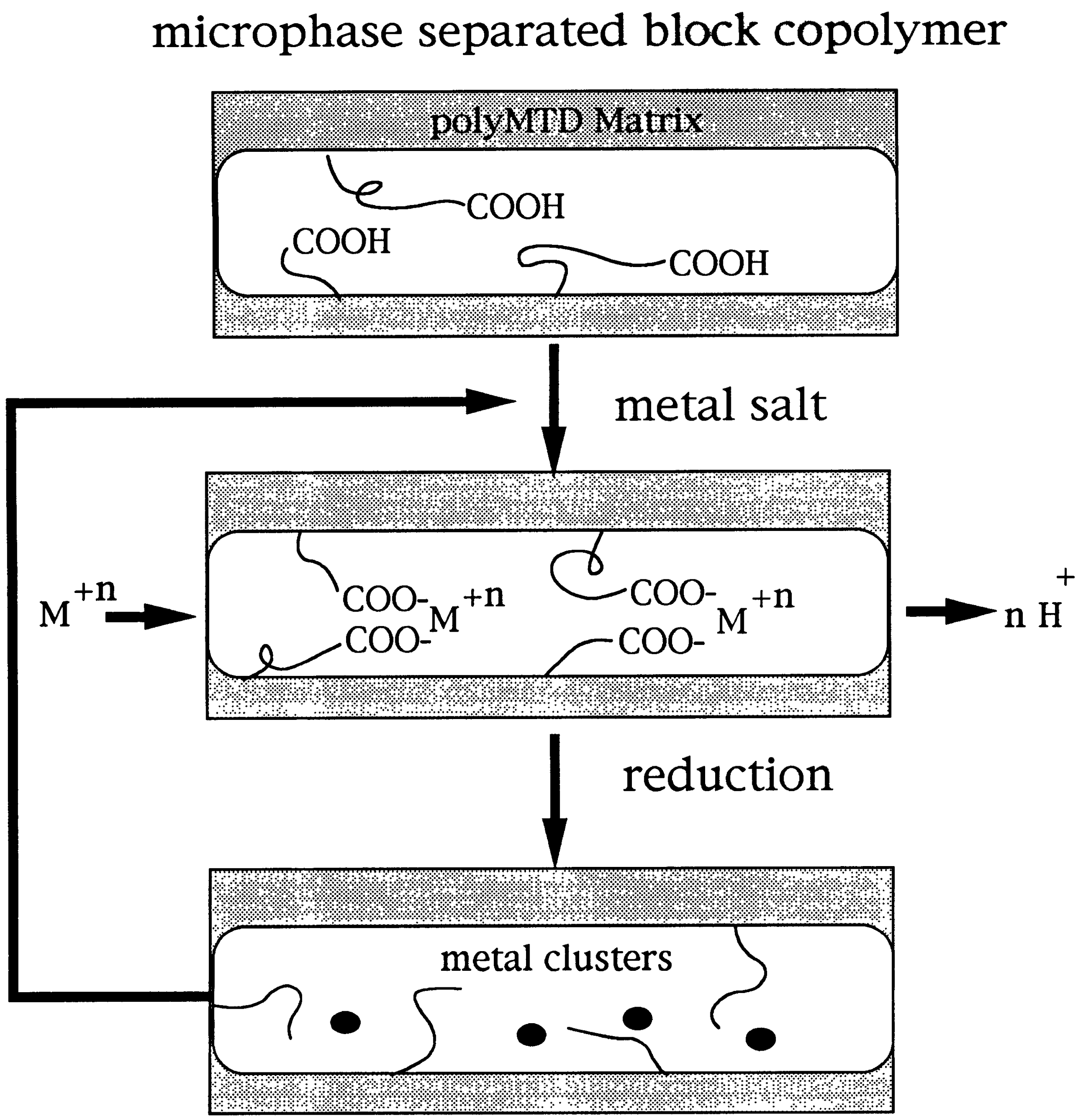

Figure 1.9: "Universal" metal cluster synthesis method

homogeneously dispersed within the polyNORCOOH domains. This cluster synthesis scheme uses the microphase-separated morphology of the block copolymer as a kinetic barrier to both cluster aggregation and cluster migration from the glassy polyNORCOOH domains to the glassy polyMTD matrix. This technique is potentially useful because it allows simple in situ synthesis of several types of metal nanoclusters within a matrix whose morphology can be controlled by varying polymer block lengths. This technique allows for the possibility of cluster size control through multiple metal loading and reduction cycles. This technique also allows for the possibility of alloy and shell & core cluster synthesis through parallel and series metal loading and reduction respectively.

In addition to demonstrating the feasibility of our general approach to metal cluster synthesis, we also investigated the rate of metal ion transport into the block copolymer and the nature of metal loading in the polyNORCOOH domains, through a series of inductively coupled plasma atomic emission spectroscopy experiments. The color of metal cluster containing films was studied using ultraviolet-visible spectroscopy. The chemical structure of our films was studied prior to ion loading, after ion loading, and after ion reduction with infrared spectroscopy. We compared the rate and extent of metal ion uptake between carboxylic acid and sodium carboxylate functionalized films. The Ag^+ loading capacity of sodium carboxylate functionalized films was explored following several loading and reduction sequences. The relationship between the extent of Ag^+ loading and cluster size was studied, for carboxylic acid functionalized films, during a single loading and reduction sequence.

Chapter 2

Synthesis and Characterization of Monomers and Polymers

2.1. Monomers

2.1.1. MTD

Methyltetracyclododecene (MTD, C.A.S. 21681-47-0) is a strained cyclic olefin with the chemical structure shown below in Figure 2.1.

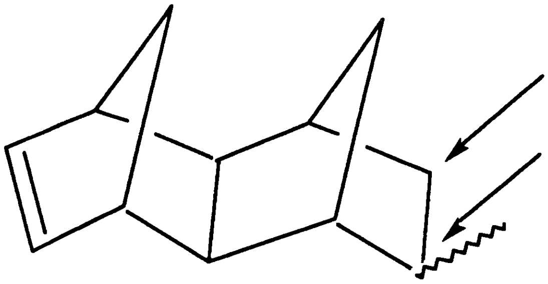

Figure 2.1: Chemical structure of MTD

The methyl group may appear on either of the designated carbon atoms, and may occur in either the endo (opposite side of the ring as bridging carbon) or exo (same side of ring as bridging carbon) orientations. MTD can be synthesized in a Diels-Alder reaction involving propylene, cyclopentadiene, and methylnorbornene, at pressures of 500-4000 psig and temperatures of 200-300 °C.[56] MTD is a clear viscous liquid which boils at 225 °C, melts at -44°C, and has a density of 0.989 g/cm^3.[57]

The MTD used in our experiments was donated by the BFGoodrich Company (Brian Goodall 216-447-5389). The donated MTD has a very slight yellowish tint which may be removed through vacuum distillation; however, I have found that only an oxygen degassing (several freeze-pump-thaw cycles) is necessary to prepare the air-stored, donated MTD for ROMP. Two bottles of degassed MTD are located in the 66-357 drybox; an additional bottle of air-stored MTD is located under hood 357-B. It seems the de-oxygenated MTD may be stored under nitrogen indefinitely prior to use.

2.1.2. NORCOOH and NORCOOTMS

2-norbornene-5,6,-dicarboxylic acid (NORCOOH) is a dicarboxylic acid functionalized norbornene with the structure shown below in Figure 2.2.

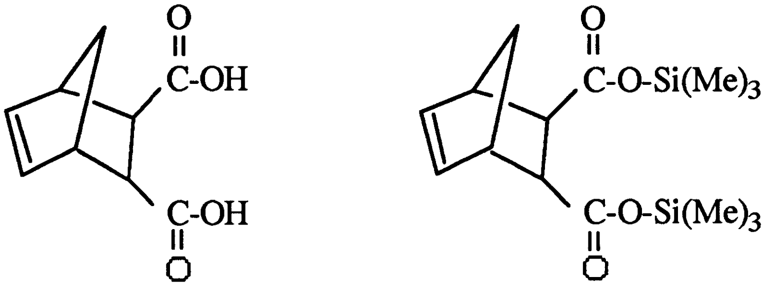

NORCOOH NORCOOTMS

Figure 2.2: Chemical structures of NORCOOH and NORCOOTMS

A mono-carboxylic acid functionalized norbornene is commercially available from Aldrich, but NORCOOH is not. NORCOOH is synthesized in a room temperature Diels-Alder reaction between cyclopentadiene and fumaric acid, as described in Appendix C. NORCOOH is a white solid. One carboxylic acid group must be endo, and the other exo due to the trans configuration of the carboxylic acid groups in fumaric acid. Prior to polymerization with a Schrock initiator, NORCOOH must be converted to 2-norbornene-5,6,-dicarboxylic acid-bis trimethylsilyl ester (NORCOOTMS), whose structure is shown in Figure 2.2, using the procedure outlined in Appendix C. Schrock initiators are deactivated by acids; therefore, the acidic groups must be capped prior to polymerization. NORCOOTMS is also a white solid. Traces of moisture will slowly convert NORCOOTMS back to NORCOOH; therefore, NORCOOTMS must be refrigerated under N_2 and recrystallized from pentane every six months or so to minimize the NORCOOH content.

2.1.3. NORCOH and NORCOTMS

2-norbornene-5-methanol (NORCOH) is available from Aldrich and has the structure shown below in Figure 2.3.

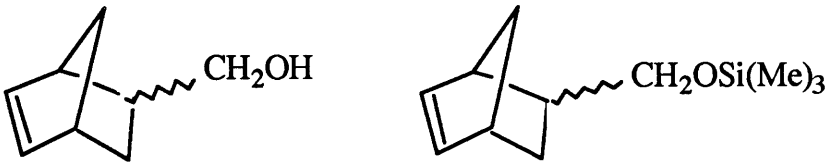

NORCOH NORCOTMS

Figure 2.3: Chemical structures of NORCOH and NORCOTMS

Both endo and exo isomers are present. NORCOH is a slightly yellowish liquid which boils at 97 °C (20 mm Hg), and has a density of 1.027 g/cm^3.[58] Prior to polymerization with a Schrock initiator, NORCOH must be converted to NORCOTMS, whose structure is shown in Figure 2.3, using the procedure outlined in Appendix C. Schrock initiators are deactivated by acids; therefore, the mildly acidic alcohol groups must be capped prior to polymerization. NORCOTMS is also a yellowish liquid, and should be refrigerated under N_2 to prevent conversion back to the alcohol form.

2.2. Polymers

2.2.1 Synthesis

MTD, NORCOOTMS, and NORCOTMS monomers all undergo ROMP with Schrock initiators in anhydrous toluene. As an example, a $[MTD]_{400}[NORCOOH]_{50}$ diblock copolymer was synthesized, where the numerical subscripts refer to the number of equivalents of each monomer that were sequentially added to 1 equivalent of metal alkylidene initiator, $Mo(CHCMe_2Ph)(NAr)(O\text{-}t\text{-}Bu)_2$.[18,59] As shown in Figure 2.4, a solution of $Mo(CHCMe_2Ph)(NAr)(O\text{-}t\text{-}Bu)_2$ (7 mg, 0.014 mmol) in 0.874 ml anhydrous toluene was added in one shot to a rapidly stirred solution of MTD (1.02 g, 5.85 mmol) in 20 ml anhydrous toluene. After 35 min., 0.175 ml of solution was removed for gel permeation chromatography analysis and quenched with 10 μl benzaldehyde. NORCOOTMS (0.234 g, 0.717 mmol) in 5 ml anhydrous toluene was added to the remaining solution, and the mixture was stirred for 30 min. and then quenched with excess benzaldehyde (20 μl, 45 min. reaction time). Only one mole of benzaldehyde per mole of living polymer is stoichiometrically required; however, approximately 10 moles of benzaldehyde per mole of living polymer are generally added to assure complete termination. Previous studies with metal alkylidene initiators have shown the number of equivalents of each monomer added is approximately equal to the degree of polymerization of the individual blocks.[18] The polymerization was conducted at room temperature in an Innovative Technology drybox, under a nitrogen atmosphere, since $Mo(CHCMe_2Ph)(NAr)(O\text{-}t\text{-}Bu)_2$ is rapidly deactivated by moisture and oxygen.[60]

The block copolymer containing reaction mixture was removed from the drybox. According to Figure 2.5, 10 ml of de-ionized water was added to acidify the polyNORCOOTMS. Soon after stirring begins, the mixture becomes milky and takes on a gluey consistency. However, the mixture was stirred overnight to assure complete acidification. The diblock copolymer was precipitated in 300 ml of stirred pentane, washed twice with 100 ml of pentane (to remove the initiator), and isolated by filtration. The block

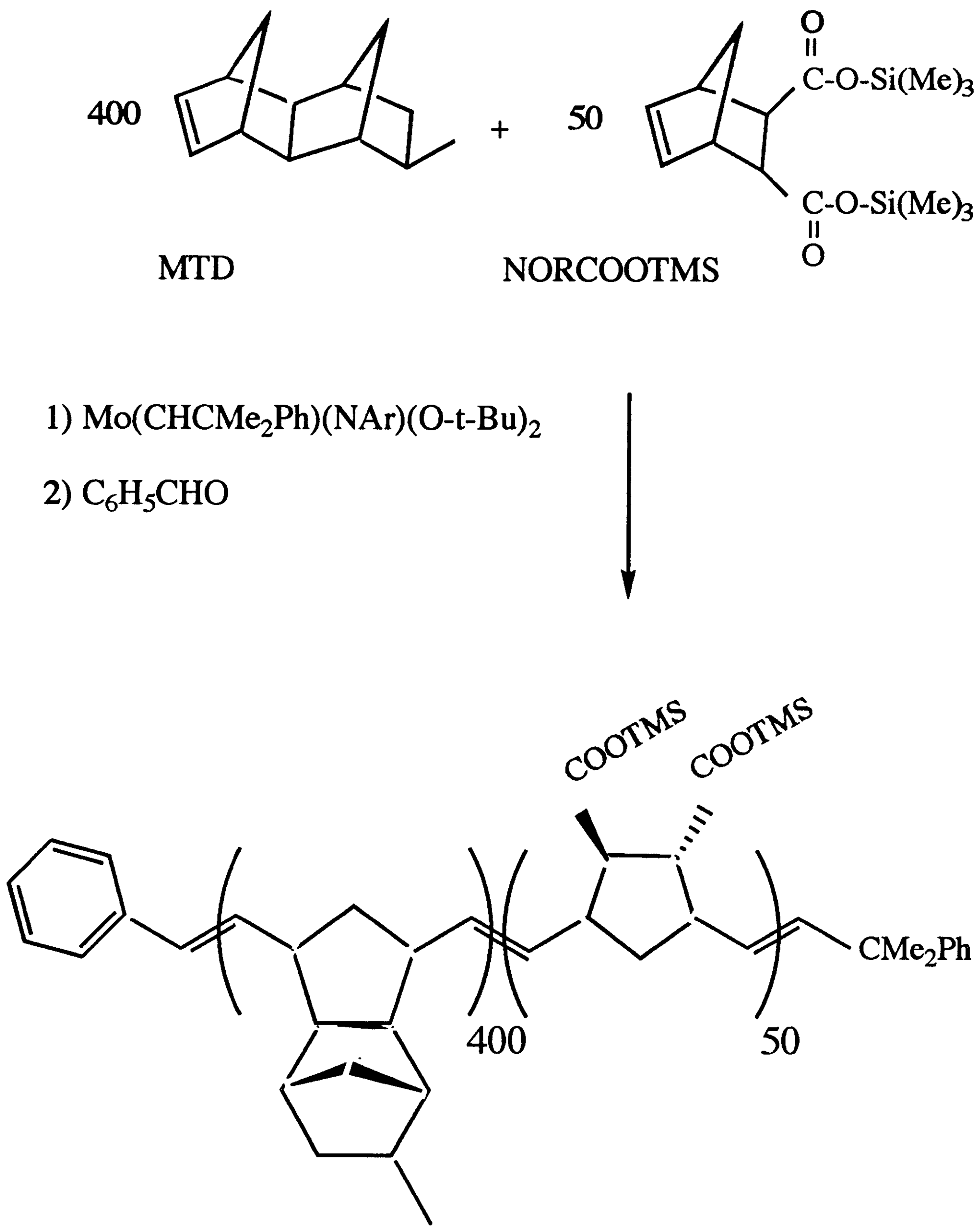

$[MTD]_{400}[NORCOOTMS]_{50}$

Figure 2.4: Block copolymer synthesis

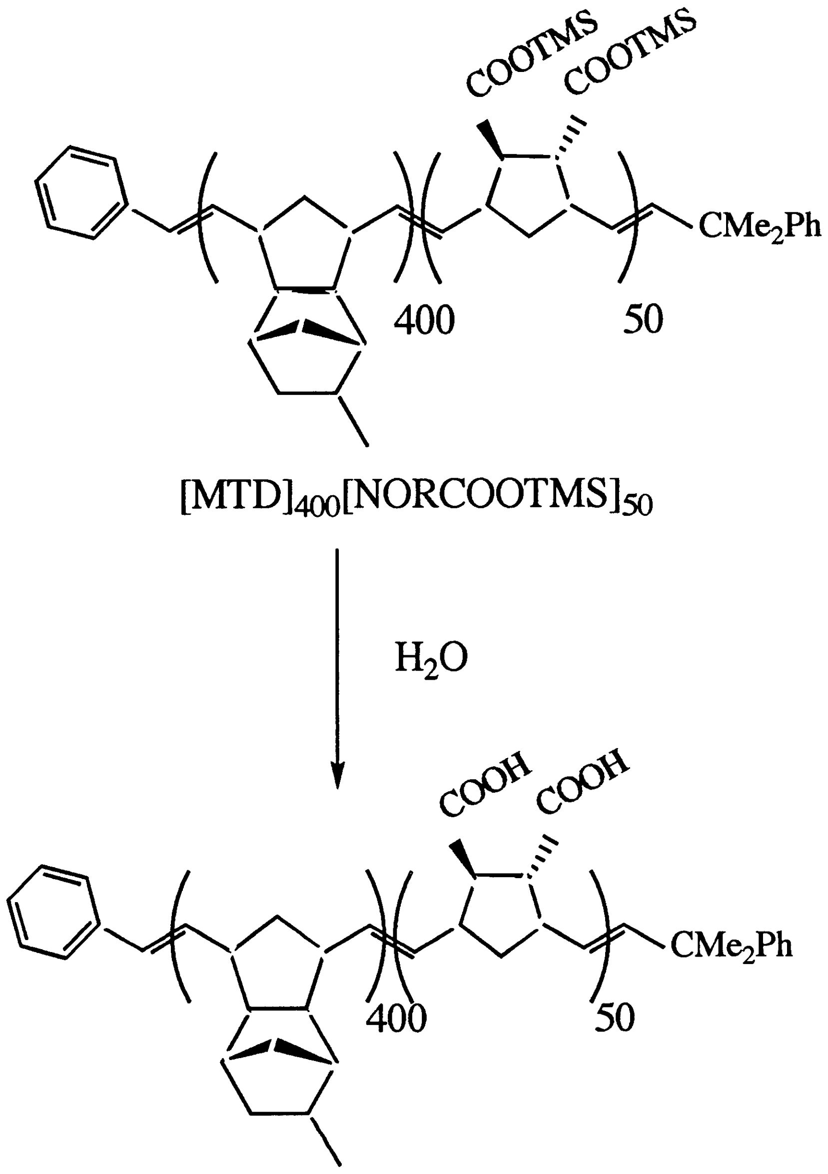

$[MTD]_{400}[NORCOOTMS]_{50}$

$[MTD]_{400}[NORCOOH]_{50}$

Figure 2.5: PolyNORCOOTMS acidification

copolymer was then pressed to remove excess pentane, cut into small pieces, and dried at room temperature for several days under vacuum, until the mass of the film stopped decreasing. This procedure typically results in recoverable polymer yields of 90-95%, assuming zero residual pentane or toluene. Higher yields are not achievable due to polymer adhesion to the glassware. The final polymer is often slightly yellowish in color, presumably due to residual initiator. Deionized water must be used for polyNORCOOTMS acidification because ions present in tap water will coordinate to carboxylic acid groups in polyNORCOOH.

GPC analysis of the homo-$[\mathrm{MTD}]_{400}$ block usually yields polydispersity indices between 1.05 and 1.1. However, both moisture and oxygen contamination can greatly increase the polydispersity. Traces of moisture are believed to increase the activity of the Schrock initiator and result in undesired, very high molecular weight (MW) polymer.[60] Oxygen contamination is believed to cause linking of living chains during quenching, which results in a final product containing some fraction of polymer with twice the desired MW.[60] Using fresh anhydrous toluene, stirred over sodium spheres (1-3 days, under nitrogen) prior to use, it is possible to prevent formation of very high MW polymer; however, GPC analysis frequently indicates that approximately 10% of the polymer product has twice the desired MW. It was observed that delays between polymerization and benzaldehyde quenching tended to increase the fraction of doubled MW polymer. It is often possible to prevent formation of polymer with twice the desired MW by conducting the polymerization of hydrocarbon (non-functionalized) monomers in the presence of sodium. I recommend against the use of sodium during polymerization of functionalized monomers, because it may lead to undesirable reductions. The block copolymer was not analyzed using GPC because polyNORCOOTMS precipitates as polyNORCOOH in wet toluene.

PolyMTD, polyNORCOOH, and polyNORCOH all contain carbon-carbon double bonds (c=c), which are less stable to oxidation than carbon-carbon single bonds. These c=c bonds may be easily hydrogenated by reaction with diimide (NH=NH) in p-xylene at 1 atm and 120 °C.[61]

NEVER ALLOW SODIUM TO COME INTO DIRECT CONTACT WITH TEFLON COATED STIR BARS! Both the sodium and stir bar must be immersed in a solvent, under nitrogen, otherwise a fire and explosion may result. Sodium reacts exothermically with halogens.

2.2.2 PolyMTD

$[MTD]_x$ can be synthesized using the same procedure as outline above; in which case, the living polyMTD should be quenched with benzaldehyde, and no second type of monomer added. GPC analysis indicates that $Mo(CHCMe_2Ph)(NAr)(O\text{-}t\text{-}Bu)_2$ can polymerize 400 units of MTD within 25 minutes. Figure 2.6 shows the infrared (IR) spectra of a 10 μm thick $[MTD]_{200}$ film, static cast from a 0.5 wt. % solution in toluene. The most prominent feature is the strong C-H absorption at 2850-2960 cm^{-1}.

PolyMTD is a glassy polymer; however, no endotherms were observed during our attempts to determine the glass transition temperature of $[MTD]_{200}$ using differential scanning calorimetry (DSC). $[MTD]_{200}$ was observed to flow after heating, in air, to temperatures greater than 180 °C, for a period of five minutes. PolyMTD was chosen as the matrix block because it is transparent, easily processable (toluene solubility > several wt. %), readily available, and has a relatively high thermal stability.

2.2.3 PolyNORCOOTMS and PolyNORCOOH

$[NORCOOTMS]_x$ can be polymerized by a procedure similar to the one outlined above. Add a NORCOOTMS solution (~0.05-0.1 g/ml) in anhydrous toluene to an appropriate amount of $Mo(CHCMe_2Ph)(NAr)(O\text{-}t\text{-}Bu)_2$, also dissolved in anhydrous toluene. Functional groups often slow ROMP reactions[60], so I allow 30 minutes for the polymerization of a 40 unit chain. Terminate the living polymer chains with excess

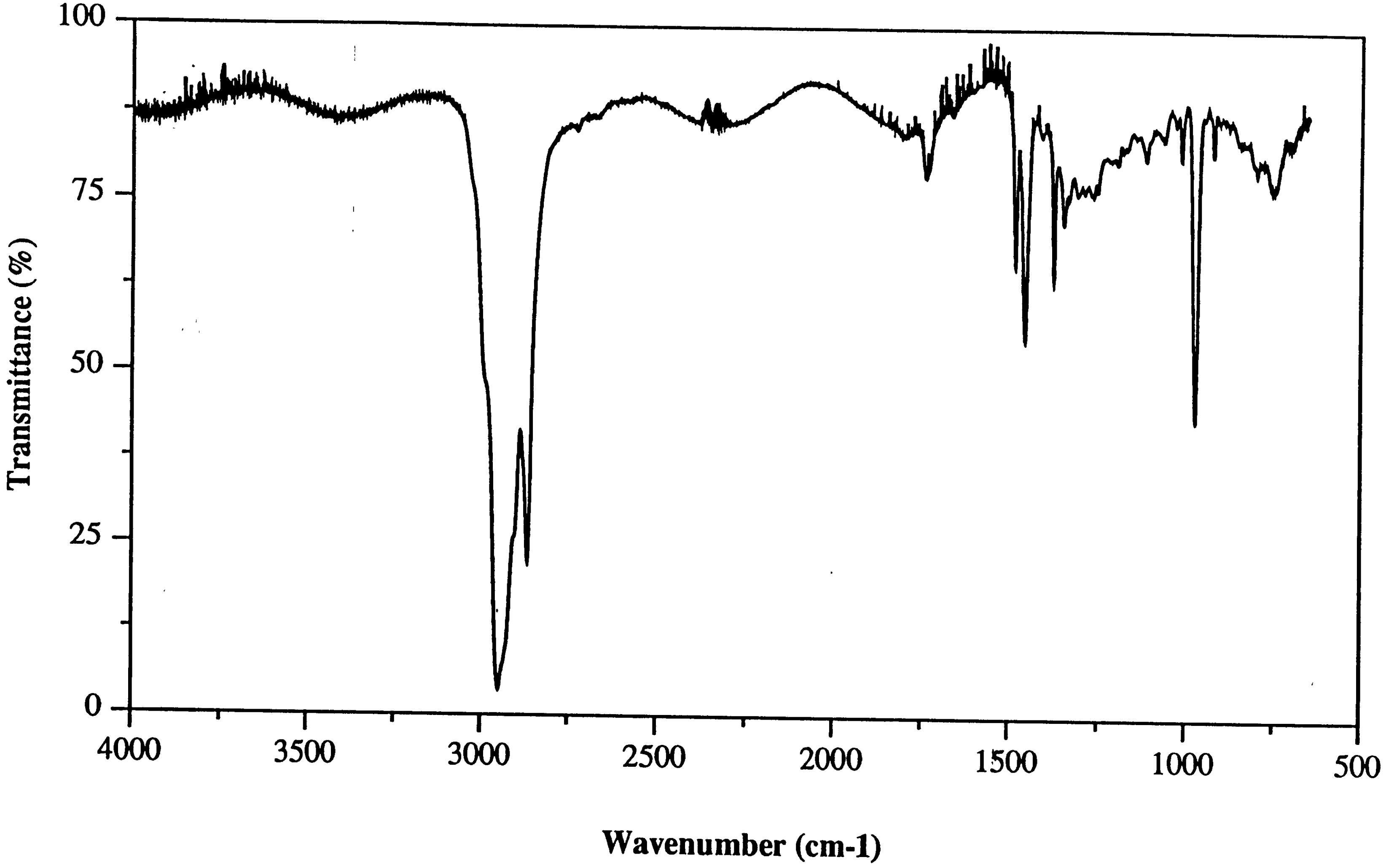

Figure 2.6: Infrared spectra of [MTD]200

benzaldehyde. Consult Randall Saunders' thesis (ref. 60, p. 200) for more detailed synthesis directions.

Remove the polymer solution from the drybox and mix with 8 ml pentane and 10 ml 20 wt. % aqueous acetic acid solution for each ml of polymer solution. Shake vigorously and stir three hours. $[NORCOOTMS]_x$ acidification will occur and $[NORCOOH]_x$ will accumulate at the aqueous/organic interface. Vacuum filter the entire mixture through a disk of filter paper, supported by a Buchner funnel. A bit of greenish-yellow, initiator rich, polymer residue will remain on the filter paper. Most of the polymer remains in the filtered solution. Remove the yellow, initiator rich, organic layer from the clear, aqueous, polyNORCOOH rich layer with a pipette. Recover the polyNORCOOH by allowing water to evaporate from the aqueous solution in a glass dish.

Figure 2.7 shows the IR spectra of a ca. 30 μm thick $[NORCOOH]_{200}$ film, static cast as outlined above. The O-H (2500-3300 cm^{-1}) and C=O (1670-1780 cm^{-1}) absorptions are clearly visible, while the C-H (2850-2960 cm^{-1}) absorption is obscured by the O-H absorption.[62]

PolyNORCOOH is a glassy polymer; however, no endotherms were observed during our attempts to determine the glass transition temperature of $[NORCOOH]_{200}$ using DSC. $[NORCOOH]_{200}$ was observed to decompose (turn from clear to brownish) after heating, in air, to temperatures greater than 180 °C, for a period of five minutes.

Several functional groups such a amines,[60] phosphines,[49] and iminodiacetic acids,[63] are known to coordinate metal ions. We chose to sequester metal ions within our polymer films using carboxylic acid groups because of the relative ease with which polyNORCOOH can be synthesized. However, polyNORCOOH is a difficult homopolymer to work with because it has a very low solubility in solvents such as acetone, methanol, THF, and toluene. PolyNORCOOH has a water solubility of at least 3 wt. %, but attempts to cast films from 3 wt. % solutions of polyNORCOOH in water produced thick, porous lumps. In order to cast

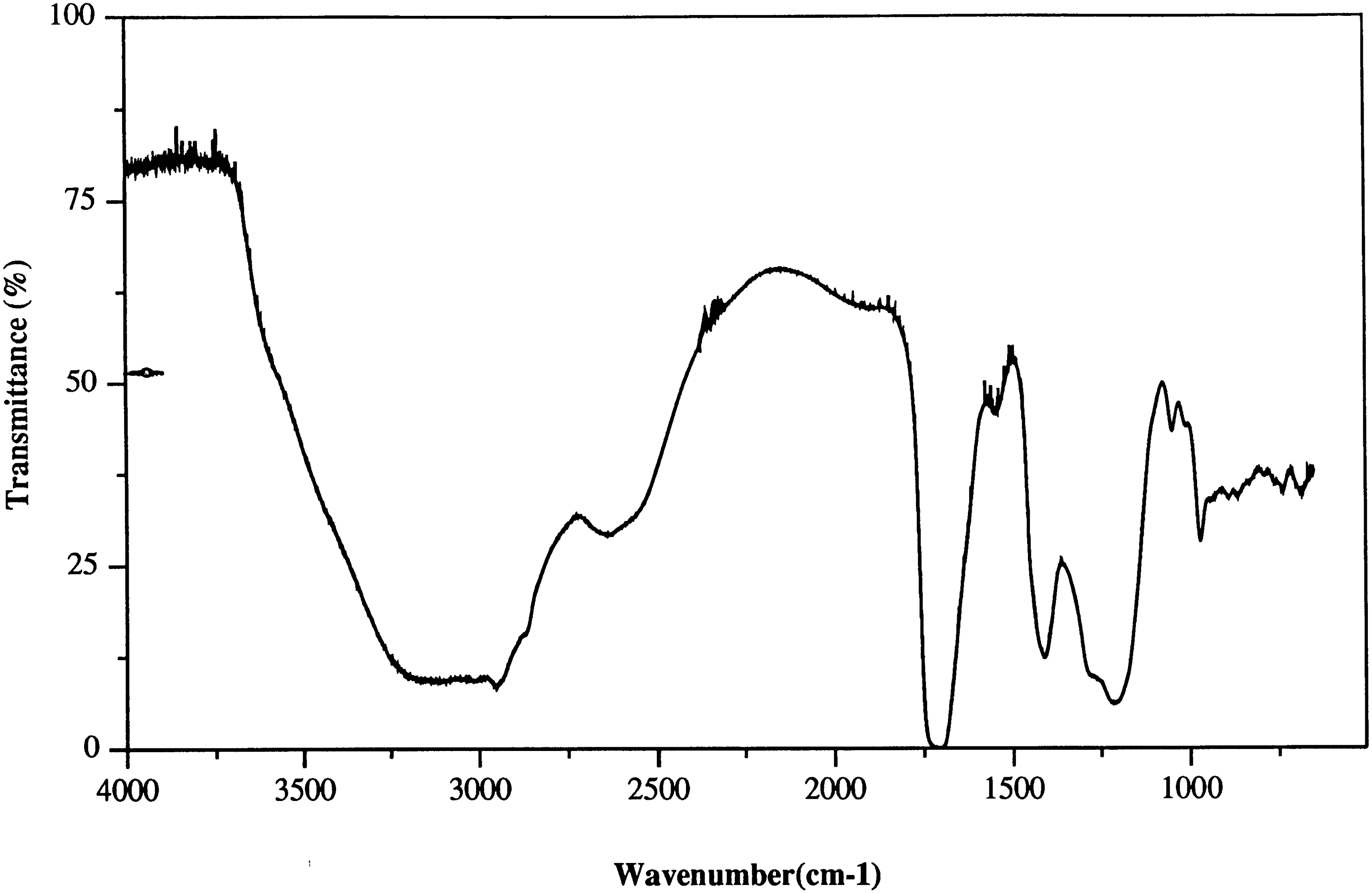

Figure 2.7: Infrared spectra of [NORCOOH]200

clear, non-porous polyNORCOOH films, begin with a freshly polymerized polyNORCOOTMS solution (in toluene) as outlined above.

2.2.4 PolyNORCOTMS and PolyNORCOH

$[NORCOTMS]_x$ can be polymerized by a procedure similar to the one outlined above. Add a NORCOTMS solution (~0.05-0.1 g/ml) in anhydrous toluene to an appropriate amount of $Mo(CHCMe_2Ph)(NAr)(O\text{-}t\text{-}Bu)_2$, also dissolved in anhydrous toluene. Little is known about the polymerization kinetics of NORCOTMS, so I allow 30 minutes for each 50 NORCOTMS units in the polymer. Terminate the living polymer chains with excess benzaldehyde.

Remove the polymer solution from the drybox and mix with 0.5 ml of de-ionized water for each ml of polymer solution. Shake vigorously and stir overnight. $[NORCOTMS]_x$ acidification will occur forming $[NORCOH]_x$, and the mixture will become milky and viscous. Precipitate polyNORCOH by adding dropwise to methanol. Isolate polyNORCOH by filtration, press to remove excess methanol, and dry under vacuum at room temperature. $[NORCOH]_{200}$ is insoluble in toluene, but forms a suspension, suitable for film casting, in THF (2 wt. % $[NORCOH]_{200}$).

$[MTD]_{400}[NORCOH]_{50}$ was synthesized by the same procedure outlined for $[MTD]_{400}[NORCOOH]_{50}$; however, the $[MTD]_{400}[NORCOH]_{50}$ was precipitated from 200 ml of stirred methanol rather than pentane. Methanol appears to extract a large fraction of the residual initiator from $[MTD]_{400}[NORCOH]_{50}$, as evidenced by the white color of the polymer precipitate. $[MTD]_{400}[NORCOH]_{50}$ appears to dissolve rapidly to form 3 wt. % solutions in toluene; however, when stirring is stopped, phase separation occurs. Both an upper polymer poor layer and a lower (cloudy) polymer rich layer were observed. $[MTD]_{400}[NORCOH]_{50}$ forms homogeneous solutions in THF; however, the solubility is less than 3 wt. %.

2.3. References for Chapters 1 & 2

(1) Noshay, A. and McGrath, J.E. 'Block Copolymers: Overview and Critical Survey', Academic Press Inc., New York, 1977.

(2) Flory, P.J. 'Principles of Polymer Chemistry', Cornell University Press, Ithaca, 1953, p. 508.

(3) Sadron, C. and Gallot, B. *Die Makromolekulare Chemie* **1973**, 164, 301.

(4) Helfand, E. and Wasserman, Z.R. *Macromolecules* **1976**, 9, 879.

(5) Helfand, E. and Wasserman, Z.R. *Macromolecules* **1978**, 11, 960.

(6) Helfand, E. and Wasserman, Z.R. *Macromolecules* **1980**, 13, 994.

(7) Thomas, E.L., Alward, D.B., Kinning, D.J., Martin, D.C., Handlin, D.L., and Fetters, L.J. *Macromolecules* **1986**, 19, 2197.

(8) Csernica, J., Baddour, R.F., and Cohen, R.E. *Macromolecules* **1990**, 23, 1429.

(9) Merrill, W. and Rempp, P. 'Polymer Synthesis', 2nd Ed., Huthig & Wepf Verlag Basel, New York, 1991, p. 116.

(10) Truett, W.L., et al. *J. Am. Chem. Soc.* **1960**, 82, 2337.

(11) Dall'Asta, G., Mazzanti, G., Natta, G., and Porri, L. *Makromol. Chem.* **1962**, 69, 224.

(12) Calderon, N., Ofstead, E.A., Ward, J.P., Judy, W.A., and Scott, K.W. *J. Am. Chem. Soc.* **1968**, 90, 4133.

(13) Dall'Asta, G., Motroni, G., and Motta, L. *J. Polym. Sci.: Part A-1* **1972**, 10, 1601.

(14) Herisson, P.J. and Chauvin, Y. *Die Makromolekulare Chemie.* **1970**, 141, 161.

(15) Ivin, K.J. 'Olefin Metathesis', Academic Press, New York, 1983, p. 332.

(16) Ivin, K.J. In 'Ring Opening Polymerization', K.J. Ivin and T. Saegusa, Ed., Elsevier Applied Science Publishers, New York, 1984, Vol. 1, p. 121.

(17) Calderon, N., Chen, H.Y., and Scott, K.W. *Tetrahedron Lett.* **1967**, 3327.

(18) Schrock, R.R, Murdzek, J.S., Bazan, G.C., Robbins, J., DiMare, M., and O'Regan, M.J. *J. Am. Chem. Soc.* **1990**, 112, 3875.

(19) Schrock, R.R., DePue, R.T., Feldman, J., Yap, K.B., Yang, D.C., Davis, W.M., Park, L.Y., DiMare, M., Schofield, M., Anhaus, J., Walborsky, E., Evitt, E., Kruger, C., and Betz, P. *Organometallics.* **1990**, 9, 2262.

(20) Bazan, G.C., Schrock, R.R., Cho, H.N., and Gibsson, V.C. *Macromolecules* **1991**, 24, 4495.

(21) Nguyen, S.T. and Grubbs, R.H. *J. Am. Chem. Soc.* **1993**, 115, 9858.

(22) Kanaoka, S. and Grubbs, R.H. *Macromolecules* **1995**, 28, 4707.

(23) Henglein, A. *Chem. Rev.* **1989**, 89, 1861.

(24) Bradley, J.S., Hill, E.W., Behal, S., Klein, C., Chaudret, B., and Duteil, A. *Chem. Mater.* **1992**, 4, 1234.

(25) Ercolessi, F., Andreoni, W., and Tosatti, E. *Physical Review Letters.* **1991**, 66, 911.

(26) Buffat, P. and Borel, J.P. *Physical Review A.* **1976**, 13, 2287.

(27) Hache, F., Ricard, D., and Flytzanis, C. *J. Opt. Soc. Am. B.* **1986**, 3, 1647.

(28) Craig, G.S.W. Ph.D. Thesis (Chem. E.), Massachusetts Institute of Technology, **1993**.

(29) Laurent, C. and Kay, E. *J. Appl. Phys.* **1988**, 64, 336.

(30) Canet, P., Laurent, C., Akinnifesi, J. and Despax, B. *J. Appl. Phys.* **1992**, 72, 2423.

(31) Satterfield, C.N. 'Heterogeneous Catalysis In Industrial Practice', 2nd Ed., McGraw-Hill, Inc., New York, 1991.

(32) Kilty, P.A. and Sachtler, W.M.H. *Catal. Rev.-Sci. Eng.* **1974**, 10, 1.

(33) Seglin, L., Geosits, R., Franko, B.R., and Gruber, G. In 'Methanation of Synthesis Gas', L. Seglin, Ed., ACS Symposium on Methanation of Synthesis Gas, Atlantic City, NJ, Sept. 9, 1974, American Chemical Society, Washington, 1975.

(34) Luengo, C.A., Cabrera, A.L., MacKay, H.B., and Maple, M.B. *J. Catalysis.* **1977**, 47, 1.

(35) Sinfelt, J.H. 'Bimetallic Catalysts', John Wiley & Sons, New York, 1983.

(36) Toshima, N., Harada, M., Yamazaki, Y., and Asakura, K. *J. Phys. Chem..* **1992**, 96, 9927.

(37) Brandrup, J. and Immergut, E.H. (Eds.) 'Polymer Handbook', 3rd Edition, John Wiley & Sons, New York, 1989.

(38) Pittman, C.U. In 'Comprehensive Organometallic Chemistry', Vol. VIII, G. Wilkinson, F.G.A. Stone, E.W. Abel, Eds., Pergamon Press, New York, 1982.

(39) Boutonnet, M., Kizling, J., Stenius, P., and Maire, G. *Colloids and Surfaces.* **1982**, 5, 209.

(40) Yatsuya, S., Mihama, K., and Uyeda, R. *Japan. J. Appl. Phys.* **1974**, 13, 749.

(41) Brus, L.E. and Siegel, R.W., et al. *J. Mater. Res.* **1989**, 4, 704.

(42) Klabunde, K.J., Habdas, J., and Cardenas-Trivino, G. *Chem. Mater.* **1989**, 1, 481.

(43) Heilmann, A. and Hamann, C. *Progr. Colloid Polym. Sci.* **1991**, 85, 102.

(44) Spatz, J.P., Roescher, A., Sheiko, S., Krausch, G. and Moller, M. *Adv. Mater.* **1995**, 7, 731.

(45) Spatz, J.P., Roescher, A., and Moller, M. *ABS 211th ACS National Meeting*, POLY 387, New Orleans, 1996.

(46) Mayer, A.B.R. and Mark, J.E. *ABS 211th ACS National Meeting*, POLY 396, New Orleans, 1996.

(47) Watkins, J.J. and McCarthy, T.J. *Chem. Mater.* **1995**, 7, 1991.

(48) Chan, Y.N.C., Schrock, R.R., Cohen, R.E. *J. Am. Chem. Soc.* **1992**, 114, 7295.

(49) Chan, Y.N.C. and Schrock, R.R. *Chem. Mater.* **1992**, 4, 24.

(50) Partenheimer, W. and Johnson, E.H. *Inorganic Chemistry.* **1973**, 12, 1274.

(51) Schmidbaur, H. and Shiotani, A. *Chem. Ber.* **1971**, 104, 2821.

(52) Chan, Y.N.C. and Schrock, R.R. *Chem. Mater.* **1993**, 5, 566.

(53) Chan, Y.N.C., Craig, G.S.W., Schrock, R.R., and Cohen, R.E. *Chem. Mater.* **1992**, 4, 885.

(54) Sankaran, V. Ph.D. Thesis (Chem. E.), Massachusetts Institute of Technology, **1993**.

(55) Yue, J. and Cohen, R.E. *Supramolec. Science* **1994**, 1, 117.

(56) Schneider, W., US Patent 4 320 239, **1982**.

(57) BFGoodrich, Materials Safety Data Sheet: Methyltetracyclododecene (C.A.S. 21681-47-0), DOC 86177, 1986.

(58) Aldrich, 'Catalog Handbook of Fine Chemicals', Aldrich Chemical Company, Inc., 1994-1995.

(59) Schrock, R.R. *Acc. Chem. Res.* **1990**, 24, 158.

(60) Saunders, R.S. Ph.D. Thesis (Chem.E.), Massachusetts Institute of Technology, **1992**.

(61) Sohn, B.H., Gratt, J.A., Lee, J.K., and R.E. Cohen *J. Apply. Polym. Sci.* **1995**, 58, 1041.

(62) McMurray, J. 'Organic Chemistry', 2nd Ed., Brooks/Cole Publishing, Pacific Cove, 1988, p. 397.

(63) Amberlite® IRC-718, Rohm and Haas Company, IE-313, 1993.

Chapter 3

Synthesis of Metal Nanoclusters within Microphase-Separated Diblock Copolymers: A "Universal" Approach

3.1. Summary

We now demonstrate the feasibility of the "universal" synthesis method, described in Figure 1.9, for the synthesis of several transition metal nanoclusters (Ag, Au, Cu, Ni, Pb, Pd, and Pt), stabilized within the carboxylic acid functionalized domains of microphase-separated $[MTD]_x[NORCOOH]_y$ films. In this technique the films are soaked in aqueous metal salt solutions prior to reduction of the sequestered metal ions with hydrogen or aqueous $NaBH_4$. Transmission electron microscopy (TEM) observation, scanning transmission electron microscopy observation, electron scattering analysis, and wide-angle X-ray scattering analysis, were used to characterize the size, composition, and crystal structure of the resulting metal nanoclusters. In many cases, the nanoclusters were uniformly sized, homogeneously dispersed within the polyNORCOOH domains, and composed of single crystals.

A variation of this "universal" technique was reported previously by our group for the particular case of pure and mixed semiconductor (metal sulfide) cluster synthesis.[1] In that case, metal loading of the polymer films was followed by treatment with hydrogen sulfide gas to produce clusters. Here we address the issue of reduction of the metallic species in loaded films and the quality of the zero-valent metal clusters formed in the process.

3.2. Experimental

$[MTD]_{400}[NORCOOH]_{50}$ and $[MTD]_{400}[NORCOOH]_{40}$ diblock copolymers were synthesized in a ring-opening metathesis polymerization, as described in section 2.2.1. Microphase-separated block copolymer films were static cast from a 3 wt. % solution in tetrahydrofuran (THF). The THF was allowed to evaporate over 5 days, and the resulting transparent yellowish films were dried under vacuum for 24 hr before further processing. As shown in Figure 3.1, TEM observation of microtomed (500 Å thick), Ag^+ stained, sections of $[MTD]_{400}[NORCOOH]_{40}$ revealed a non-equilibrium interconnected cylindrical morphology of polyNORCOOH cylinders within a polyMTD matrix. Both $[MTD]_{400}[NORCOOH]_{50}$ and $[MTD]_{400}[NORCOOH]_{40}$ are believed to have hexagonally packed cylindrical morphologies at equilibrium, because several hexagonally packed regions are also visible in Figure 3.1.

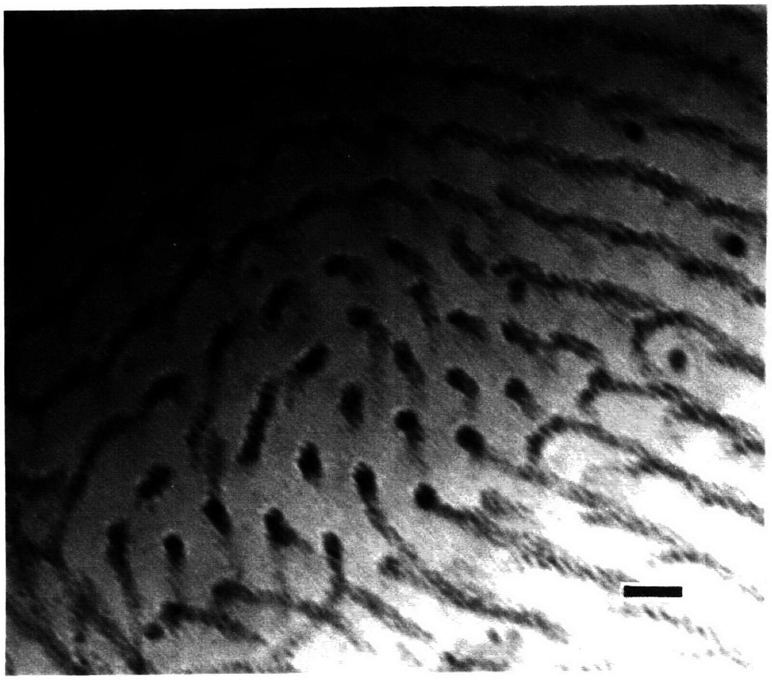

Figure 3.1: Electron micrograph of Ag^+ stained $[MTD]_{400}[NORCOOH]_{40}$ (bar = 300Å)

3.2.1. Immobilization of Metal Ions and Complexes

Both microtomed and bulk block copolymer films were loaded with metals. Microtomed films (400 Å) were first sliced thin, then metal loaded and reduced. Bulk films (4 mm x 4 mm x 0.5 mm) were loaded, reduced, and then microtomed prior to transmission electron microscopy (TEM) observation. Metal ions and complexes were loaded into the microtomed films by floating film-covered grids (gold, 400 mesh) upside-down on aqueous metal salt solutions according to Table 3.1.

Table 3.1 Metal loading of microtomed films

Species	Concentration, M	Temperature, °C	Time, hr
$Ag(OOCCH_3)$	0.005	25	30
$AuCl_3$	0.005	25	30
$Cu(OOCCH_3)_2$	0.005	25	30
$H_2PtCl_6x6H_2O$	0.005	65	18.5
$Na_2PdCl_4x3H_2O$	0.005	25	30
$NiCl_2$	0.1	25	54
$PbCl_2$	0.005	25	30

Bulk block copolymer samples were loaded with metal ions and complexes by immersing in aqueous metal salt solutions (10 ml) according to Table 3.2. Following reduction, the Ag, Au, Cu, Pd, and Pt containing films were loaded a second time with the same metal using the same procedure. Loading with $Ag(OOCCH_3)$ and $H_2PtCl_6x6H_2O$ was done in the dark to avoid photo-induced reduction of silver or platinum ions.

Table 3.2 Metal loading of bulk films

Species	Concentration, M	Temperature, °C	Time, hr
$Ag(OOCCH_3)$	0.06	25	330
$AuCl_3$	0.1	25	330
$Cu(OOCCH_3)_2$	0.1	25	330
$H_2PtCl_6x6H_2O$	0.1	65	167
$Na_2PdCl_4x3H_2O$	0.1	25	330
$NiCl_2$	0.1	25	330
$PbCl_2$	0.036	25	330

3.2.2. Reduction of Metal Ions and Complexes

Shown in Table 3.3 are standard electrochemical reduction potentials for the reduction of several metal ions and complexes to zero-valent metals.[2] The higher the reduction potential, the more easily the metal ions and complexes are reduced. Therefore, under the same conditions, Au^{+3} and Eu^{+2} are expected to be the most and least easily reduced ions respectively. Reduction, by hydrogen gas, of metal ions and complexes with positive reduction potentials is thermodynamically favored. Hydrogen gas reduction of metal ions and complexes with negative reduction potentials is not thermodynamically favored.

As outlined in Tables 3.4 and 3.5, for microtomed and bulk films respectively, samples loaded with Ag^+, Au^{+3}, $[PtCl_6]^{-2}$, $[PdCl_4]^{-2}$, and Cu^{+2}, were reduced with hydrogen gas, while those loaded with Pb^{+2} and Ni^{+2} were reduced in aqueous $NaBH_4$ solutions. The bulk Ag, Au, Cu, Pd, and Pt containing films which were loaded a second time, were then reduced a second time using the same procedure.

Table 3.3 Standard electrochemical reduction potentials

$Au^{+3} + 3e^-$	---> Au^0	1.401 V
$Pt^{+2} + 2e^-$	---> Pt^0	1.118 V
$Pd^{+2} + 2e^-$	---> Pd^0	0.951 V
$Ag^+ + e^-$	---> Ag^0	0.800 V
$[PtCl_4]^{-2} + 2e^-$	---> $Pt^0 + 4Cl^-$	0.755 V
$[PtCl_6]^{-2} + 2e^-$	---> $[PtCl_4]^{-2} + 2Cl^-$	0.680 V
$[PdCl_4]^{-2} + 2e^-$	---> $Pd^0 + 4Cl^-$	0.591 V
$Cu^{+2} + 2e^-$	---> Cu^0	0.342 V
$2H^+ + 2e^-$	**---> H_2**	**0.000 V**
$Fe^{+3} + 3e^-$	---> Fe^0	-0.037 V
$Pb^{+2} + 2e^-$	---> Pb^0	-0.126 V
$Ni^{+2} + 2e^-$	---> Ni^0	-0.257 V
$Co^{+2} + 2e^-$	---> Co^0	-0.280 V
$Fe^{+2} + 2e^-$	---> Fe^0	-0.447 V
$Eu^{+3} + 3e^-$	---> Eu^0	-2.407 V
$Na^+ + e^-$	---> Na^0	-2.710 V
$Eu^{+2} + 2e^-$	---> Eu^0	-3.395 V

Table 3.4 Reduction of metal loaded microtomed films

Species	Reduction Method	Temperature, °C	Time
Au^{+3}	H_2, 2 atm	115	135 hr
Ag^{+}	H_2, 2 atm	115	65 hr
$[PtCl_6]^{-2}$	H_2, 2 atm	115	65 hr
$[PdCl_4]^{-2}$	H_2, 2 atm	115	135 hr
Cu^{+2}	H_2, 2 atm	115	135 hr
Pb^{+2}	1 wt. % aqueous $NaBH_4$	25	10 min.
Ni^{+2}	1 wt. % aqueous $NaBH_4$	25	10 min.

Table 3.5 Reduction of metal loaded bulk films

Species	Reduction Method	Temperature, °C	Time, hr
Au^{+3}	H_2, 2 atm	115	144
Ag^{+}	H_2, 2 atm	115	144
$[PtCl_6]^{-2}$	H_2, 2 atm	115	144
$[PdCl_4]^{-2}$	H_2, 2 atm	115	144
Cu^{+2}	H_2, 2 atm	115	144
Pb^{+2}	1 wt. % aqueous $NaBH_4$	25	140
Ni^{+2}	1 wt. % aqueous $NaBH_4$	25	140

3.3. Results and Discussion

GPC analysis of the homo-MTD block yielded a polydispersity index of 1.10. The block copolymer was not analyzed using GPC because polyNORCOOTMS precipitates as polyNORCOOH in wet toluene. The static cast films were flexible, transparent, and pale yellow in color, probably due to trace residues of $Mo(CHCMe_2Ph)(NAr)(O\text{-}t\text{-}Bu)_2$.

3.3.1. Microtomed Films

Very low metal salt concentrations were necessary to prevent formation of metal salt crystals on the film surface during loading. In the case of $NiCl_2$, a 0.1M solution and 54 hr loading time was required to obtain sufficient contrast for TEM observation, possibly due to a low affinity of carboxylic acid groups for Ni^{+2} ions . In the case of $H_2PtCl_6x6H_2O$, floating on a 0.005 M aqueous solution for 30 hr failed to produce sufficient contrast for TEM observation; however, floating at 65°C for 18.5 hr, under ultrasonication, produced sufficient contrast . It is possible that the large size of the $[PtCl_6]^{-2}$ ions results in slow diffusion.

Several microtomed films remained intact on each grid following the metal loading and reduction procedures. The gold grids showed no evidence of degradation as a result of exposure to the metal salt solutions. As shown in Table 3.6, there was TEM evidence of metal loading and cluster formation following reduction in all metal loaded films. TEM revealed no contrast in the block copolymer films prior to metal loading. However, a non-equilibrium interconnected cylindrical morphology, with cylinder diameters of approximately 80 Å, became visible after metal loading selectively in the polyNORCOOH domains. It is believed that the metal ions and complexes are transported within the block copolymer primarily through the interconnected cylindrical network of polyNORCOOH.

Table 3.6 TEM results of metal loading and reduction in microtomed films

Species	**Evidence of Loading**	**H_2 Reduction Cluster Size, Å**	**$NaBH_4$ Reduction Cluster Size, Å**
Au^{+3}	Yes	10-20, 100+	-
Ag^{+}	Yes	40-70	-
$[PtCl_6]^{-2}$	Yes	20-30	-
$[PdCl_4]^{-2}$	Yes	25-50	-
Cu^{+2}	Yes	25-80	-
Pb^{+2}	Yes	-	30-40 and 100
Ni^{+2}	Yes	-	30-100

Hydrogen reduction of palladium, platinum , and silver loaded films resulted in the formation of clusters, primarily restricted to the polyNORCOOH domains. Hydrogen reduction of gold and copper loaded films led to the formation of clusters with a broader size distribution, also largely restricted to the polyNORCOOH domains. In the case of gold, most clusters were in the 10-20 Å size range; however, several 100+ Å clusters appeared to grow beyond the boundaries of the polyNORCOOH domains. Aqueous $NaBH_4$ reduction of both the lead and nickel loaded films resulted in formation of lead and nickel clusters in the 30-40 Å and 30-100 Å size ranges respectively. The lead clusters were uniformly sized (except for occasional ~100 Å aggregates of several clusters) and were restricted to the polyNORCOOH domains. The nickel clusters were polydisperse, and several appeared outside the polyNORCOOH domains.

Shown in Figures 3.2, 3.3, 3.4, and 3.5 are electron micrographs of silver and platinum loaded films before and after reduction. Figures 3.2 and 3.3, respectively, show dark outlines of the interconnected cylindrical polyNORCOOH domains after silver and platinum loading. Figure 3.2 also seems to suggest some cluster formation prior to reduction. Figures 3.4 and 3.5, respectively, show 40-70 Å silver clusters and 20-30 Å platinum clusters within the polyNORCOOH domains of the silver and platinum loaded films after hydrogen reduction.

Shown in Figures 3.6, 3.7, and 3.8, respectively, are electron micrographs of gold, palladium, and copper loaded films after reduction. Figure 3.9 is an electron micrograph of the nickel loaded film after $NaBH_4$ reduction. The nickel clusters ranged in size from 30 to 100 Å, and several appear to have grown beyond the polyNORCOOH domains. Outlines of the nickel loaded polyNORCOOH domains are still visible, possibly due to incomplete nickel reduction.

Palladium, platinum, and silver loaded films were examined using STEM (electron microprobe analysis mode) following reduction. The clusters were found to consist primarily of palladium, platinum, and silver respectively, with trace contaminants from other elements. The crystal structure of the Ag, Au, Cu, Ni, Pb, Pd, and Pt clusters in all seven cluster containing films was studied using electron diffraction. The electron diffraction pattern of the silver loaded film was consistent with the face-centered cubic (f.c.c.) d-spacings tabulated by the U.S. Bureau of Standards.[3] The electron diffraction patterns of the lightly loaded Au, Cu, Ni, Pb, Pd, and Pt cluster containing films were obscured by amorphous scattering from the polymer.

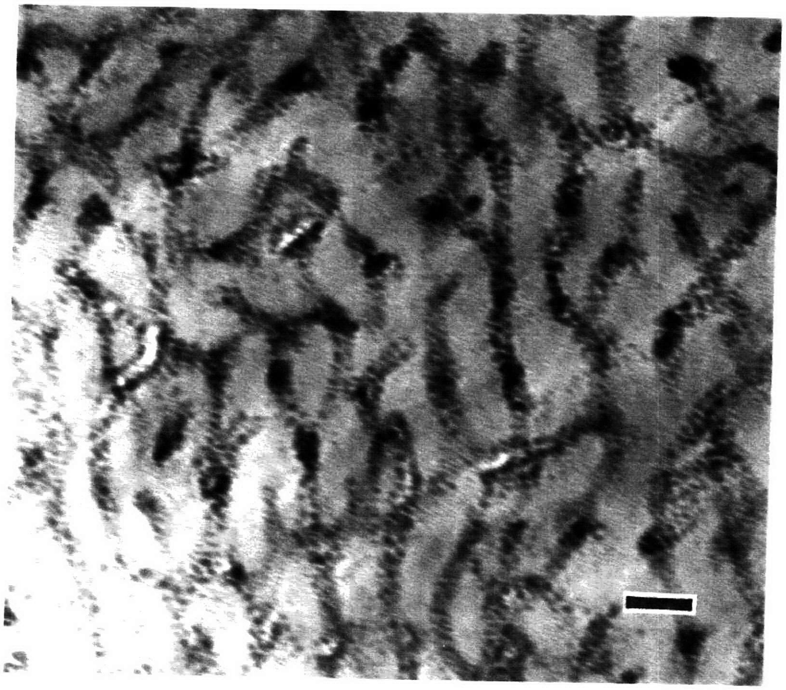

Figure 3.2: Electron micrograph of microtomed Ag^+ loaded film (bar = 300 Å)

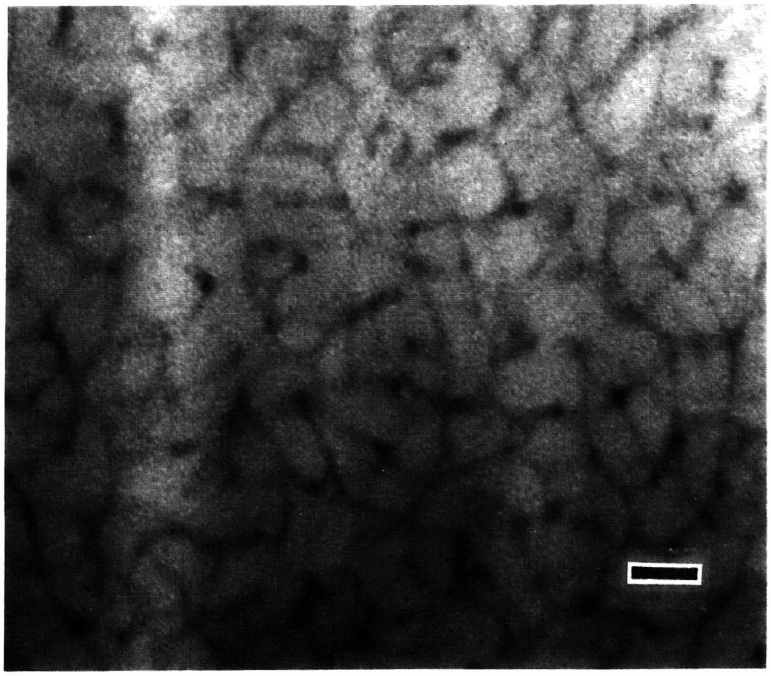

Figure 3.3: Electron micrograph of microtomed $[PtCl_6]^{-2}$ loaded film (bar = 300 Å)

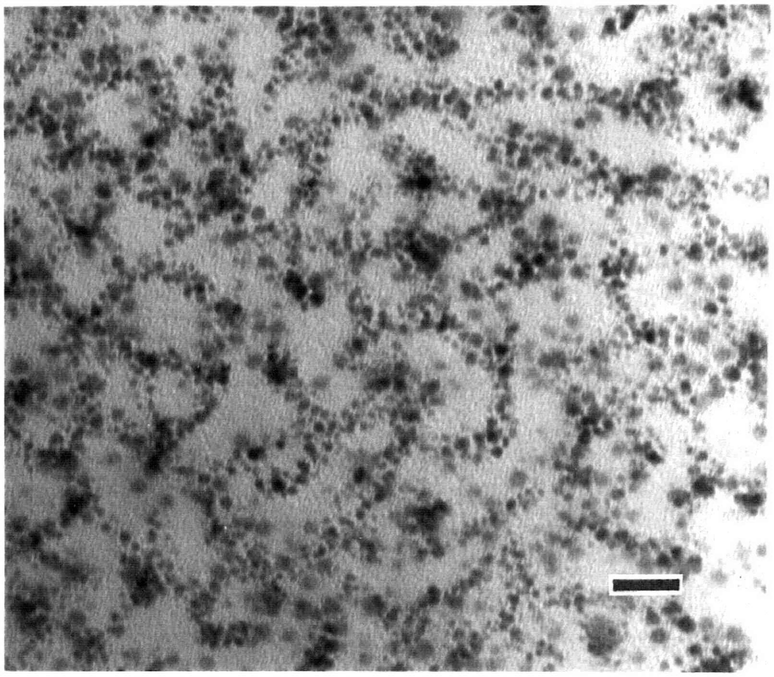

Figure 3.4: Electron micrograph of microtomed Ag^+ loaded and reduced film (bar = 300 Å)

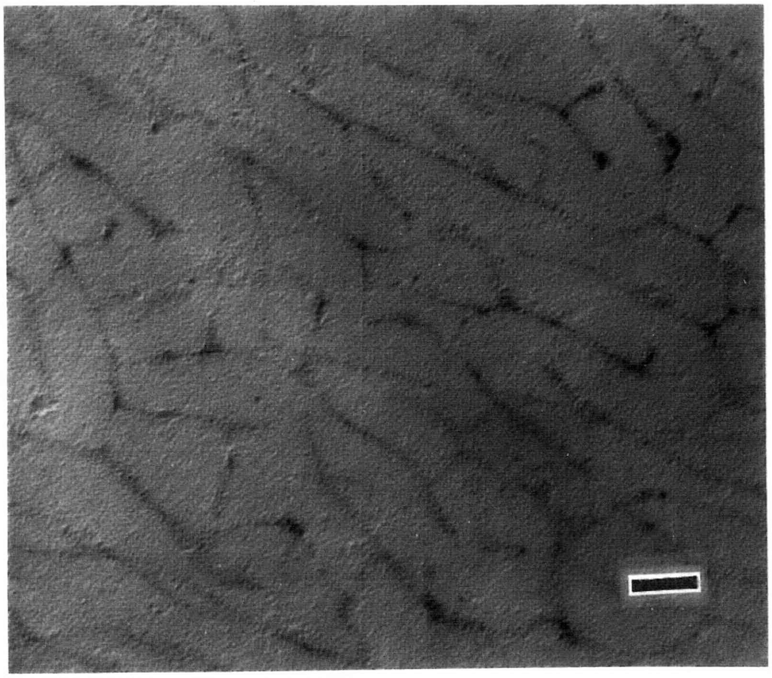

Figure 3.5: Electron micrograph of microtomed $[PtCl_6]^{-2}$ loaded and reduced film (bar = 300 Å)

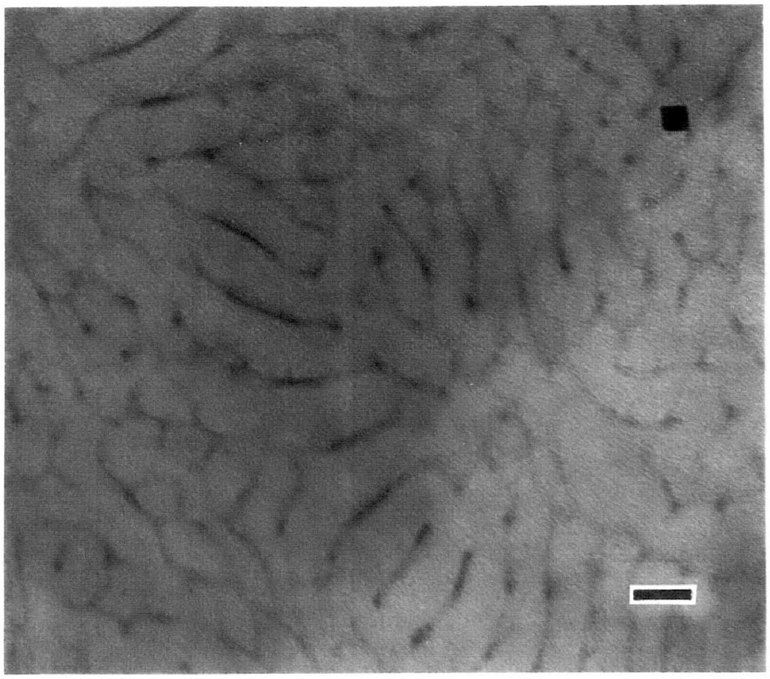

Figure 3.6: Electron micrograph of microtomed Au^{+3} loaded and reduced film (bar = 500 Å)

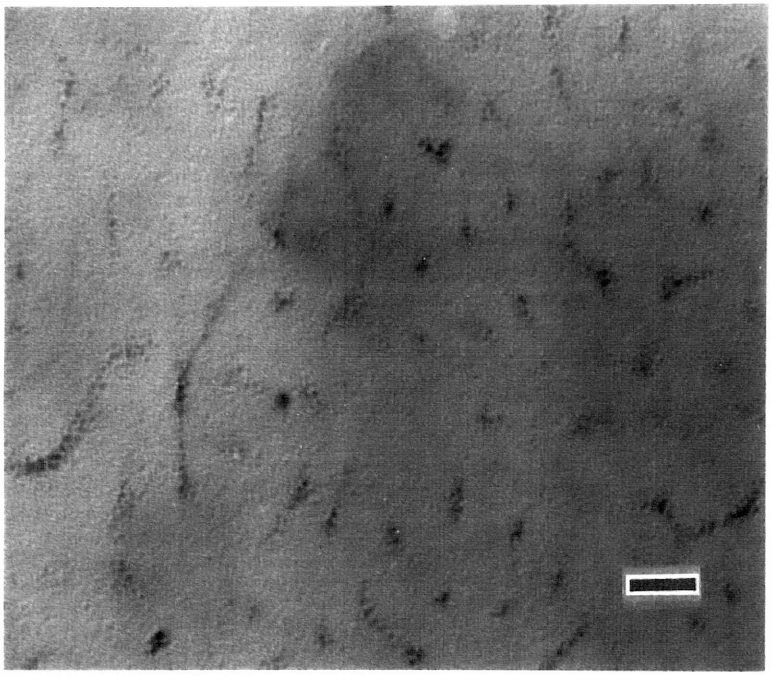

Figure 3.7: Electron micrograph of microtomed $[PdCl_4]^{-2}$ loaded and reduced film (bar = 300 Å)

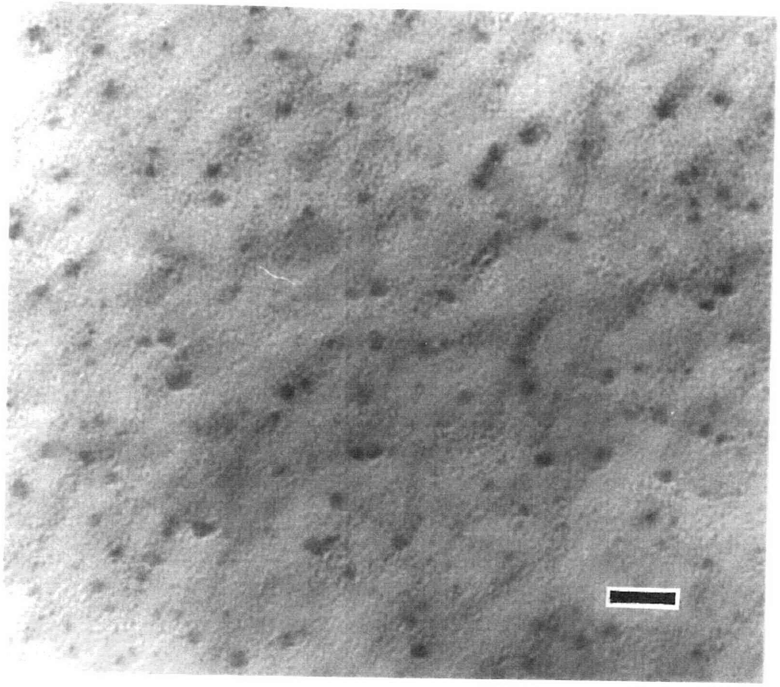

Figure 3.8: Electron micrograph of microtomed Cu^{+2} loaded and reduced film (bar = 300 Å)

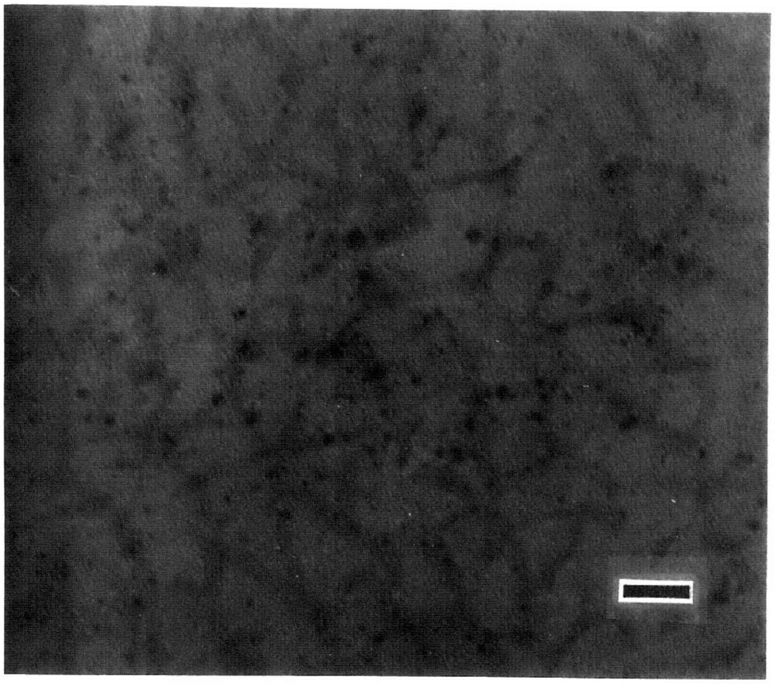

Figure 3.9: Electron micrograph of microtomed Ni^{+2} loaded and reduced film (bar = 300 Å)

Prior to synthesis of the $[MTD]_{400}[NORCOOH]_{50}$ block copolymer, similar metal loading and reduction experiments were done with a different diblock copolymer, $[MTD]_{400}[NORCOOH]_{40}$, which also had a non-equilibrium interconnected cylindrical morphology. Hydrogen reduction of lead and nickel loaded films was attempted; however, no clusters were observed using TEM. Copper and silver loaded films were reduced successfully using aqueous $NaBH_4$; however, the resulting cluster size distributions were larger than those observed following hydrogen reduction. Figure 3.10 is an electron micrograph of a 500 Å thick, Ag^+ loaded (0.01 M, 66 °C, 5 hr), $[MTD]_{400}[NORCOOH]_{40}$ film following reduction in 1 wt. % aqueous $NaBH_4$ (25 °C, 1 min.). Clusters aggregates are visible, several of which are larger than 150 Å and extend beyond the polyNORCOOH domains.

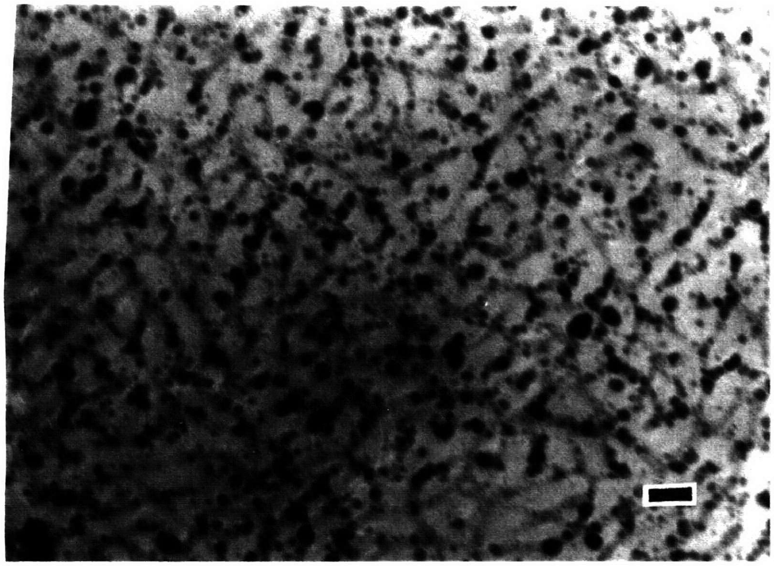

Figure 3.10: Electron micrograph of Ag^+ loaded $[MTD]_{400}[NORCOOH]_{40}$ film following reduction in 1 wt. % aqueous $NaBH_4$ (bar = 300 Å)

These results demonstrate it is possible to coordinate, from aqueous solution, metal ions and complexes to the carboxylic acid substituted domains in ultra-thin microphase-separated block copolymer films. Hydrogen reduction of the metal loaded films results in the formation of metal clusters which are in most cases uniform in size and spatially restricted to the polyNORCOOH domains. Aqueous $NaBH_4$ reduction, however, often results in larger cluster size distributions with several clusters apparently lying outside the polyNORCOOH domains. It is possible that the enhanced mobility afforded by the aqueous $NaBH_4$ facilitates diffusion and aggregation.

3.3.2. Bulk Films

A summary of the TEM observations for metal loaded, reduced, and microtomed bulk films is shown below in Table 3.7.

Table 3.7 TEM results of metal loading and reduction in bulk films

Species	**Evidence of Loading**	**1st H_2 Reduction Cluster Size, Å**	**2nd H_2 Reduction Cluster Size, Å**
Au^{+3}	No	10-15 and 200-500	10-15
Ag^{+}	Yes	25-35	40-90
$[PdCl_4]^{-2}$	Yes	10-20	20-30
Pb^{+2} [a]	Yes	-	-

[a] $[MTD]_{400}[NORCOOH]_{40}$

Microtomed (400 Å thick) sections of bulk films loaded with Ag^{+}, $[PdCl4]^{-2}$, Au^{+3}, and Pb^{+2}, were observed with TEM. In the Ag^{+}, $[PdCl4]^{-2}$, and Pb^{+2} loaded films, a faint outline of the interconnected cylindrical morphology was visible. No contrast was visible between microdomains in the Au^{+3} loaded block copolymer. Films loaded with Ag^{+}, $[PdCl4]^{-2}$, and Au^{+3}, were observed following a single loading and reduction sequence (LARS) and following a second LARS. Uniformly sized silver (25-35 Å) and palladium clusters (10-20 Å) appeared restricted to the polyNORCOOH domains of the Ag^{+} and $[PdCl4]^{-2}$ loaded films respectively.

No larger silver or palladium particles were observed. After a single reduction, the interconnected cylindrical morphology became visible in the Au^{+3} loaded films. Numerous gold clusters (10-15 Å) were observed in the polyNORCOOH domains, and a few gold particles (200-500 Å) appeared to have gown beyond the polyNORCOOH domains. The silver and palladium clusters increased in size following the second LARS. Silver (40-90 Å) and palladium (20-30 Å) clusters appeared restricted to the polyNORCOOH domains in the silver and palladium containing films respectively. This observation indicates that pre-existing metal clusters can act as nucleation sites for further cluster growth during subsequent LARS. The gold clusters did not grow appreciably during the second LARS.

The peculiar cluster forming properties of gold are not well understood. They may be due in part to the unusually high electrochemical reduction potential (1.401 V) of the Au^{+3} ion. Since Au^{+3} is very easily reduced, more nucleation sites may be available for Au^{+3} than for the other metal ions. If this is the case, the larger number of nucleation sites may lead to the observed high concentration of very small clusters. Furthermore, these very small clusters may be mobile enough to aggregate into the larger particles (200-500 Å) which were also observed. A large excess of nucleation sites may also explain the lack of gold cluster growth observed during the second LARS. Metal ions reduced during the second LARS can form new clusters or add to pre-existing clusters. In the case of gold, the ratio of atoms forming new clusters to those adding to pre-existing clusters may be larger than for silver or palladium, where cluster growth was observed during the second LARS.

Shown in Figures 3.11, 3.12, 3.13, and 3.14, respectively, are electron micrographs of the bulk silver containing film, after a single loading, after a single LARS, after a second loading (prior to the second reduction), and after a second LARS. The ability to control and modify cluster size using the methodology of Figure 1.9 is evident in this case. Figure 3.13 is particularly interesting because both the silver clusters, formed during the first LARS, and dark outline of the Ag^{+} containing (second loading) polyNORCOOH domains are visible. Differences in cluster density between Figures 3.12 and 3.13 are probably due to variations in

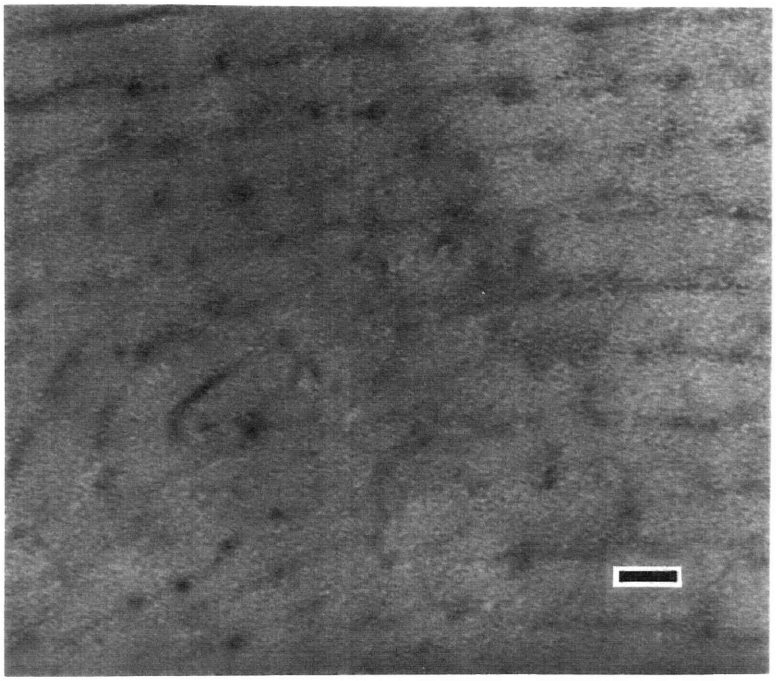

Figure 3.11: Electron micrograph of bulk Ag^+ loaded film (bar = 300 Å)

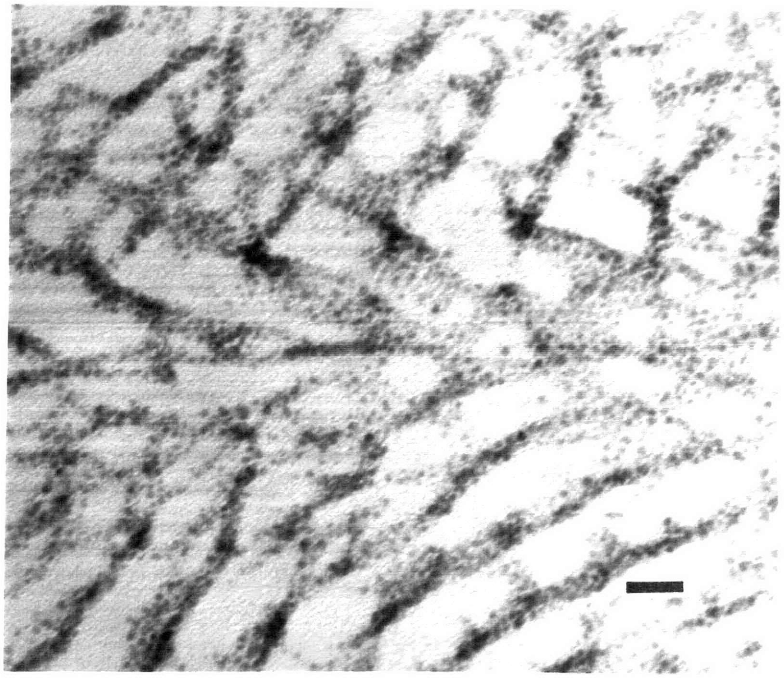

Figure 3.12: Electron micrograph of bulk silver containing film after 1st LARS (bar = 300 Å)

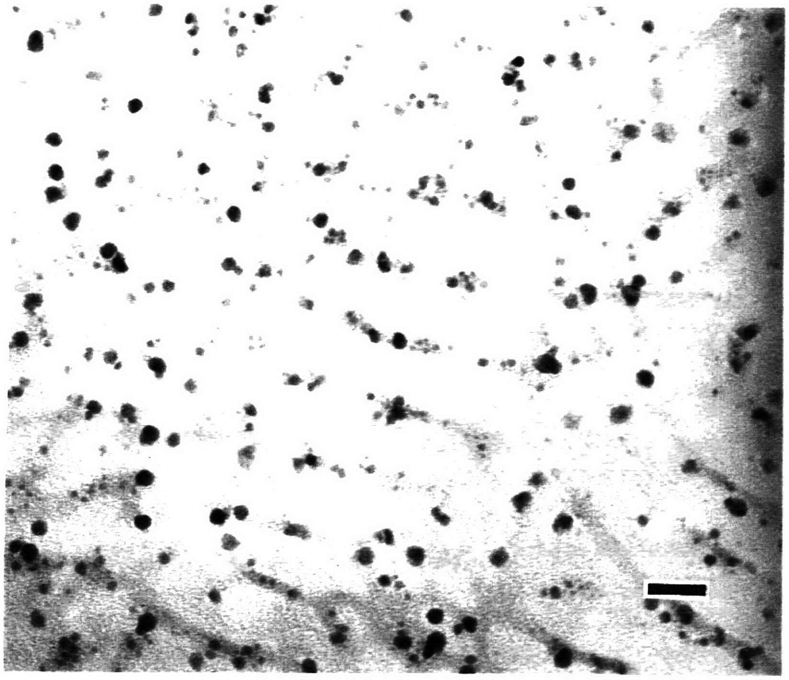

Figure 3.13: Electron micrograph of bulk silver containing film after 2nd loading and prior to 2nd reduction (bar = 300 Å)

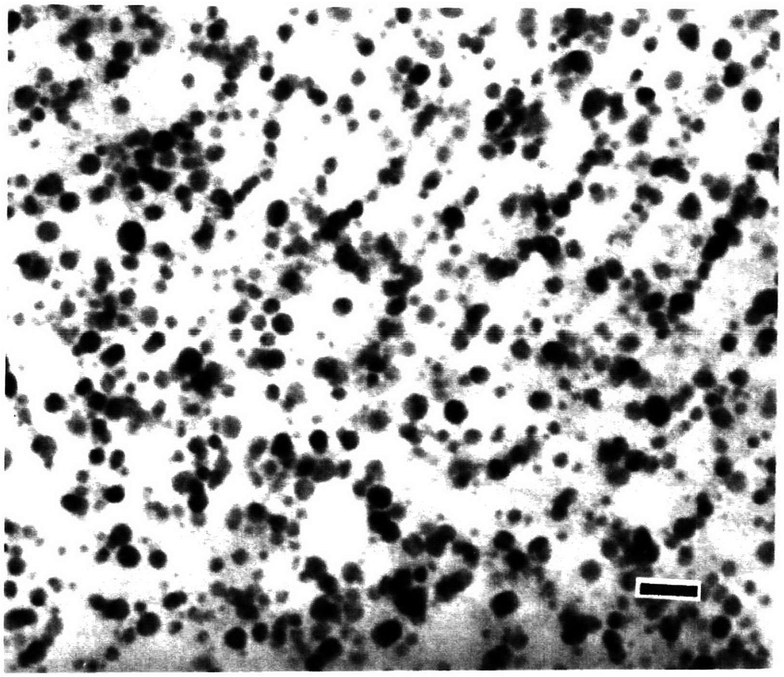

Figure 3.14: Electron micrograph of bulk silver containing film after 2nd LARS (bar = 300 Å)

microtomed film thickness; however, many clusters present in Figure 3.13 are larger than the 25-35 Å clusters shown in Figure 3.12. It is possible that immersion in water leads to some cluster mobility and aggregation.

Shown in Figure 3.15 is an electron micrograph of the bulk gold containing film after the first LARS. Figure 3.16 is an electron micrograph of the bulk palladium containing film after the second LARS.

All seven metal-loaded films were examined using WAXS, both after metal loading and after reduction. Ag^{+}, Au^{+3}, Cu^{+2}, $[PdCl4]^{-2}$, and $[PtCl6]^{-2}$ loaded films were also examined after a second LARS. The diffracted X-ray intensities shown in Figures 3.17, 3.18, and 3.19 have been normalized through division by the maximum intensity of the polymer peak (amorphous halo). Shown in Figure 3.17 are WAXS data for the Ag^{+} loaded film. Figures 3.17b, 3.17c, and 3.17d correspond to the electron micrographs shown in Figures 3.11, 3.12, and 3.14 respectively. Comparison of Figures 3.17a and 3.17b shows that little or no f.c.c. silver crystal formation occurred, prior to reduction, after a single Ag^{+} loading. Figures 3.17c and 3.17d correspond to bulk films after one and two LARS respectively. They show broad scattering peaks at angles consistent with those found in the literature[3] for scattering from the [111] ($2\theta = 38.1°$), [200] ($2\theta = 44.3°$), and [220] ($2\theta = 64.4$) planes of the f.c.c. silver lattice. The mean Scherrer length, $L_{hkl,}$, of the silver crystals in the twice loaded and reduced film was determined by applying the Scherrer equation[4] to the [111] peak of Figure 3.17d. The Scherrer equation is given by

$$L_{hkl,} = K\lambda/(\beta_0\cos\theta) \qquad (3\text{-}1)$$

Where K is a constant (shape factor) commonly assigned a value of unity, λ is the wavelength of the radiation (Å), β_0 is the full peak width at half-maximum (radians), and θ is half the scattering angle (°). A mean silver crystal diameter, D, of 53 Å was then estimated using equation (3-2):[5]

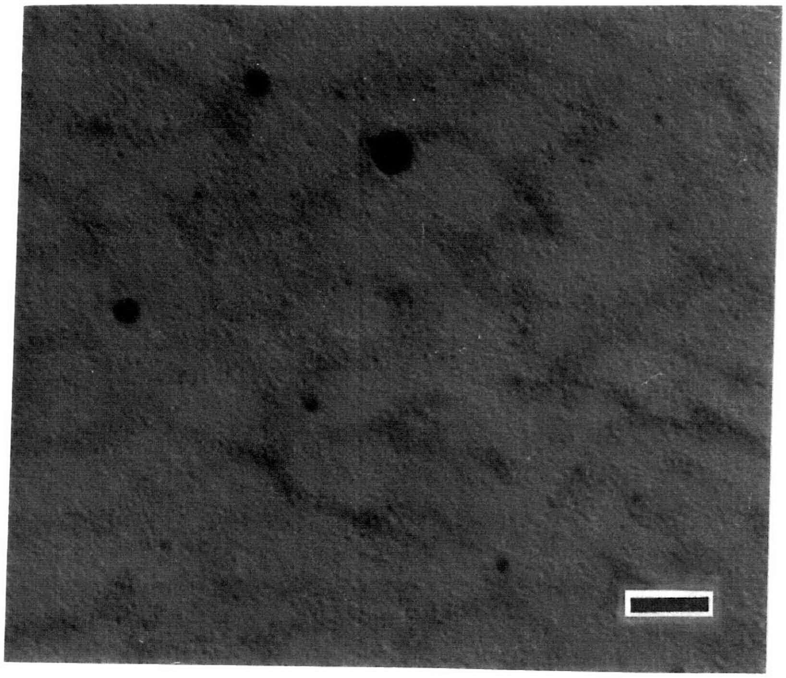

Figure 3.15: Electron micrograph of bulk gold containing film after 1st LARS (bar = 300 Å)

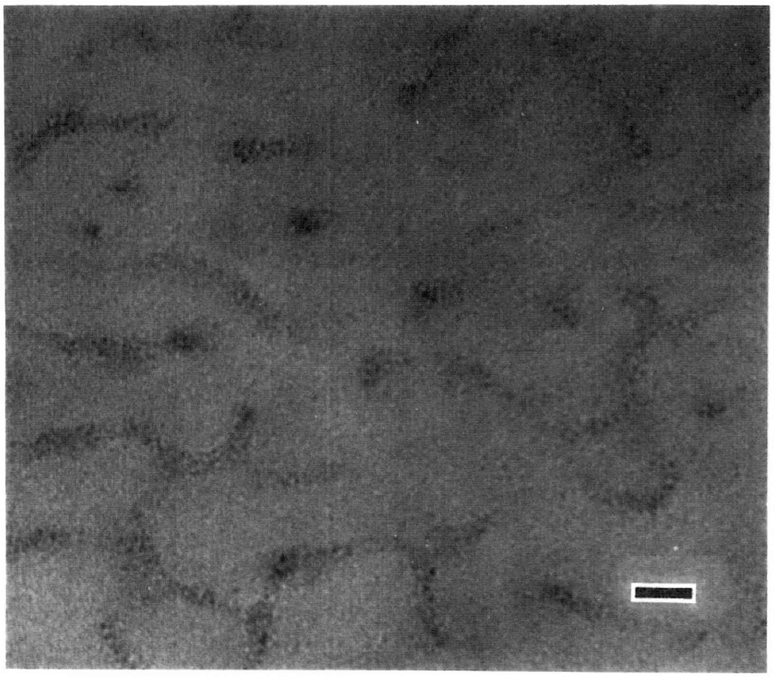

Figure 3.16: Electron micrograph of bulk palladium containing film after 2nd LARS (bar = 200 Å)

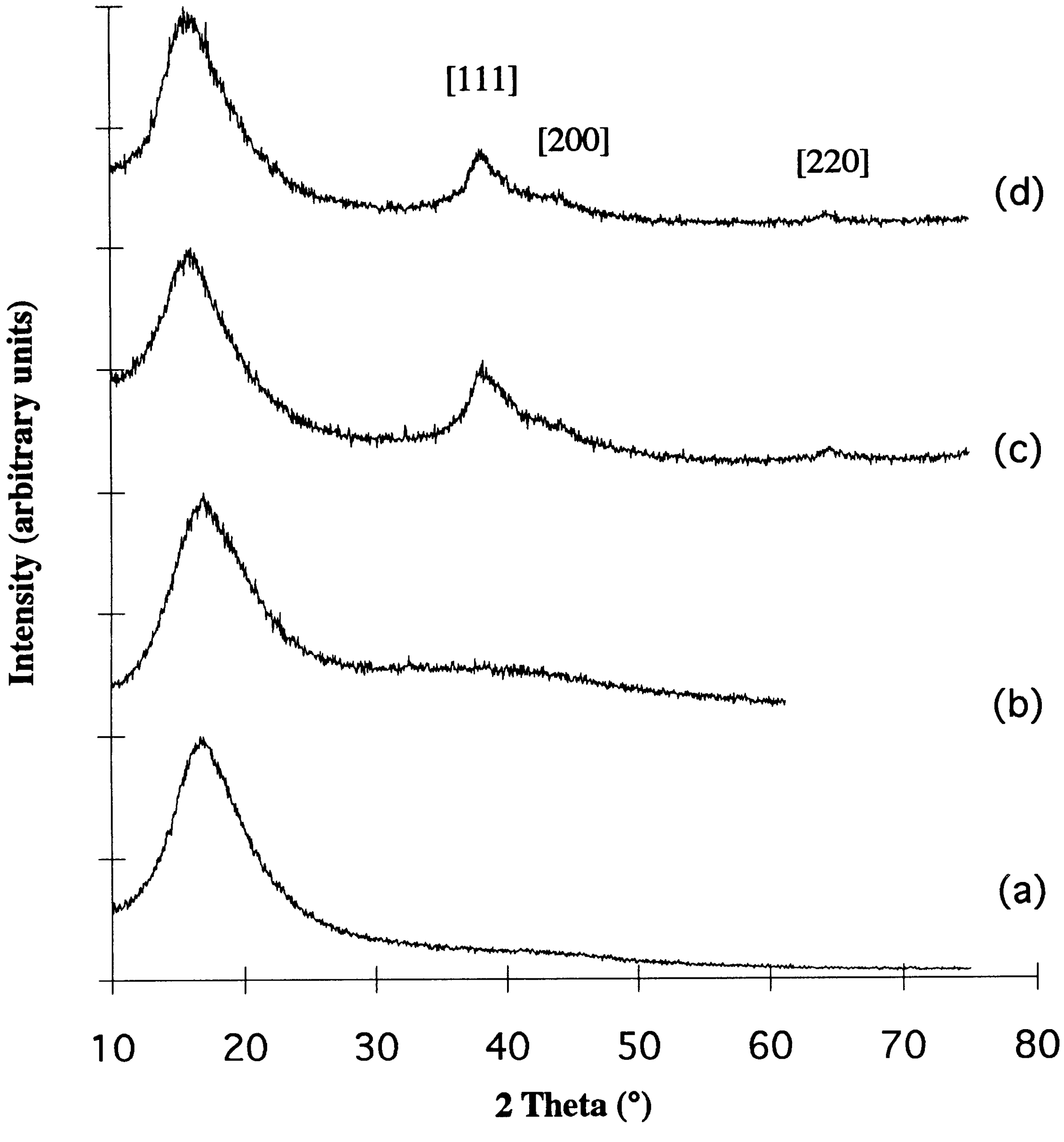

Figure 3.17: WAXS data from bulk silver containing film: (a) unloaded film; (b) Ag^+ loaded film; (c) film after 1st LARS; (d) film after 2nd LARS

$$D = 4/3\ L_{hkl}, \qquad (3\text{-}2)$$

Since the peak breadth at half-maximum intensity was not corrected for instrumental broadening, 53 Å represents a lower bound on the estimated silver crystal size, indicating that most nanoclusters appearing in Figure 3.14 are single silver crystals.

Shown in Figure 3.18 are WAXS data from the palladium containing film after two LARS, corresponding to the electron micrograph in Figure 3.16. A small peak consistent with scattering from the [111] ($2\theta = 40.1$) plane[3] of the f.c.c. palladium lattice is visible, indicating the clusters observed with TEM are composed of f.c.c. palladium. WAXS data from the bulk film after a single loading and a single LARS appear identical to that from the unloaded polymer, indicating that the 10-20 Å palladium clusters observed by TEM after a single LARS are too small or insufficiently concentrated to cause observable scattering.

Shown in Figure 3.19 are WAXS data from the Au^{+3} loaded film. Comparison of Figures 3.19a and 3.19b show that some f.c.c. gold crystal formation occurred, prior to reduction, after a single Au^{+3} loading. Figures 3.19c and 3.19d correspond to bulk films after one and two LARS respectively. They show scattering peaks at angles consistent with those found in the literature[3] for scattering from the [111] ($2\theta = 38.2°$), [200] ($2\theta = 44.4°$), and [220] ($2\theta = 64.6$) planes of the f.c.c. gold lattice. The signal to noise ratio is lower in Figure 3.19d than in Figure 3.19c because increased X-ray absorption in the twice loaded and reduced film lowered the absolute intensity of the scattered X-rays which were detected. A mean gold crystal diameter of 200 Å, for the twice loaded and reduced film, was estimated as outlined above through application of the Scherrer equation[4] to the [111] peak of Figure 3.19d. This large mean crystal size indicates that the occasional large gold clusters were the dominant scatterers. Increasing sharpness of the gold scattering peaks and the slight upturn, at low angles, of the WAXS data shown in Figure 3.19d, indicate the presence of large (several hundred angstrom) gold clusters in the twice loaded and reduced film. However, very few such clusters were observed with TEM. It is possible that the large gold clusters occur

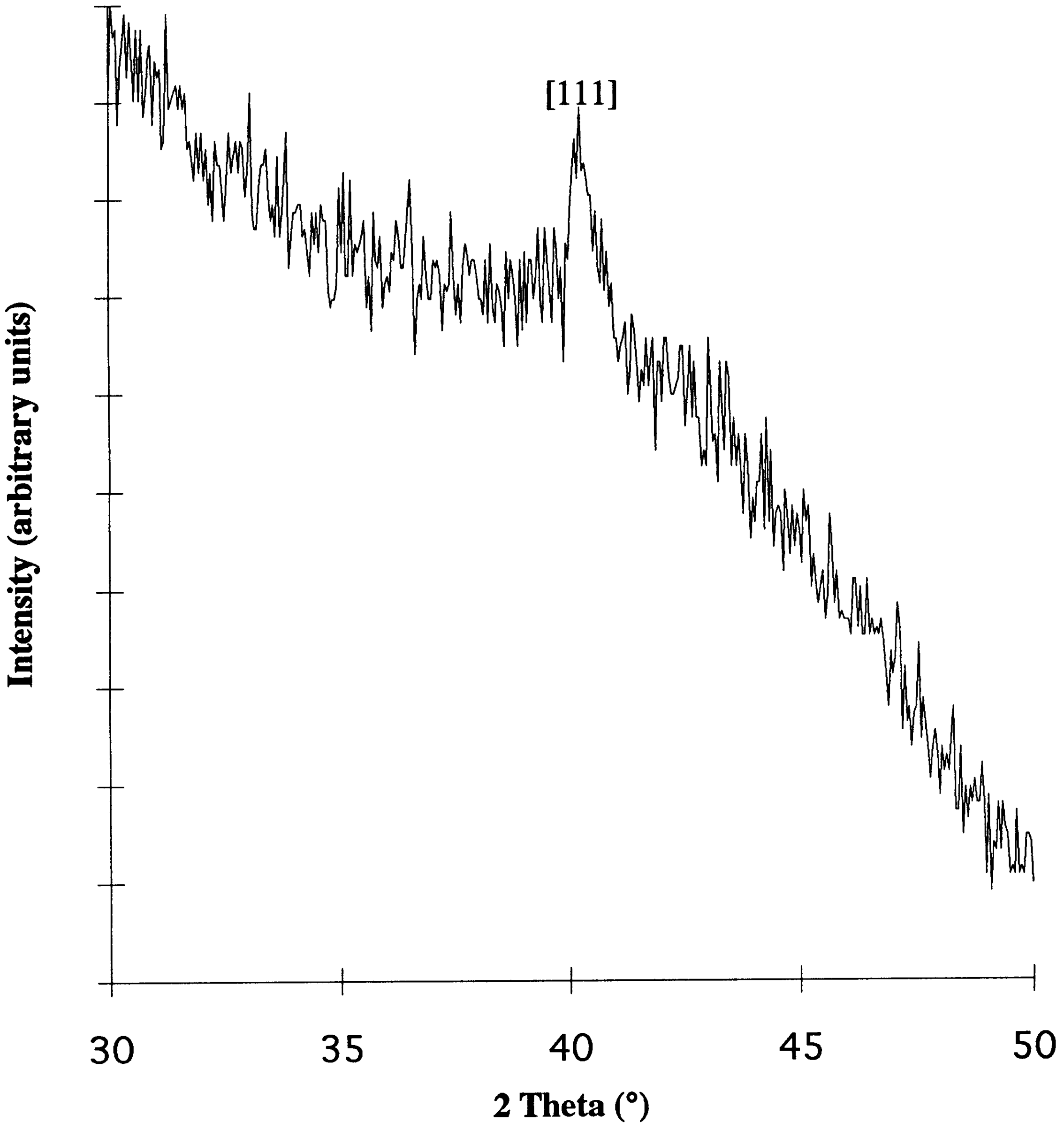

Figure 3.18: WAXS data from bulk palladium containing film after 2nd LARS

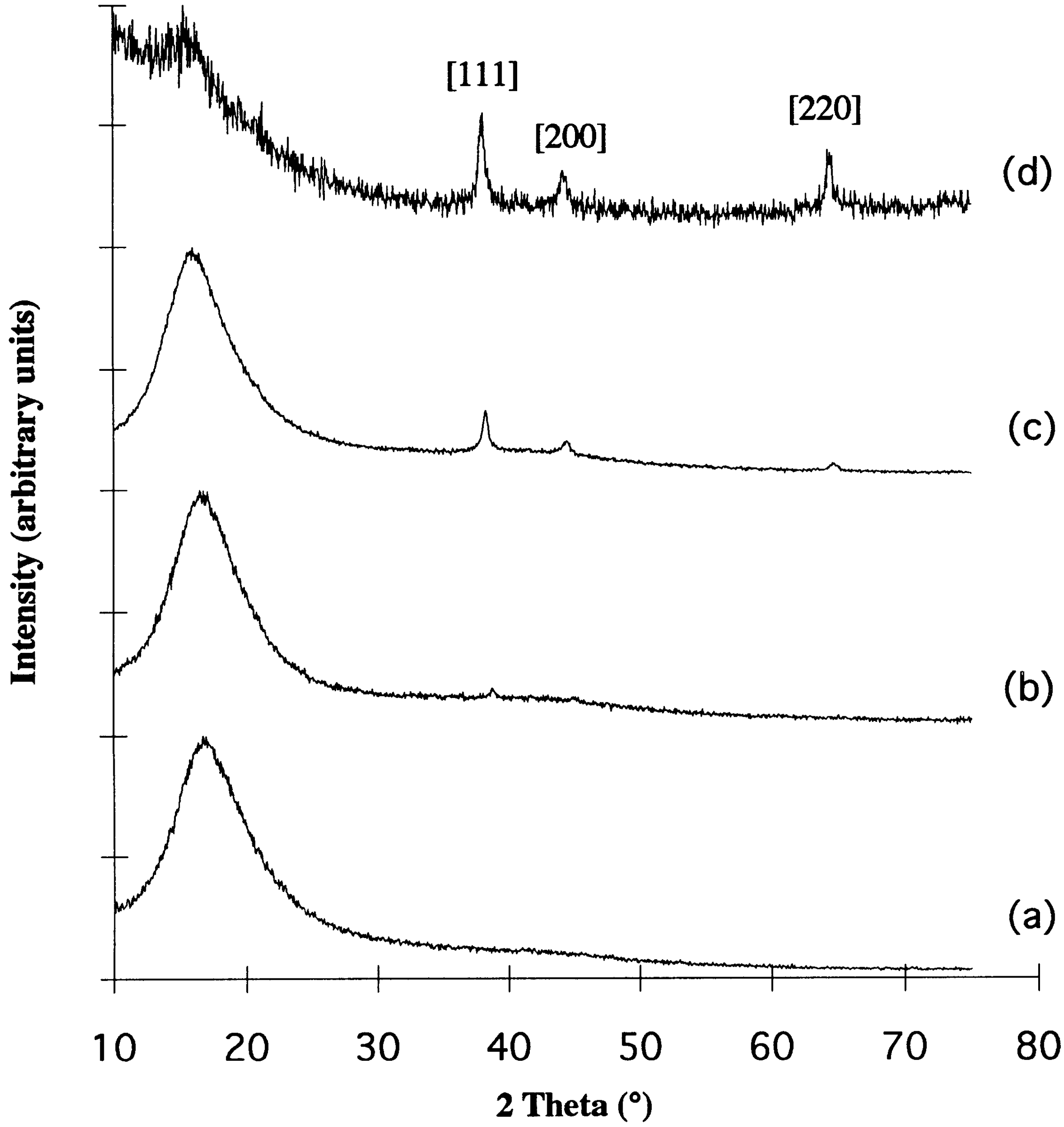

Figure 3.19: WAXS data from bulk gold containing film: (a) unloaded film; (b) Au^{+3} loaded film; (c) film after 1st LARS; (d) film after 2nd LARS

preferentially near the surface of the bulk films and were not seen using TEM because the microtomed sections were taken from the center of the bulk films.

WAXS data from the once loaded and reduced lead and nickel containing bulk films exhibited only a single broad peak due to scattering from the amorphous polymer. WAXS data from the platinum and copper containing films exhibited only a single amorphous scattering peak after two loading and reduction cycles. The absence of copper, lead, nickel, and platinum clusters is attributed to insufficient metal ion loading in the bulk films.

3.4. Conclusions

A variety of transition metal nanoclusters can be synthesized within the carboxylic acid functionalized domains of microphase-separated $[MTD]_{400}[NORCOOH]_{50}$ and $[MTD]_{400}[NORCOOH]_{40}$ block copolymer films, using a technique in which the films are soaked in aqueous metal salt solutions prior to reduction of the sequestered metal ions with hydrogen gas or aqueous $NaBH_4$. The resulting metal nanoclusters can be nearly monodisperse, are primarily restricted to the polyNORCOOH domains, and can be synthesized in both microtomed and bulk films. In the case of microtomed films, hydrogen reduction usually produces uniformly sized clusters, largely restricted to the polyNORCOOH domains, while $NaBH_4$ reduction produces clusters with a larger size distribution, sometimes appearing outside the polyNORCOOH domains. In the case of bulk films, cluster size increased after the second LARS, indicating that pre-existing metal clusters can act as nucleation sites for further cluster growth. Analysis of WAXS data indicates that many clusters in twice loaded and reduced gold and silver containing films consist of single gold and silver crystals respectively.

Overall, it is clear that the methodology outlined in Figure 1.9 is a versatile approach for zero-valent metal cluster synthesis. The various types of clusters are formed in-situ, always starting from a single diblock copolymer precursor. Size control is apparently achievable in some cases via multiple passages through the cluster synthesis scheme.

3.5. References for Chapter 3

(1) Yue, J. and Cohen, R.E. *Supramolecular Science* **1994**, 1, 117.

(2) Vanysek, P. in 'Handbook of Chemistry and Physics' (Eds R. Weast), CRC Press, Inc., Boca Raton, 1987, p. D-151.

(3) Swanson, H.E. and Tatge, E. 'U.S. National Bureau of Standards Standard X-Ray Diffraction Patterns', NBS Circular 539, Volume 1, U.S. Government Printing Office, Washington D.C., June 15, 1953.

(4) Klug, H.P. and Alexander, L.E. 'X-Ray Diffraction Procedures', John Wiley & Sons, Inc., New York, 1954, p. 491.

(5) Bawendi, M.G., Kortan, A.R., Steigerwald, M.L., and Brus, L.E. *J. Chem. Phys.* **1989**, 91, 7282.

Chapter 4

Synthesis of Metal Nanoclusters within Microphase-Separated Diblock Copolymers: ICP-AES Analysis of Metal Ion Uptake

4.1. Summary

We previously reported a general methodology, shown in Figure 1.9, for the synthesis of several transition metal nanoclusters (Ag, Au, Cu, Ni, Pb, Pd, and Pt) stabilized within microphase-separated diblock copolymers. In our strategy, metal ions or complexes are coordinated to carboxylic acid groups within the water soluble polyNORCOOH domains of a $[MTD]_{400}[NORCOOH]_{50}$ block copolymer (MTD = methyltetracyclododecene and NORCOOH = 2-norbornene-5,6,-dicarboxylic acid) by immersion of the polymer in aqueous metal salt solutions. The metal ions and complexes are subsequently reduced by heating the metal loaded polymer under hydrogen or by immersion in an aqueous sodium borohydride solution. For several transition metals, the resulting nanoclusters are uniformly sized and homogeneously dispersed within the polyNORCOOH domains.

We now expand the scope and depth of our previous work by investigating the rate of metal ion transport into the block copolymer and the nature of metal loading in the polyNORCOOH domains. The rate and extent of loading from aqueous solutions of numerous metal ions (Ag^{+}, Au^{+3}, Cu^{+2}, Eu^{+2}, Eu^{+3}, Fe^{+2}, Fe^{+3}, Gd^{+3}, Ni^{+2}, Pd^{+2}, Pt^{+2}, and Pt^{+4}) was measured using inductively coupled plasma atomic emission spectroscopy (ICP-AES). In the cases of Cu^{+2}, Fe^{+2}, and Pd^{+2}, we compare the rate and extent of loading from aqueous solutions containing the same metal ion but different co-ions.

Metal loaded and metal cluster containing films were characterized with infrared (IR) and ultraviolet-visible (UV) spectroscopy. Continuous interconnected polyNORCOOH domains were found to be necessary for metal ion uptake. The metal-bound carboxylate ions in the polyNORCOOH domains were found to be re-protonated during hydrogen reduction,

rendering them active for further participation in metal binding. Following reduction, metal nanocluster containing films were characterized using wide-angle X-ray scattering.

4.2. Experimental

$[MTD]_{400}$, $[MTD]_{400}[NORCOOH]_{50}$, and $[MTD]_{800}[NORCOOH]_{30}$ diblock copolymers were synthesized as previously reported, using a ring-opening metathesis polymerization in anhydrous toluene with a $Mo(CHCMe_2Ph)(NAr)(O\text{-}t\text{-}Bu)_2$ ($Ar = 2,6\text{-}C_6H_3\text{-}i\text{-}Pr_2$) initiator.

10 µm and 0.5 mm thick polymer films were static cast from 0.5 and 3 wt. % solutions in tetrahydrofuran (THF) respectively. See Appendix D. Transmission electron microscopy observation of microtomed sections of 0.5 mm thick, Ag^+ stained $[MTD]_{800}[NORCOOH]_{30}$ and $[MTD]_{400}[NORCOOH]_{50}$ films, revealed spherical and non-equilibrium interconnected cylindrical morphologies respectively. The microphase-separated spherical and cylindrical polyNORCOOH domains had diameters of approximately 100 and 80 Å respectively.

4.2.1. Metal Ion Uptake in Carboxylic Acid Functionalized Films

Inductively coupled argon plasma atomic emission spectroscopy (ICP-AES) is a very powerful and simple technique for determining the concentration of various elemental species in solution.[1-3] This technique can, in principle, be used for the determination of all elements other than argon. In ICP-AES, a solution containing the elements of interest is introduced to a high temperature inductively coupled argon plasma. Power is transferred into the plasma gas by inductive heating. The argon passes continuously through a plasma torch, within an induction coil, carrying a high frequency alternating current. The electrically conducting ionized gas acts as the secondary coil of a transformer, allowing the gas to reach temperatures of 10,000 K.

Electrons within the elements of interest are excited to higher energy states within the plasma, and emit light at characteristic frequencies, as the excited electrons drop to lower energy levels. Over a concentration range of several orders of magnitude, the intensity of these characteristic emissions is linearly related to the elemental concentration in solution. Several wavelengths of different sensitivity are available for the determination of any element, making ICP-AES useful over a concentration range from < 0.1 ppm to 1000 ppm mass.

We studied the concentration of elements, one at a time, within aqueous solutions containing multiple elements of interest. Each calibration standard contained only de-ionized water and the element of interest, ranging in concentration from 10 to 30 ppm, all prepared in 100 g batches by dilution of Aldrich 1000 ppm elemental atomic absorption standard solutions. De-ionized water was used as the calibration blank. The ICP-AES was calibrated with blank, 10 ppm, 20 ppm, and 30 ppm standard solutions prior to analysis of each element. ICP-AES may be used for determining element concentrations in organic solutions, but equipment modifications are necessary to prevent the torch head from overheating.

According to Table 4.1, metal loading experiments were carried out at 25°C using a batch equilibration method in which 100 mg samples of 10 μm thick polymer films were submerged in 20 g of 0.005 M aqueous metal salt solutions. Agitation was maintained with magnetic stir bars. The metal ion concentration remaining in the supernatant solution was measured periodically by withdrawing small aliquots of supernatant solution. The withdrawn aliquots were diluted with water to metal ion concentrations of < 30 ppm and analyzed using ICP-AES.

The extent of metal ion uptake was calculated using equation (4-1):

$$A = W_s(C_i-C_f)/W_p \tag{4-1}$$

where A (mg/g) is the mass of metal loaded per mass polyNORCOOH in the block copolymer ; W_s, the mass (g) of metal salt solution; W_p, the mass (g) of polyNORCOOH in the block copolymer; C_i, the solution concentration (ppm) of metal prior to loading; and C_f, the solution concentration (ppm) of metal after loading. Loading with $Ag(OOCCH_3)$ was done in the dark.

Table 4.1 Aqueous ICP-AES metal loading experiments

Species	pH	$[MTD]_{400}$	$[MTD]_{800}$ $[NORCOOH]_{30}$	$[MTD]_{400}$ $[NORCOOH]_{50}$
$Ag(OOCCH_3)$	5.5	X	X	X
$AuCl_3$	3.5	X		X
$Cu(OOCCH_3)_2$	5	X		X
$CuCl_2$	4	X		X
$Eu(OOCCH_3)_3xH_2O$	5			X
$EuCl_2$	4			X
$EuCl_3x6H_2O$	3.5			X
$Fe(OOCCH_3)_2$	4			X
$FeCl_2$	4			X
$FeCl_3$	2			X
$Gd(OOCCH_3)_3x4H_2O$	5			X
$GdCl_3$	4			X
$NiCl_2$	5	X		X
$Pd(OOCCH_3)_2^*$	4			X
$PdCl_2^{**}$	2			X
$PtCl_4$	2			X
$Na_2PdCl_4x3H_2O$	2.5	X		X
$H_2PtCl_6x6H_2O$	2	X		X
$Na_2PtCl_4xH_2O$	3.5			X

* 0.003 M, ** 0.001 M

In order to determine the effect of organic solvents on the rate and extent of metal ion uptake, loading experiments were also conducted using methanol as the solvent. According to Table 4.2, metal loading experiments were carried out at 25°C using a batch equilibration method in which 100 mg samples of 10 µm thick polymer films were submerged in 16 g of 0.005 M metal salt solutions in methanol. Agitation was maintained with magnetic stir bars. The metal ion concentration remaining in the supernatant solution was measured as previously described. **Methanol was found to damage the ICP-AES torch head.** The methanol was evaporated, and the remaining metal salt was diluted with water prior to analysis.

Table 4.2 ICP-AES metal loading experiments in methanol

Species	**pH**	**$[MTD]_{400}$ $[NORCOOH]_{50}$**
$Ag(OOCCH_3)$	4.5	X
$AuCl_3$	4.5	X
$Cu(OOCCH_3)_2$	4.5	X
$CuCl_2$	4.5	X
$NiCl_2$	4.5	X
$Na_2PdCl_4x3H_2O$	4.5	X
$Na_2PtCl_4xH_2O$	4.5	X

4.2.2. Reduction of Metal Ions and Complexes

After loading, the metal ion containing films were rinsed in de-ionized water and dried under vacuum at 25 °C for 15 hr. After drying, films loaded from aqueous $Ag(OOCCH_3)$, $AuCl_3$, $Cu(OOCCH_3)_2$, and $Na_2PdCl_4x3H_20$, were reduced by heating (115°C) under hydrogen gas (2 atm) for 6 days. Reduction of films loaded from metal salt solutions in methanol was not attempted.

4.3. Results and Discussion

GPC analysis of the homo-MTD blocks yielded polydispersities of approximately 1.1. The block copolymer was not analyzed using GPC because polyNORCOOTMS precipitates as polyNORCOOH in wet toluene. The static cast block copolymer films were flexible and transparent with a slight yellowish tint, probably due to trace residues of $Mo(CHCMe_2Ph)(NAr)(O\text{-}t\text{-}Bu)_2$.

4.3.1. Metal Ion Uptake in Carboxylic Acid Functionalized Films

Figure 4.1 shows the loading capacity of the polyNORCOOH in the $[MTD]_{400}[NORCOOH]_{50}$ films as a function of time for selected aqueous metal salt solutions.

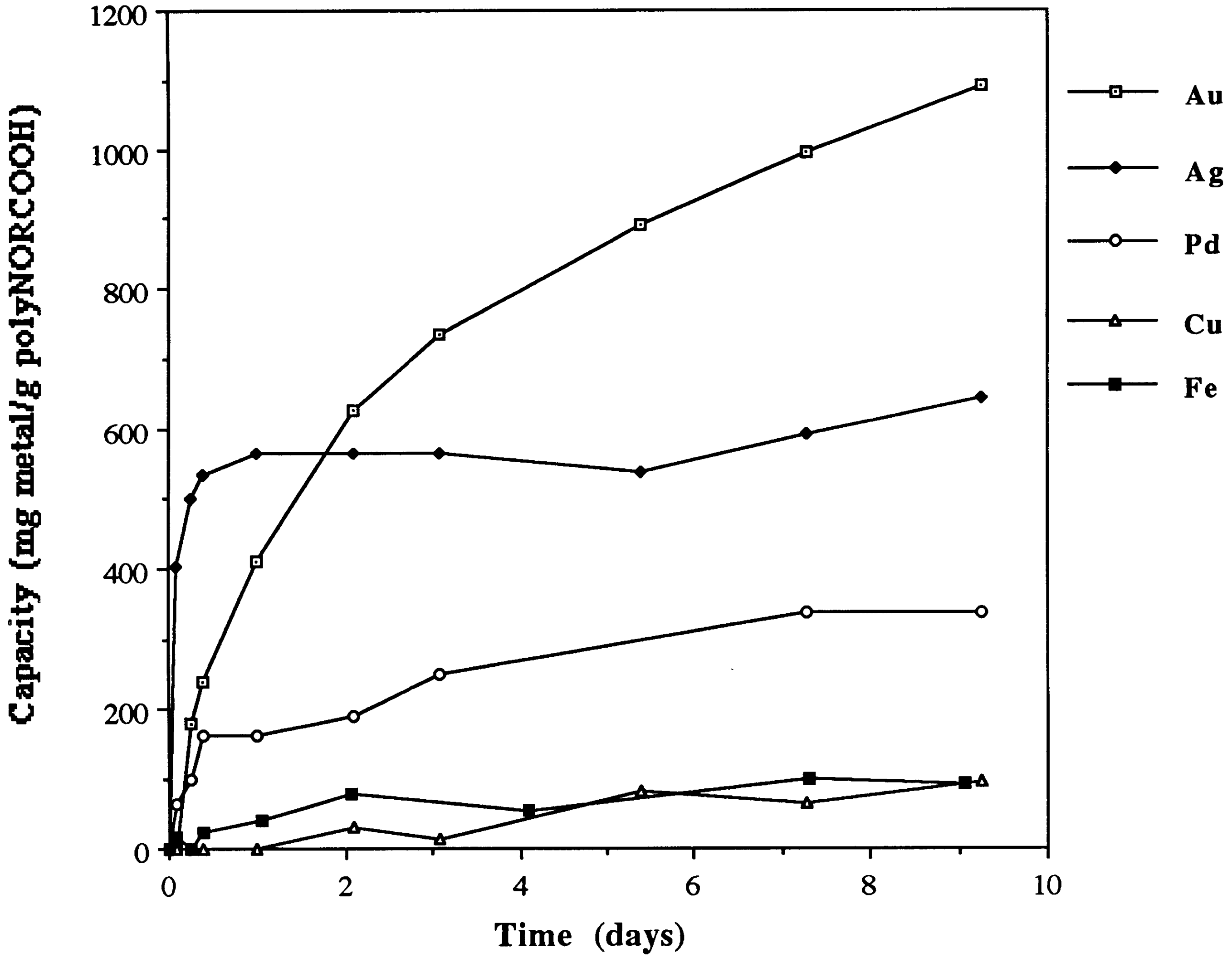

Figure 4.1: Loading capacity of $[MTD]_{400}[NORCOOH]_{50}$ as a function of time: Au^{+3} ($AuCl_3$), Ag^+ ($Ag(OOCCH_3)$), Pd^{+2} ($Na_2PdCl_4x3H_2O$), Cu^{+2} ($Cu(OOCCH_3)_2$), Fe^{+2} ($Fe(OOCCH_3)_2$)

Ag^+ ($Ag(OOCCH_3)$), Au^{+3} ($AuCl_3$), and Pd^{+2} ($Na_2PdCl_4x3H_2O$) initially load rapidly, but the rate of metal ion uptake decreases as the metal ion concentration in solution decreases. Cu^{+2} ($Cu(OOCCH_3)_2$) and Fe^{+2} ($Fe(OOCCH_3)_2$) load more slowly and to a lessor extent. In all cases except Au^{+3}, metal loading approaches equilibrium within 9 days. In the case of Ag^+, an effective diffusion coefficient of $3x10^{-12}$ cm^2/s was estimated using equation (4-2):

$$D_{eff} \sim (h/2)^2/t \qquad (4\text{-}2)$$

where D_{eff} (cm^2/s) is the effective diffusion coefficient; h, the block copolymer film thickness (cm); and t, the time (s) required to approach metal ion uptake equilibrium. Thus, our D_{eff} is a combined measure of the time required for ion diffusion within the film, and ion binding to the carboxylic acid groups. The measured value of D_{eff} is reasonable (order of magnitude) for the diffusion of a liquid within a solid given that gas/solid and solid/solid diffusivities generally range from 10^{-10} to 10^{-8} cm^2/s and from 10^{-15} to 10^{-30} cm^2/s, respectively.[4]

Table 4.3 shows the loading capacity of polyNORCOOH, after 9 days of loading, for all metal salt solutions studied. On a molar basis, Ag^+ ($Ag(OOCCH_3)$) and Au^{+3} ($AuCl_3$) load to the greatest extent, followed by Pd^{+2} ($Na_2PdCl_4x3H_2O$), Pd^{+2} ($Pd(OOCCH_3)_2$), Fe^{+2} ($Fe(OOCCH_3)_2$), Cu^{+2} ($Cu(OOCCH_3)_2$), Fe^{+3} ($FeCl_3$), and Pt^{+4} ($H_2PtCl_6xH_2O$). Little or no loading was observed from $CuCl_2$, $FeCl_2$, $NiCl_2$, $PdCl_2$, $PtCl_4$, $Na_2PtCl_4xH_2O$, or the Eu and Gd containing compounds. **Ag^+ loaded films should be stored in the dark to minimize photo-induced reduction.**

Exchange between protons and metal ions is the primary binding mechanism for carboxylic acid groups.[5,6] Assuming "ion exchange" as the sole binding mechanism, a maximum Au^{+3} loading of 0.33 (moles metal/mole COOH) is predicted. Therefore, our observed Au^{+3} loading of 0.51 is unexpectedly high, especially since many carboxylic acid groups will not participate in exchange reactions below pH 7.0.[7] However, no Au^{+3} loading was observed in the case of $[MTD]_{400}$ homopolymer, and the large WAXS peak areas from the

Table 4.3 Loading capacity of polyNORCOOH* from aqueous solutions

Species	**mg metal per g polyNORCOOH**	**moles metal per mole COOH unit**
$Ag(OOCCH_3)$	650	0.54
$AuCl_3$	1100	0.51
$Cu(OOCCH_3)_2$	100	0.14
$CuCl_2$	< 20	-
$Eu(OOCCH_3)_3xH_2O$	< 20	-
$EuCl_2$	< 20	-
$EuCl_3x6H_2O$	< 20	-
$Fe(OOCCH_3)_2$	100	0.17
$FeCl_2$	< 20	-
$FeCl_3$	80	0.13
$Gd(OOCCH_3)_3x4H_2O$	< 20	-
$GdCl_3$	< 20	-
$NiCl_2$	< 20	-
$Pd(OOCCH_3)_2$	230	0.20
$PdCl_2$	< 20	-
$PtCl_4$	< 20	-
$Na_2PdCl_4x3H_2O$	340	0.29
$H_2PtCl_6x6H_2O$	180	0.08
$Na_2PtCl_4xH_2O$	< 20	-

* $[MTD]_{400}[NORCOOH]_{50}$

Au^{+3} loaded and reduced $[MTD]_{400}[NORCOOH]_{50}$ films are consistent with the high Au^{+3} loading measured using ICP-AES. We attribute the unusually high Au^{+3} loading to reduction of Au^{+3} to lower oxidation states, including Au^0, by residual THF (casting solvent, see Appendix D) and trace amounts of Mo from the polymerization catalyst. Small peaks characteristic of scattering from fcc gold clusters are apparent in Figure 3.19b, corresponding to a Au^{+3} loaded film (0.5 mm thick) prior to hydrogen reduction.

The selectivity of a resin for aqueous metal ions depends on many variables including: the electronic structure of the metal, pH, ionic charge, hydrated ionic radius, and the presence of other species in solution.[7,8,9] We will not attempt to explain all observed metal loading trends; however, the data in Table 4.3 indicate a dependence of the loading capacity on the chemical nature of the compound from which the metal is introduced. In the cases of Cu, Fe, and Pd, loading of M^{+2} from $M(OOCCH_3)_2$ is significantly higher than loading from MCl_2, due in part to pH effects (discussed in section 5.3.1) and favorable interactions between acetate and carboxylic acid groups. Fe^{+3} ($FeCl_3$) and Pt^{+4} ($H_2PtCl_6x6H_2O$) load to greater extents than Fe^{+2} ($FeCl_2$) and Pt^{+2} ($Na_2PtCl_4xH_2O$), due in part to increasing selectivity with increasing ionic charge.[9]

No metal loading was observed in $[MTD]_{400}$ homopolymer or in the $[MTD]_{800}[NORCOOH]_{30}$ diblock (spherical morphology) after soaking in the metal salt solutions listed in Table 4.1. This indicates that essentially all metal loading occurs within the polyNORCOOH domains, and that transport of metal ions within $[MTD]_{400}[NORCOOH]_{50}$ (cylindrical morphology) occurs primarily through the interconnected cylindrical network of polyNORCOOH rather than through the polyMTD matrix. No loading was observed within $[MTD]_{800}[NORCOOH]_{30}$ because ions are unable to penetrate the polyMTD matrix to reach the isolated spherical polyNORCOOH domains. However, spherical polyNORCOOH domains may be loaded with metals from organometallic vapors such as dimethyl cadmium.[10]

Figure 4.2 shows the loading capacity of $[MTD]_{400}[NORCOOH]_{50}$ films as a function of time from aqueous $Ag(OOCCH_3)$. An unloaded film (Figure 4.2a) has nearly the same uptake capacity, 650 mg Ag/g polyNORCOOH, as a film previously loaded with Ag^+ and reduced under hydrogen (Figure 4.2b, 600 mg Ag/g polyNORCOOH); however, a previously loaded but unreduced film (Figure 4.2c) takes up a considerably lower amount of Ag^+, 280 mg Ag/g polyNORCOOH, after 9 days. These data support the hypothesis that hydrogen reduction re-protonates metal-bound carboxylate ions allowing them to participate in further metal binding. The lower initial slope of Figure 4.2b compared to Figure 4.2a may be attributed to additional diffusional resistance caused by the Ag nanoclusters that are present (in the case of Figure 4.2b) within the polyNORCOOH domains. The fact that some loading was observed in

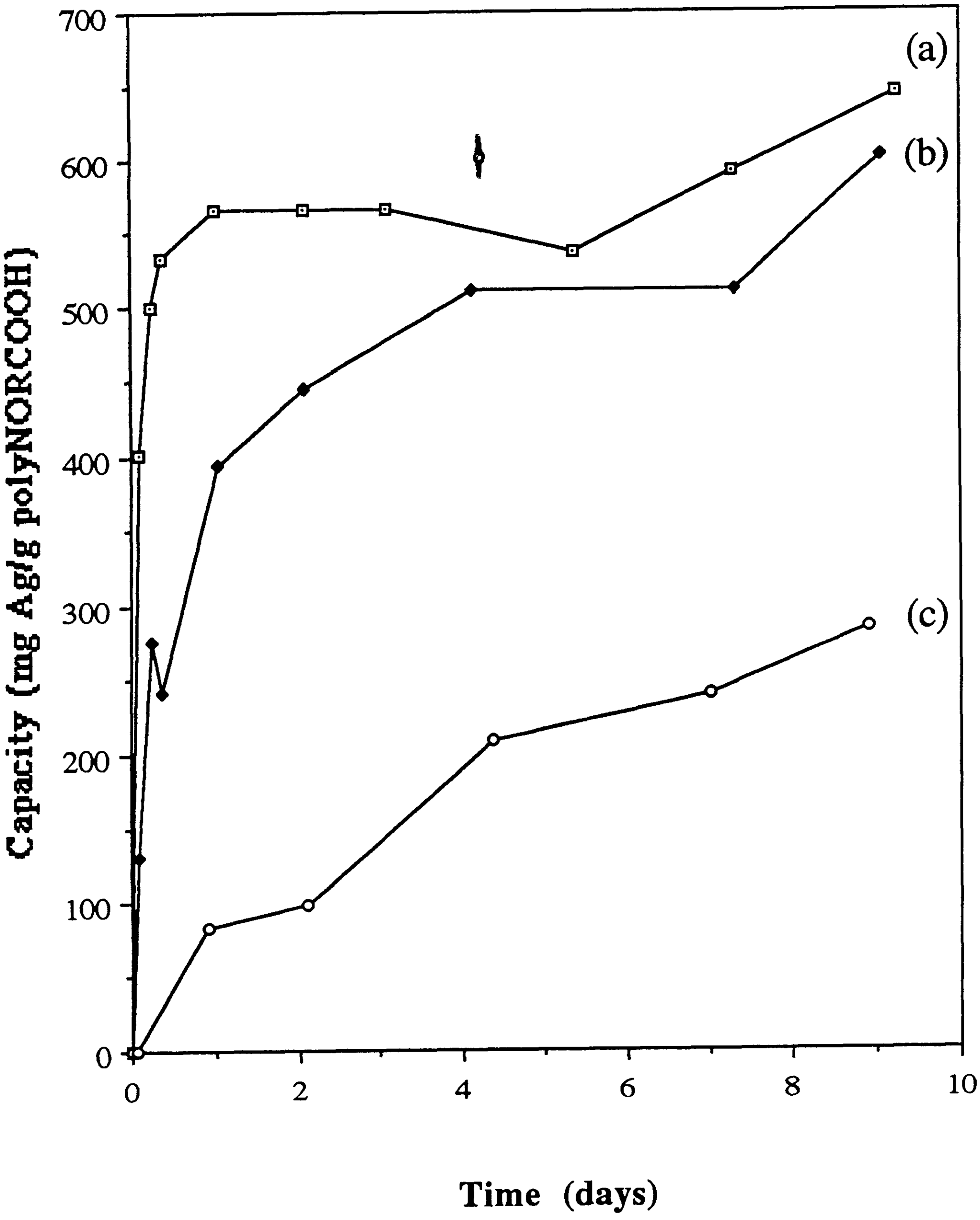

Figure 4.2: Loading capacity of $[MTD]_{400}[NORCOOH]_{50}$ for Ag^+ as a function of time: (a) unloaded film; (b) previously loaded with Ag^+ and reduced; (c) previously loaded with Ag^+ but not reduced

Figure 4.2c indicates that the loading capacity shown in Figure 4.2a is limited by the decreasing Ag^+ concentration in solution rather than by the depletion of all available carboxylic acid groups. Little or no Ag^+ ion release was detected with ICP-AES after soaking a 10 μm thick Ag^+ loaded film in de-ionized water for 6 days.

Table 4.4 shows the loading capacity of polyNORCOOH, after 9 days of loading, from metal salt solutions in methanol.

Table 4.4 Loading capacity of polyNORCOOH* from methanol

Species	**mg metal per g polyNORCOOH**	**moles metal per mole COOH unit**
$Ag(OOCCH_3)$	insoluble	-
$AuCl_3$	reduced	-
$Cu(OOCCH_3)_2$	85	0.12
$CuCl_2$	< 20	-
$NiCl_2$	< 20	-
$Na_2PdCl_4x3H_2O$	210	0.18
$Na_2PtCl_4xH_2O$	reduced	-
$PbCl_2$	insoluble	-

* $[MTD]_{400}[NORCOOH]_{50}$

Both $Ag(OOCCH_3)$ and $PbCl_2$ were nearly insoluble in methanol, so no meaningful ion uptake data was obtained. Furthermore, methanol is known to act as a mild reducing agent,[11] and reduction of both Au^{+3} ($AuCl_3$) and Pt^{+2} ($Na_2PtCl_4xH_2O$) occurred within two days, in methanol, as indicated by a metallic sheen on the solution containers. $CuCl_2$, $Cu(OOCCH_3)_2$, $NiCl_2$, and $Na_2PdCl_4x3H_2O$ were soluble in methanol at 0.005 M concentrations, but no metal ion uptake was observed from $CuCl_2$ or $NiCl_2$ (as was the case for aqueous solutions). Metal uptake was observed from both $Cu(OOCCH_3)_2$) and $Na_2PdCl_4x3H_2O$, but to lessor extents than observed with aqueous solutions.

4.3.2. IR Spectroscopy

Shown in Figure 4.3 are IR spectra of $[MTD]_{400}[NORCOOH]_{50}$ films. Figure 4.3a corresponds to an unloaded film, Figure 4.3b corresponds to a Ag^+ loaded film prior to hydrogen reduction, and Figure 4.3c corresponds to a Ag^+ loaded film following reduction. All three spectra show the expected C-H (2850-2960 cm^{-1}), C=O (1670-1780 cm^{-1}), and O-H (2500-3300 cm^{-1}) absorptions[12]. Figures 4.3b and 4.3c show an additional absorption at ca. 1540 cm^{-1}. The asymmetrical stretching mode ($\nu_a(COO^-)$) of carboxylate ions is known to absorb at ca. 1556 cm^{-1},[13] and complexation of carboxylate ions with metal cations has been observed to shift $\nu_a(COO^-)$ by +/- 20 cm^{-1}.[13] Therefore, the appearance of the 1540 cm^{-1} absorption in Figure 4.3b indicates partial ionization of the carboxylic acid groups and complexation with Ag^+. Loss of peak intensity at the $\nu_a(COO^-)$ absorption relative to the C=O absorption in Figure 4.3c is consistent with re-protonation of most carboxylate ions during the hydrogen reduction process.

4.3.3. WAXS Characterization

Shown in Figures 4.4 (Ag^+) and 4.5 (Au^{+3}) are WAXS data for $[MTD]_{400}[NORCOOH]_{50}$ films following metal loading and hydrogen reduction. The diffracted X-ray intensities have been normalized through division by the maximum intensity of the polymer peak (amorphous halo). Figure 4.4a shows a broad peak ($2\theta=38.1°$) consistent with scattering from the [111] plane of f.c.c. silver,[14] following a single loading and reduction sequence. Figure 4.4b shows growth of the [111] peak and emergence of the [200] peak ($2\theta=44.3°$), following a second loading and reduction sequence. Shown in Figure 4.5 are peaks consistent with scattering from the [111] ($2\theta=38.2°$), [200] ($2\theta=44.4°$), and [220] ($2\theta=64.6°$) planes of f.c.c. gold,[14] following a single loading and reduction sequence. The narrow gold peaks relative to those of silver are consistent with TEM observations of occasional large (> 200 Å) gold crystals reported in section 3.3.2. The large peak areas are consistent with

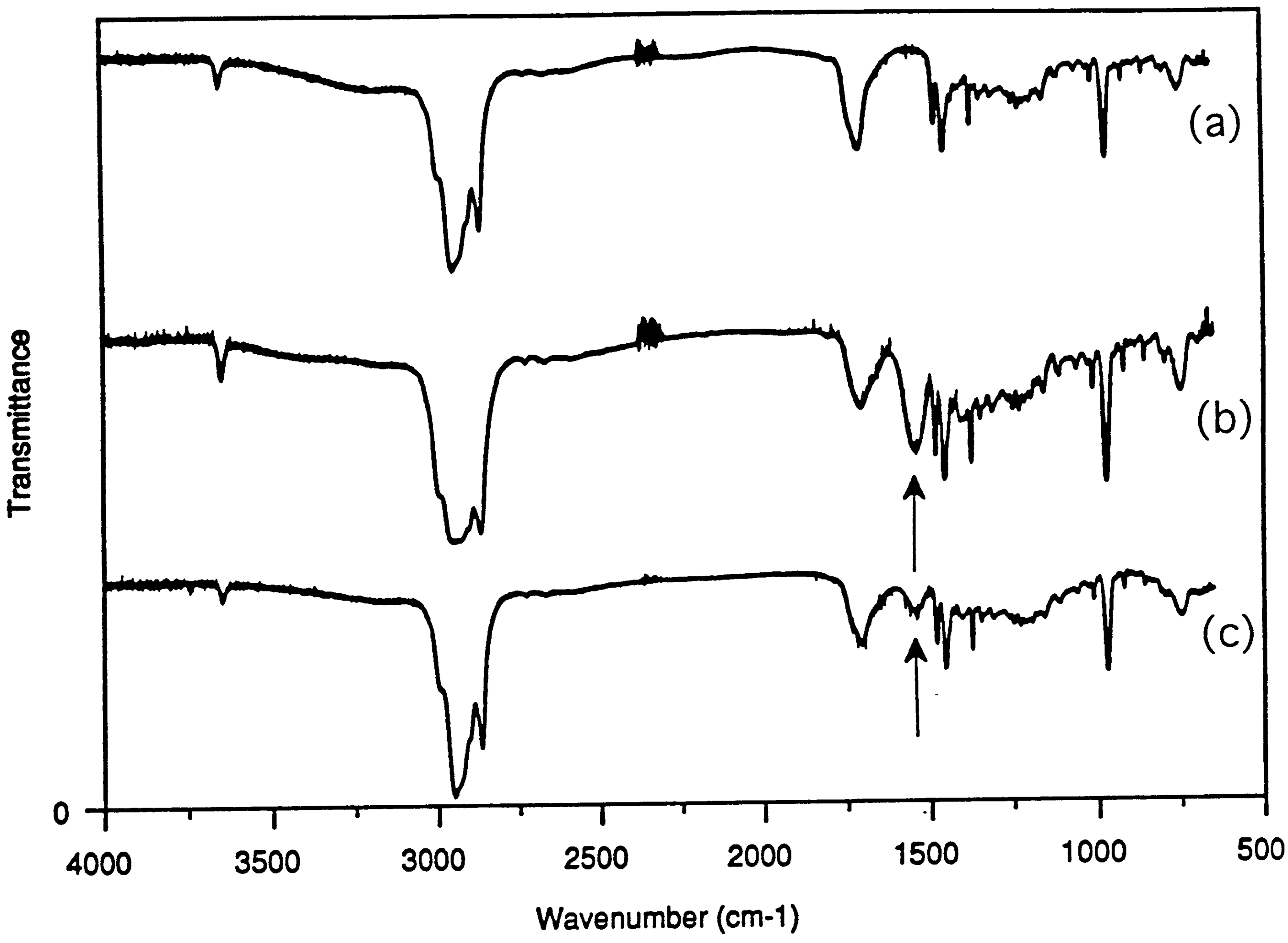

Figure 4.3: IR spectra of $[MTD]_{400}[NORCOOH]_{50}$: (a) unloaded film; (b) previously loaded with Ag^+ but not reduced; (c) previously loaded with Ag^+ and reduced

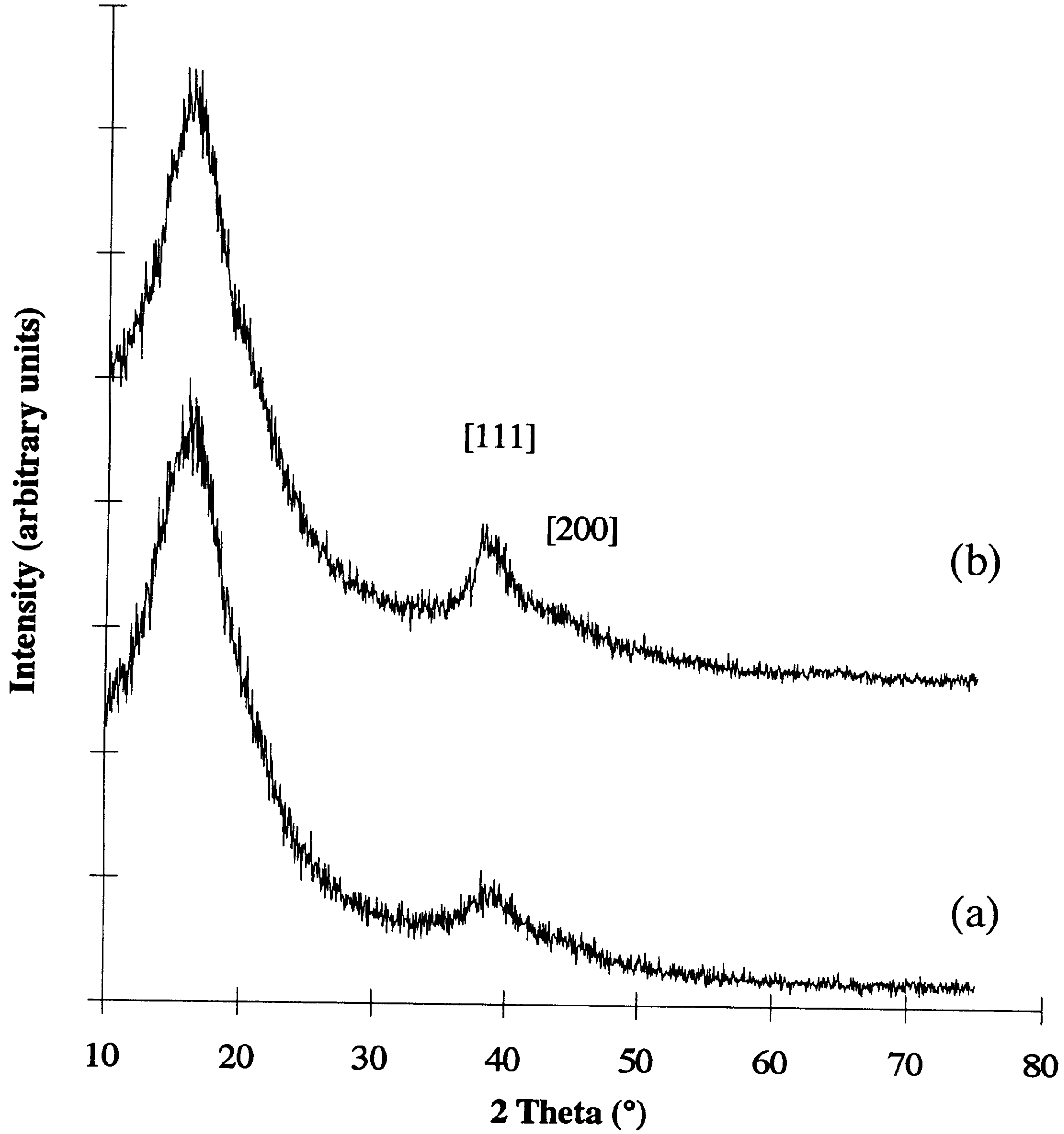

Figure 4.4: WAXS data from silver nanocluster containing $[MTD]_{400}[NORCOOH]_{50}$ film: (a) after 1st loading/reduction sequence; (b) after 2nd loading/reduction sequence

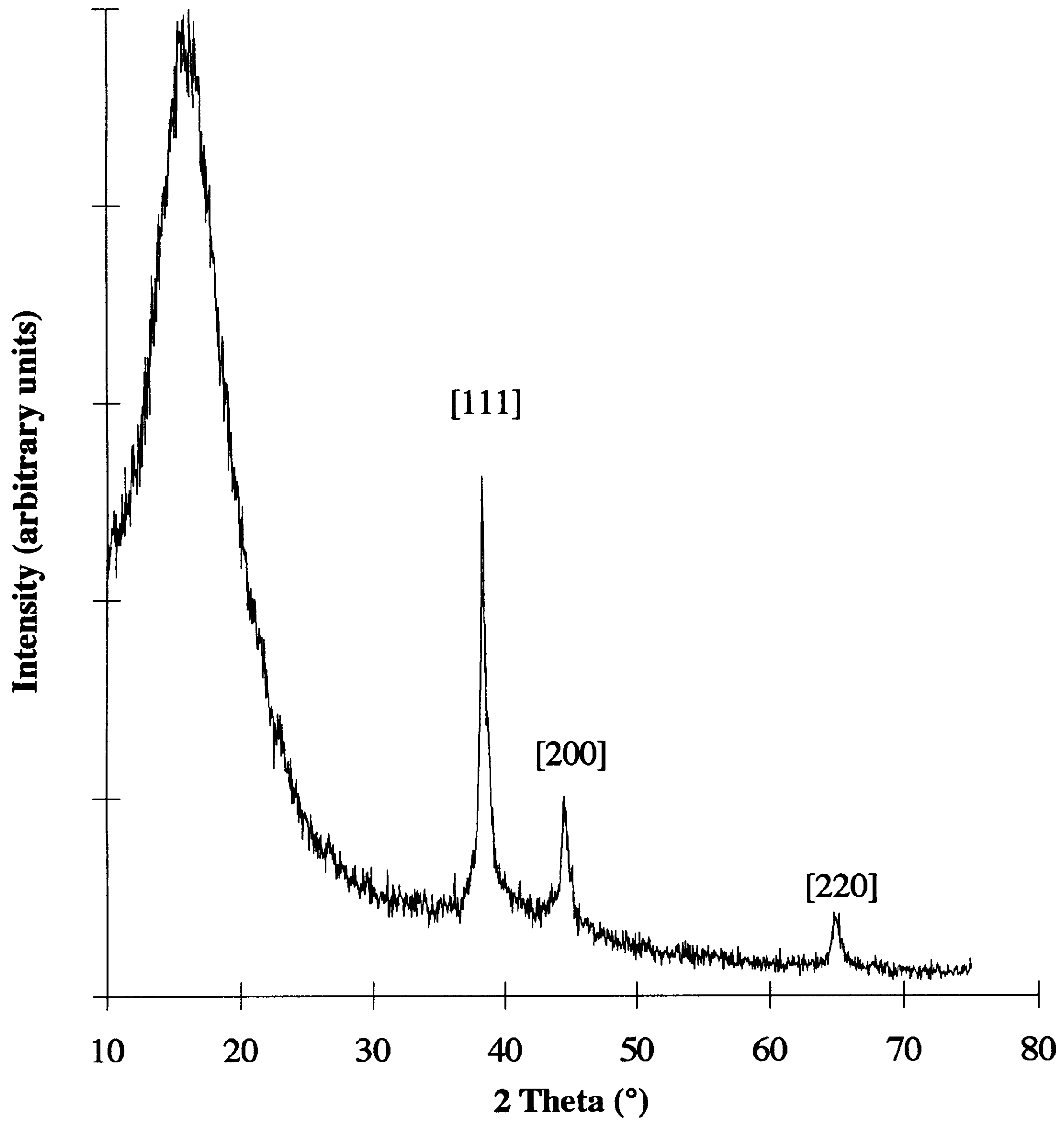

Figure 4.5: WAXS data from gold nanocluster containing $[MTD]_{400}[NORCOOH]_{50}$ film

the high gold loading capacity measured with ICP-AES. Smaller WAXS peaks (not shown), consistent with scattering from f.c.c. palladium ($Na_2PdCl_4x3H_2O$) and f.c.c. copper ($Cu(OOCCH_3)_2$) were observed following loading and reduction of palladium and copper respectively.

Mean crystal diameters of 40 Å, 293 Å, and 100 Å, respectively, were estimated for the silver, gold, and copper clusters using the Scherrer equation (3-1) and equation (3-2).[15] These estimated crystal diameters are in agreement with TEM observations of 400 Å thick sections of the 10 μm thick silver and copper cluster containing films, shown in Figures 4.6 and 4.7 respectively. Figure 4.6 shows silvers clusters, predominantly in the 35-45 Å size range, and Figure 4.7 shows copper clusters, predominantly in the 70-140 Å size range. Although the 10 μm thick gold cluster containing film was not observed with TEM, the mean crystal diameter estimated through WAXS is consistent with TEM observations of a 0.5 mm thick gold cluster containing film (Figure 3.15).

4.3.4. UV-Visible Spectroscopy

Shown in Figures 4.8, 4.9, and 4.10, respectively, are UV-visible spectra of gold, silver, and copper ($Cu(OOCCH_3)_2$) loaded $[MTD]_{400}[NORCOOH]_{50}$ films following reduction. The gold cluster containing film (Figure 4.8) appears violet in color following reduction and has a surface plasmon absorption at ca. 540 nm. The silver cluster containing film (Figure 4.9) appears orange in color following reduction and exhibits a strong surface plasmon absorption at ca. 430 nm. The copper cluster containing film appeared reddish-purple following reduction, but turned bluish-green after 48 hours in air. We attribute this color change to formation of a very thin surface copper oxide layer on each cluster. Following the color change, WAXS revealed only the copper [111] peak. No scattering associated with CuO or Cu_2O was detected. Figure 4.10 shows the UV-visible spectra of the oxidized copper cluster containing film, with an absorption peak at ca. 590 nm. Shown in Figures 4.11a, 4.11b, and

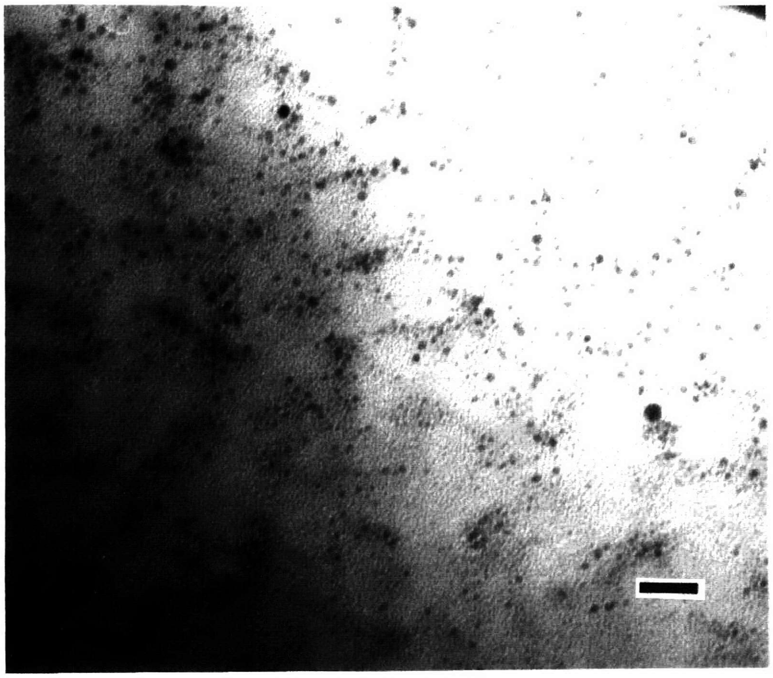

Figure 4.6: Electron micrograph of 10 μm thick silver nanocluster containing film (bar = 300 Å)

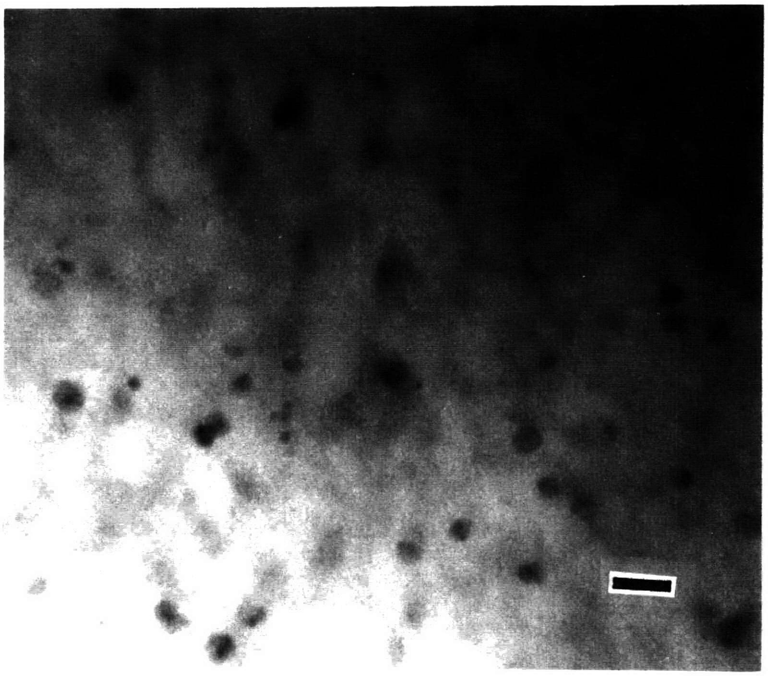

Figure 4.7: Electron micrograph of 10 μm thick oxidized copper nanocluster containing film (bar = 300 Å)

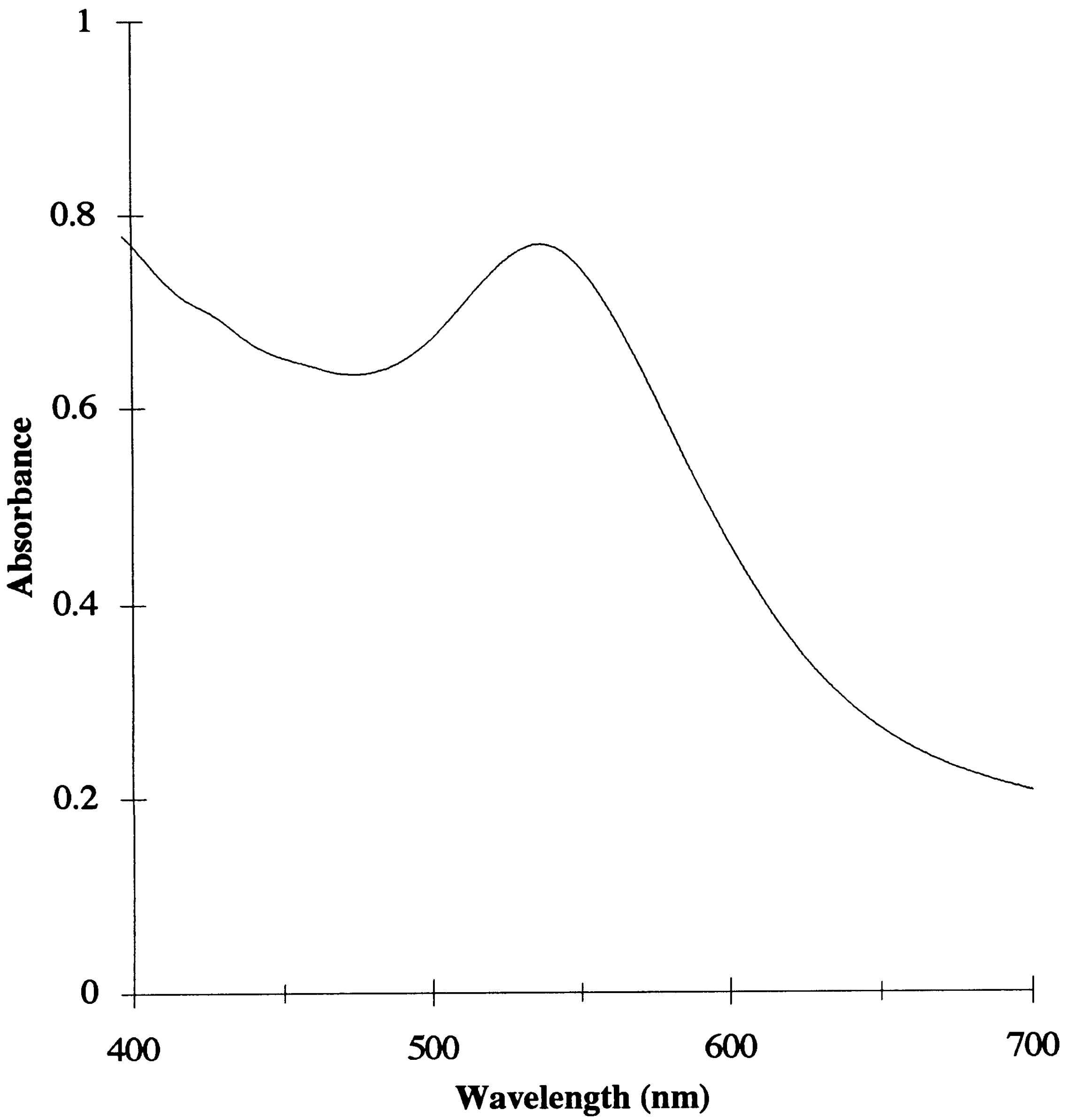

Figure 4.8: UV-Visible spectra of 10 μm thick gold nanocluster containing $[MTD]_{400}[NORCOOH]_{50}$ film

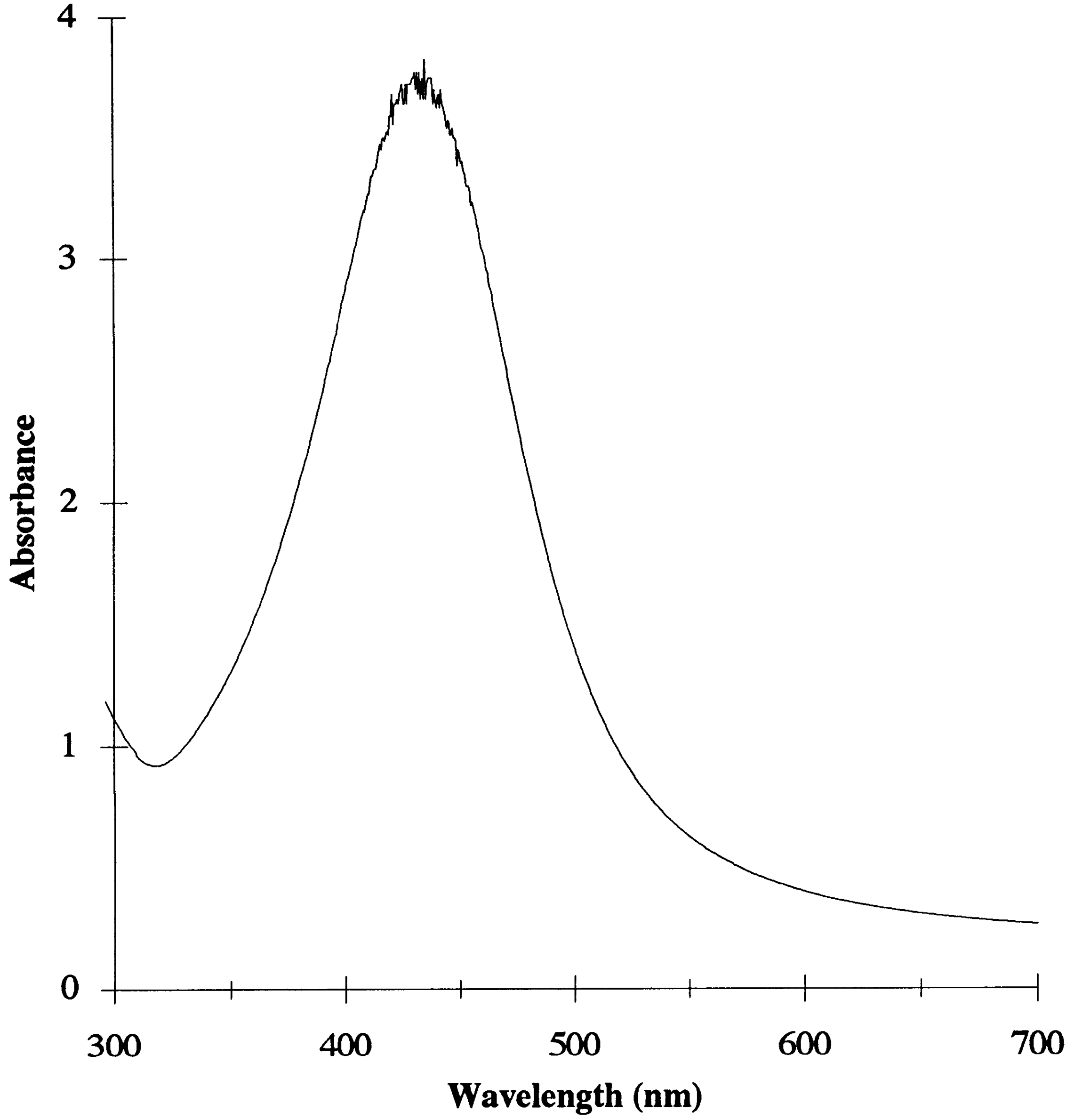

Figure 4.9: UV-Visible spectra of 10 μm thick silver nanocluster containing $[MTD]_{400}[NORCOOH]_{50}$ film

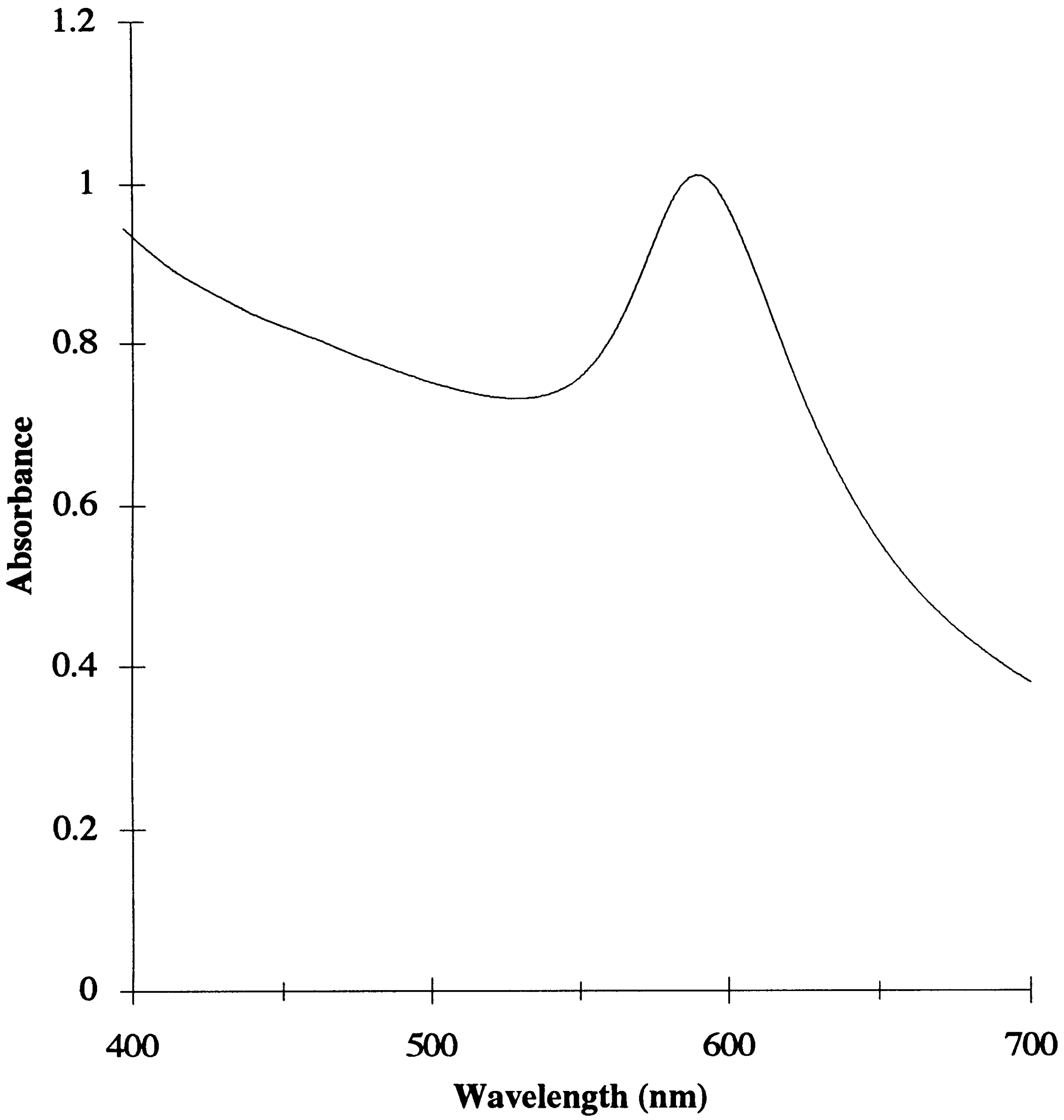

Figure 4.10: UV-Visible spectra of 10 μm thick oxidized copper nanocluster containing $[MTD]_{400}[NORCOOH]_{50}$ film

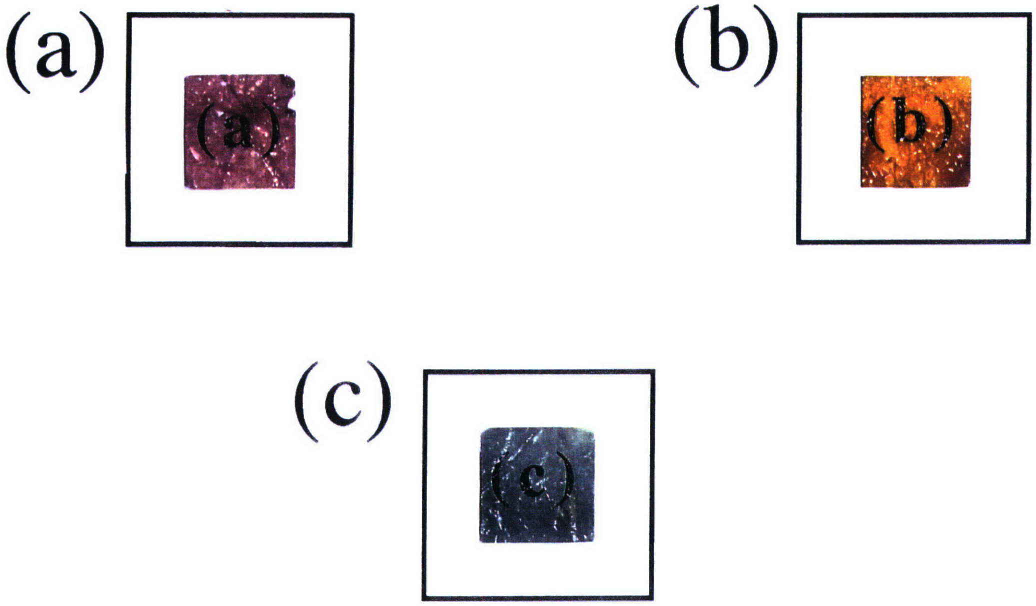

Figure 4.11:

Ten micron thick $[MTD]_{400}[NORCOOH]_{50}$ films after aqueous metal loading (0.005 M, 25 °C, 9 days) and H_2 reduction (2 atm H_2, 115 °C, 6 days): (a) $AuCl_3$; (b) $Ag(OOCCH_3)$; (c) $Cu(OOCCH_3)_2$

4.11c are photographs of the 10 μm thick metal cluster containing films corresponding to the UV-visible spectra in Figures 4.8 (gold), 4.9 (silver), and 4.10 (oxidized copper) respectively.

The Ag^+ loaded film changed color from clear to transparent orange during the first few minutes of the reduction process (warm-up to 115 °C). A slow color change from clear to transparent orange was apparent after placing the Ag^+ loaded film under hydrogen prior to heating. The entire Ag^+ reduction process may occur within a minute at the steady-state temperature of 115 ° C. The reduction time of 6 days was adopted before we knew how rapidly the reaction occurred. We did not make kinetic observations during Au^{+3} or Cu^{+2} reduction.

The oxidized copper cluster containing film became greenish (transparent) in color, after storing in air, at room temperature, for approximately a year. WAXS from the greenish oxidized copper cluster containing film revealed only scattering from the polymer. No Cu, CuO, Cu_2O peaks were observed, possibly indicating complete oxidation of the f.c.c. copper clusters to amorphous copper oxide.

The rich colors displayed by gold, silver, and copper nanoclusters, isolated in dielectric matrices, are a result of the selective absorption of visible light into the particle's surface plasmon mode.[16] The Mie theory (1908), for non-interacting particles, provides a clear classical description of most experimental observations.[16,17] Mie theory predicts that small particles have well-defined surface plasmon modes in the visible range of wavelengths, with a width that varies inversely with the particle size, and an intensity which is proportional to the metal concentration.

Given a small isolated spherical particle with a complex dielectric constant,

$$\varepsilon = \varepsilon_1 + i\,\varepsilon_2 \tag{4-3}$$

embedded in a dielectric medium of dielectric constant, ε_m, an oscillating electric field will cause a build-up of surface charge. This accumulation of charge provides a restoring force, leading to resonant density oscillations of conduction electrons at visible frequencies (the surface plasmon mode). The total absorption coefficient, K, is given by,

$$K = 18\pi f \varepsilon_m^{3/2} / \lambda \bullet \varepsilon_2 / [(2\varepsilon_m + \varepsilon_1)^2 + \varepsilon_2^2] \tag{4-4}$$

where f is the volume fraction of metal, and λ is the wavelength of incident light. K reaches a maximum value at a resonance frequency where,

$$\varepsilon_1 = -2\varepsilon_m \tag{4-5}$$

The dielectric constant of the metal is often assumed to be in the Drude-Sommerfeld form,

$$\varepsilon(\omega) = \varepsilon_o(\omega) + 4\pi i \sigma(\omega)/\omega \tag{4-6}$$

where $\varepsilon_o(\omega)$ is the dielectric constant of the metal associated with bound charges, and $\sigma(\omega)$ is the frequency dependent conductivity,

$$\sigma(\omega) = (ne^2\tau/m)/(1 - i\omega\tau) \tag{4-7}$$

The free charge density, electron mass, and Drude relaxation time, respectively, are represented by n, m, and τ. In the high-frequency limit ($\omega\tau >> 1$), it can be shown from equations (4-6) and (4-7) that,

$$\varepsilon_1 = \varepsilon_o - \omega_p^2/ \omega^2 \tag{4-8}$$

$$\varepsilon_2 = \omega_p^2/ \omega^3\tau \tag{4-9}$$

The bulk plasma resonance frequency is given by,

$$\omega_p^2 = 4\pi n e^2/m. \qquad (4\text{-}10)$$

The surface plasmon resonance frequency, ω_{sp}, is then determined from equation (4-5),

$$\omega_{sp}/\omega_p = (\varepsilon_o + 2\varepsilon_m)^{-1/2} \qquad (4\text{-}11)$$

Kawabata and Kubo (1966)[18] developed a more realistic quantum mechanical description of the surface plasmon absorption, which accounts for the discrete electronic structure of nanoscale metal particles. When dealing with discrete electronic structures, Drude theory is inappropriate; therefore, Kawabata and Kubo expressed the frequency-dependent conductivity in terms of current-current correlation functions, using fluctuation-dissipation theory.

It is has been well established both theoretically and experimentally, that when aggregation occurs, absorption is modified with respect to systems of strongly absorbing, but non-interacting spheres.[19-21] The surface plasmon absorptions of isolated spheres split into many new resonances for aggregates, with most new absorptions occurring at larger wavelengths than the isolated sphere resonance. Shown in Figure 4.12 are eigenfrequency spectra of various silver particle aggregates, computed by Clippe et al.,[21] which account for overlap between the electric field of all oscillating spheres. The frequency spectra of the aggregates were calculated assuming that mutual particle interactions can be completely described by dipole-dipole interaction Hamiltonians. As shown in the inset, the frequency splitting for a pair of interacting particles depends on the ratio (L/r) of the pair center-to-center distance, L, to the particle radius, r. When (L/r) = 2, the particles are in physical contact, and the frequency splitting will be a maximum. For (L/r) > 4, little frequency splitting is predicted.

The (L/r) ratio was calculated for the 10 μm thick, $[\mathrm{MTD}]_{400}[\mathrm{NORCOOH}]_{50}$, silver cluster containing film whose electron micrograph and UV-visible absorption spectrum appear

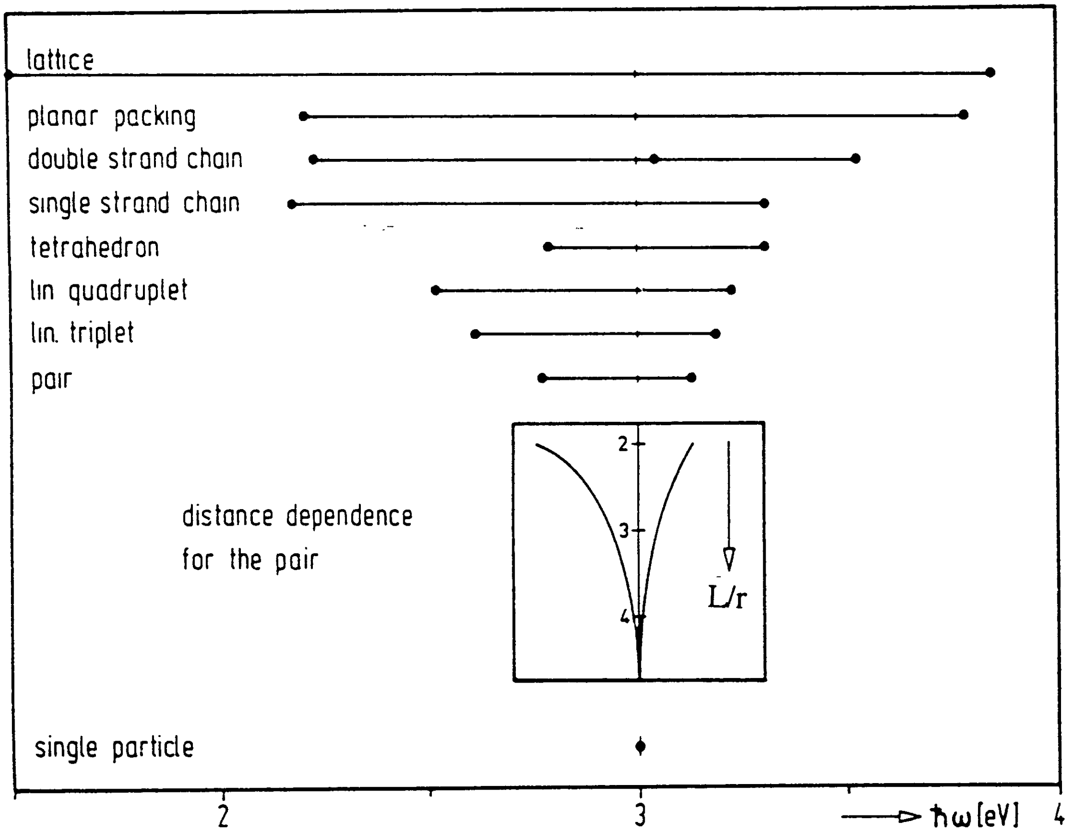

Figure 4.12: Eigenfrequency spectra of various Ag particle clusters as computed from the theory of Clippe et al.. The points indicate the modes with strongest absorption. The optical constants for Ag were taken from the literature; ε_m=2.37. Inset: dependence of the frequency splitting of a dipole coupled particle pair on center-to-center distance, L, and particle radius, r.

Kreibig, U., Althoff, A., and Pressmann, H. *Surface Science* **1981**, 106, 308.

in Figures 4.6 and 4.9 respectively. A mean cluster radius, r, of 20 Å was estimated from Figure 4.6. The mass of a single cluster, M_c, was then calculated as shown below,

$$M_c = 4/3\pi r^3 \rho_{Ag} \tag{4-12}$$

where ρ_{Ag} (10.5 g/cm^3) is the density of silver. The total number of clusters, N, in the 92 mg polymer film (pure polymer, excluding 8 mg residual THF and the mass of the loaded silver) was calculated to be 1.63×10^{16},

$$N = M_{Ag}/M_c \tag{4-13}$$

where M_{Ag} (5.72 mg) was the total mass of silver loaded into the film. Given 10.7 mg of polyNORCOOH in the 92 mg film and assuming a polyNORCOOH density of 1 g/cm^3, we calculated a total polyNORCOOH volume, V_p, of 0.0107 cm^3. The cluster density, n, within the polyNORCOOH domains was then calculated to be 1.52×10^{18} cm^{-3},

$$n = N/V_p. \tag{4-14}$$

For comparison, the density of COOH groups within the polyNORCOOH domains was calculated to be 6.6×10^{21} cm^{-3}. The average, pair center-to-center distance was determined by assuming a homogeneous simple cubic arrangement of clusters within the polyNORCOOH domain, with each cluster positioned in the center of a cube of volume 1/n. The average, pair center-to-center distance or cube edge length, L, is then calculated as,

$$L = (1/n)^{1/3} \tag{4-15}$$

which in this case was 87 Å. Therefore, the (L/r) ratio for the silver cluster containing film was found to be 4.35. Since (L/r) > 4, we should not expect to observe splitting of the surface plasmon absorption peak. Thus, the single absorption peak appearing in Figure 4.9 is consistent with the scattering theory of Clippe et al.. However, particle interactions may become apparent at metal higher loading.

Combining equations (4-12) through (4-15), it is apparent that the (L/r) ratio is given by,

$$L/r = [(4\pi V_p)/(3V_{Ag})]^{1/3} \tag{4-16}$$

where V_{Ag} is the total volume of silver loaded into the film. Therefore, the (L/r) ratio is independent of the estimated cluster size.

Figure 4.13 shows a scale 2-dimensional projection of clusters homogeneously distributed throughout the polyNORCOOH domain on a hypothetical simple cubic lattice. The preceding analysis involves two assumptions: 1) All loaded Ag^+ ions are reduced to silver nanoclusters and 2) All silver nanoclusters are restricted to the polyNORCOOH domains. We believe both assumptions are reasonable, but not entirely true. The IR-spectrum in Figure 4.3c demonstrates that at least a small fraction of the loaded Ag^+ ions remain unreduced following hydrogen treatment. In addition, electron micrographs of silver nanocluster containing films sometimes reveal larger μm sized silver particles. Therefore, some fraction of the loaded Ag^+ ions do not form silver nanoclusters, which leads to an underestimation of L and the (L/r) ratio. Similarly, some migration of silver nanoclusters beyond the polyNORCOOH domains is possible, also contributing to an underestimation of L and the (L/r) ratio. Finally, although simple cubic packing is not a realistic representation of a random, homogeneous distribution of particles, it should provide a reasonable estimate of the closest, average L for such a case. It is not known whether the presence of the silver clusters increases the volume of the polyNORCOOH domain; however, even if the volume of the polyNORCOOH domain expanded by an amount equal to the volume of the embedded clusters, the total volume of the polyNORCOOH/cluster composite would only be 5 % larger than the volume of the pure polyNORCOOH domain.

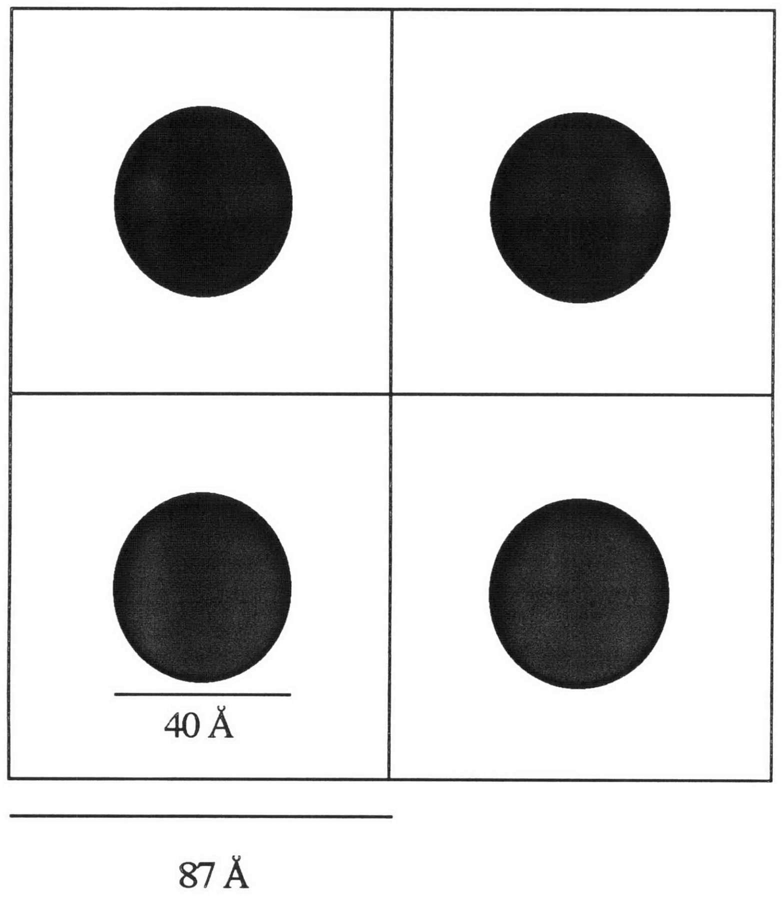

Figure 4.13: 2-D projection of silver nanoclusters homogeneously dispersed on a hypothetical simple cubic lattice

It may also be possible to obtain (L/r) estimates directly from electron micrographs such as Figure 4.6, using the observed average cluster size and thickness normalized cluster density. However, I recommend against this procedure because it requires a good estimate of the sample thickness under observation. This average sample thickness (i.e. 400 Å) can be selected during the microtoming process; however, the actual thickness of an area under observation, may deviate by a factor of 2 or more from the average sample thickness. This deviation will usually be toward thinner sections, since they provide bright, high contrast images.

We attempted to shift the surface plasmon absorption frequency, ω_{sp}, of the Ag clusters, whose UV-visible absorption spectrum appears in Figure 4.9, by exposing the film to pyridine vapor in a sealed jar (13 days, 25 °C, nitrogen atmosphere). We hoped that coordination between pyridine and the Ag clusters would lead to changes in ε_o, and thus alter ω_{sp} according to equation (4-11). However, no shift in the shape or position of the UV-visible absorption spectrum was observed after pyridine exposure.

4.4. Conclusions

Transport of metal ions within $[MTD]_{400}[NORCOOH]_{50}$ (cylindrical morphology) occurs primarily through the interconnected cylindrical network of polyNORCOOH rather than through the polyMTD matrix. No metal loading was observed within $[MTD]_{800}[NORCOOH]_{30}$ (spherical morphology) because metal ions are unable to penetrate the polyMTD matrix to reach the isolated spherical polyNORCOOH domains. On a molar basis as shown in Table 4.3, Ag^+ (0.54, $Ag(OOCCH_3)$) and Au^{+3} (0.51, $AuCl_3$) load to the greatest extent, followed by Pd^{+2} (0.29, $Na_2PdCl_4x3H_2O$), Pd^{+2} (0.20, $Pd(OOCCH_3)_2$), Fe^{+2} (0.17, $Fe(OOCCH_3)_2$), Cu^{+2} (0.14, $Cu(OOCCH_3)_2$), Fe^{+3} (0.13, $FeCl_3$), and Pt^{+4} (0.08, $H_2PtCl_6xH_2O$). An effective diffusion coefficient of $3x10^{-12}$ cm^2/s for Ag^+ within $[MTD]_{400}[NORCOOH]_{50}$ was estimated. Little or no loading was observed from $CuCl_2$, $FeCl_2$, $NiCl_2$, $PdCl_2$, $Na_2PtCl_4xH_2O$, or the Eu and Gd containing compounds.

Loading capacity was found to depend on the compound from which the metal was introduced. In the cases of Cu, Fe, and Pd, loading of M^{+2} from $M(OOCCH_3)_2$ was significantly higher than loading from MCl_2. Fe^{+3} ($FeCl_3$) and Pt^{+4} ($H_2PtCl_6x6H_2O$) loaded to greater extents than Fe^{+2} ($FeCl_2$) and Pt^{+2} ($Na_2PtCl_4xH_2O$). Hydrogen reduction of metal loaded films was found to re-protonate metal-bound carboxylate ions allowing participation in further metal binding.

Both UV-visible spectra and the absorption theory of Clippe et al. indicated our silver nanoclusters were electronically isolated within 10 μm thick $[MTD]_{400}[NORCOOH]_{50}$ films following a single loading and reduction sequence.

4.5 References for Chapter 4

(1) Thompson, M. and Walsh, J.N. 'Handbook of Inductively Coupled Plasma Spectrometry' 2nd Ed., Chapman and Hall, New York, 1989.

(2) Boumans, P.W.J.M. *Science and Engg.* **1978**, 12, 1.

(3) Boumans, P.W.J.M. 'Inductively Coupled Plasma Atomic Emission Spectroscopy. Part I: Methodology, Instrumentation and Performance. Part II: Applications and Fundamentals.' Wiley-Interscience, New York, 1987.

(4) Bird, R.B., Stewart, W.E., and Lightfoot, E.N. 'Transport Phenomena' John Wiley & Sons, New York, 1960, p. 505.

(5) Helfferich, F.G. 'Ion Exchange', McGraw-Hill, Inc., New York, 1962, p. 279.

(6) Calmon, C. in 'Adsorption and Ion Exchange'; AIChE Symp. Ser. 1984, 80, No. 233.

(7) Amberlite® IRC-50, Rohm and Hass Company, IE-232a, 1989.

(8) Amberlite® IRC-718, Rohm and Hass Company, IE-313, 1993.

(9) Marcus, Y. and Kertes, A.S. 'Ion Exchange and Solvent Extraction of Metal Complexes', John Wiley and Sons Ltd., New York, 1969, p.284.

(10) Yue, J. and Cohen, R.E. *Supramolecular Science* **1994**, 1, 117.

(11) Hirai, H., Nakao, Y., and Toshima, N. *J. Macromol. Sci.-Chem.* **1978**, A12, 1117.

(12) McMurray, J. 'Organic Chemistry', 2nd Ed., Brooks/Cole Publishing, Pacific Cove, 1988, p. 397.

(13) McCluskey, P.H., Snyder, R.L. and Condrate, R.A. *J. Sol. State Chem.*, **1989**, 83, 332.

(14) Swanson, H.E. and Tatge, E. 'U.S. National Bureau of Standards Standard X-Ray Diffraction Patterns', NBS Circular 539, Volume 1, U.S. Government Printing Office, Washington D.C., June 15, 1953

(15) Klug, H.P. and Alexander, L.E. 'X-Ray Diffraction Procedures', John Wiley & Sons, Inc., New York, 1954, p. 491.

(16) Halperin, W.P. *Rev. Mod. Phys.* **1986**, 58, 533.

(17) Mie, G. *Ann. Phys.* **1908**, 25, 377.

(18) Kawabata, A. and Kubo, R. *J. Phys. Soc. Jpn.* **1966**, 21, 1765.

(19) Quinten, M. and Stier, J. *J. Colloid Polym. Sci.* **1995**, 273, 233.

(20) Kreibig, U., Althoff, A., and Pressmann, H. *Surface Science* **1981**, 106, 308.

(21) Clippe, P., Evrard, R., and Lucas, A. *Phys. Rev. B.* **1976**, 14, 1715.

Chapter 5

Synthesis of Metal Nanoclusters within Microphase-Separated Diblock Copolymers: Sodium Carboxylate vs. Carboxylic Acid Functionalization

5.1. Summary

In Chapter 3, we reported a general methodology for the synthesis of transition metal nanoclusters (Ag, Au, Cu, Ni, Pb, Pd, and Pt) stabilized within microphase-separated diblock copolymers. In our strategy, outlined in Figure 1.9, metal ions or complexes are coordinated to carboxylic acid groups within the water soluble polyNORCOOH domains of a $[MTD]_{400}[NORCOOH]_{50}$ block copolymer (MTD = methyltetracyclododecene and NORCOOH = 2-norbornene-5,6,-dicarboxylic acid) by immersion of the polymer in aqueous metal salt solutions. The metal ions and complexes are subsequently reduced by heating the metal loaded polymer under hydrogen or by immersion in an aqueous sodium borohydride solution. For several transition metals, the resulting nanoclusters are uniformly sized and homogeneously dispersed within the polyNORCOOH domains.

We demonstrated (Chapter 4), using inductively coupled plasma atomic emission spectroscopy (ICP-AES), that metal ion transport occurs primarily through the interconnected cylindrical network of polyNORCOOH rather than through the polyMTD matrix. We also showed that the loading capacity is dependent on the compound from which the metal is introduced, with metals such as Ag ($Ag(OOCCH_3)$) and Au ($AuCl_3$) loading to greater extents than Cu ($CuCl_2$), Fe ($FeCl_2$), or Ni ($NiCl_2$). We found, using IR spectroscopy, that hydrogen reduction of metal loaded films re-protonates metal-bound carboxylate ions, allowing participation in further metal binding.

We now report on a method used to increase the rate and extent of metal uptake into our films, shown in Figure 5.1. In our modified strategy, carboxylic acid groups are first converted to the sodium carboxylate form, by soaking in aqueous NaOH; transition metal and

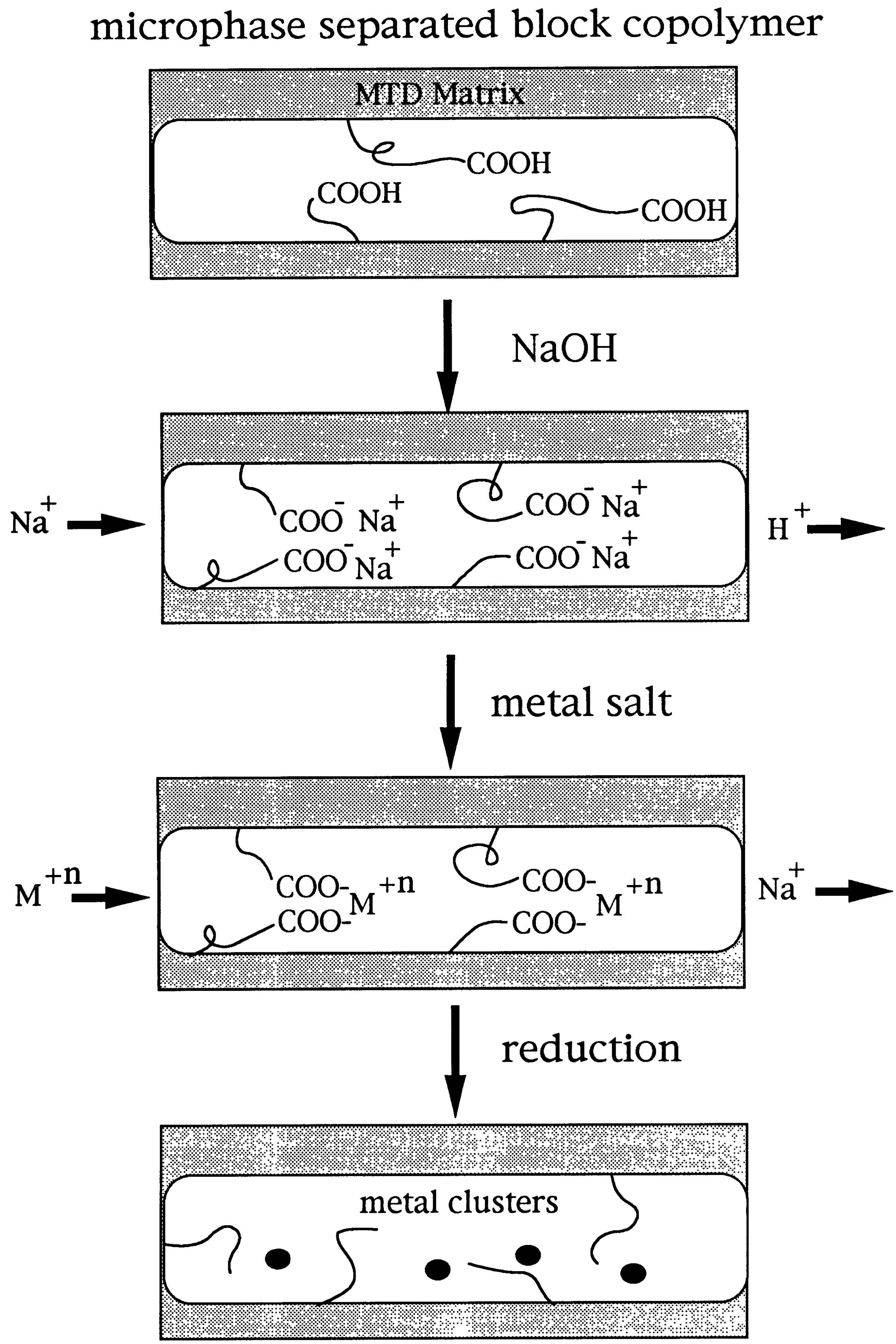

Figure 5.1: Metal cluster synthesis scheme

rare earth ions are then substituted for Na^+ ions by immersion of the sodium carboxylate functionalized polymer in aqueous metal salt solutions. The Ag loading capacity of sodium carboxylate functionalized films is explored following several loading and reduction sequences (LARS). The relationship between the extent of Ag^+ loading and cluster size is studied, for carboxylic acid functionalized films, during a single LARS.

Conversion of carboxylic acid groups, within the morphologies of $[MTD]_{400}[NORCOOH]_{50}$ diblock copolymers, to the sodium carboxylate form, $[MTD]_{400}[NORCOONa]_{50}$, results in large increases in both the rate and extent of transition metal and rare earth ion uptake from metal acetates, chlorides, nitrates, and sulfates. A $[MTD]_{400}[NORCOONa]_{50}$ film was subjected to four consecutive Ag^+ loading and reduction sequences, resulting in a cumulative loading of approximately 26 wt. % Ag in the overall polymer/Ag composite. Mean crystal diameters of 37 Å, 50 Å, 64 Å, and 65 Å were estimated following the first, second, third, and fourth, loading and reduction sequences respectively. During a single loading and reduction sequence, cluster size (ca. 30 Å) within $[MTD]_{400}[NORCOOH]_{50}$ was found to be relatively insensitive to the extent of Ag^+ uptake, for loadings between 40 and 500 mg Ag^+/g polyNORCOOH, consistent with a nucleation controlled cluster formation process.

5.2. Experimental

$[MTD]_{400}[NORCOOH]_{50}$ diblock copolymer was synthesized using a ring-opening metathesis polymerization in anhydrous toluene with a $Mo(CHCMe_2Ph)(NAr)(O\text{-}t\text{-}Bu)_2$ (Ar = $2,6\text{-}C_6H_3\text{-}i\text{-}Pr_2$) initiator.

10 μm and 0.25 mm thick polymer films were static cast from 1 wt. % and 3 wt. % solutions in tetrahydrofuran (THF) respectively. See Appendix D. Transmission electron microscopy observation of sections of 0.25 mm thick films, revealed irregular interconnected regions of polyNORCOOH within a polyMTD matrix. Carboxylic acid groups within 10 μm

thick films were converted to the sodium carboxylate form ($[MTD]_{400}[NORCOONa]_{50}$) by soaking in 0.015 M aqueous NaOH solutions at 25°C.

5.2.1. Metal Ion Uptake in Sodium Carboxylate Functionalized Films

Metal loading experiments were carried out at 25°C using a batch equilibration method in which 100 mg samples of 10 μm thick films ($[MTD]_{400}[NORCOOH]_{50}$ or $[MTD]_{400}[NORCOONa]_{50}$) were submerged in 20 g solutions of 0.005 M aqueous metal salts. Agitation was maintained with magnetic stir bars. The metal ion concentration remaining in the supernatant solution was measured periodically by withdrawing small aliquots of supernatant solution. The withdrawn aliquots were diluted with water to metal ion concentrations of < 30 ppm and analyzed using ICP-AES.

The extent of metal ion uptake was calculated using equation (4-1). Loading with $Ag(OOCCH_3)$ was done in the dark.

5.2.2. Analysis of Ag^+ Loading Capacity (Multiple LARS)

The Ag loading capacity of 0.4 g of 10 μm thick polymer film was evaluated using ICP-AES during each of four consecutive LARS, where a LARS consists of the following steps: 1. Conversion of carboxylic acid groups to the sodium carboxylate form (soak $[MTD]_{400}[NORCOOH]_{50}$ film in 0.015 M aqueous NaOH for 48 hr at 25 °C, 100 mg film per 20 g solution), 2. Rinse and dry (rinse $[MTD]_{400}[NORCOONa]_{50}$ film in de-ionized water and dry under vacuum at 25 °C for 15 hr), 3. Conversion of sodium carboxylate groups to the silver carboxylate form (soak $[MTD]_{400}[NORCOONa]_{50}$ film in 0.005 M aqueous $Ag(OOCCH_3)$ for 48 hr at 25 °C, 100 mg film per 25 g solution), 4. Rinse and dry (rinse $[MTD]_{400}[NORCOOAg]_{50}$ film in de-ionized water and dry under vacuum at 25 °C for 15 hr), and 5. Ag^+ reduction (heat $[MTD]_{400}[NORCOOAg]_{50}$ film under 2 atm of hydrogen for 24 hr at 115 °C). The film was examined using IR spectroscopy following each step of the first two

LARS. The average cluster size was estimated following each LARS using both TEM and WAXS.

5.2.3. Extent of Ag^+ Loading vs. Cluster Size (Single LARS)

The relationship between the extent of Ag^+ loading and cluster size was studied within 0.25 mm thick $[MTD]_{400}[NORCOOH]_{50}$ films. 100 mg sections of film were each soaked in separate 20 g solutions of 0.0075 M aqueous $Ag(OOCCH_3)$ at 25 °C, for periods ranging from 1 day to 7 weeks. The extents of loading were measured using ICP-AES. All Ag^+ loaded films were reduced by heating under 2 atm of hydrogen for 6 days at 115 °C. The average cluster size was estimated for each extent of loading using both TEM and WAXS.

5.3. Results and Discussion

GPC analysis of the homo-MTD blocks yielded polydispersities of approximately 1.1. The block copolymer was not analyzed using GPC because polyNORCOOH precipitates in toluene. The static cast 10 μm thick $[MTD]_{400}[NORCOOH]_{50}$ films were clear; however, the 0.25 mm thick films had a slight yellowish tint, probably due to trace residues of $Mo(CHCMe_2Ph)(NAr)(O\text{-}t\text{-}Bu)_2$.

5.3.1. Metal Ion Uptake in Sodium Carboxylate Functionalized Films

ICP-AES measurements showed that Na^+ loading was complete within 7 hr, with 1.1 moles of Na^+ per mole of carboxylic acid entering the film. Given the estimated accuracy of our measurements of +/- 15%, this implies essentially complete exchange of carboxylic acid H^+ ions for Na^+ ions. Figure 5.2 compares the loading capacity of $[MTD]_{400}[NORCOONa]_{50}$ with that of $[MTD]_{400}[NORCOOH]_{50}$, for Cu^{+2} from $Cu(OOCCH_3)_2$. Figure 5.2a shows Cu^{+2} loads rapidly into $[MTD]_{400}[NORCOONa]_{50}$, reaching an equilibrium loading capacity of 330 mg Cu^{+2} per gram of polyNORCOOH originally present, or 0.47 (moles Cu^{+2}/mole

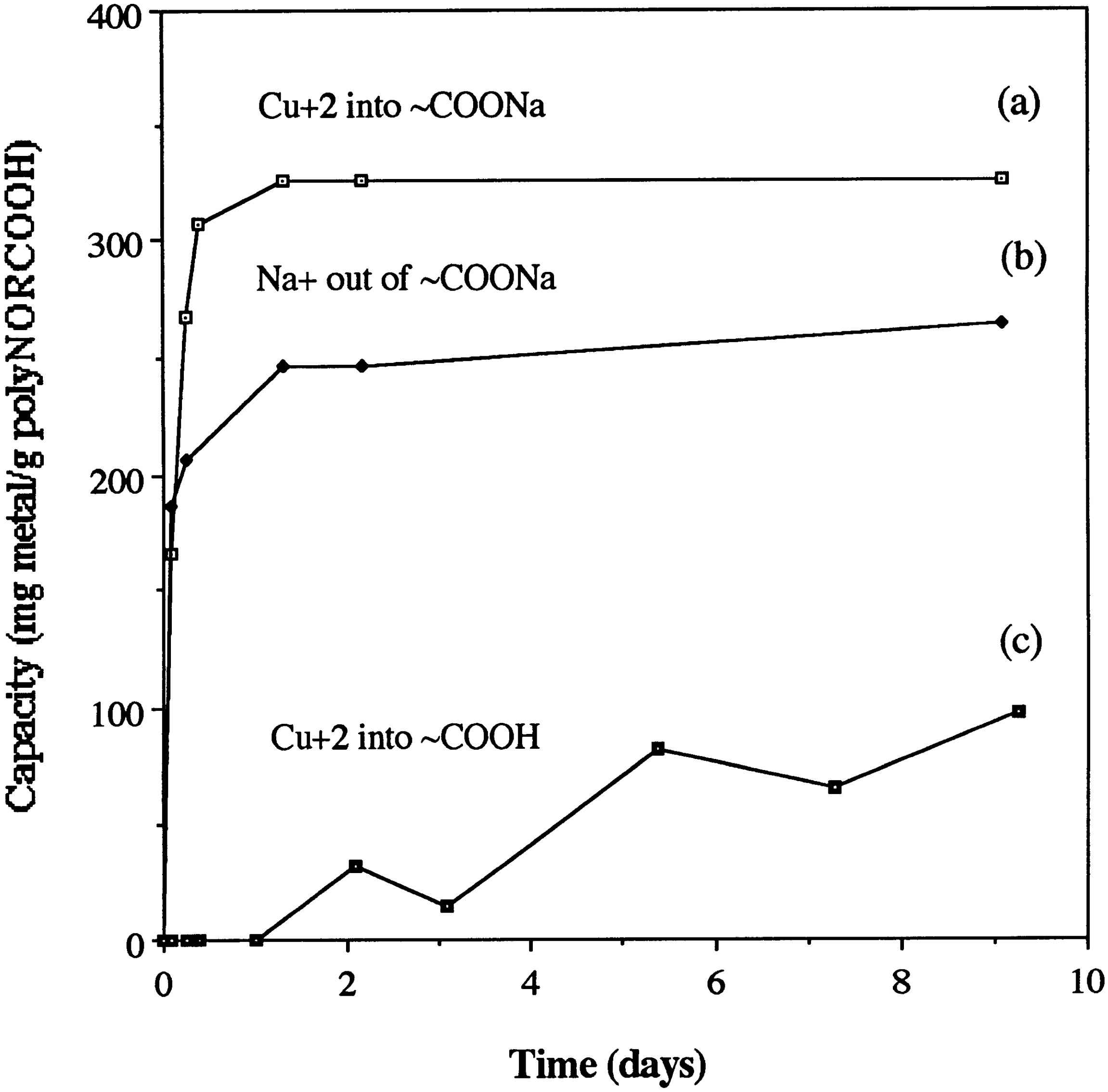

Figure 5.2: Loading capacity of $[MTD]_{400}[NORCOONa]_{50}$ vs. $[MTD]_{400}[NORCOOH]_{50}$ for Cu^{+2} ($Cu(OOCCH_3)_2$): (a) Cu^{+2} into $[MTD]_{400}[NORCOONa]_{50}$; (b) Na^+ out of $[MTD]_{400}[NORCOONa]_{50}$; (c) Cu^{+2} into $[MTD]_{400}[NORCOOH]_{50}$

COONa) after approximately a day. This measured extent of loading compares well with the maximum theoretical loading capacity (1/metal ion oxidation state) of 0.5, assuming ion exchange as the only binding mechanism.[1,2] Figure 5.2b demonstrates the corresponding release of Na^+ ions as Cu^{+2} ions enter the film, with an equilibrium value of 1.05 moles Na^+ released per mole COONa. Figure 5.2c shows that Cu^{+2} uptake occurs more slowly within $[MTD]_{400}[NORCOOH]_{50}$ than in $[MTD]_{400}[NORCOONa]_{50}$, reaching a loading of only 0.14 (moles Cu^{+2}/mole COOH) after 9 days.

Table 5.1 illustrates that in most cases, metal ions from acetates, chlorides, nitrates, and sulfates, load faster and to significantly greater extents within $[MTD]_{400}[NORCOONa]_{50}$ than within $[MTD]_{400}[NORCOOH]_{50}$. In the cases of Co, Eu, Gd, and Ni containing compounds, no loading was observed into $[MTD]_{400}[NORCOOH]_{50}$. However, significant extents of loading were observed into $[MTD]_{400}[NORCOONa]_{50}$, often within only a few hours. The loadings in Table 5.1 are given as a % of the maximum theoretical capacity.

In the case of Ag^+, an effective diffusion coefficient of 3.5×10^{-11} cm^2/s was estimated using equation (4-2). This D_{eff} value for Ag^+ within $[MTD]_{400}[NORCOONa]_{50}$ is larger than that for Ag^+ within $[MTD]_{400}[NORCOOH]_{50}$ ($D_{eff} = 3 \times 10^{-12}$ cm^2/s) by nearly a factor of ten. This indicates that D_{eff} for Ag^+ within $[MTD]_{400}[NORCOOH]_{50}$ is limited by the rate of ion exchange between H^+ and Ag^+, rather than by the actual rate of Ag^+ diffusion through the polyNORCOOH domains.

The significant improvement in the rate and extent of loading observed within $[MTD]_{400}[NORCOONa]_{50}$ films can be understood by examining stability constants, K_n, between various cations and the acetate anion, defined in equations (5-1) and (5-2):

$$ML_{n-1} + L = ML_n \qquad (5\text{-}1)$$

$$K_n = \frac{[ML_n]}{[ML_{n-1}][L]} \qquad (5\text{-}2)$$

Table 5.1 Loading capacity: $[MTD]_{400}[NORCOOH]_{50}$ vs. $[MTD]_{400}[NORCOONa]_{50}$

	NORCOOH		**NORCOONa**		
Species 0.005 M aqueous	**Loading** % Theoretical Capacity	**Time** hr	**Loading** % Theoretical Capacity	**Loading** mg metal per g polyNORCOOH	**Time** hr
$Ag(OOCCH_3)$	48	24	92	1110	2
$Co(OOCCH_3)_2x6H_2O$	0	220	68	220	5.5
$CoCl_2x6H_2O$	0	220	60	190	2
$Co(NO_3)_2x6H_2O$	0	220	61	200	5.5
$Cu(OOCCH_3)_2$	28	222	93	330	32
$CuCl_2$	0	220	60 (66)	230	2 (6)
$Eu(OOCCH_3)_3xH_2O$	0	220	102	570	241
$EuCl_2$	0	220	55	450	121
$EuCl_3x6H_2O$	0	220	63	350	2
$Fe(OOCCH_3)_2$	31	176	104	320	97
$FeCl_2$	0	220	65	200	2
$FeCl_3$	39	218	65	130	121
$Gd(OOCCH_3)_3x4H_2O$	0	220	90	510	24
NaOH (0.015 M)	100	< 7	-	-	-
$NiCl_2$	0	220	73	240	2
$Ni(NO_3)_2x6H_2O$	0	220	61	200	29
$NiSO_4x6H_2O$	0	220	52	170	2
$Pd(OOCCH_3)_2$	39	96	PPT	PPT	PPT
$PtCl_4$	0	190	0	0	190
$Na_2PdCl_4x3H_2O$	58	175	51	300	218
$Na_2PtCl4xH2O$	0	220	0	0	220

where M represents the cation, and L represents the acetate ion (CH_3COO^-), chosen because of its structural similarity to the carboxylate ions within our films.

It is known that H^+ ions bind strongly to acetate ions, $K_1 \sim 6.3x10^4$ (mole/l $)^{-1}$,[3] transition metal and rare earth ions bind with intermediate strength to acetate ions, $K_1 \sim 3\text{-}1600$ (mole/l $)^{-1}$,[3,4] and Na^+ ions bind weakly to acetate ions, $K_1 \sim 0.7$ (mole/l $)^{-1}$.[4] It is possible to exchange H^+ ions for Na^+ ions under basic conditions where OH^- ions remove H^+ ions from the carboxylic acid groups. Transition metal or rare earth ions are then substituted for the more weakly binding Na^+ ions. A comparison of stability constants also helps explain why M^{+2} ions from metal acetates often load into $[MTD]_{400}[NORCOOH]_{50}$ films, while the same M^{+2} ions from metal chlorides do not. M^{+2} loading from metal chlorides causes HCl formation. However, the K_1 of HCl is essentially zero, so free H^+ ions in solution prevent significant M^{+2} binding. M^{+2} loading from metal acetates causes acetic acid formation, $K_1 \sim 6.3x10^4$ (mole/l $)^{-1}$. Therefore, most H^+ ions liberated from carboxylic acid groups become bound to acetate ions, and loading is possible for Ag^+, Cu^{+2}, Fe^{+2}, and Pd^{+2} (See Table 5.1).

Table 5.2 lists the average stability constants between selected metal ions and the acetate ion, in aqueous solution, obtained from data compiled in references 3 and 4. Table 5.2 also lists the typical number of water molecules observed in the first coordination shell of metal ions in aqueous solution, and the average distance between the metal ion and oxygen atoms in the water molecules of the first coordination shell. The information in the third and fourth columns of Table 5.2 was taken from a review article by Yizhak Marcus.[5]

The information in Table 5.2 helps explain a why Fe^{+3} was observed to load into $[MTD]_{400}[NORCOOH]_{50}$ from $FeCl_3$, while Fe^{+2} was not observed to load from $FeCl_2$. Uptake of both Fe^{+3} and Fe^{+2} cause the release of H^+, which is unfavorable to further metal ion uptake. However, Fe^{+3} is able to load to a measurable extent because its stability constant with the acetate ion is greater by a factor of 24, than that of Fe^{+2}. Furthermore, based on its stability constant, Gd^{+3} from $Gd(OOCCH_3)_3x3H_2O$ might be expected to load into

$[MTD]_{400}[NORCOOH]_{50}$. However, no Gd^{+3} uptake was observed, possibly due to its unusually large coordination shell.

A precipitate was observed while attempting to load Pd^{+2} into $[MTD]_{400}[NORCOONa]_{50}$ from $Pd(OOCCH_3)_2$. Neither Pd^{+2}, from $Na_2PdCl_4x3H_20$, nor Pt^{+2}, from $Na_2PtCl_4xH_2O$, exhibited improved loading into $[MTD]_{400}[NORCOONa]_{50}$, possibly because the Pd and Pt can be present within anions ($PdCl_4^{-2}$ or $PtCl_4^{-2}$) rather than as cations in aqueous solution.

Table 5.2 Stability constants between selected metal ions and the acetate ion

Species	**Stability Constant** $\log_{10}K_1$, $[K_1, (mol/l)^{-1}]$	**Number of Water Molecules in 1st Coordination Shell**	**Metal-Oxygen Distance** nm
Co^{+2}	0.5 [3]	5-6	0.211
Cu^{+2}	2.1 [126]	4 equatorial	0.197 equatorial
		2 axial	0.240 axial
Eu^{+3}	1.9 [79]	8.3	0.245
Fe^{+2}	1.8 [66]	5-6	0.211
Fe^{+3}	3.2 [1600]	2.7-4.2	0.203
Gd^{+3}	2.2 [160]	8-10	0.239
H^+	4.8 $[6.3x10^4]$	-	-
Na^+	-0.18 [0.66]	4-8	0.236
Ni^{+2}	0.84 [7]	5-8.2	0.206
Pb^{+2}	2.1 [123]		

Unlike Ag^+ ions, which bind rather strongly to carboxylate ions, ICP-AES measurements indicated that 45 % of the Na^+ ions were released from a 10 μm thick Na^+ loaded film after soaking in de-ionized water for 8 days.

5.3.2. Analysis of Ag^+ Loading Capacity (Multiple LARS)

Figure 5.3 shows Ag^+ loading capacity within $[MTD]_{400}[NORCOONa]_{50}$ as a function of time. Figures 5.3a, 5.3b, 5.3c, and 5.3d, reveal equilibrium Ag^+ loading capacities of 0.77,

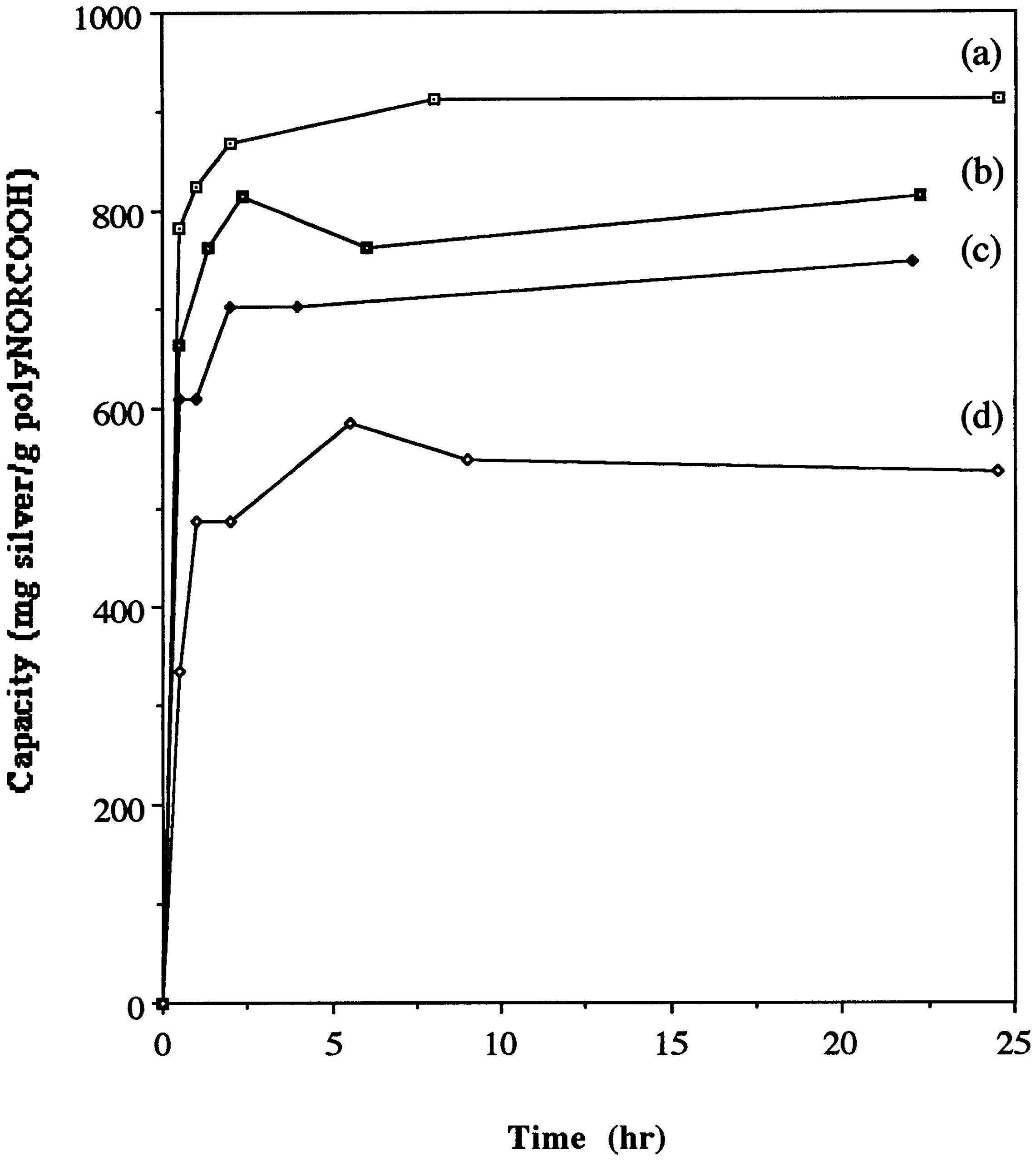

Figure 5.3: Loading capacity of $[MTD]_{400}[NORCOONa]_{50}$ for Ag^+ (multiple LARS): (a) first loading; (b) third loading; (c) second loading; (d) fourth loading

0.69, 0.67, and 0.45 moles Ag^+/mole COONa, during the first, third, second, and fourth loadings respectively. This corresponds to a cumulative loading, following four LARS, of 3.0 g Ag per gram of polyNORCOOH initially present, or approximately 26 wt. % Ag in the overall $[MTD]_{400}[NORCOOH]_{50}$/Ag composite. The decrease in equilibrium Ag^+ loading following multiple LARS is probably due to the increasing volume fraction of Ag nanoclusters within the polyNORCOONa domains, which may sterically prevent exchange between Na^+ and Ag^+ ions. Possible degradation of carboxylic acid groups during multiple LARS may also contribute to the decrease in Ag^+ loading capacity. During each loading, ICP-AES measurements demonstrated the release of corresponding amounts of Na^+, as Ag^+ entered the film. No additional Ag^+ uptake was detected, with ICP-AES, into $[MTD]_{400}[NORCOONa]_{50}$ films which were previously loaded with Ag^+, but not yet reduced. This is the case because few sodium carboxylate groups remain to bind additional Ag^+ ions.

The films appeared transparent and colorless, both after Na^+ loading, and after Ag^+ loading prior to reduction. The Ag^+ loaded films changed from transparent and colorless to transparent and light orange, within minutes during the first reduction sequence, prior to reaching a steady-state temperature of 115 °C. Following the first and second LARS, the films were transparent and appeared light orange and dark orange in color respectively. The orange color is a result of the surface plasmon absorption of Ag nanoclusters within a dielectric matrix[6], and we previously reported a visible absorption at ca. 430 nm for Ag cluster containing films (Figure 4.9). The films appeared opaque and black following the third and fourth LARS. During the second, third, and fourth Na^+ loadings, a slight orange tint was observed in the NaOH solution, indicating the leaching of some Ag clusters from the film. However, the mass of the leached Ag clusters was too low to accurately measure through our ICP-AES experiments.

The loading capacity of 0.77 shown in Figure 5.3a is lower than that of 0.92 presented in Table 5.1, because the two loading experiments were done using different batches of polymer. The NORCOOH carboxylic acid groups must be converted to trimethylsilyl ester groups prior to polymerization to prevent catalyst deactivation.[7] The trimethylsilyl ester groups are then re-acidified following polymerization. However, the protected monomer used to produce polymer for the multiple LARS experiment was stored for several months under nitrogen prior to use. Moisture contamination is believed to have prematurely re-acidified a fraction of the trimethylsilyl ester groups, causing a lower than expected yield of carboxylic acid functionalized polymer.

Shown in Figure 5.4 are IR spectra of the film following each step of the first two LARS. Figure 5.4a is from the $[MTD]_{400}[NORCOOH]_{50}$ film prior to Na^+ loading, and shows the expected C-H (2850-2960 cm^{-1}) and C=O (1670-1780 cm^{-1}) absorptions[8]. The O-H (2500-3300 cm^{-1}) absorption is not apparent due to its great breadth, low number of O-H groups in the polymer, and overlap with the C-H absorption. Figures 5.4b and 5.4c correspond to the film following Na^+ and Ag^+ loading respectively. In both cases, the C=O absorption is absent, but new absorptions appear at 1570 cm^{-1} (Figure 5.4b) and 1540 cm^{-1} (Figure 5.4c). The asymmetrical stretching mode ($\nu_a(COO^-)$) of carboxylate ions is known to absorb at ca. 1556 cm^{-1},[9] and complexation of carboxylate ions with metal cations has been observed to shift $\nu_a(COO^-)$ by +/- 20 cm^{-1}.[9] Therefore, the appearance of the 1570 cm^{-1} absorption indicates ionization of the carboxylic acid groups and complexation with Na^+. The appearance of the 1540 cm^{-1} absorption indicates an exchange between Na^+ and Ag^+ during Ag^+ loading. Loss of peak intensity at 1540 cm^{-1} and reappearance of the C=O absorption in Figure 5.4d is consistent with re-protonation of a large fraction of carboxylate ions during the hydrogen reduction process. Figures 5.4e, 5.4f, and 5.4g, correspond to films following Na^+ loading, Ag^+ loading, and hydrogen reduction, during the second LARS, and demonstrate that the process of ion loading and reduction is repeatable. The peak intensities in Figures 5.4d

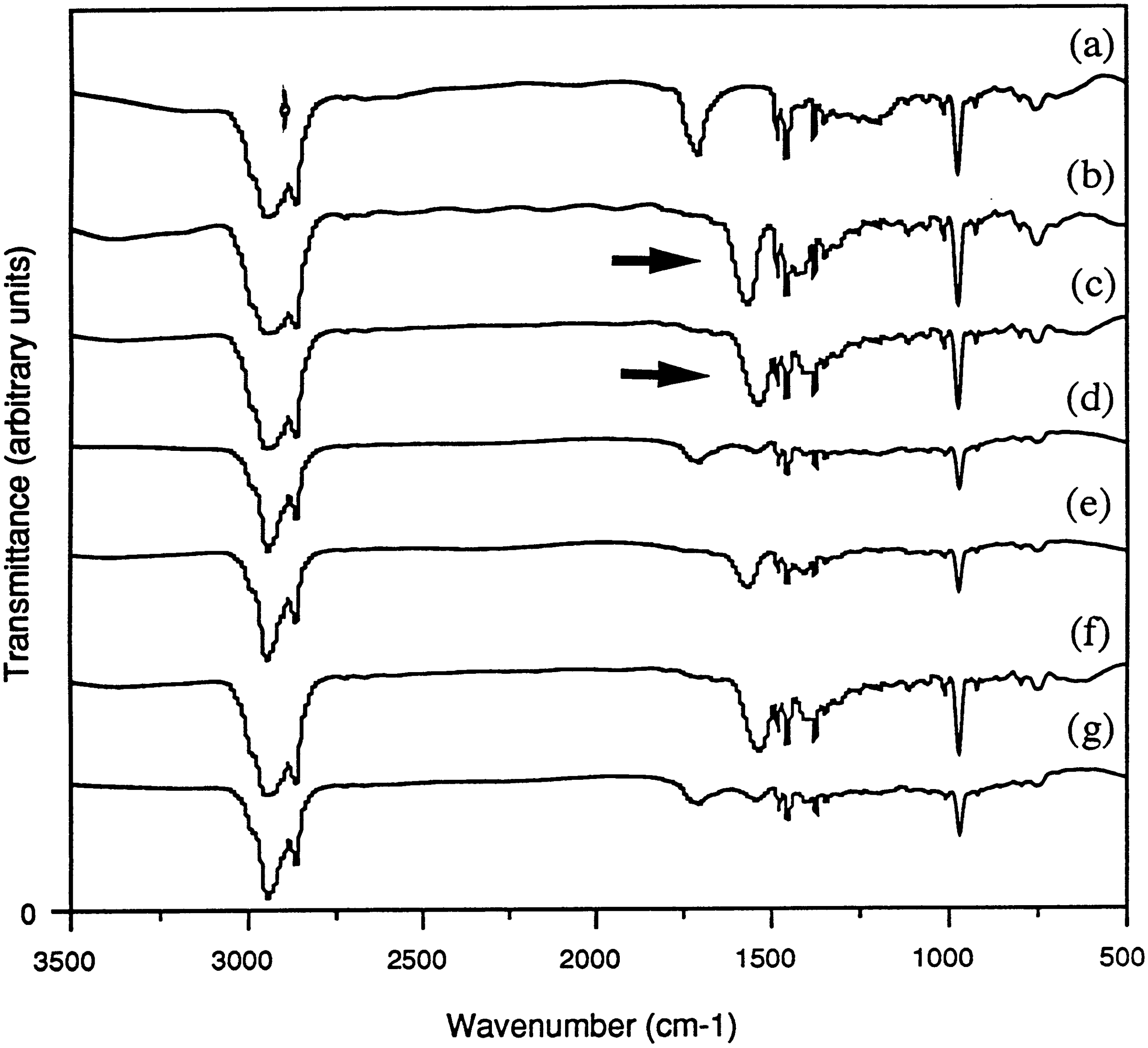

Figure 5.4: IR spectra of block copolymer film following each step of the first two LARS: (a) unloaded film; (b) first Na^+ loading; (c) first Ag^+ loading; (d) first reduction; (e) second Na^+ loading; (f) second Ag^+ loading; (g) second reduction

through 5.4g fluctuate because variations in the film thickness cause differences in the intensity of light transmitted, following coloration of the film during the first reduction.

Shown in Figures 5.5a, 5.5b, 5.5c, and 5.5d, are WAXS data for the films following the first, second, third, and fourth LARS respectively. They show scattering peaks from the [111] ($2\theta = 38.1°$), [200] ($2\theta = 44.3°$), and [220] ($2\theta = 64.4°$) planes of the f.c.c. silver lattice.[10] The diffracted X-ray intensities have been normalized through division by the maximum intensity of the polymer peak (amorphous halo). As the number of LARS increases, the silver peaks become narrower and increase in size relative to the polymer peak. The mean diameter of the silver crystals was determined by applying the Scherrer equation (3-1) and equation (3-2), to the [111] peak following each LARS.

We estimated mean crystal diameters of 37 Å, 50 Å, 64 Å, and 65 Å following the first, second, third, and fourth LARS respectively. It appears that Ag nanoclusters produced in previous LARS act as nucleation sites for further cluster growth during subsequent LARS. Figures 5.6 and 5.7 are micrographs of the film following the first and third LARS respectively. They show cluster size distributions consistent with the mean crystal diameters estimated using WAXS.

5.3.3. Extent of Ag^+ Loading vs. Cluster Size (Single LARS)

Given in Table 5.3 is the Ag^+ loading in each 100 mg section of $[MTD]_{400}[NORCOOH]_{50}$ film as a function of time. The loading is slower and to a lessor extent than that shown in Table 5.1, both because of increased diffusional resistance due to the thicker film, and because the carboxylic acid groups were not converted to the sodium carboxylate form prior to Ag^+ loading. We believe some Ag^+ loading occurred during the first 3 days, but it was too little to accurately measure through our ICP-AES experiments. Following hydrogen reduction, mean silver crystal diameters were estimated from WAXS data

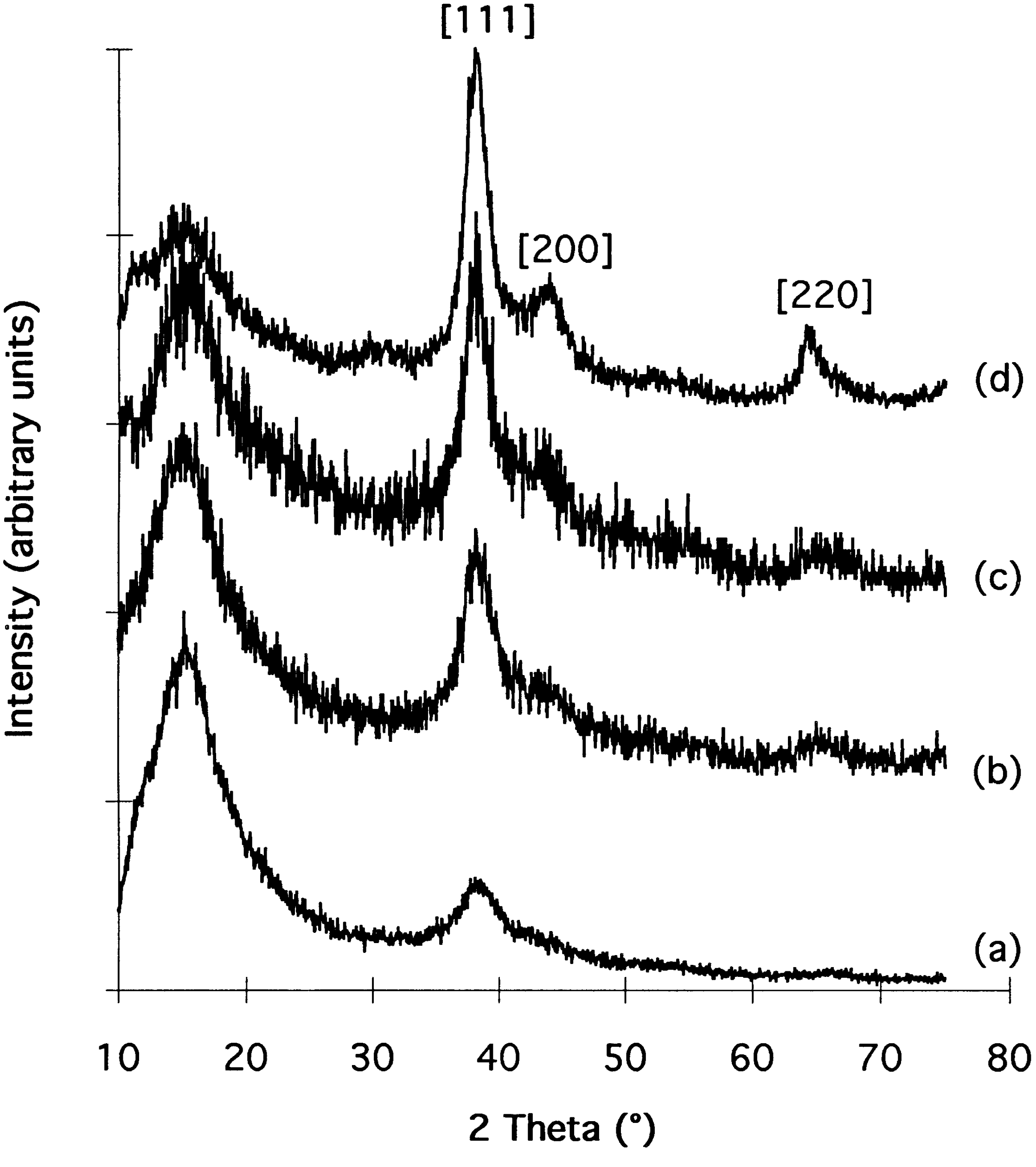

Figure 5.5: WAXS data from silver nanocluster containing $[MTD]_{400}[NORCOOH]_{50}$ film (multiple LARS): (a) first LARS; (b) second LARS; (c) third LARS; (d) fourth LARS

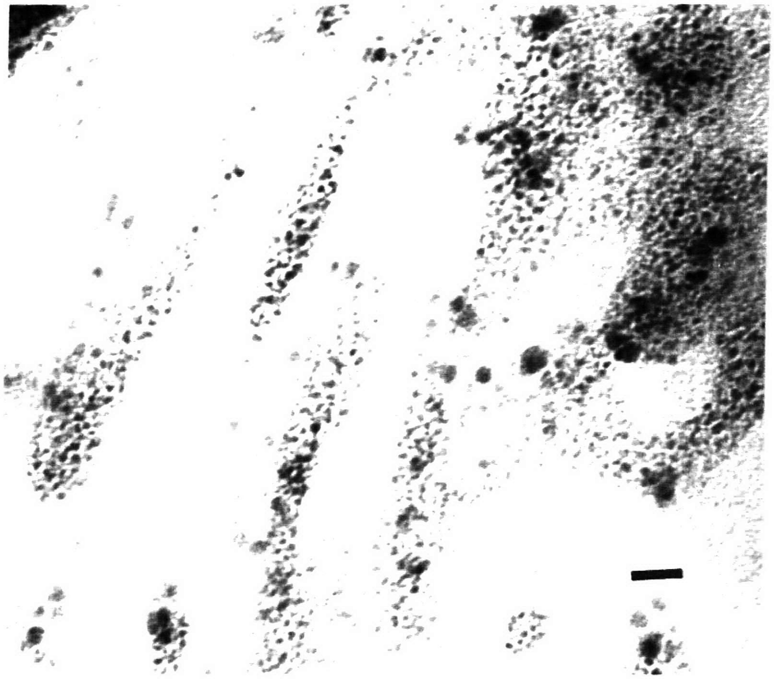

Figure 5.6: Electron micrograph of silver nanocluster containing $[MTD]_{400}[NORCOOH]_{50}$ film after first LARS (bar = 200 Å)

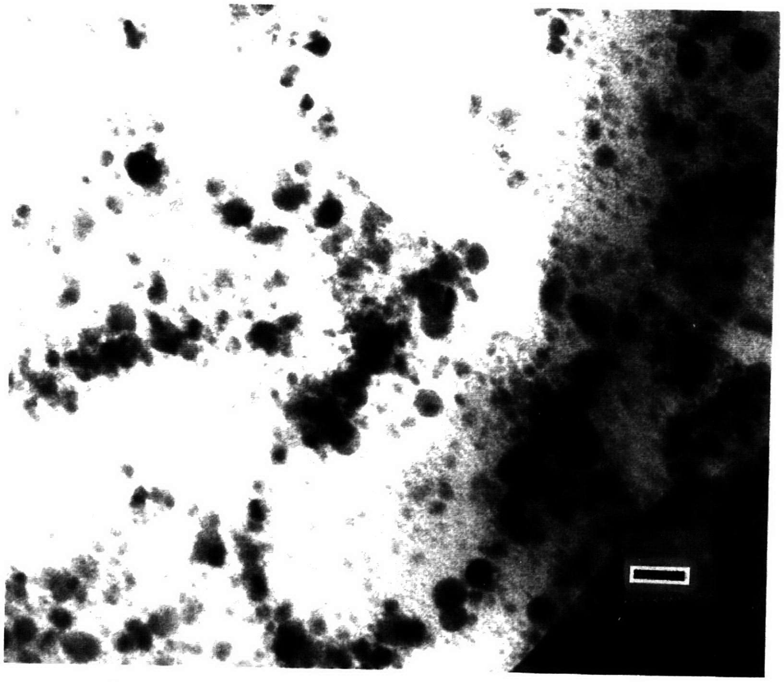

Figure 5.7: Electron micrograph of silver nanocluster containing $[MTD]_{400}[NORCOOH]_{50}$ film after third LARS (bar = 200 Å)

Table 5.3 Mean silver crystal diameter vs. extent of loading

Time	**Loading** mg Ag^+/g polyNORCOOH	**Loading** moles Ag^+/mole COOH	**Mean Crystal Diameter** Å
1 day	~0	~0	-
2 day	~0	~0	-
3 day	~0	~0	-
1 wk	40	0.03	28
2 wk	280	0.23	24
3 wk	300	0.26	24
5 wk	450	0.38	35
7 wk	500	0.43	25

as previously described (See Table 5.3). The mean crystal diameter (30 +/- 5 Å) was found to be relatively insensitive to the extent of Ag^+ uptake for loadings between 40 and 500 mg Ag^+/g polyNORCOOH. Shown in Figures 5.8 and 5.9, respectively, are micrographs of reduced films following 2 weeks and 7 weeks of loading. The micrographs are consistent with WAXS estimates of the mean silver crystal diameters. Both micrographs show Ag clusters in the 20 to 30 Å size range, with a higher cluster density after 7 weeks of loading than after 2 weeks of loading. The WAXS estimate of 35 Å silver crystals, following 5 weeks of loading and reduction, was confirmed with TEM. It is possible that this larger cluster size was due to slight differences in temperature, between film samples, during reduction.

Table 5.4 lists the density of Ag clusters within the polyNORCOOH domains calculated as described on page 99. Our observation that cluster size is relatively insensitive to the extent of loading over a wide range of loading, indicates that nucleation is fast relative to growth. If the polyNORCOOH domain contains a fixed concentration of nucleation sites, capable of forming only a single nucleus (per reduction cycle), then the density of nucleation sites must be equal to or greater

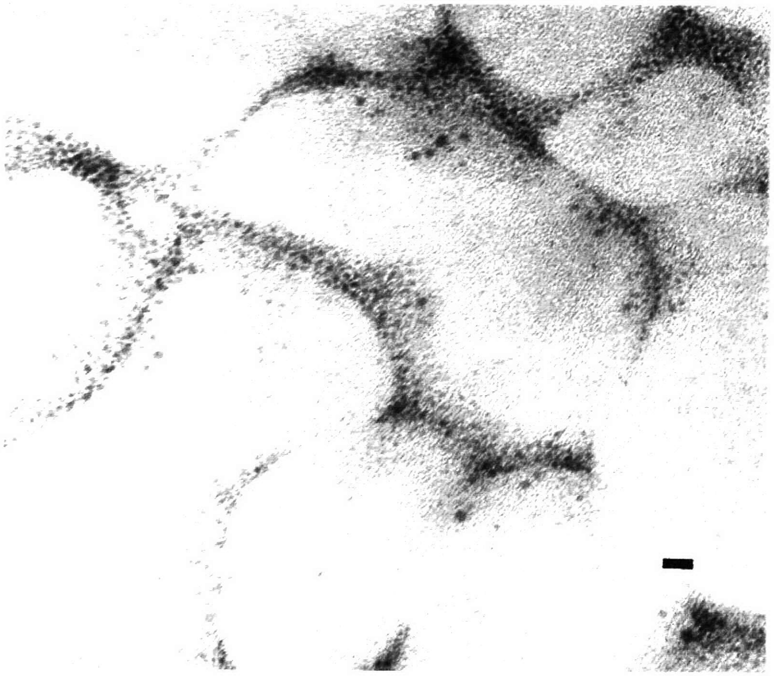

Figure 5.8: Electron micrograph of silver nanocluster containing $[MTD]_{400}[NORCOOH]_{50}$ film after 2 weeks of loading and reduction (bar = 100 Å)

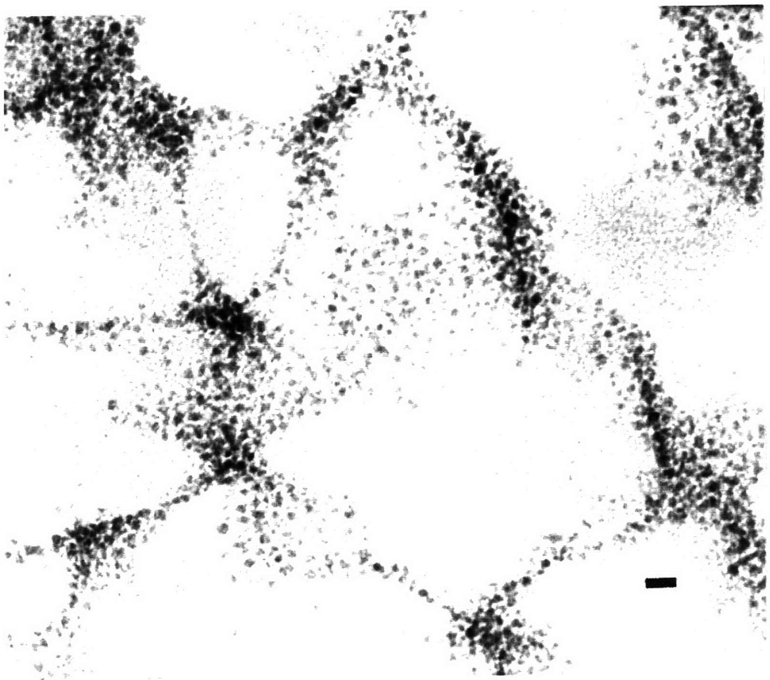

Figure 5.9: Electron micrograph of silver nanocluster containing $[MTD]_{400}[NORCOOH]_{50}$ film after 7 weeks of loading and reduction (bar = 100 Å)

Table 5.4 Density of Ag clusters within polyNORCOOH domain vs. loading

Loading mg Ag^+/g polyNORCOOH	**Cluster Radius** Å	**Cluster Density** cm^{-3}	**Radius of Hypothetical Volume Element** contributing Ag atoms to Ag cluster Å
40	~ 15	2.7×10^{17}	96
500	~ 15	3×10^{18}	41

than the cluster density observed after the highest loading (following reduction). Our experimental observation indicates that the polyNORCOOH **does not** contain a fixed concentration of such nucleation sites, which is small relative to the cluster density after the highest loading (3×10^{18} cm^{-3}). For example, if the nucleation site density were equal to the cluster density observed after the lowest loading (2.7×10^{17} cm^{-3}), we would expect to see an increase in cluster size with an increase in loading (constant cluster density, but an increase in average cluster size).

Since it is not clear what constitutes a nucleation site, it may be more appropriate to state that the "number of initial nucleation events" must be equal to or greater than the number of clusters observed after the highest loading. Previous studies implicated interfaces between blocks, within microphase separated block copolymers, as possible causes of heterogeneous nucleation.[11]

The following is a description of our very general understanding of the cluster formation process. We start with a Ag^+ loaded block copolymer, with the Ag^+ ions homogeneously dispersed within the polyNORCOOH domains. Upon exposure to hydrogen at elevated temperature, a reaction occurs in which Ag^+ ions are converted to Ag atoms and carboxylate ions are re-protonated to form carboxylic acid groups. We believe cluster growth occurs by a mechanism in which X single atoms or X groups of a few atoms (if the $Ag^+ \rightarrow Ag^0$

mechanism requires more than one silver atom) diffuse primarily within the polyNORCOOH domains, occasionally colliding with each other to form < 0.5 X two-atom nuclei. These small nuclei continue diffusing within the polyNORCOOH domains, and may collide with each other or lone Ag atoms. This process continues until the clusters reach a limiting size, large enough to effectively prevent diffusion within the polymer over the time scale of several days .

Figure 5.10 shows a schematic of the cluster formation process, within a small volume element, in which a single Ag cluster eventually forms. A 30 Å diameter cluster contains ~ 800 Ag atoms. It is not known how many two-atom nuclei form in each volume element; however, this number must be at least 1 and less than or equal to 400. It is quite likely that the number of two-atom nuclei incorporated into each Ag cluster is intermediate between 1 and 400 (i.e. 20, 101, 254, etc.).

It is not clear whether thermodynamics or kinetics is responsible for the final mean crystal (cluster) size. Our observed mean crystal diameter may correlate with the critical nuclei radius (minimum size for a stable nucleus), r^*, determined by setting the derivative of the Gibbs free energy, ΔG, of cluster formation equal to zero.[12] As shown in Figure 5.11, ΔG is the sum of surface free energy (ΔG_s) and volume free energy (ΔG_v) terms, which reaches a maximum at r^*. All nuclei with $r < r^*$ will tend to fall apart, while those with $r > r^*$ will continue to grow. ΔG and r^* are defined in equations (5-3) and (5-4) below:

$$\Delta G = \sigma 4\pi r^2 + 4/3(\pi r^3 \Delta g) \tag{5-3}$$

and

$$r^* = -2\sigma/\Delta g \tag{5-4}$$

where σ is the interfacial free energy, in J/m^2, between the Ag clusters and their surroundings, Δg is the Gibbs free energy difference, in J/m^3, between the bound Ag^+ ions and the Ag clusters, and r is the cluster radius in meters. The critical nuclei radius is difficult to calculate for our particular case due to uncertainty in both σ and Δg. However, we did calculate r^* as a

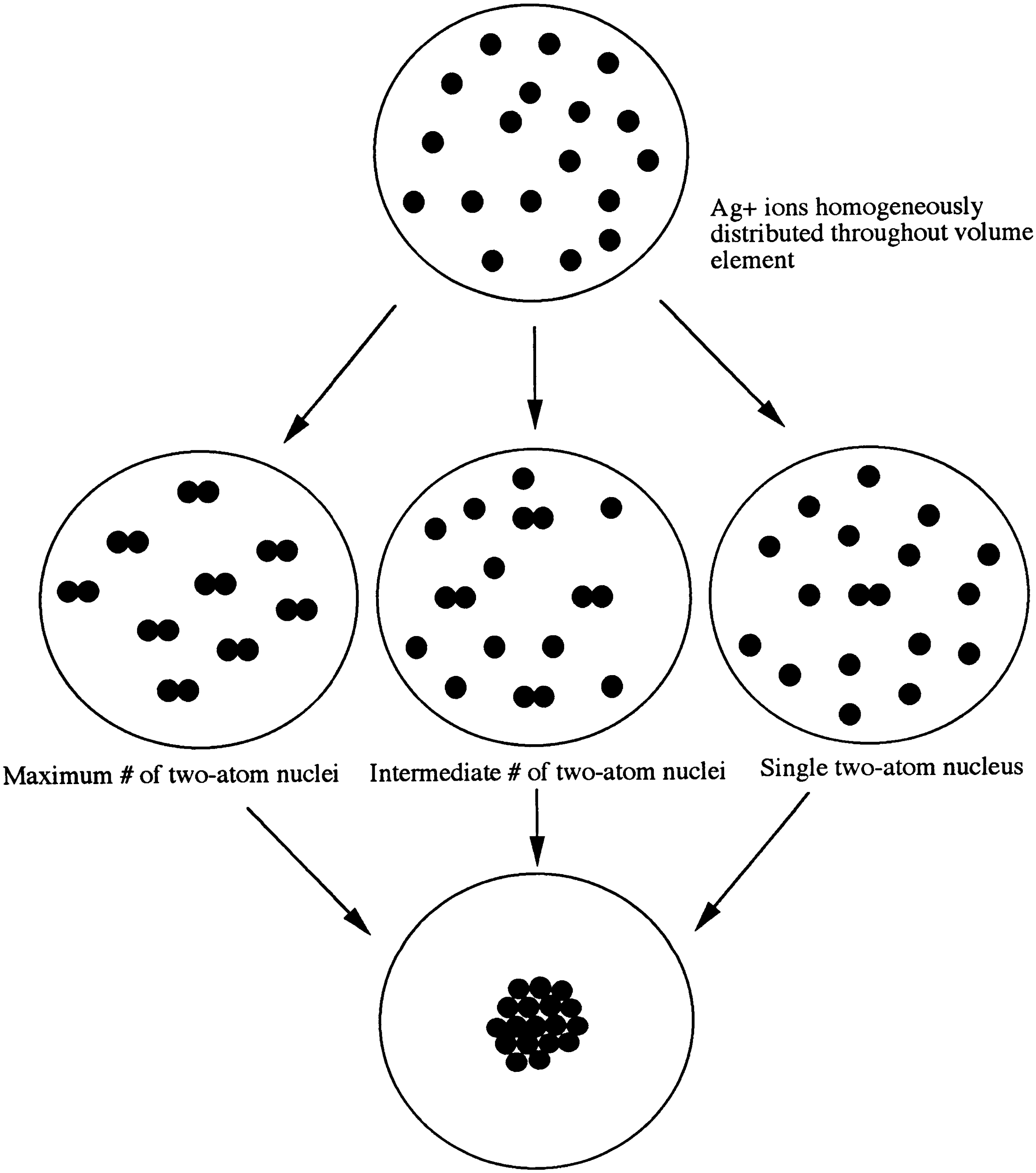

Figure 5.10: Cluster growth within a volume element contributing to single cluster

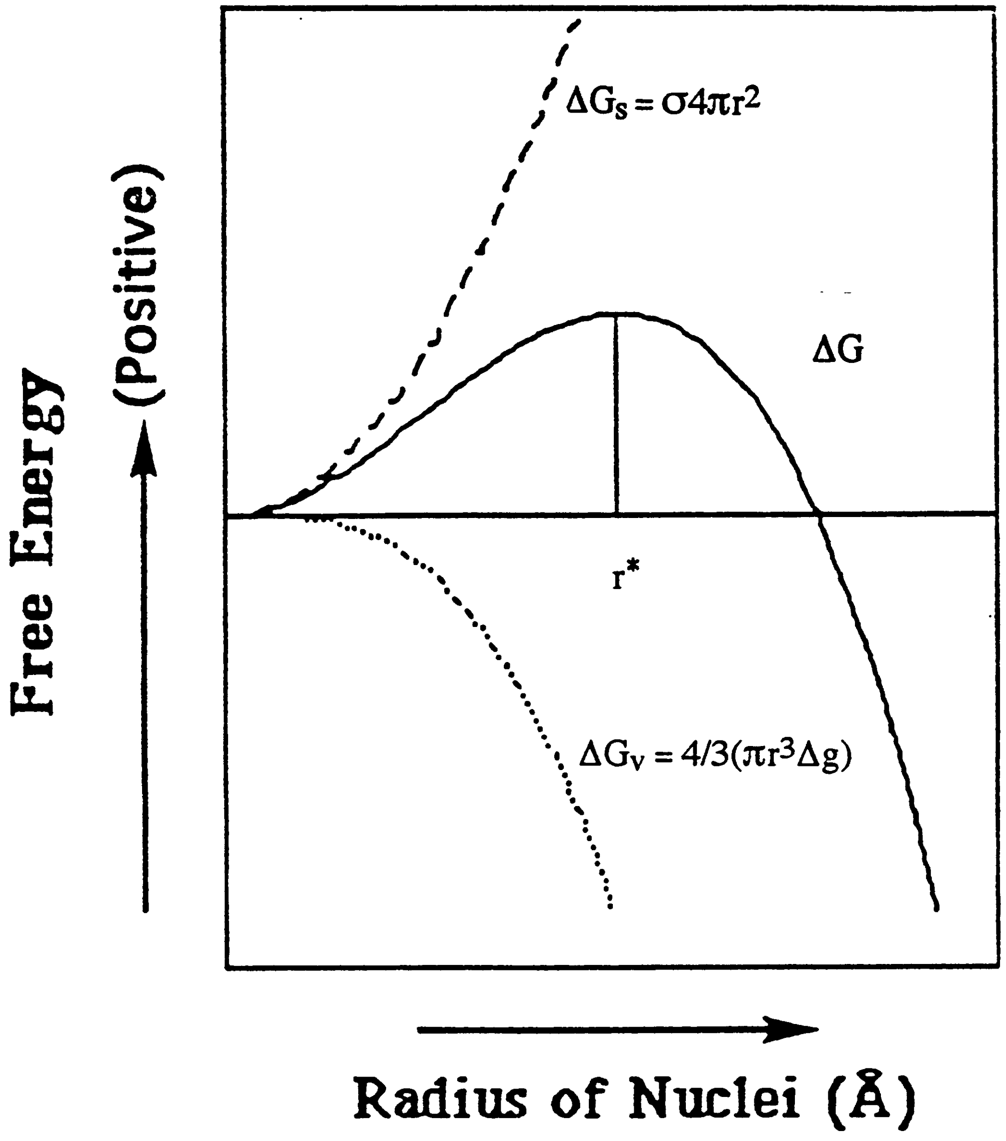

Figure 5.11: Gibbs free energy of formation (ΔG) as a function of critical nuclei radius (r*)
Sankaran, V. Ph.D. Thesis (Chem. E.), Massachusetts Institute of Technology, **1993**.

function of undercooling, ΔT, for the crystallization of Ag from a melt. In this case, Δg is given by equation (5-5):

$$\Delta g = -\Delta S_f \Delta T \tag{5-5}$$

where ΔS_f is the entropy of fusion in J/m^3K. Using published values of σ ($0.126\ J/m^2$)[13] and ΔS_f ($1.16x10^6\ J/m^3K$)[14], we calculated values of r^* between 20 Å and 40 Å for ΔT between 100 K and 50 K respectively.

Alternatively, cluster growth may be kinetically limited. In this case, cluster growth will cease when the Ag clusters grow large enough to become kinetically locked within the surrounding polymer. If we expand the volume element shown in Figure 5.10 such that it contributes to the formation of many Ag clusters, we see that an increase in the concentration of two-atom nuclei leads to a decrease in cluster size, provided that: 1) the cluster diffusivity decreases rapidly with increasing cluster size and 2) the radius of the clusters is greater than r^* (or clusters with radius less than r^* disintegrate slowly relative to the reduction time under hydrogen).

Refering to Tables 3.3 and 3.6, it is interesting to note that the observed cluster size, within 400 Å thick microtomed films, seems to vary inversely with both the electrochemical reduction potential and the mass of the metal ions being reduced (with the exception of the relatively small number of 100+ Å gold clusters). It is possible that an increase in the reduction potential leads to an increase in nucleation. Alternatively, larger metal atoms may nucleate more rapidly than smaller metal atoms.

Variations in r^*, reduction potential, and/or atomic mass, may contribute to the variations in cluster size observed for different metals.

5.4. Conclusions

Conversion of carboxylic acid groups, within $[MTD]_{400}[NORCOOH]_{50}$, to the sodium carboxylate form, $[MTD]_{400}[NORCOONa]_{50}$, results in large increases in both the rate and extent of transition metal and rare earth ion uptake from metal acetates, chlorides, nitrates, and sulfates. In the cases of Co, Eu, Gd, and Ni containing compounds, significant loading can often be achieved from 0.005 M aqueous metal salt solutions into 10 μm thick $[MTD]_{400}[NORCOONa]_{50}$ films within hours; whereas, no loading was observed into $[MTD]_{400}[NORCOOH]_{50}$ films. The improvement in loading is due largely to the acetate ion's much lower stability constant with Na^+, $K_1 \sim 0.7$ (mole/l $)^{-1}$, than with H^+, $K_1 \sim 6.3 \times 10^4$ (mole/l $)^{-1}$, which allows transition metal and rare earth ions, $K_1 \sim 3\text{-}1600$ (mole/l $)^{-1}$, to more easily exchange with the weakly bound Na^+ ions than with the much more strongly bound H^+ ions.

A 10 μm thick $[MTD]_{400}[NORCOONa]_{50}$ film was subjected to several loading and reduction sequences (LARS), and displayed equilibrium Ag^+ uptake capacities of 0.77, 0.69, 0.67, and 0.45 moles Ag^+/mole COONa, during the first, third, second, and fourth loadings respectively. This corresponds to a cumulative loading of approximately 26 wt. % Ag in the overall polymer/Ag composite. The decrease in equilibrium Ag^+ loading following several LARS is probably due to the increasing volume fraction of Ag nanoclusters within the polyNORCOONa domains, which may sterically prevent exchange between Na^+ and Ag^+ ions. Mean crystal sphere diameters of 37 Å, 50 Å, 64 Å, and 65 Å were estimated, from WAXS data, following the first, second, third, and fourth LARS respectively. Thus, Ag nanoclusters produced in previous LARS act as nucleation sites for further cluster growth during subsequent LARS.

During a single LARS, cluster size within $[MTD]_{400}[NORCOOH]_{50}$ is relatively insensitive to the extent of Ag^+ uptake, for loadings between 40 and 500 mg Ag^+/g polyNORCOOH. Nucleation is believed to be fast relative to growth. It is not known whether the mean observed cluster size of ca. 30 Å is a result of thermodynamic or kinetic constraints.

5.5. References for Chapter 5

(1) Helfferich, F.G. 'Ion Exchange', McGraw-Hill, Inc.New York, 1962, p. 279.

(2) Calmon, C. in 'Adsorption and Ion Exchange'; AIChE Symp. Ser. 1984, 80, No. 233.

(3) Perrin, D.D. 'Stability Constants of Metal-Ion Complexes Part B: Organic Ligands', Pergamon Press, New York, 1979, p. 38.

(4) Sillen, L.G, and Martell, A.E. 'Stability Constants of Metal-Ion Complexes', The Chemical Society, London, 1971, p. 253.

(5) Marcus, Y. *Chem. Rev.* **1988**, 88, 1475.

(6) Halperin, W.P. *Rev. Mod. Phys.* **1986**, 58, 533.

(7) Clay, R.T. and Cohen R.E. *Supramolecular Science* **1995**, 2, 183.

(8) McMurray, J. 'Organic Chemistry', 2nd Ed., Brooks/Cole Publishing, Pacific Cove, 1988, p. 397.

(9) McCluskey, P.H., Snyder, R.L. and Condrate, R.A. *J. Sol. State Chem.* **1989**, 83, 332.

(10) Swanson, H.E. and Tatge, E. 'U.S. National Bureau of Standards Standard X-Ray Diffraction Patterns', NBS Circular 539, Volume 1, U.S. Government Printing Office, Washington D.C., June 15, 1953.

(11) Sohn, B.H. and Cohen, R.E. *Acta Polymer* **1996**, 47, 340.

(12) Kurz, W. and Fisher, D.J. 'Fundamentals of Solidification', 3rd Ed., Trans Tech Publications, Switzerland, 1992, p. 26.

(13) Turnbull, D. *J. Apply. Phys.* **1950**, 21, 1022.

(14) 'Handbook of Chemistry and Physics' (Ed. R. Weast), CRC Press, Boca Raton, FL, 1987, p. D-44.

Chapter 6

Oxidation of Silver Nanoclusters by Palladium or Platinum Ions

6.1. Summary

In Chapter 3, we reported a general methodology for the synthesis of transition metal nanoclusters (Ag, Au, Cu, Ni, Pb, Pd, and Pt) stabilized within microphase-separated diblock copolymers. In our strategy, outlined in Figure 1.9, metal ions or complexes are coordinated to carboxylic acid groups within the water soluble polyNORCOOH domains of a $[MTD]_{400}[NORCOOH]_{50}$ block copolymer (MTD = methyltetracyclododecene and NORCOOH = 2-norbornene-5,6,-dicarboxylic acid) by immersion of the polymer in aqueous metal salt solutions. The metal ions and complexes are subsequently reduced by heating the metal loaded polymer under hydrogen or by immersion in an aqueous sodium borohydride solution. For several transition metals, the resulting nanoclusters are uniformly sized and homogeneously dispersed within the polyNORCOOH domains.

We expanded the scope and depth of our previous work, in Chapter 4, by investigating the rate of metal ion transport into our block copolymer films and the nature of metal ion uptake within the polyNORCOOH domains. In Chapter 5 (See Figure 5.1), we reported that the conversion of carboxylic acid groups within $[MTD]_{400}[NORCOOH]_{50}$, to the sodium carboxylate form, $[MTD]_{400}[NORCOONa]_{50}$, results in large increases in both the rate and extent of metal ion uptake from metal acetates, chlorides, nitrates, and sulfates.

Now, we describe a method for synthesizing bimetallic Pd/Ag and Pt/Ag nanoclusters, by soaking Ag nanocluster containing $[MTD]_{400}[NORCOOH]_{50}$ films in aqueous solutions of $Na_2PdCl_4x3H_2O$ or $Na_2PtCl_4xH_2O$. Species of the form X_2MCl_4, where X is an alkali metal and M is palladium or platinum, generally dissociate in aqueous solution according to equation (6-1):[1]

$$X_2MCl_4 \text{-----}> 2\,X^+ + MCl_4^{-2} \qquad (6\text{-}1)$$

However, neither the reduction of $[PdCl4]^{-2}$ (0.591 V) nor $[PtCl4]^{-2}$ (0.755 V) by metallic silver (-0.800 V) is thermodynamically favorable at room temperature, because the electromotive force (emf) of the overall reactions is negative (-0.209 V and -0.045 V respectively).[2] Therefore, it can be inferred that the palladium and platinum ions must exist in some form, more easily reducible than Ag^+, prior to reduction by metallic silver. It is not known whether the palladium and platinum are present as lone metal cations (Pd^{+2}, 0.951 V and Pt^{+2}, 1.118 V) or within more complex ions. We will refer to the palladium and platinum containing species as palladium ions and platinum ions, respectively, throughout this chapter. Since the electrochemical reduction potential of Ag^+ (0.800 V) is less than that of the palladium or platinum ions, pre-existing Ag clusters act as reducing agents for incoming palladium or platinum ions. See Table 3.3. The Ag clusters are oxidized to Ag^+, while the palladium and platinum ions are reduced to Pd and Pt respectively.

6.2. Experimental

A $[MTD]_{400}[NORCOOH]_{50}$ diblock copolymer was synthesized as previously reported, using a ring-opening metathesis polymerization in anhydrous toluene with a $Mo(CHCMe_2Ph)(NAr)(O\text{-}t\text{-}Bu)_2$ ($Ar = 2,6\text{-}C_6H_3\text{-}i\text{-}Pr_2$) initiator.

10 μm and 0.5 mm thick polymer films were static cast from 0.5 and 3 wt. % solutions in tetrahydrofuran (THF) respectively. See Appendix D. Transmission electron microscopy observation of microtomed sections of 0.5 mm thick, Ag^+ stainedfilms, revealed a non-equilibrium interconnected cylindrical morphology (cylinder diameters ca. 80 Å).

6.2.1. Oxidation of Ag Nanoclusters in 10 Micron Thick Films

Silver loading was done at 25°C using a batch equilibration method in which 100 mg samples of 10 μm thick $[MTD]_{400}[NORCOOH]_{50}$ films were submerged in 20 g solutions of

0.005 M aqueous $Ag(OOCCH_3)$. Loading was conducted in the dark for a period of 9 days. Agitation was maintained with magnetic stir bars. The metal ion concentration remaining in the supernatant solution was measured periodically by withdrawing small aliquots of supernatant solution. The withdrawn aliquots were diluted with water to metal ion concentrations of < 30 ppm and analyzed using inductively coupled plasma atomic emission spectroscopy (ICP-AES). The extent of metal ion uptake was calculated using equation (4-1). After loading, the films were rinsed in de-ionized water and dried under vacuum at 25 °C for 15 hr. The Ag^+ ions were then reduced to Ag nanoclusters by heating (115 °C) the ion loaded films under hydrogen gas (2 atm) for 6 days.

Eight separate 10 μm thick Ag nanocluster containing films of approximately 100 mg in mass were submerged in 20 g solutions of 0.005 M aqueous $Na_2PdCl_4x3H_2O$ or $Na_2PtCl_4xH_2O$. The soaking was conducted at 25 °C for periods of time ranging from 54 hr to 845 hr, given in Table 6.1. Agitation was maintained with magnetic stir bars. The palladium and platinum ion concentrations remaining in the supernatant solution, and concentration of Ag^+ ions released from the film, were measured after soaking for the specified period of time, using ICP-AES as previously described. The soaking was done in the dark to prevent photo-induced reduction of Ag^+. After soaking, the films were rinsed in de-ionized water and dried under vacuum at 25 °C for 15 hr.

Table 6.1 Soaking schedule for 10 μm thick Ag nanocluster containing films

Species	**Time** hr			
$Na_2PdCl_4x3H_2O$	54	172	526	845
$Na_2PtCl_4xH_2O$	54	172	526	845

6.2.2. Oxidation of Ag Nanoclusters in Microtomed Films

A silver nanocluster containing $[MTD]_{400}[NORCOOH]_{50}$ film was synthesized by subjecting a 0.5 mm thick $[MTD]_{400}[NORCOOH]_{50}$ film to a series of 3 loading and reduction sequences (LARS), each consisting of the following steps: 1. Ag^+ loading (soak film in 0.06 M aqueous $Ag(OOCCH_3)$ for 330 hr at 25 °C, 10 mg film per 10 g solution), 2. Rinse and dry (rinse film in de-ionized water and dry under vacuum at 25 °C for 15 hr), and 3. Ag^+ reduction (heat film under 2 atm of hydrogen for 6 days at 115 °C).

Microtomed (400 Å thick) sections of the Ag cluster containing $[MTD]_{400}[NORCOOH]_{50}$ film were placed on 400 mesh gold TEM grids. The grids were floated (polymer-side-down), each on separate 0.005 M aqueous solutions (3-4 drops) of $Na_2PdCl_4x3H_2O$, at 25 °C, for periods of time between 30 min. and 103 hr. Both Ag^+ loading and $Na_2PdCl_4x3H_2O$ soaking were done in the dark. After soaking, the microtomed sections were rinsed in de-ionized water and dried under vacuum at 25 °C for 15 hr.

6.3. Results and Discussion

GPC analysis of the homo-MTD blocks yielded polydispersities of approximately 1.1. The block copolymer was not analyzed using GPC because polyNORCOOTMS precipitates as polyNORCOOH in wet toluene. The static cast block copolymer films were flexible and transparent with a slight yellowish tint, probably due to trace residues of $Mo(CHCMe_2Ph)(NAr)(O\text{-}t\text{-}Bu)_2$.

6.3.1. Oxidation of Ag Nanoclusters in 10 Micron Thick Films

ICP-AES measurements indicated a Ag^+ ion loading of 590 mg Ag^+/g polyNORCOOH or 0.50 moles Ag^+/mole COOH, in the 10 μm thick films after 9 days of loading. The Ag^+ uptake profile was similar to that shown in Figure 4.1. Following reduction, a mean Ag cluster diameter of 46 Å was calculated by applying the Scherrer equation (3-1) and equation (3-2), to the silver [111] WAXS peak. Although TEM was not performed on these particular Ag cluster containing films, we believe the Ag clusters were homogeneously distributed within the polyNORCOOH domains, as shown in Figure 4.6 for a similar Ag cluster containing film.

During the first few minutes of the reduction process, the color of the Ag^+ loaded films was observed to change from clear to transparent orange.

The 10 μm thick Ag cluster containing films gradually changed color from transparent orange to transparent amber, during 845 hr of soaking in 0.005 M aqueous $Na_2PdCl_4x3H_2O$ and $Na_2PtCl_4xH_2O$. The orange color is a result of surface plasmon absorption by the Ag nanoclusters. Our Pd nanocluster containing films appear amber in color. Figure 6.1 shows that pure Pd cluster containing films (synthesized as outlined in Chapter 4) absorb throughout the visible spectrum, without any well-defined absorption peaks.

ICP-AES measurements indicated that the palladium concentration in the supernatant solution decreased. Large fluctuations in the measured platinum concentration made it difficult to determine whether or not the platinum concentration decreased. In both cases, the silver concentration (originally zero) was observed to increase. Quantitative analysis, however, was not attempted due to the large fluctuations in ICP-AES measurements between consecutive time intervals. Small pieces of metal ion loaded polymer, torn from the main film during the long period of agitation, entered the ICP-AES with the supernatant solution and interfered with solution concentration measurements. The supernatant solution was not filtered prior to ICP-AES analysis, because $Na_2PdCl_4x3H_2O$ was observed to adsorb on both paper and 0.5 μm Millipore Millex-LCR (polymeric membrane) filters.

Given the mass of Ag in the polymer film, the mass of Pd^{+2} or Pt^{+2} in 20 g of 0.005 M solution, and the fact that two moles of Ag are required to reduce one mole of Pd^{+2} or Pt^{+2}, the mass of Pd^{+2} or Pt^{+2} in solution was sufficient to oxidize 3.4 times the mass of Ag present in the film.

Figures 6.2 and 6.3 show WAXS data from the 10 μm thick films after soaking in 0.005 M aqueous $Na_2PdCl_4x3H_2O$. The diffracted X-ray intensities shown in Figures 6.2 and 6.3 have been normalized through division by the maximum intensity of the polymer peak (amorphous halo, $2\theta \sim 17°$). Figure 6.2a corresponds to a Ag cluster containing film prior to soaking, and shows a broad scattering peak at $2\theta \sim 38.1°$, consistent with scattering from the

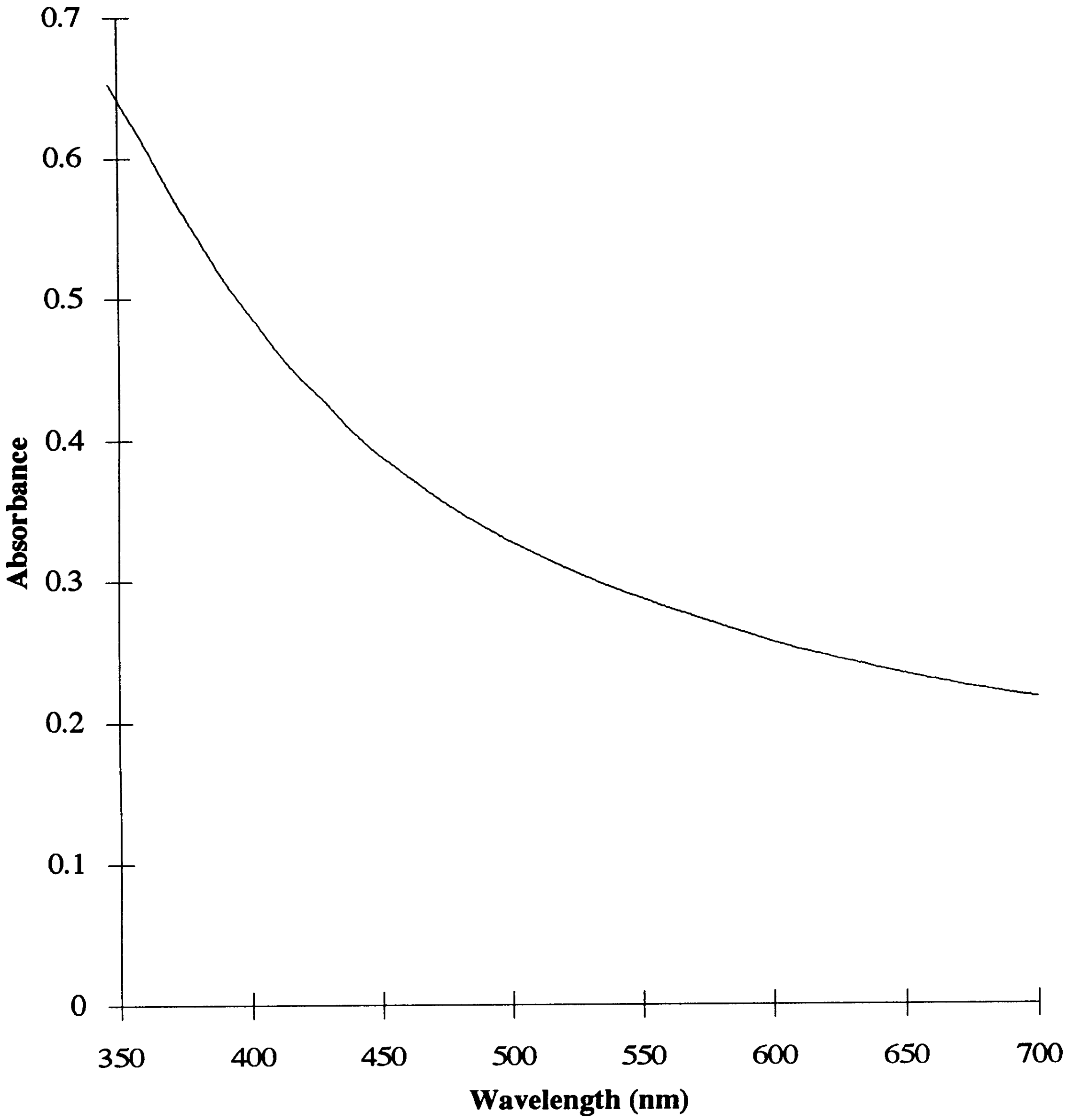

Figure 6.1: UV-visible absorption spectrum of 10 μm thick Pd nanocluster containing $[MTD]_{400}[NORCOOH]_{50}$ film

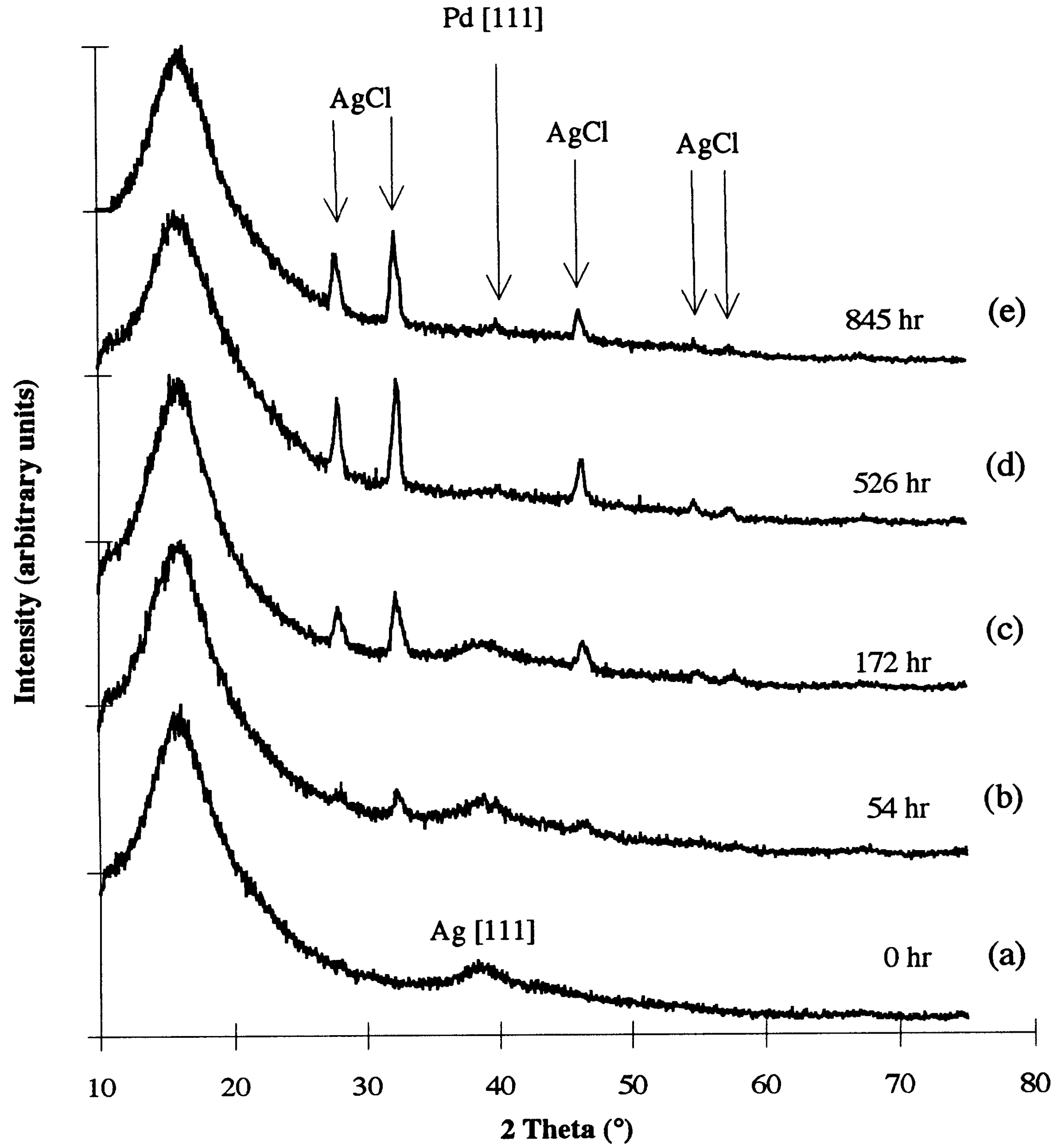

Figure 6.2: WAXS data from 10 μm thick Ag cluster containing film after soaking in 0.005 M aqueous $Na_2PdCl_4x3H_2O$

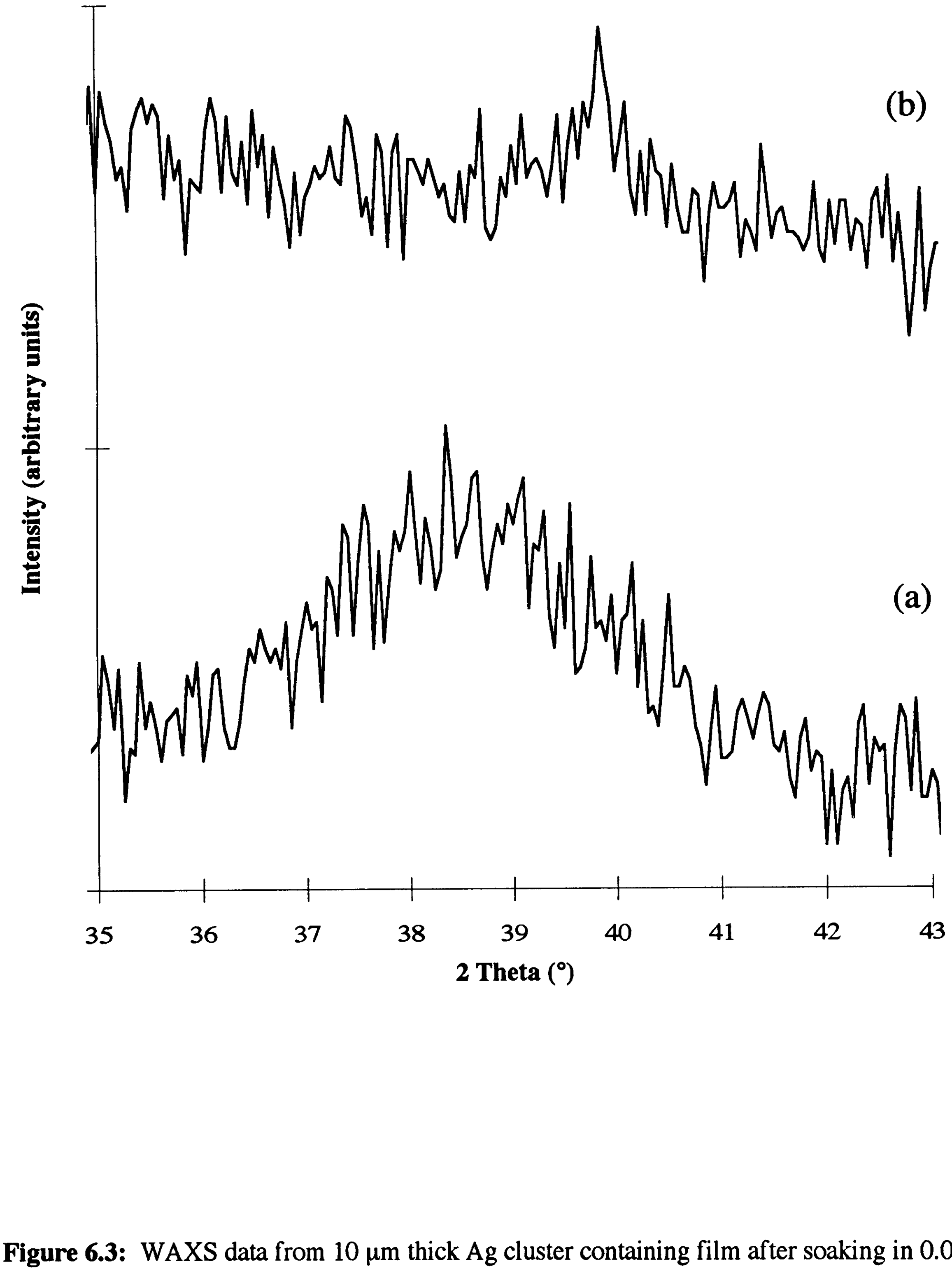

Figure 6.3: WAXS data from 10 μm thick Ag cluster containing film after soaking in 0.005 M aqueous $Na_2PdCl_4x3H_2O$: (a) 0 hr; (b) 845 hr

[111] plane of f.c.c. silver crystals.[3] Figures 6.2b through 6.2e correspond to films after 54, 172, 526, and 845 hr of soaking respectively. Progressing from Figure 6.2a to Figure 6.2e, we notice the gradual disappearance of the broad silver peak at $2\theta \sim 38.1°$ and the appearance of a new peak at $2\theta \sim 40.1°$, consistent with scattering from the [111] plane of f.c.c. palladium crystals.[3] We also observe the appearance and growth of additional peaks at $2\theta \sim$ 27.8°, 32.2°, 46.2°, 54.8°, and 57.5°, consistent with scattering from the [111], [200], [220], [311], and [222] planes of f.c.c. AgCl crystals, respectively.[4] AgCl crystals scatter at angles very similar to those of f.c.c. NaCl crystals; however, AgCl may be distinguished from NaCl by the relative intensities of the scattering peaks.[5] Figures 6.3a and 6.3b are enlargements of the silver and palladium scattering peaks from Figures 6.2a and 6.2e respectively.

The data shown in Figures 6.2 and 6.3 are consistent with the observed change in film color from transparent orange to transparent amber during soaking. Most Ag within the films appears to be oxidized to Ag^+ as the incoming palladium ions are reduced to metallic palladium. Although previous metal ion uptake experiments demonstrated that Ag^+ ions have a relatively high affinity for carboxylate ions, a large fraction of the Ag^+ ions appear to react with Cl^- ions forming AgCl, rather than displacing protons on carboxylic acid groups. The accumulation of AgCl within the film is due to its low solubility in cold water (9×10^{-5} g/100 ml).[6] Therefore, if all the Ag within the film were converted to AgCl, only 0.2 wt. % of the resulting AgCl would be present in solution. The remaining 99.8 wt. % should exist as solid AgCl. It is not known whether the silver concentration in the supernatent solution increased as a result of free Ag^+ ions or small AgCl crystals washed from the film.

The reduction of $[PdCl4]^{-2}$ (0.591 V) by metallic silver (-0.800 V) is not thermodynamically favorable at room temperature because the electromotive force (emf) of the overall reaction is negative (-0.209 V). Therefore, it can be inferred that the palladium ions must exist in some form, more easily reducible than Ag^+, prior to reduction by metallic silver (i.e. Pd^{+2}, 0.951 V).

Figure 6.4 shows WAXS data from the 10 μm thick films after soaking in 0.005 M aqueous $Na_2PtCl_4xH_2O$. The diffracted X-ray intensities shown in Figure 6.4 have been normalized through division by the maximum intensity of the polymer peak (amorphous halo, $2\theta\sim17°$). Figure 6.4a corresponds to a Ag cluster containing film prior to soaking. Figures 6.4b through 6.4e correspond to films after 54, 172, 526, and 845 hr of soaking, respectively. The explanation of the scattering data shown in Figure 6.4 is identical to that for Figure 6.2, except for the fact that platinum ions rather than palladium ions are reduced by metallic silver. Progressing from Figure 6.4a to Figure 6.4e, we notice a decrease in intensity of the broad silver peak, indicating oxidation of some fraction of the metallic silver initially present. In Figure 6.4e unlike in Figure 6.2e, there remains a silver scattering peak, but no distinguishable f.c.c. platinum [111] peak ($2\theta \sim 39.8°$).[3] We again observe the appearance and growth of additional AgCl peaks; however, they have a lower relative intensity than those in Figure 6.2. The presence of AgCl peaks indicates some fraction of the platinum ions were reduced to metallic platinum; however, a comparison between Figures 6.2 and 6.4 indicates that less platinum was reduced than palladium. The platinum [111] peak is probably obscured by the silver [111] peak of the remaining silver clusters.

The reduction of $[PtCl_4]^{-2}$ (0.755 V) by metallic silver (-0.800 V) is not thermodynamically favorable at room temperature because the electromotive force (emf) of the overall reaction is negative (-0.045 V). Therefore, it can be inferred that the platinum ions must exist in some form, more easily reducible than Ag^+, prior to reduction by metallic silver (i.e. Pt^{+2}, 1.118 V).

Although it is difficult to conclusively determine which reactions are occurring, the overall reactions outlined in equations (6-2) and (6-3) are consistent with experimental observations for the cases of $Na_2PdCl_4x3H_2O$ and $Na_2PtCl_4xH_2O$ respectively.

$$Na_2PdCl_4 + 2\,Ag^0 \text{--->} Pd^0 + 2\,NaCl + 2\,AgCl \qquad (6\text{-}2)$$

$$Na_2PtCl_4 + 2\,Ag^0 \text{--->} Pt^0 + 2\,NaCl + 2\,AgCl \qquad (6\text{-}3)$$

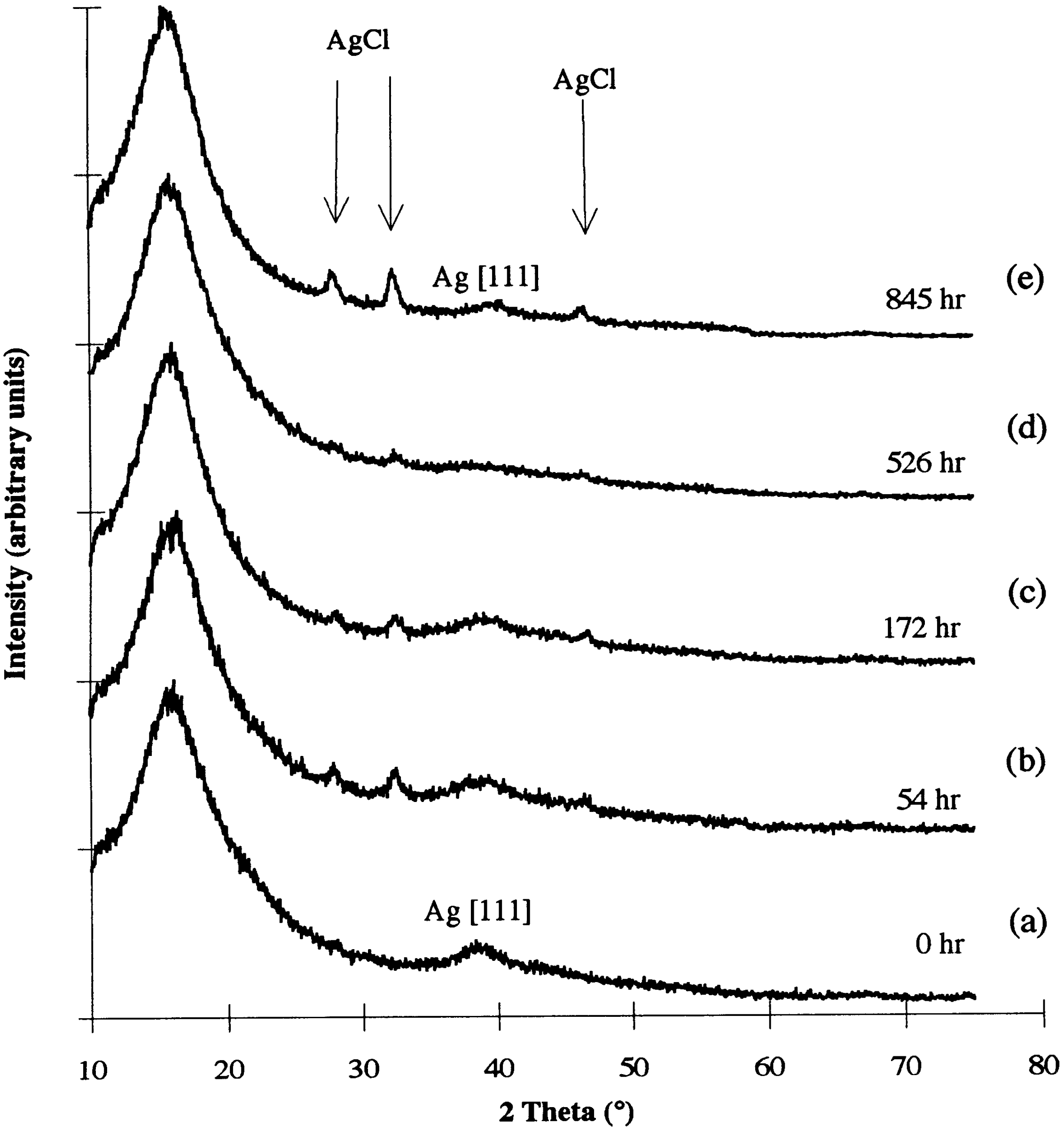

Figure 6.4: WAXS data from 10 µm thick Ag cluster containing film after soaking in 0.005 M aqueous $Na_2PtCl_4xH_2O$

No scattering attributable to NaCl was observed in either case; however, the maximum amount of NaCl which could have been produced is negligible compared with the solubility limit of the solutions. It is likely that most NaCl dissolved and was washed from the films.

6.3.2. Oxidation of Ag Nanoclusters in Microtomed Films

ICP-AES was not used to quantify the mass of Ag^+ which entered the 0.5 mm thick $[MTD]_{400}[NORCOOH]_{50}$ film during each of the three LARS. However, TEM observation of 400 Å thick film sections, revealed Ag clusters in the 25-35 Å, 40-90 Å, and 40-120 Å size ranges, respectively, following the first, second, and third LARS.

After floating on 0.005 M $Na_2PdCl_4x3H_2O$ solutions for various periods of time, the 400 Å thick polymer sections were observed with transmission electron microscopy (TEM). The composition of clusters within the films was estimated using scanning transmission electron microscopy (STEM) in the electron probe microanalysis (EPMA) mode. It was extremely difficult to quantify the mass of Ag in the 400 Å thick sections; however, the mass of Pd^{+2} in solution was believed to be many times in excess of that required to oxidize all Ag present.

Figure 6.5 is an electron micrograph of a Ag cluster containing film following a series of three LARS, prior to floating. It shows Ag clusters primarily in the 40-120 Å size range. Figure 6.6 shows a film after 3 hr of floating. We observe several 100+ Å clusters in addition to a few larger particles in the 200-400 Å size range. The larger particles appear very dark except for lighter regions around the outside edges. EPMA indicates that the particle centers contain mostly Ag (71 wt. % Ag, 14 wt. % Pd) while the outside edges contain mostly Pd (88 wt. % Pd, 0 wt. % Ag). Several wt. % of chlorine and sulfur were detected in both regions. The chlorine is introduced from $Na_2PdCl_4x3H_2O$ and may be present as AgCl. Sulfur is an impurity frequently encountered in silver compounds.[7] The EPMA composition analysis was conducted without standards using theoretical K-factors. Since both the Ag L_α and Pd L_α

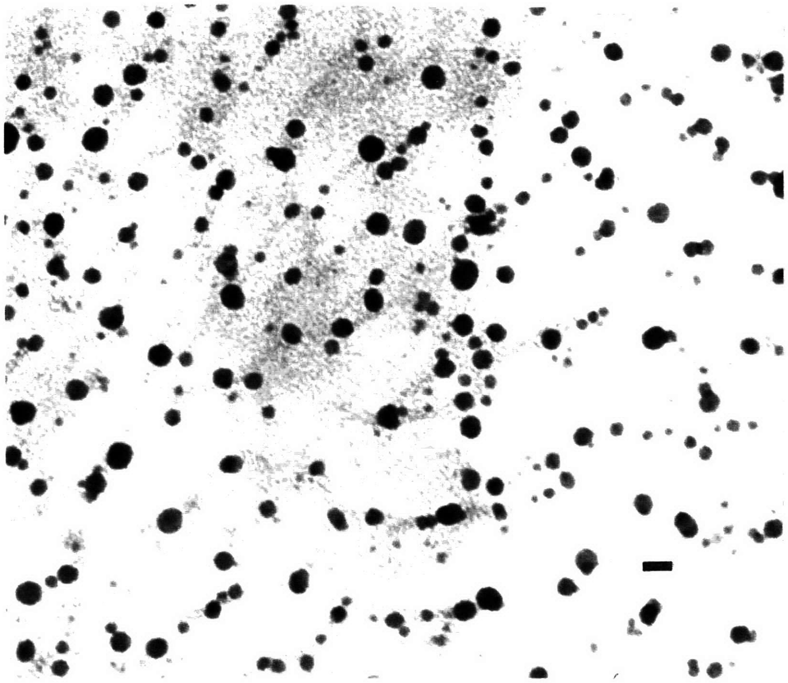

Figure 6.5: Electron micrograph of a Ag cluster containing film (bar = 150 Å)

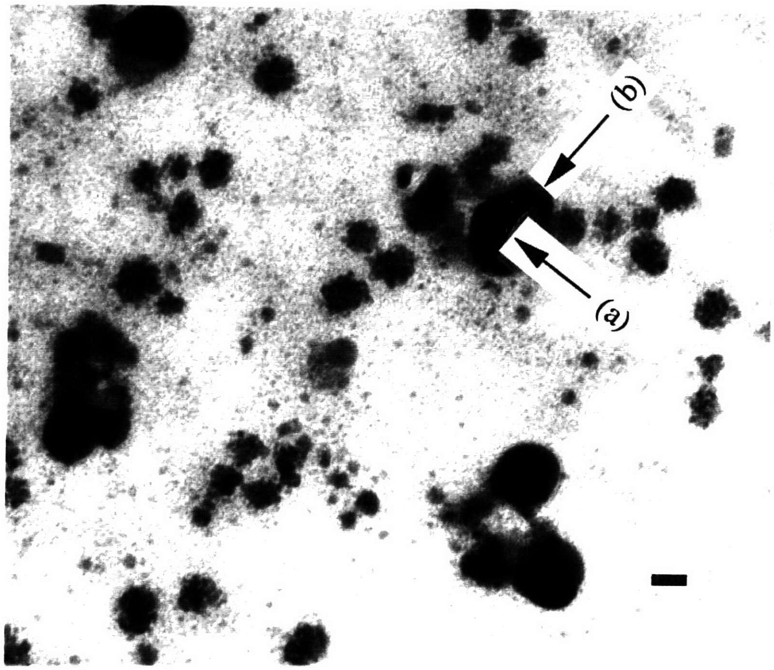

Figure 6.6: Electron micrograph of a Ag cluster containing film after 3 hr on 0.005 M aqueous $Na_2PdCl_4x3H_2O$ (bar = 150 Å)

emissions occur at similar energies, errors may occur during deconvolution of the Ag and Pd X-ray emission peaks. Therefore, estimated Ag and Pd contents may be in error by +/- 10 wt. %.

Figure 6.7 shows an enlarged view of a film after 15 hr of floating. We observe several 100+ Å clusters in addition to the reappearance of the block copolymer morphology. The 100+ Å clusters appear to consist of many discrete particles in the 15-30 Å size range. EPMA indicates that the particles consist of 90 wt. % Pd, 1 wt. % Ag, and several wt. % each of Cl and S. The polyNORCOOH domains appear to contain numerous smaller 10-15 Å clusters. EPMA indicates these smallest particles consist of 79 wt. % Pd, 6 wt. % Ag, and several wt. % each of Cl and S.

Figure 6.8 is an electron micrograph of a film after 103 hr of floating. Very few 100+ Å cluster aggregates remain; however, dark outlines of the polyNORCOOH domains are clearly visible. The polyNORCOOH domains appear to contain numerous 10-15 Å clusters with the same composition as those observed after 15 hr. Although the $[\mathrm{MTD}]_{400}[\mathrm{NORCOOH}]_{50}$ appears to have a lamellar morphology in Figures 6.7 and 6.8, it most often takes on an interconnected cylindrical morphology.

Table 6.2 is a summary of the EPMA measurements of cluster composition, corresponding to clusters appearing in Figures 6.6 through 6.8. Figures 6.5 through 6.8 indicate that Pd^{+2} ions are reduced to Pd, by Ag, upon contact with the Ag cluster surfaces. Palladium initially appears to form a coating on portions of the Ag cluster (40-120 Å) surfaces. However, instead of forming continuous shells on the Ag cluster cores, the Pd atoms form smaller (10-30 Å), Pd rich particles.

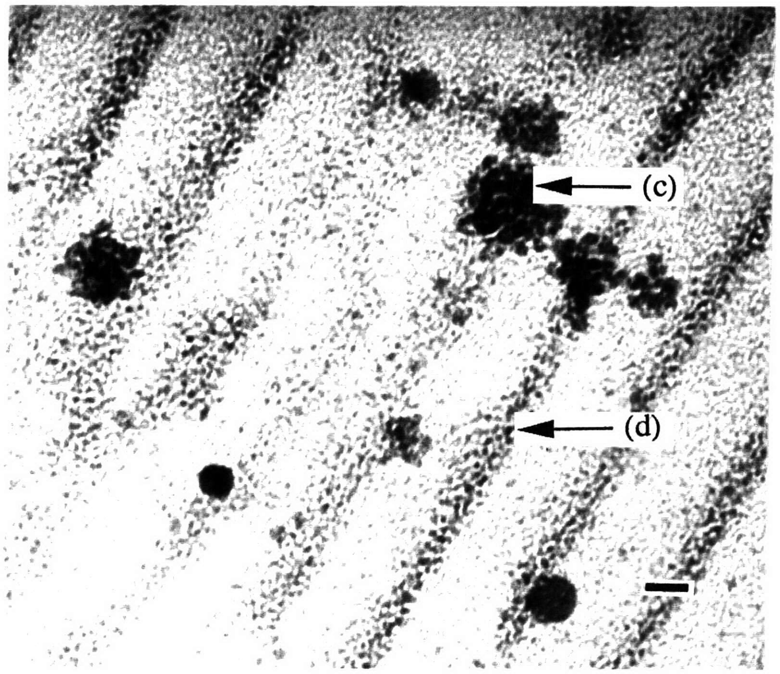

Figure 6.7: Electron micrograph of a Ag cluster containing film after 15 hr on 0.005 M aqueous $Na_2PdCl_4x3H_2O$ (bar = 100 Å)

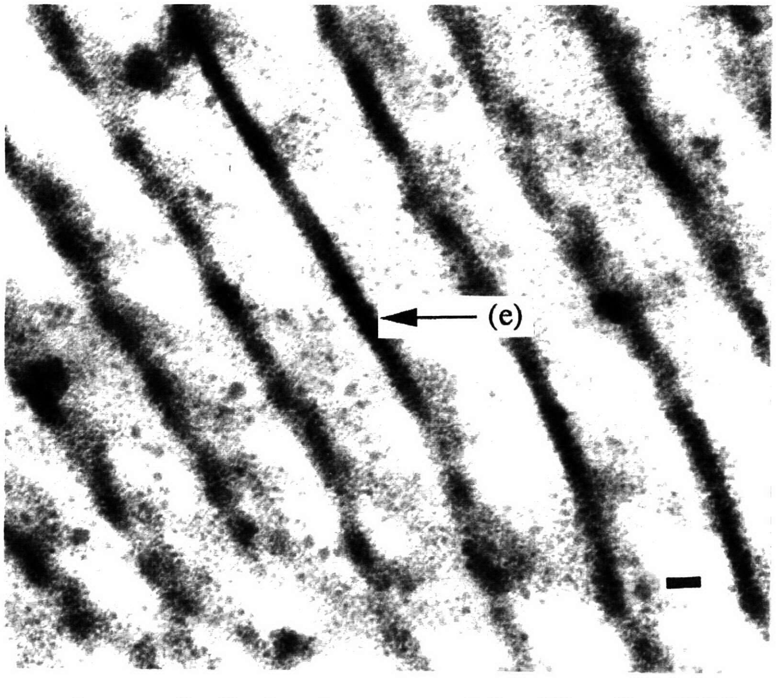

Figure 6.8: Electron micrograph of a Ag cluster containing film after 103 hr on 0.005 M aqueous $Na_2PdCl_4x3H_2O$ (bar = 150 Å)

Table 6.2 EPMA measurements of cluster composition

Position	**Composition, wt. %**			
	Ag	Pd	S	Cl
(a)	71	14	several	several
(b)	0	88	several	several
(c)	1	90	several	several
(d)	6	79	several	several
(e)	6	79	several	several

6.4. Conclusions

Silver nanoclusters (ca. 46 Å) within 10 μm thick $[MTD]_{400}[NORCOOH]_{50}$ films were oxidized by soaking the films in 0.005 M aqueous $Na_2PdCl_4x3H_2O$ or $Na_2PtCl_4xH_2O$ solutions. WAXS demonstrates that within 845 hr, most Ag present within the films is oxidized to Ag^+ as palladium ions are reduced to Pd. The accumulation of AgCl within the films indicates that a significant fraction of the Ag^+ ions combine with Cl^-, rather than displacing carboxylic acid protons. The reduction of $[PdCl_4]^{-2}$ (0.591 V) by silver (-0.800 V) is not thermodynamically favorable at room temperature; therefore, it can be inferred that the palladium ions must exist in some form, more easily reducible than Ag^+, prior to reduction by metallic silver (i.e. Pd^{+2}, 0.951 V). WAXS data for films soaked in aqueous $Na_2PtCl_4xH_2O$ are nearly identical to those for films soaked in aqueous $Na_2PdCl_4x3H_2O$. However, after 845 hr of soaking some platinum ions seem to have been reduced, but a significant fraction of the Ag remains in the film.

Silver nanoclusters (40-120 Å) within 400 Å thick $[MTD]_{400}[NORCOOH]_{50}$ sections were oxidized to Ag^+ by floating on 0.005 M aqueous $Na_2PdCl_4x3H_2O$ for a period of 103 hr. TEM observation and EPMA analysis indicate that the reduced Pd atoms form Pd rich (> 80 wt. %) nanoclusters (10-30 Å), rather than continuous Pd shells on the Ag cluster cores. The Pd rich nanoclusters appear confined to the polyNORCOOH domains.

Synthesis of bimetallic shell-and-core particles may still be possible using our general approach. However, one must begin with cluster cores of a more easily reducible metal (A^{+n}), and then load the carboxylic acid groups with ions of a less easily reducible metal (B^{+n}). The oxidation of metallic A by B^{+n} ions will not occur due to the negative emf of the overall reaction. Previous experiments involving a single metal and multiple LARS (Chapter 5), lead us to believe that subsequent reduction will cause the deposition of metal B onto pre-existing cluster cores of metal A. This process will also likely result in the nucleation of additional clusters of pure metal B.

6.5. References for Chapter 6

(1) Hartley, F.R. 'The Chemistry of Platinum and Palladium' Applied Science Publishers LTD, London, 1973, p. 234.

(2) Zumdahl, S.S. 'Chemistry' D.C. Heath and Company, Lexington, 1986, p. 718.

(3) Swanson, H.E. and Tatge, E. 'U.S. National Bureau of Standards Standard X-Ray Diffraction Patterns', NBS Circular 539, Volume I, U.S. Government Printing Office, Washington D.C., June 15, 1953.

(4) Swanson, H.E. and Fuyat, R.K. 'U.S. National Bureau of Standards Standard X-Ray Diffraction Patterns', NBS Circular 539, Volume IV, U.S. Government Printing Office, Washington D.C., March 1, 1955.

(5) Swanson, H.E. and Fuyat, R.K. 'U.S. National Bureau of Standards Standard X-Ray Diffraction Patterns', NBS Circular 539, Volume II, U.S. Government Printing Office, Washington D.C., June 15, 1953.

(6) 'Handbook of Chemistry and Physics' (Ed. R. Weast), CRC Press, Boca Raton, FL, 1987, p. B-127.

(7) 'Handbook of Chemistry and Physics' (Ed. R. Weast), CRC Press, Boca Raton, FL, 1987, p. B-35.

Chapter 7

Synthesis of Cobalt and Nickel Containing Nanoclusters within Microphase-Separated Diblock Copolymers

7.1. Summary

In Chapter 3, we reported a general methodology for the synthesis of transition metal nanoclusters (Ag, Au, Cu, Ni, Pb, Pd, and Pt) stabilized within microphase-separated diblock copolymers. In our strategy, outlined in Figure 1.9, metal ions or complexes are coordinated to carboxylic acid groups within the water soluble polyNORCOOH domains of a $[MTD]_{400}[NORCOOH]_{50}$ block copolymer (MTD = methyltetracyclododecene and NORCOOH = 2-norbornene-5,6,-dicarboxylic acid) by immersion of the polymer in aqueous metal salt solutions. The metal ions and complexes are subsequently reduced by heating the metal loaded polymer under hydrogen or by immersion in an aqueous sodium borohydride ($NaBH_4$) solution. For several transition metals, the resulting nanoclusters are uniformly sized and homogeneously dispersed within the polyNORCOOH domains.

We now investigate, in greater depth, the $NaBH_4$ reduction of Co^{+2} and Ni^{+2} loaded $[MTD]_{400}[NORCOOH]_{50}$ films in both aqueous and organic solutions. We also describe the synthesis of a transparent, ferromagnetic, cobalt containing $[MTD]_{400}[NORCOOH]_{50}$ film via the thermal reduction of dicobalt octacarbonyl ($Co_2(CO)_8$).

7.2. Experimental

$[MTD]_{400}[NORCOOH]_{50}$ diblock copolymer was synthesized as previously reported, using a ring-opening metathesis polymerization in anhydrous toluene with a $Mo(CHCMe_2Ph)(NAr)(O\text{-}t\text{-}Bu)_2$ (Ar = $2,6\text{-}C_6H_3\text{-}i\text{-}Pr_2$) initiator.

10 μm and 0.5 mm thick $[MTD]_{400}[NORCOOH]_{50}$ films were static cast from 0.5 and 3 wt. % solutions in tetrahydrofuran (THF) respectively. TEM observation of microtomed,

Ag^+ loaded, $[MTD]_{400}[NORCOOH]_{50}$ films revealed a non-equilibrium interconnected cylindrical morphology (cylinder diameters ca. 80 Å).

10 μm thick polymer films were loaded with Co^{+2} or Ni^{+2} using a batch equilibration method in which 100 mg samples of film were submerged in 20 g of 0.005 M aqueous metal salt solutions ($Co(OOCCH_3)_2$ or $NiCl_2$) at 25°C. Agitation was maintained with magnetic stir bars. The metal ion concentration remaining in the supernatant solution was measured periodically by withdrawing small aliquots of supernatant solution. The withdrawn aliquots were diluted with water to metal ion concentrations of < 30 ppm and analyzed using ICP-AES. Approximate (+/- 15 %) metal ion uptakes of 220 mg Co^{+2} (0.34 moles Co^{+2}/mole COOH) and 240 mg Ni^{+2} (0.37 moles Ni^{+2}/mole COOH) per gram polyNORCOOH were calculated using equation (4-1). The Co^{+2} and Ni^{+2} loaded films were both transparent; however, the Co^{+2} containing film had a slight pink tint.

7.2.1. Reduction of Co^{+2} and Ni^{+2} Loaded $[MTD]_{400}[NORCOOH]_{50}$ in Aqueous Sodium Borohydride Solutions

Reduction of Co^{+2} and Ni^{+2} within 10 μm thick Co^{+2} and Ni^{+2} loaded films was attempted by soaking each film (ca. 100 mg) in 20 g of 1 wt. % aqueous $NaBH_4$ for 48 hr at 25 °C. Bubbling was observed following the addition of both the Co^{+2} and Ni^{+2} loaded films to the aqueous $NaBH_4$ solutions. In the case of Ni^{+2}, the bubbling slowed considerably within 24 hr, and the film became greyish (but remained transparent) minutes after immersing in the $NaBH_4$ solution. In the case of Co^{+2}, the bubbling slowed gradually over 48 hr, and the film became greyish (but remained transparent) after several hours of soaking in the $NaBH_4$ solution. After reduction, the films were rinsed in de-ionized water and dried under vacuum for 15 hr at 25 °C.

The reduction of ions with negative electrochemical reduction potentials (Co^{+2}, -0.280 V; Ni^{+2}, -0.257 V), by hydrogen, is not thermodynamically favorable at temperatures less than several hundred degrees Celsius. Aqueous $NaBH_4$ was chosen as a reducing agent for Co^{+2}

and Ni^{+2}, because of its large negative electrochemical reduction potential (-0.43 V in acidic solution, -1.37 V in basic solution)[1] and relatively low toxicity compared to other reducing agents such as hydrazine monohydrate.

$NaBH_4$ reacts very slowly with water, forming sodium metaborate and hydrogen according to equation (7-1):[1]

$$NaBH_4 + 2\ H_2O \text{ -----> } NaBO_2 + 4\ H_2 \qquad (7\text{-}1)$$

However, aqueous $NaBH_4$ may still be used as a reducing agent, since it reacts rapidly with easily reducible metal ions (i.e. Au^{+3}, 1.40 V and Cu^{+2}, 0.34 V)[2,3], according to equation (7-2):[1]

$$4\ M^{+2} + BH_4^- + 2\ H_2O \text{ -----> } 4\ M^0 + BO_2^- + 8\ H^+ \qquad (7\text{-}2)$$

Less easily reducible solution phase ions such as Co^{+2} and Ni^{+2}, however, often react with aqueous $NaBH_4$ to form almost amorphous metal borides, according to equation (7-3):[2,4]

$$2\ M^{+2} + 4\ BH_4^- + 9\ H_2O \text{ -----> } M_2B + 12.5\ H_2 + 3\ B(OH)_3 \qquad (7\text{-}3)$$

If reduction occurs by reaction (7-2), 20 g of 1 wt. % aqueous $NaBH_4$ solution contains 400 times more $NaBH_4$ than necessary to reduce all Co^{+2} or Ni^{+2} present in the film . If reduction occurs by reaction (7-3), 20 g of 1 wt. % aqueous $NaBH_4$ solution contains 50 times more $NaBH_4$ than necessary to reduce all Co^{+2} or Ni^{+2} present in the film .

7.2.2. Reduction of Co^{+2} and Ni^{+2} Loaded $[MTD]_{400}[NORCOOH]_{50}$ in Organic Sodium Borohydride Solutions

Reduction of Co^{+2} and Ni^{+2} loaded films was also attempted with organic $NaBH_4$ solutions. A 10 μm thick Co^{+2} containing film (ca. 100 mg) was soaked in 20 g of 1 wt. % $NaBH_4$ solution in anhydrous diglyme (2-methoxy ethyl ether) for 76 hr at 25 °C under a nitrogen atmosphere. The film became greyish (but remained transparent) hours after immersing in the $NaBH_4$ solution. It was difficult to determine whether or not bubbling occurred. After reduction, the film was dried under vacuum for 15 hr at 25 °C.

10 μm thick Co^{+2} and Ni^{+2} containing films (ca. 100 mg) were each soaked in 20 g of 0.1 wt. % $NaBH_4$ solution in anhydrous THF for 123 hr at 25 °C under a nitrogen atmosphere. Bubbling was observed in both cases, and the films became greyish (but remained transparent) immediately after immersing in the $NaBH_4$ solution. After reduction, the films were rinsed in anhydrous THF and dried under vacuum for 15 hr at 25 °C. Although $[MTD]_{400}[NORCOOH]_{50}$ is soluble in THF, the Co^{+2} and Ni^{+2} containing films remained intact after several days of soaking, due to physical crosslinking caused by the divalent metal ions.

7.2.3. Thermal Decomposition of Dicobalt Octacarbonyl within $[MTD]_{400}[NORCOOH]_{50}$

Dicobalt octacarbonyl (0.04 g, 0.118 mmol) was incorporated into the polyNORCOOH domains of $[MTD]_{400}[NORCOOH]_{50}$ (0.2 g polymer, 0.236 mmol COOH) by mixing 4 g of a 1 wt. % $Co_2(CO)_8$ solution in anhydrous THF with 6.67 g of a 3 wt. % polymer solution in anhydrous THF (15 hr, 25 °C, under nitrogen). No precipitate was observed upon mixing. A O.2 mm thick film was cast by allowing the THF to evaporate (under nitrogen) from a Teflon cup over 6 days. A portion of the $Co_2(CO)_8$ loaded film was heated under vacuum at 90 °C for 72 hr, to cause the decomposition of $Co_2(CO)_8$. Dicobalt octacarbonyl is known to decompose at 52 °C,[5] forming metallic cobalt, carbon monoxide, and $Co_4(CO)_{12}$.[6,7]

7.3. Results and Discussion

GPC analysis of the homo-MTD blocks yielded polydispersities of approximately 1.1. The block copolymer was not analyzed using GPC because polyNORCOOTMS precipitates as polyNORCOOH in wet toluene. The static cast block copolymer films were flexible and transparent with a slight yellowish tint, probably due to trace residues of $Mo(CHCMe_2Ph)(NAr)(O\text{-}t\text{-}Bu)_2$.

7.3.1. Reduction of Co^{+2} and Ni^{+2} Loaded $[MTD]_{400}[NORCOOH]_{50}$ in Aqueous Sodium Borohydride Solutions

Both the Co^{+2} and Ni^{+2} loaded films were examined with WAXS after soaking in the aqueous $NaBH_4$ solutions, immediately after drying. Only the amorphous halo due to polymer interchain scattering was observed from the nickel containing film. However, as shown in Figure 7.1, a small but distinct peak was observed at $2\theta = 47.6°$ in the case of the cobalt containing film. This peak is consistent with scattering from the [101] plane of h.c.p. cobalt.[8] Following 18 hr of storage in air, the same films were examined a second time with WAXS, and only the amorphous halos were observed.

The fact that color changes were observed after soaking seems to indicate that reduction reactions occurred. It is very likely that the Co^{+2} and Ni^{+2} ions were reduced primarily to almost amorphous Co_2B and Ni_2B as outlined in equation (7-3). The small amount of crystalline cobalt which did form, appears to have oxidized as a result of storage in air.

Amorphous Co_2B and Ni_2B can be converted to their crystalline forms by heating under argon at 500 °C for 2 hr.[2,4] We heated our cobalt and nickel loaded films under vacuum at 110 °C for 72 hr; however, subsequent WAXS characterization failed to reveal the presence of crystalline metal borides. It is likely that our films contained amorphous metal borides, and that 110 °C was too low a temperature to cause the transformation of amorphous metal borides to crystalline metal borides. The cobalt and nickel loaded films were not heated to higher temperatures, because heating to 110 °C caused the films to become very brittle. Previous

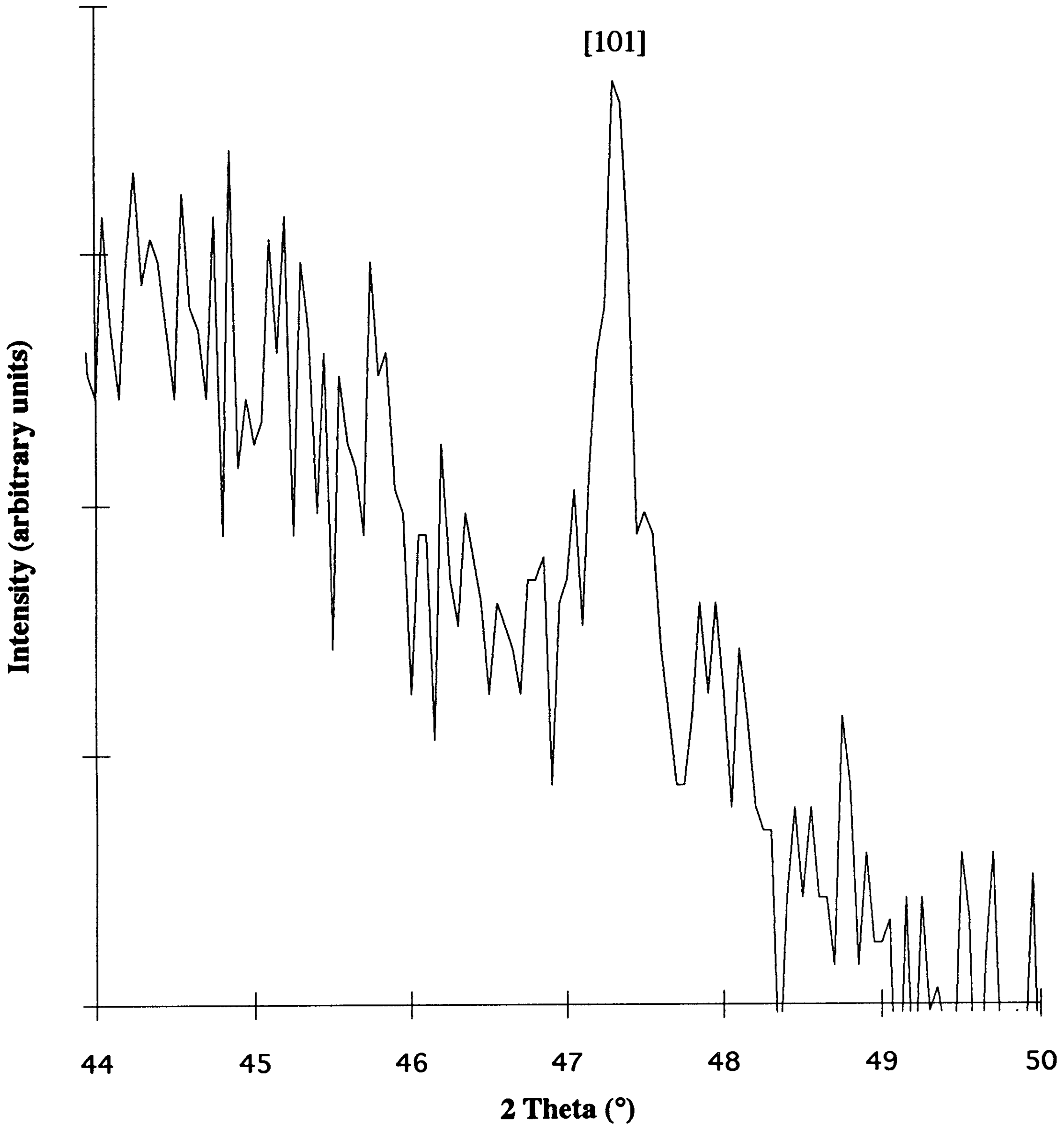

Figure 7.1: WAXS data from Co^{+2} loaded $[MTD]_{400}[NORCOOH]_{50}$ film after soaking in aqueous $NaBH_4$

soaking in aqueous $NaBH_4$ causes the films to become brittle when heated. Unsoaked films can be heated to 110 °C, for over a week in an oxygen free environment, without becoming brittle.

7.3.2. Reduction of Co^{+2} and Ni^{+2} Loaded $[MTD]_{400}[NORCOOH]_{50}$ in Organic Sodium Borohydride Solutions

Both the Co^{+2} and Ni^{+2} loaded films were examined with WAXS after soaking in the anhydrous diglyme/$NaBH_4$ solutions, prior to air exposure. Only the amorphous halos due to polymer interchain scattering were observed. Klabunde et al.[2,9] demonstrated that Co^{+2} and Ni^{+2} ions react with $NaBH_4$ in diglyme to form amorphous cobalt, nickel, and nickel boride according to equations (7-4), (7-5), and (7-6):

$$M^{+2} + 2\ BH_4^- \xrightarrow{L=\text{diglyme}} (L)_nM(BH_4)_2 \tag{7-4}$$

$$(L)_nCo(BH_4)_2 \xrightarrow{-nL} Co + H_2 + B_2H_6 \tag{7-5}$$

$$2(L)_nNi(BH_4)_2 \xrightarrow{-2nL} Ni + 1/2\ Ni_2B + 7/2\ H_2 + 3/2\ B_2H_6 \tag{7-6}$$

The amorphous cobalt can be converted to f.c.c cobalt by heating under argon at 500 °C for 2 hr. F.c.c. cobalt is the stable structure at temperatures greater than 450 °C, while h.c.p. cobalt is stable at lower temperatures.[8] We heated our cobalt and nickel loaded films under vacuum at 110 °C for 90 hr; however, subsequent WAXS characterization failed to reveal the presence of crystalline metals or metal borides. It is likely that our films contained amorphous metals or metal borides.

Figures 7.2 and 7.3, respectively, are electron micrographs of Ni^{+2} and Co^{+2} loaded films prior to soaking in THF/$NaBH_4$ solutions. They both show the dark outlines of

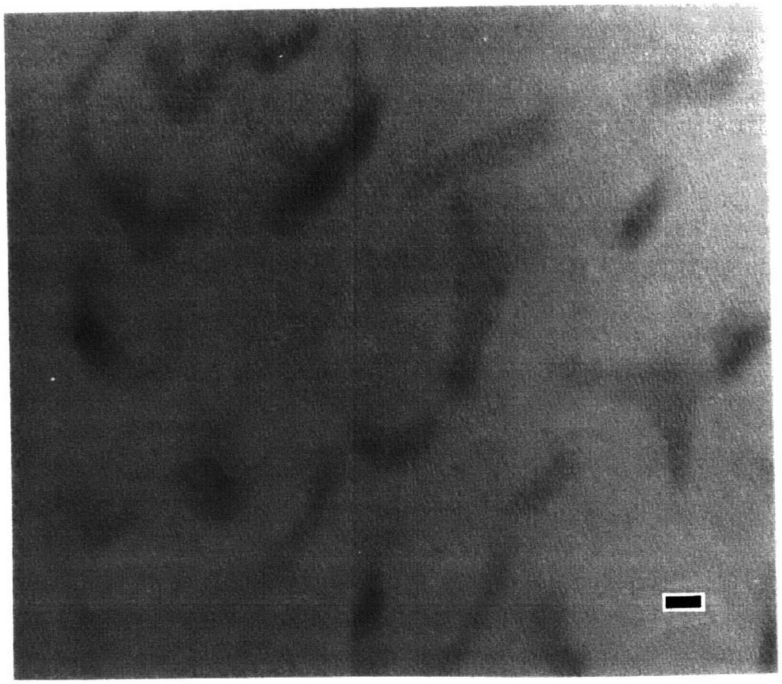

Figure 7.2: Electron micrograph of Ni^{+2} loaded $[MTD]_{400}[NORCOOH]_{50}$ film (bar = 200 Å)

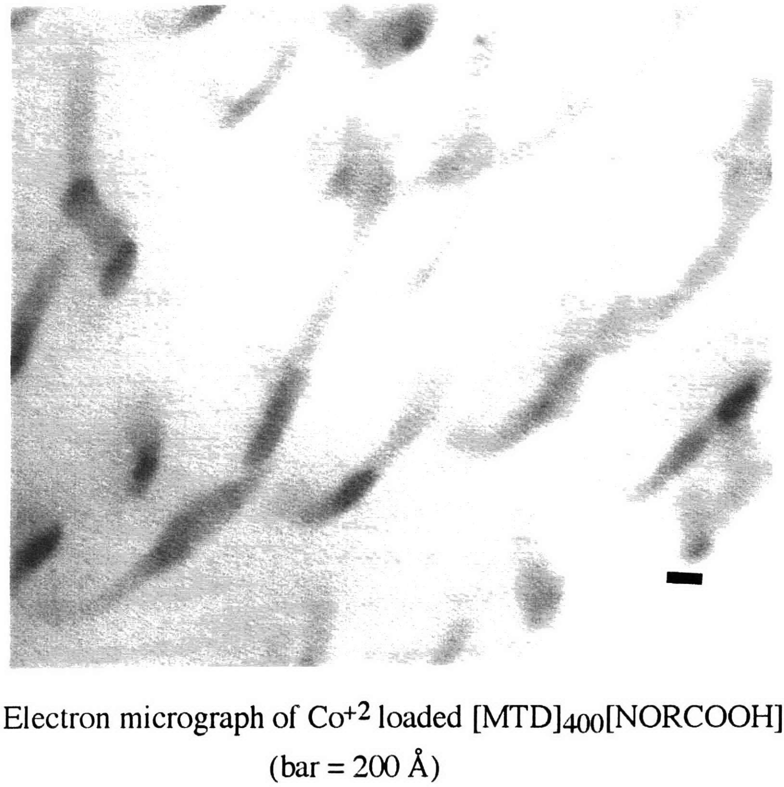

Figure 7.3: Electron micrograph of Co^{+2} loaded $[MTD]_{400}[NORCOOH]_{50}$ film (bar = 200 Å)

interconnected cylindrical, metal ion loaded, polyNORCOOH domains in a polyMTD matrix. Figures 7.4 and 7.5, respectively, are electron micrographs of nickel and cobalt containing films after soaking in THF/$NaBH_4$ solutions. Figure 7.4 clearly shows the presence of 50-200 Å particles, which in most cases, are in close proximity to the polyNORCOOH domains. Figure 7.5 also appears to show 100-200 Å particles, but fewer than in Figure 7.4.

The electron diffraction pattern corresponding to Figure 7.4 contains seven discernible rings, attributable to scattering from randomly oriented crystalline material within the film. The d-spacings of each scattering plane are listed in Table 7.1, and were calculated using equation (7-7):

$$d = \lambda(L/R) \qquad (7\text{-}7)$$

where λ is the wavelength (0.02507 Å) of 200 kV electrons, L is the camera length (53.96 cm), and R is the radius of the scattering ring in cm. The 55 cm camera length setting was used to collect the diffraction pattern. The true camera length was calculated from the diffraction ring radii of a thallous chloride diffraction standard.

Table 7.1 D-spacings: Calculated vs. NiB

Calculated d-spacings, Å	**NiB d-spacings, Å**	**h k l**
	3.68	020
2.87 +/- 0.12	2.72	110
2.43 +/- 0.09	2.31	021
1.98 +/- 0.06	2.01	111
	1.885	130
	1.845	040
1.58 +/- 0.04	1.593	131
	1.568	041
1.47 +/- 0.03	1.484	002
1.25 +/- 0.02		
0.94 +/- 0.02		

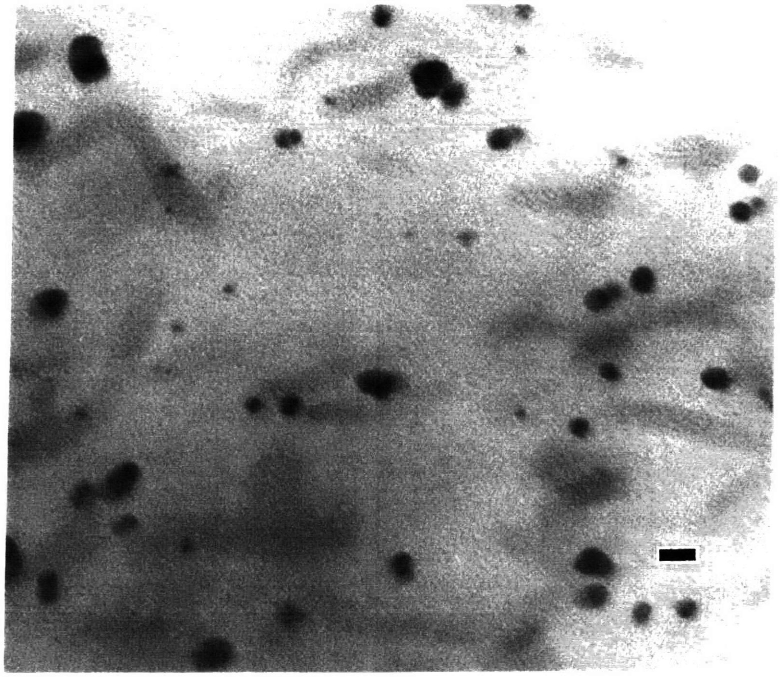

Figure 7.4: Electron micrograph of Ni^{+2} loaded $[MTD]_{400}[NORCOOH]_{50}$ film after soaking in THF/$NaBH_4$ solution (bar = 200 Å)

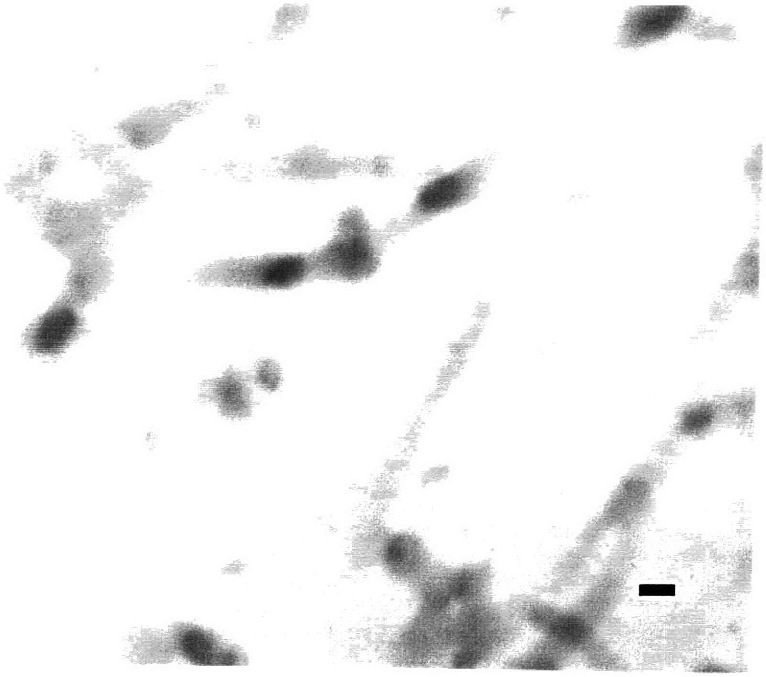

Figure 7.5: Electron micrograph of Co^{+2} loaded $[MTD]_{400}[NORCOOH]_{50}$ film after soaking in THF/$NaBH_4$ solution (bar = 200 Å)

The calculated d-spacings correspond more closely to those of orthorhombic NiB[10] than other likely materials including Ni, Ni_2B, B_2O_3, and $NaBH_4$. The standard deviations were calculated assuming that R (0.47 cm to 1.44 cm) was the only source of error and could be determined to +/- 0.02 cm. D-spacings greater than 3 Å could not be observed because the scattering rings were obscured by the primary beam. No tabulated data was available for NiB d-spacings smaller than 1.484 Å. The rings observed at d-spacings of 2.87 Å and 2.43 Å appeared most intense, consistent with NiB [110] (2.72 Å) and [021] (2.31 Å) relative scattering intensities of 75 and 100 respectively.[10]

No crystalline scattering was observed in the electron diffraction pattern of the cobalt containing film. WAXS characterization did not reveal the presence of crystalline metals or metal borides in either film. Electron diffraction tends to be a more sensitive technique than WAXS because the electron beam can be focused specifically on the particle containing polyNORCOOH domains.

Klabunde et al.[2] did not observe the formation of crystalline NiB following reduction of unbound Ni^{+2} in a $NaBH_4$/diglyme solution. It is not known whether the reduction of Ni^{+2} loaded films in our $NaBH_4$/THF solution also lead to the formation of amorphous nickel and Ni_2B as in Klabunde's experiment.

7.3.3. Thermal Decomposition of Dicobalt Octacarbonyl within $[MTD]_{400}[NORCOOH]_{50}$

Prior to air exposure the $Co_2(CO)_8$ containing films appeared greenish-brown and transparent, both before and after heating. However, following several hours in air both heated and unheated films became violet but remained transparent. Figures 7.6a and 7.6b, respectively, are UV-visible spectra of air stored, $Co_2(CO)_8$ loaded films before and after heating. They both show absorption peaks at ca. 560 nm. The difference in absolute absorbance is due to differing film thicknesses. The color changes were probably due to the oxidation of cobalt and/or cobalt carbonyls to cobalt oxides.

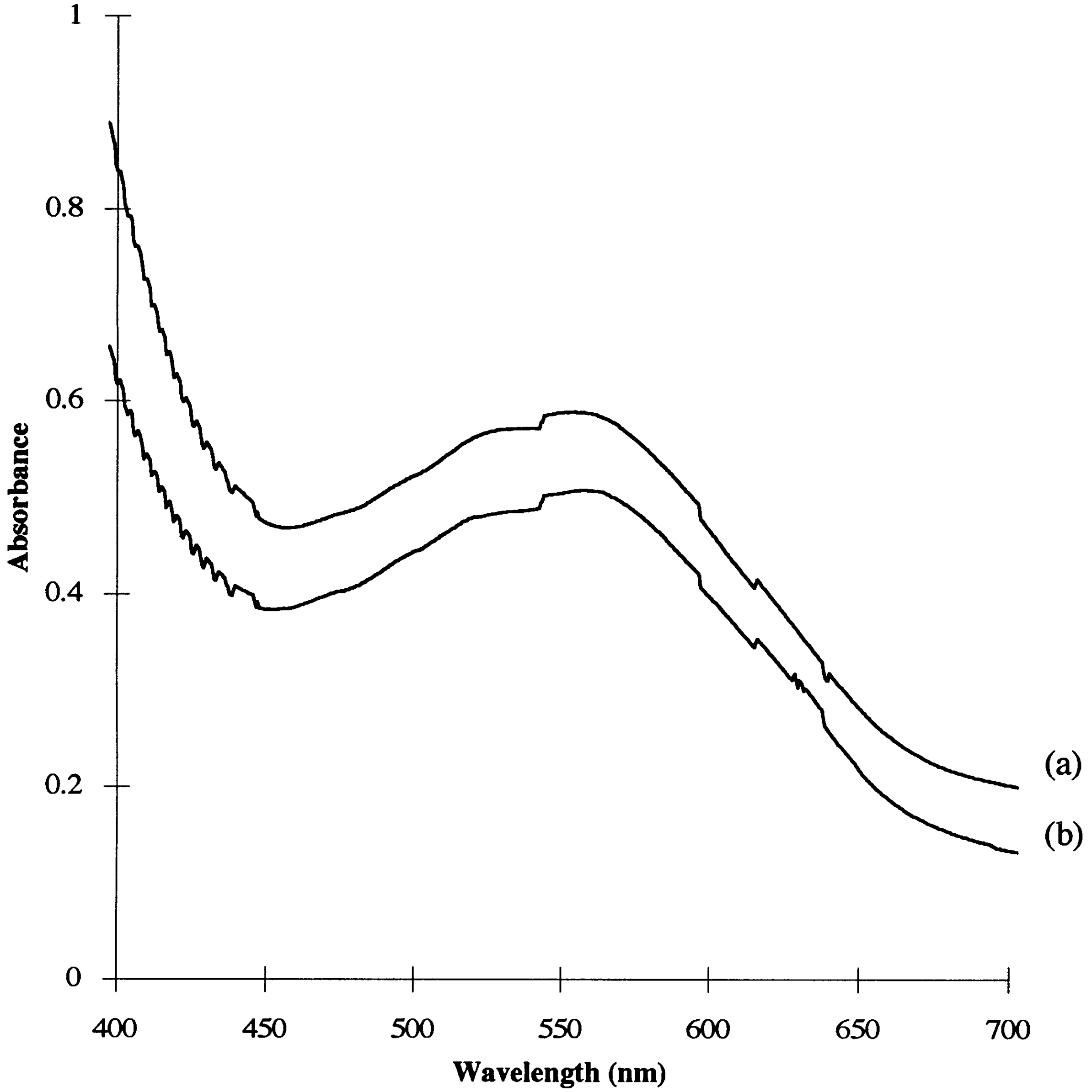

Figure 7.6: UV-visible spectra of air stored $Co_2(CO)_8$ loaded films: (a) unheated; (b) heated

Figure 7.7 is an electron micrograph of the $Co_2(CO)_8$ containing film prior to heating. It shows the dark outlines of the $Co_2(CO)_8$ loaded, interconnected cylindrical polyNORCOOH domains. Figure 7.8 is an electron micrograph of the same film after heating under vacuum at 90 °C for 72 hr. It also shows dark outlines of the cobalt containing polyNORCOOH domains; however, the shaded polyNORCOOH domains appear discontinuous in many locations, indicating the possible formation of discrete particles. Neither electron diffraction, from an air exposed film, nor WAXS, prior to air exposure, revealed the presence of crystalline material within the heated film .

Figure 7.9 shows a typical magnetization (M) vs. applied magnetic field (H) hysteresis loop for a bulk ferromagnetic or ferrimagnetic material, below its Curie temperature.[11,12] These materials are composed of many small regions called domains, within which the local magnetization is saturated. However, in the absence of an applied magnetic field, the magnetizations of the different domains are not all oriented in the same direction. The specimens are not magnetically saturated in a macroscopic sense.

In the presence of an applied field (Figure 7.9), the magnetizations of the different domains become oriented parallel to one another and the direction of the applied field, through domain boundary displacements and rotations. M_s is the saturation (highest possible) magnetization, corresponding to parallel alignment of all domain magnetizations. M_r is the remanent magnetization, due to residual alignment of the domain magnetizations after the applied field has been removed. H_c is the coercivity, the reverse field required to reduce M_r to zero.

As shown in Figure 7.10, the room temperature coercivity of small particles is strongly dependent on their size. Magnetization in multidomain particles changes as a result of domain wall motions and rotations. However, below an imprecisely known critical diameter, D_s, the particles become single domains. Particles of diameter D_s and smaller change their magnetization by one or more modes of domain rotation. Crystal anisotropy is one such mode, and it results from the alignment, within an applied field, of single-domain crystals along

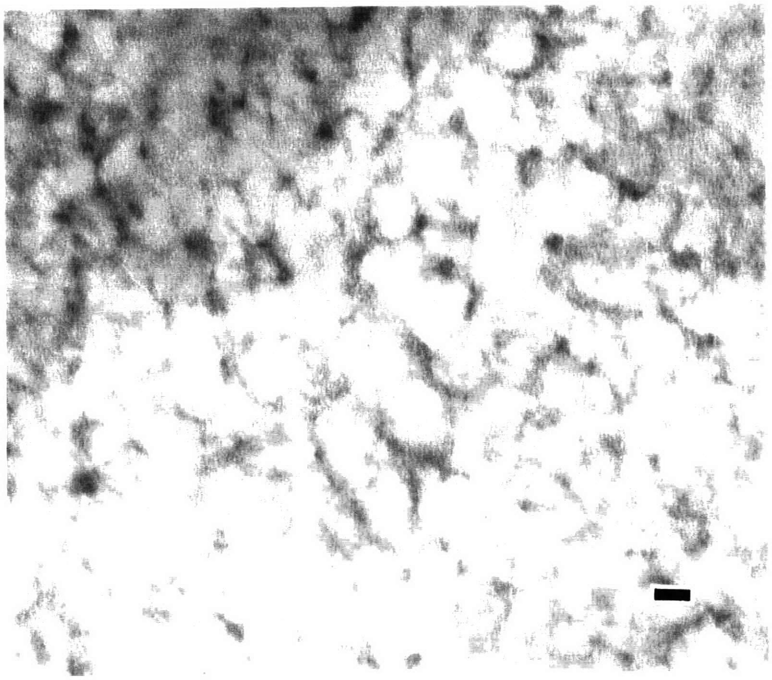

Figure 7.7: Electron micrograph of $Co_2(CO)_8$ loaded $[MTD]_{400}[NORCOOH]_{50}$ film (bar = 200 Å)

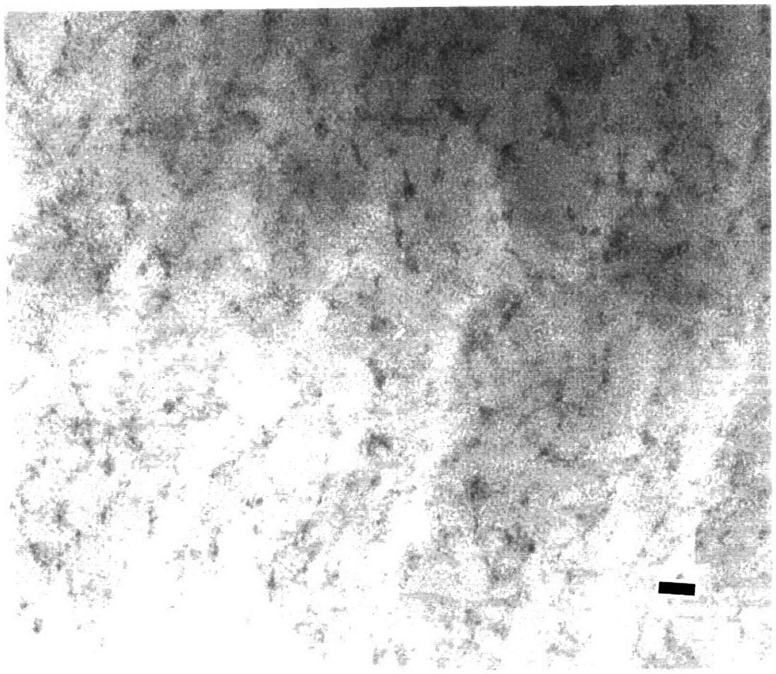

Figure 7.8: Electron micrograph of $Co_2(CO)_8$ loaded $[MTD]_{400}[NORCOOH]_{50}$ film after heating under vacuum (bar = 200 Å)

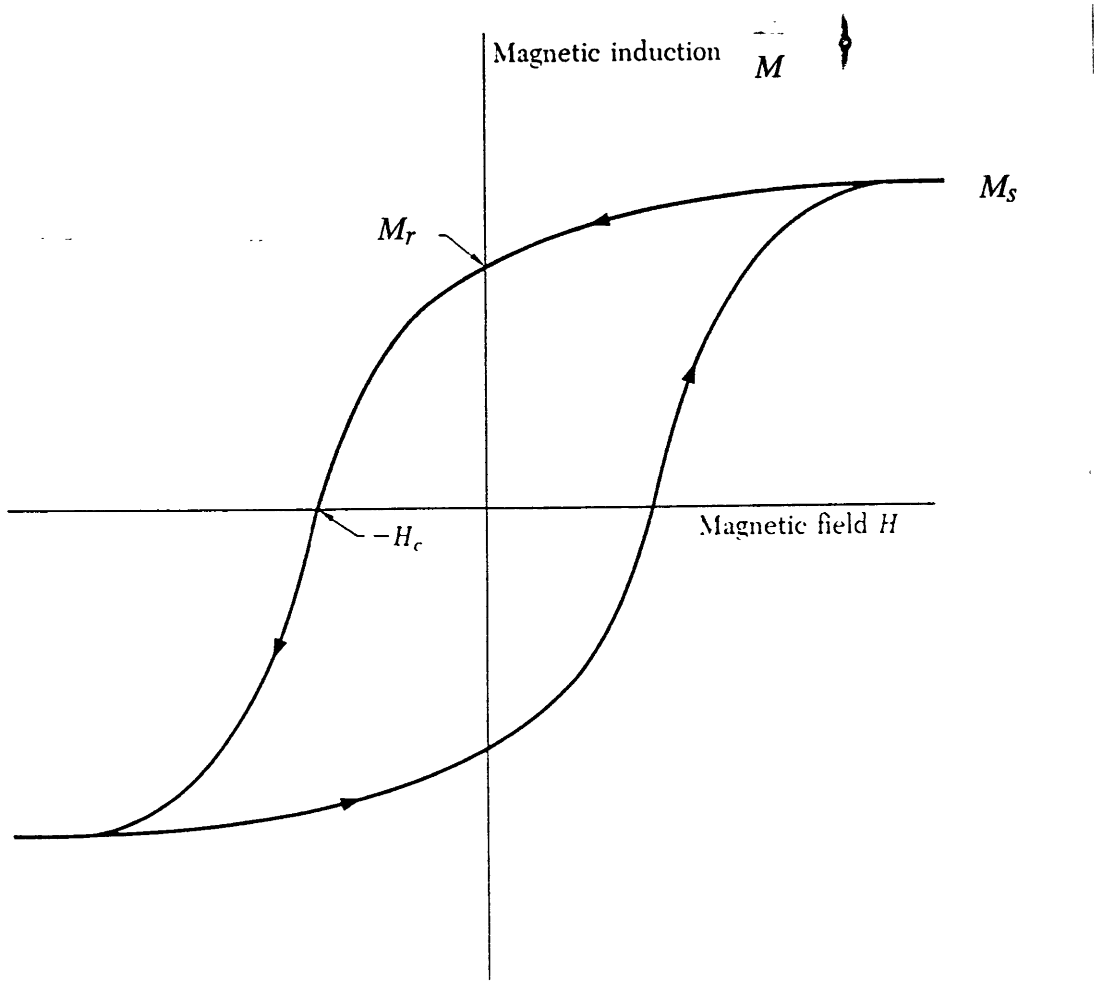

Figure 7.9: Typical M vs. H hysteresis loop for a bulk ferromagnetic or ferrimagnetic material: M_s = saturation magnetization, M_r = remanent magnetization, and H_c = coercivity

Kittel, C. 'Introduction to Solid State Physics' 6th Edn, John Wiley & Sons, Inc., New York, 1986, p. 450.

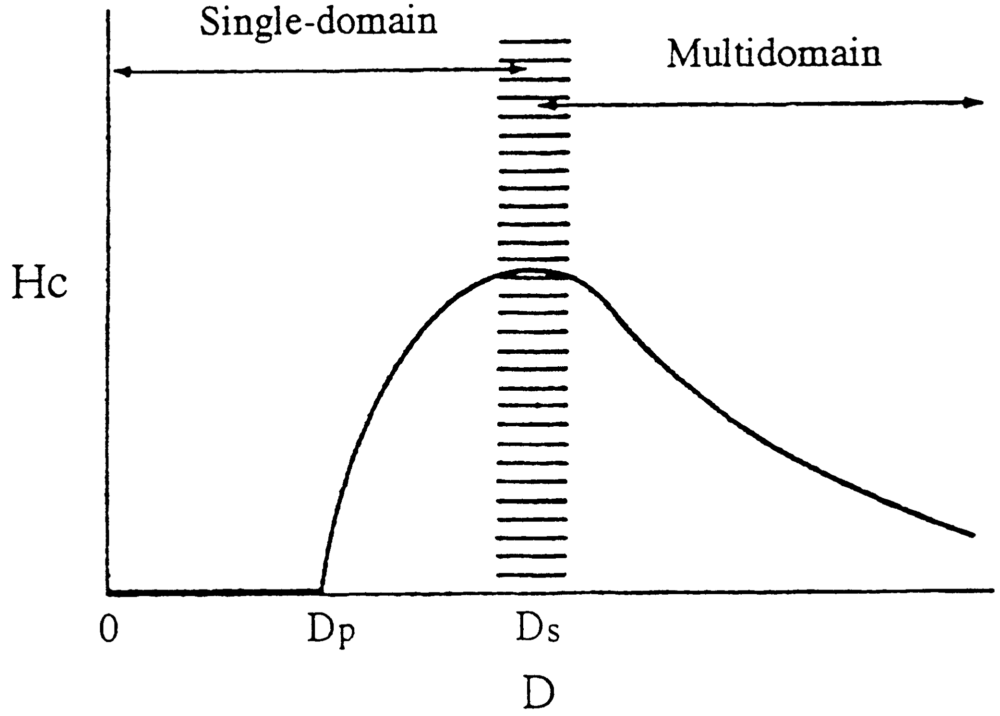

Figure 7.10: Variation of coercivity with particle diameter

Sohn, Byeonghyeok Ph.D. Thesis (Chem. E.), Massachusetts Institute of Technology, **1996**.

certain crystallographic axes called directions of easy magnetization.[11,12,13] Below D_s, the coercivity decreases with the particle size due to thermal effects. By equating the energy of a single-domain cobalt crystal with its energy when divided into several domains, it can be shown (both theoretically and experimentally) that particles less than ca. 100 Å in diameter will exist as single domains.[11,14] Below a second critical diameter, D_p, the coercivity is zero because thermal energy is sufficiently strong to spontaneously demagnetize previously saturated particles. Particles with diameters less than D_p are called superparamagnetic.

In superparamagnetic materials, the magnetic moments consist of isolated clusters (of aligned atomic magnetic dipoles) which are so small that thermal energy is sufficient to reverse the domain rotation induced by an applied magnetic field (after the field has been turned off).[11] As with paramagnetic dipoles, each cluster dipole is independent of the others, but much larger in magnitude than an atomic paramagnetic dipole. Superparamagnetic materials do not exhibit hysteresis above the blocking temperature. However, below the blocking temperature, thermal energy is no longer sufficient to reverse domain rotations caused by magnetic fields. The superparamagnetic particles become magnetically frozen, and hysteresis (remanence and coercivity) results. McHenry et al., using a SQUID magnetometer, demonstrated the blocking temperature of 50 Å f.c.c. cobalt particles to be 160 K.[15]

The energy, ΔE, required for domain rotation is given by equation (7-8):[11]

$$\Delta E = KV \tag{7-8}$$

where K is the anisotropy constant (erg/cm^3) and V is the volume of each particle. The time constant for thermal demagnetization, τ, is related to V and T by equation (7-9):[11]

$$1/\tau = f_0 e^{-KV/kT} \tag{7-9}$$

where f_0 is called the frequency factor and has a value of about 10^9 s^{-1}. It is possible to define an upper limit on the particle volume, V_p, below which superparamagnetic behavior will occur by letting $\tau = 100$ s, the approximate time required to measure the remenance of a specimen with a SQUID magnetometer. Figure 7.11 shows the results of theoretical calculations which indicate that the blocking temperature of 76 Å diameter spherical cobalt particles is 293 K.

Figure 7.12 is a M vs. H plot, at 300 K, from a heated sample after 20 days in air. It was obtained using a superconducting quantum interference device (SQUID) magnetometer, and shows a small hysteresis loop with a remanent magnetization of 0.05 emu/g and a coercivity of 250 Oe. Since Figure 7.8 does not show the presence of particles greater than 100 Å in diameter, the room temperature hysteresis is due primarily to domain rotation of particles with diameters less than D_s (ca. 100 Å) and greater than D_p (ca. 76 Å). However, we cannot rule out contributions from domain boundary movements in occasional larger multidomain particles, which may not appear in the small area of film shown in Figure 7.8.

Figure 7.13 is a M vs. H plot, at 10 K (zero field-cooled), for the same sample. It shows a larger hysteresis loop with a remanent magnetization of 0.1 emu/g and a coercivity of 450 Oe. The increase in magnetization is due to contributions from smaller cobalt particles with blocking temperatures between 10 K and 300 K. The increase in coercivity is due to additional hinderence to domain rotation caused by the lower temperature.

Although no electron or X-ray diffraction from crystalline cobalt was detected, a small amount of h.c.p. cobalt (stable < 450 °C) is almost certainly responsible for the observed magnetic hysteresis. Amorphous ferromagnetic materials are known to exhibit very large saturation magnetizations; however, they usually have coercivities of less than 1 Oe.[12] Coercivities of several hundred Oe, as observed in our samples, are most frequently a result of crystal anisotropy.

Given cobalt's saturation magnetization of 162.5 emu/g (0 K)[11] and our sample's average cobalt content of 6.4 wt. %, we would expect to observe an overall film saturation magnetization of 10.4 emu/g if all the cobalt were present as metallic cobalt. Since the film

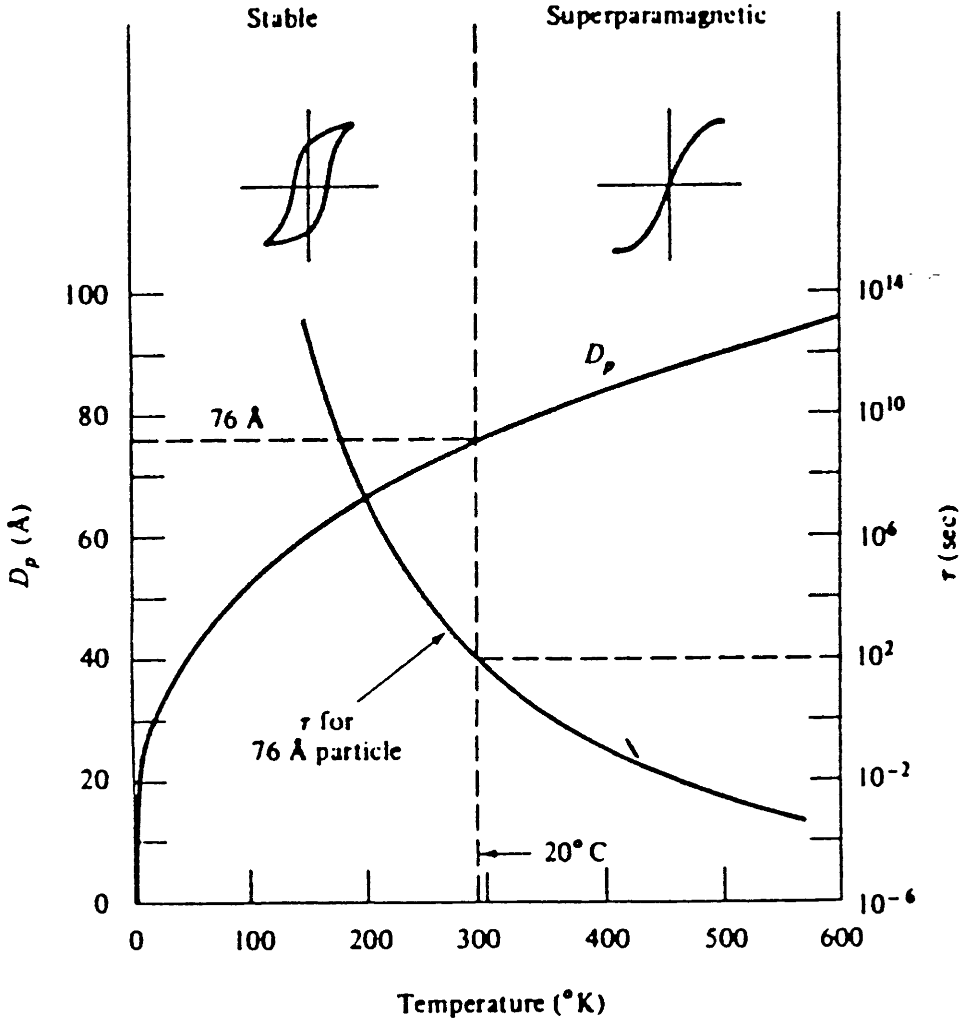

Figure 7.11: Temperature dependence of the critical diameter, D_p, for spherical cobalt particles

Cullity, B.D. 'Introduction to Magnetic Materials' Addison-Wesley Publishing Company, London, 1972, p. 415.

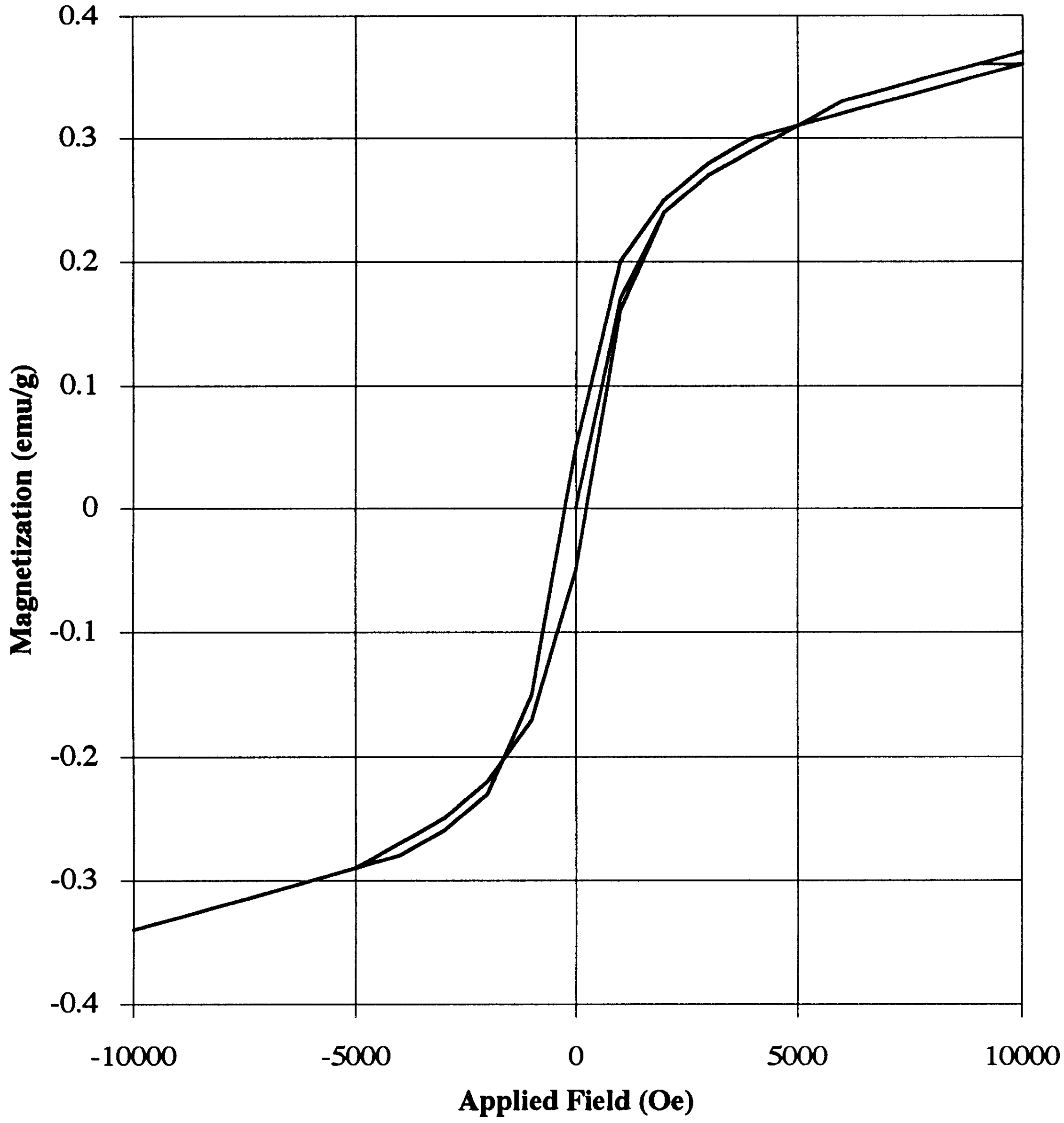

Figure 7.12: M vs. H plot for $Co_2(CO)_8$ loaded $[MTD]_{400}[NORCOOH]_{50}$ film after heating and 20 days in air (300 K)

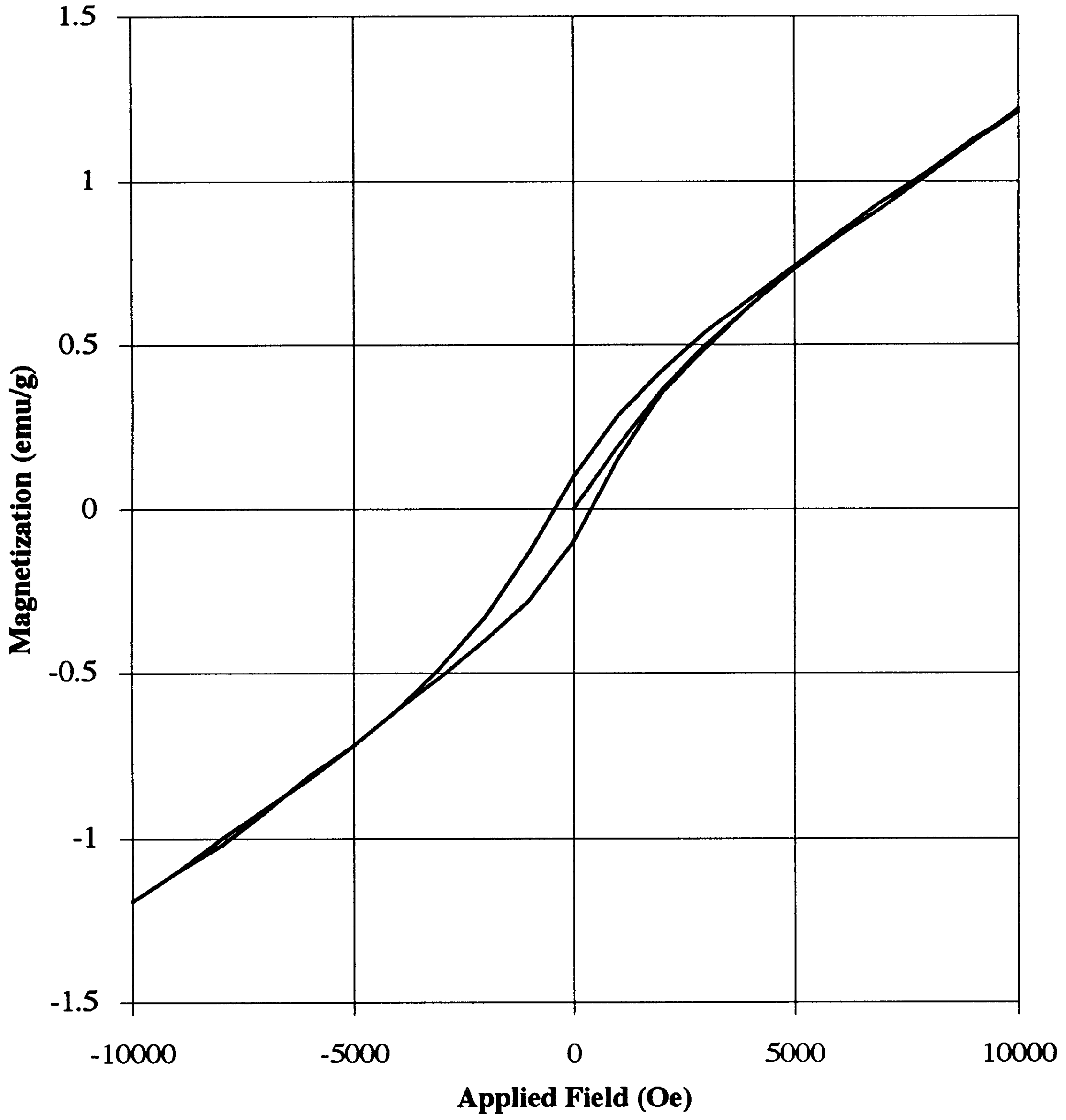

Figure 7.13: M vs. H plot for $Co_2(CO)_8$ loaded $[MTD]_{400}[NORCOOH]_{50}$ film after heating and 20 days in air (10 K)

magnetization of 1.2 emu/g is not yet saturated at 10,000 Oe (the highest field applied), it is difficult to estimate the fraction of cobalt present in metallic form. However, the observed color change after several hours storage in air suggests a significant fraction of the cobalt may be present in the form of cobalt oxides.

Figures 7.14 and 7.15, respectively, are plots of M vs. H at 300 K. Figure 7.14 corresponds to a heated film after 30 days in air, and Figure 7.15 corresponds to an unheated film after 90 days in air. Both Figures show nearly identical linear dependence of M on H, with an overall film magnetic susceptibility of 7.5×10^{-6} emu/(g Oe). Comparison of Figures 7.12 and 7.14 demonstrates that a loss of hysteresis and a reduction in magnetic susceptibility occurs upon prolonged storage of the heated film in air (20-30 days). We believe the small amount of crystalline cobalt originally present in the film slowly oxidizes to cobalt oxides during 30 days of storage in air. Assuming all cobalt in the film oxidizes to CoO, we calculate an overall CoO content of 8.1 wt. %. A CoO magnetic susceptibility of 9×10^{-5} emu/(g Oe) was then determined from the film magnetic susceptibility and weight fraction of CoO. This value is of the correct order of magnitude for the paramagnetic behavior expected from antiferromagnetic CoO above its Neel temperature (291 K).[12]

Dicobalt octacarbonyl is known to be air sensitive and unstable at room temperature. The similarity in the visible absorption spectrums (Figures 7.6a and 7.6b) seems to indicate that cobalt in both the heated and unheated, $Co_2(CO)_8$ loaded films, is oxidized to the same cobalt oxides in air.

7.4. Conclusions

We believe Co^{+2} and Ni^{+2} ions within 10 μm $[MTD]_{400}[NORCOOH]_{50}$ films are reduced primarily to amorphous cobalt and nickel borides according to equation (7-3), as a result of soaking in aqueous $NaBH_4$ solutions (in air). Futhermore, it is likely that the nanoclusters shown in Figure 3.9 (Ni^{+2} loaded film following aqueous $NaBH_4$ reduction) are composed of nickel boride rather than metallic nickel. Although h.c.p. cobalt was initially

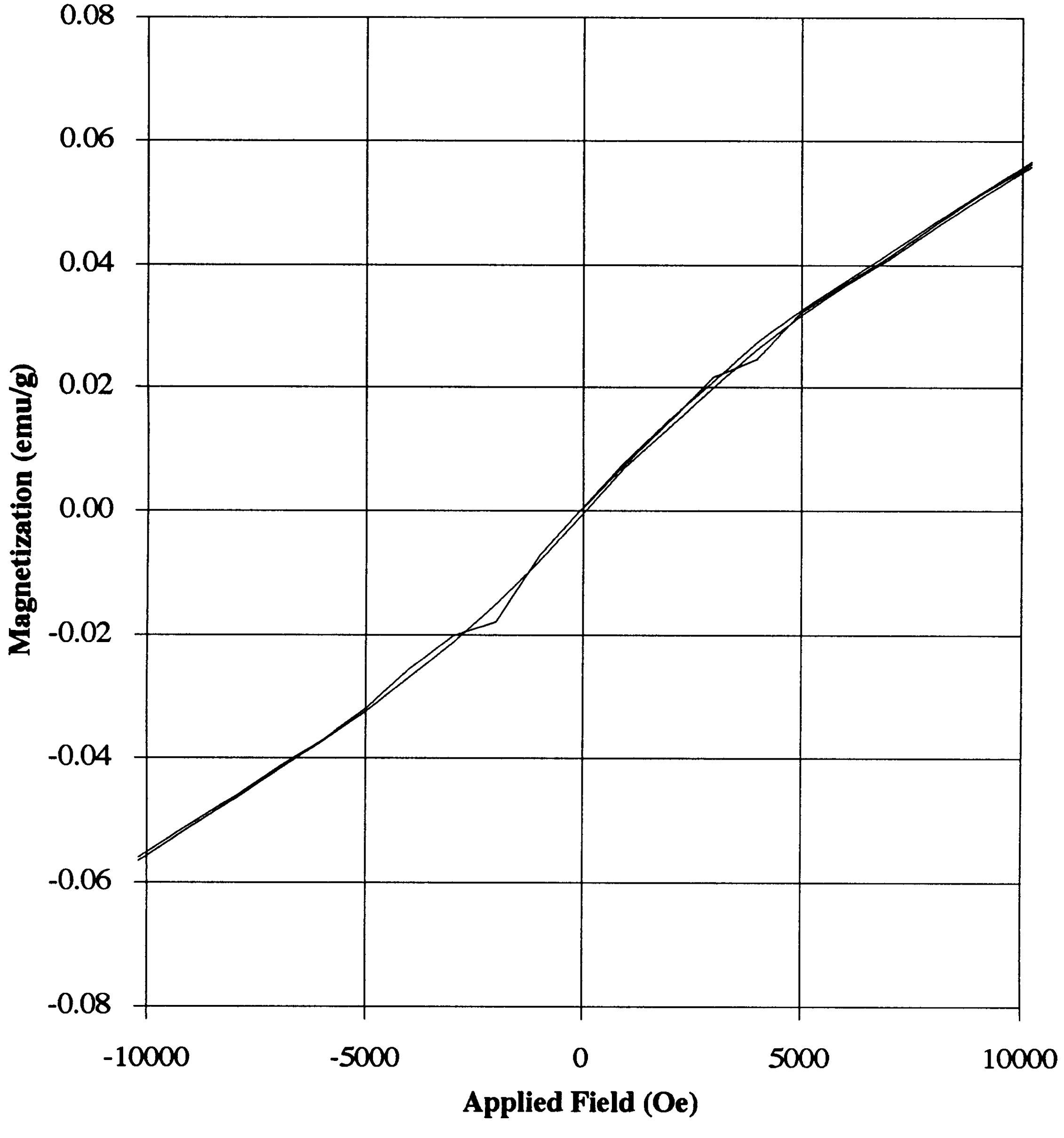

Figure 7.14: M vs. H plot for $Co_2(CO)_8$ loaded $[MTD]_{400}[NORCOOH]_{50}$ film after heating and 30 days in air (300 K)

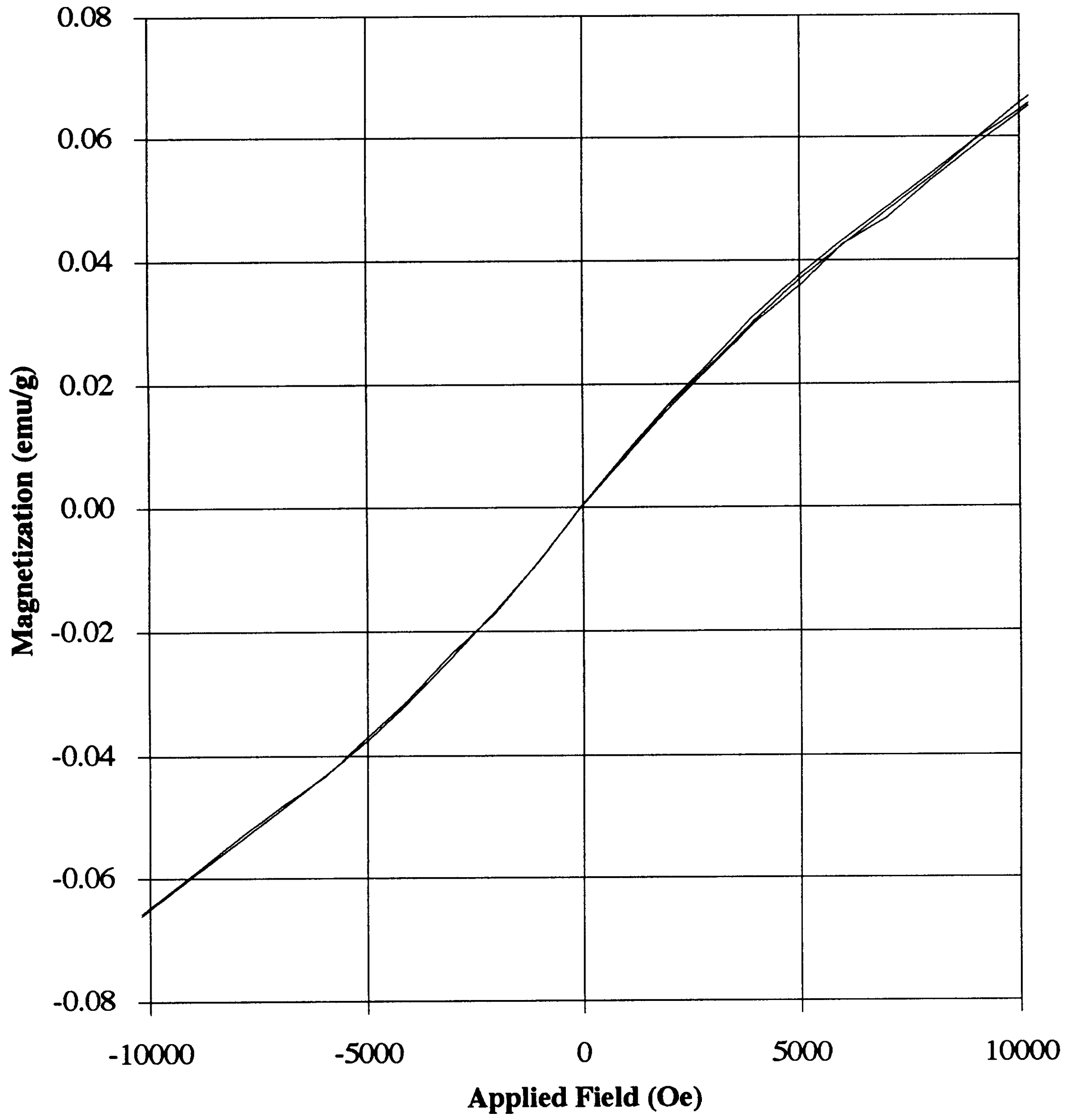

Figure 7.15: M vs. H plot for unheated $Co_2(CO)_8$ loaded $[MTD]_{400}[NORCOOH]_{50}$ film after 90 days in air (300 K)

detected (by WAXS) within the Co^{+2} loaded film (after reduction), the h.c.p. cobalt oxidized after 18 hr in air.

The Co^{+2} and Ni^{+2} ions within $[MTD]_{400}[NORCOOH]_{50}$ films also appear to be reduced by soaking the films in diglyme/$NaBH_4$ or THF/$NaBH_4$ solutions. The Co^{+2} reduction products are primarily amorphous; however, crystalline NiB was detected by electron diffraction within the Ni^{+2} loaded film. The product distribution between metals and metal borides is not known.

Thermal decomposition (90 °C) of $Co_2(CO)_8$ within $[MTD]_{400}[NORCOOH]_{50}$, under vacuum, results in the formation of transparent, air sensitive, ferromagnetic films. The thermal decomposition products include a small amount of h.c.p. cobalt, and possibly amorphous cobalt. Similar color changes within both heated and unheated films indicate that both cobalt and $Co_2(CO)_8$ begin to oxidize within hours upon storage in air. Heated films (after 20 days in air) exhibit a M vs. H hysteresis, due primarily to rotations of single domain, ferromagnetic cobalt crystals with diameters less than D_s (ca. 100 Å) and greater than D_p (ca. 76 Å). In addition, amorphous cobalt and cobalt oxides are likely to be present. M vs. H data for heated films after 30 days in air, are consistent with the complete oxidation of cobalt to CoO.

7.5. References for Chapter 7

(1) Gaylord, N.G. 'Reduction With Complex Metal Hydrides' Interscience Publishers, Inc., New York, 1956, p. 18.

(2) Glavee, G.N., Klabunde, K.J., Sorensen, C.M., and Hadjipanayis, G.C. *Langmuir* **1994**, 10, 4726.

(3) Awadalla, F.T. and Ritcey, G.M. *Separation Sci. and Tech.* **1991**, 26, 1207.

(4) Glavee, G.N., Klabunde, K.J., Sorensen, C.M., and Hadjipanayis, G.C. *Langmuir* **1992**, 8, 771.

(5) 'Handbook of Chemistry and Physics' (Ed. R. Weast), CRC Press, Boca Raton, FL, 1987, p. B-86.

(6) Pruchnik, F.P. 'Organometallic Chemistry of the Transition Elements' Plenum Press, New York, 1990, p. 85.

(7) Krinkin, D.P. and Rudkovskii, D.M. *Zh. Prikl. Khim.* **1965**, 38, 1670.

(8) 'Metals & Alloys Data Book' Vol. I, (Ed. Sigmund Weissmann), JCPDS International Centre for Diffraction Data, 1978, p. 119.

(9) Glavee, G.N., Klabunde, K.J., Sorensen, C.M., and Hadjipanayis, G.C. *Inorg. Chem.* **1993**, 32, 474.

(10) JCPDS International Centre for Diffraction Data, Electronic Data Base.

(11) Cullity, B.D. 'Introduction to Magnetic Materials' Addison-Wesley Publishing Company, London, 1972.

(12) Kittel, C. 'Introduction to Solid State Physics' 6th Edn, John Wiley & Sons, Inc., New York, 1986.

(13) Luborsky, F.E. *J. Appl. Phys.* **1961**, 32, 171S.

(14) Kittel, C. and Galt, J.K. *Solid State Physics* **1956**, 3, 437.

(15) McHenry, M.E., Majetich, S.A., Artman, J.O., DeGraef, M. and Staley, S.W. *Physical Review B* **1994**, 49, 11358.

Chapter 8

Synthesis of Palladium Nanoclusters within Microphase-Separated Diblock Copolymers: Alternative Methods

8.1. Summary

In Chapter 3, we reported a general methodology for the synthesis of transition metal nanoclusters (Ag, Au, Cu, Ni, Pb, Pd, and Pt) stabilized within microphase-separated diblock copolymers. In our strategy, outlined in Figure 1.9, metal ions or complexes are coordinated to carboxylic acid groups within the water soluble polyNORCOOH domains of a $[MTD]_{400}[NORCOOH]_{50}$ block copolymer (MTD = methyltetracyclododecene and NORCOOH = 2-norbornene-5,6,-dicarboxylic acid) by immersion of the polymer in aqueous metal salt solutions. The metal ions and complexes are subsequently reduced by heating the metal loaded polymer under hydrogen or by immersion in an aqueous sodium borohydride solution. For several transition metals, the resulting nanoclusters are uniformly sized and homogeneously dispersed within the polyNORCOOH domains.

Now, we describe similar attempts to synthesize Pd nanoclusters within a $[MTD]_{400}[NORCOH]_{50}$ block copolymer (NORCOH = 2-norbornene-5-methanol). We also describe attempts to load Pd into $[MTD]_{400}[NORCOOH]_{50}$ films from $Na_2PdCl_4x3H_2O$ solutions in THF.

8.2. Experimental

$[MTD]_{400}[NORCOH]_{50}$ and $[MTD]_{400}[NORCOOH]_{50}$ diblock copolymers were synthesized as previously reported, using a ring-opening metathesis polymerization in anhydrous toluene with a $Mo(CHCMe_2Ph)(NAr)(O\text{-}t\text{-}Bu)_2$ ($Ar = 2,6\text{-}C_6H_3\text{-}i\text{-}Pr_2$) initiator.

10 µm and 0.5 mm thick $[MTD]_{400}[NORCOH]_{50}$ films were static cast from 0.5 and 3 wt. % solutions in tetrahydrofuran (THF) respectively. 0.5 mm thick $[MTD]_{400}[NORCOOH]_{50}$ films were static cast from a 3 wt. % solution in THF. TEM

observation of microtomed, Pd loaded, $[MTD]_{400}[NORCOH]_{50}$ films did not reveal a distinct microphase-separated morphology. TEM observation of microtomed, Ag^+ loaded, $[MTD]_{400}[NORCOOH]_{50}$ films revealed a non-equilibrium interconnected cylindrical morphology (cylinder diameters ca. 80 Å).

8.2.1. Synthesis of Palladium Nanoclusters within $[MTD]_{400}[NORCOH]_{50}$

Microtomed (400 Å thick) sections of $[MTD]_{400}[NORCOH]_{50}$ film were placed on 400 mesh gold TEM grids. The grids were floated (polymer-side-down), each on separate 0.005 M aqueous solutions (3-4 drops) of $Ag(OOCCH_3)$, $Na_2PdCl_4x3H_2O$, and $PbCl_2$, at 25 °C, for 30 hr. Both $Ag(OOCCH_3)$ and $Na_2PdCl_4x3H_2O$ soaking were done in the dark. Several different metal salts were used to determine which, if any, were able to load into $[MTD]_{400}[NORCOH]_{50}$. After soaking, the microtomed sections were rinsed in de-ionized water and dried under vacuum at 25 °C for 15 hr. The Pd loaded film was reduced under 2 atm of hydrogen, at 115 ° C, for 6 days.

Metal loading experiments were carried out at 25°C using a batch equilibration method in which 100 mg samples of 10 μm thick polymer films were submerged in 20 g of 0.005 M aqueous metal salt solutions ($Ag(OOCCH_3)$, $AuCl_3$, $Cu(OOCCH_3)_2$, $CuCl_2$, $H_2PtCl_6x6H_2O$, $Na_2PdCl_4x3H_2O$, $NiCl_2$, and $PbCl_2$). Agitation was maintained with magnetic stir bars. The metal ion concentration remaining in the supernatant solution was measured periodically by withdrawing small aliquots of supernatant solution. The withdrawn aliquots were diluted with water to metal ion concentrations of < 30 ppm and analyzed using ICP-AES. The extent of metal ion uptake was calculated using equation (4-1). Loading with $Ag(OOCCH_3)$ and $H_2PtCl_6x6H_2O$ was done in the dark.

8.2.2. Palladium Uptake from Tetrahydrofuran Solutions

A 0.5 mm thick $[MTD]_{400}[NORCOOH]_{50}$ film (10 mg) was soaked in 5 ml (4 ml de-ionized water and 1 ml THF) of a 0.1 M $Na_2PdCl_4x3H_2O$ solution for two weeks at room temperature. After soaking, the film was rinsed in de-ionized water and dried under vacuum at 25 °C for 15 hr. The Pd loaded film was reduced under 2 atm of hydrogen, at 115 ° C, for 6 days. Four hundred angstrom thick slices of polymer were cut from the bulk film and examined with TEM, both prior to and after reduction.

According to Table 8.1, Pd was also loaded into solution phase $[MTD]_{400}[NORCOOH]_{50}$ by adding the appropriate mass of 0.125 M aqueous $Na_2PdCl_4x3H_2O$ solution to 2 g of a 2 wt. % $[MTD]_{400}[NORCOOH]_{50}$ solution in THF. All four solutions where stirred for 15 hr at 25 °C. Precipitates were observed immediately after mixing the polymer and $Na_2PdCl_4x3H_2O$ solutions in all four cases; however, the precipitates appeared to re-dissolve after further stirring.

Table 8.1 Mass of 0.125 M $Na_2PdCl_4x3H_2O$ solution added to 2 g of 2 wt. % polymer solution

Moles $Na_2PdCl_4x3H_2O$/Mole COOH	Mass $Na_2PdCl_4x3H_2O$ solution, g
0.05	0.02
0.25	0.10
0.50	0.20
1.00	0.40

After stirring, the solutions were allowed to settle for 15 hr at 25 °C. The solutions were then pipetted away from a dark precipitate, and the palladium loaded polymer was recovered by precipitation in de-ionized water. The appearance of the solution above the dark PPT ranged from yellow and transparent (0.05 moles $Na_2PdCl_4x3H_2O$/mole COOH) to cloudy and brown (1.0 mole $Na_2PdCl_4x3H_2O$/mole COOH). The recovered polymer samples were dried under vacuum for 15 hr at 25 °C, and then stirred for 15 hr at 25 °C in 2 g of THF (each). The polymer recovered from the 0.05, 0.25, and 0.5 moles $Na_2PdCl_4x3H_2O$/mole COOH solutions appeared to dissolve completely; however, the polymer recovered from the 1.0 mole

$Na_2PdCl_4x3H_2O$/mole COOH solution was still present as swollen lumps after 15 hr of stirring. Stirring was then stopped, and the THF was allowed to evaporate over 3 days.

All four Pd loaded polymer samples were reduced under 2 atm of hydrogen, at 115 °C, for 6 days. Four hundred angstrom thick slices of polymer were cut from the bulk films and examined with TEM, both prior to and after reduction.

8.3. Results and Discussion

GPC analysis of the homo-MTD blocks yielded polydispersities of approximately 1.1. The block copolymer was not analyzed using GPC because polyNORCOOTMS precipitates as polyNORCOOH in wet toluene. The static cast block copolymer films were flexible and transparent with a slight yellowish tint, probably due to trace residues of $Mo(CHCMe_2Ph)(NAr)(O\text{-}t\text{-}Bu)_2$.

8.3.1. Synthesis of Palladium Nanoclusters within $[MTD]_{400}[NORCOH]_{50}$

TEM observation of the 400 Å thick $[MTD]_{400}[NORCOH]_{50}$ films revealed no staining after floating on the 0.005 M aqueous $Ag(OOCCH_3)$ or $PbCl_2$ solutions. However, occasional sub-micron sized Ag particles were observed in the $Ag(OOCCH_3)$ soaked film. As shown in Figure 8.1, faceted ca. 100 Å Pd nanoclusters appeared scattered in a $Na_2PdCl_4x3H_2O$ soaked film. Figure 8.2 is an electron micrograph of a $Na_2PdCl_4x3H_2O$ soaked film after hydrogen reduction. Although the quality of Figure 8.2 is superior to that of Figure 8.1, both micrographs show the same faceted ca. 100 Å Pd nanoclusters scattered throughout the film. Electron diffraction patterns collected from the reduced film contain rings consistent with scattering from f.c.c. Pd crystals. No clear microphase-separated morphology is present in the micrographs.

The fact that significant Pd reduction occurs prior to hydrogen treatment within $[MTD]_{400}[NORCOH]_{50}$, but not $[MTD]_{400}[NORCOOH]_{50}$ (See Chapter 3), implies that the alcohol groups act as reducing agents for metal ions with high electrochemical reduction

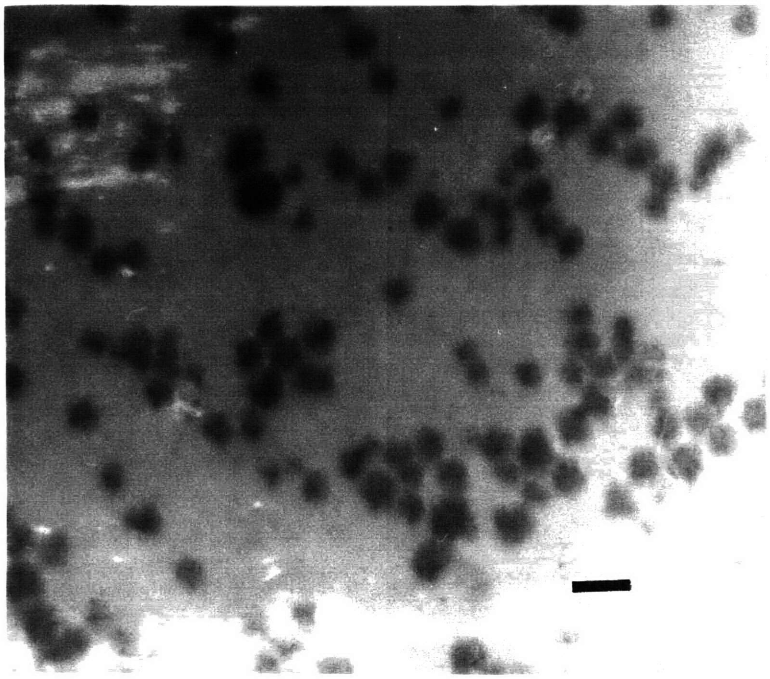

Figure 8.1: Electron micrograph of $[MTD]_{400}[NORCOH]_{50}$ film after floating on 0.005 M aqueous $Na_2PdCl_4x3H_2O$ (bar = 300 Å)

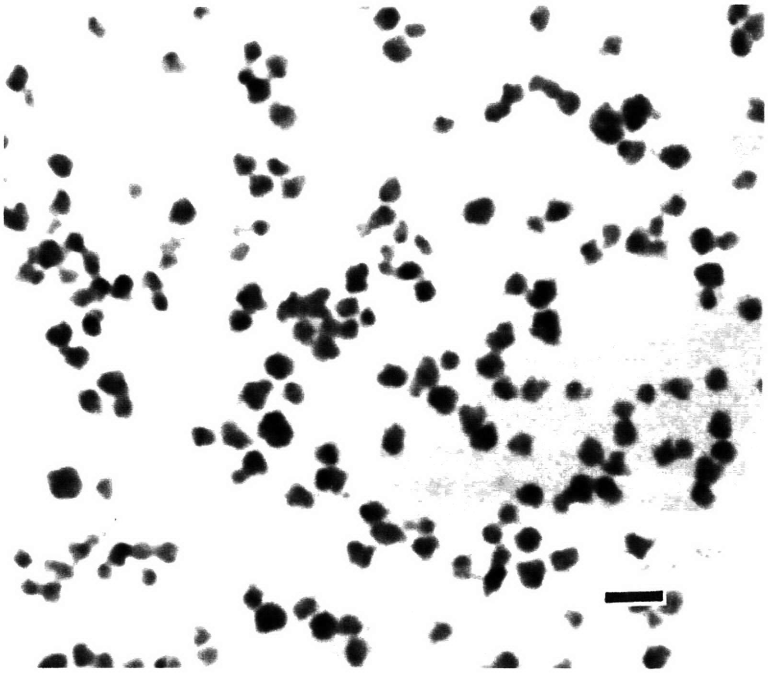

Figure 8.2: Electron micrograph of $[MTD]_{400}[NORCOH]_{50}$ film after floating on 0.005 M aqueous $Na_2PdCl_4x3H_2O$ and reduction under hydrogen (bar = 300 Å)

potentials. The use of both methanol[1,2] and ethanol[3], for the reduction of metal ions, has been documented in the literature. Toshima et al.[2] found that $RhCl_3$ could be reduced to Rh by refluxing in a water/methanol mixed solvent, with the formation of 1.5 moles of formaldehyde (HCHO) per mole of $RhCl_3$ charged. It is possible that a reaction occurs between the palladium ions and the $[MTD]_{400}[NORCOH]_{50}$ alcohol groups, in which the palladium ions are reduced and the alcohol groups are oxidized to aldehydes.

The ICP-AES experiments indicated that no metal ion uptake occurred into the 10 μm thick $[MTD]_{400}[NORCOH]_{50}$ films from any of the aqueous metal salt solutions studied. Since we observed Pd nanocluster formation in the 400 Å thick films, the lack of Pd uptake may be due to a non-interconnected polymer morphology. Alcohols can bind metal ions through ion exchange with the hydroxide proton,[4] or chelation with hydroxide oxygen atoms.[3] However, as evidenced by the lack of Ag^+ or Pb^{+2} uptake in the 400 Å thick films, no measurable loading would be expected for several metal ions, even in the case of an interconnected morphology.

8.3.2. Palladium Uptake from Tetrahydrofuran Solutions

After soaking in 5 ml (4 ml de-ionized water and 1 ml THF) of a 0.1 M $Na_2PdCl_4x3H_2O$ solution (two weeks, 25 °C), the 0.5 mm thick $[MTD]_{400}[NORCOOH]_{50}$ film appeared dark amber and transparent. Similar films soaked in pure aqueous $Na_2PdCl_4x3H_2O$ solutions appear pale yellow and transparent, prior to reduction. Figure 8.3 is an electron micrograph of the film. It shows 200-300 Å Pd particles which appear, in some cases, to consist of several smaller Pd nanoclusters. The Pd stained outline of the polymer's interconnected cylindrical morphology is also visible. Electron microscopy observation revealed little change in the appearance of the Pd particles, following 6 days of reduction (115 °C) under 2 atm of hydrogen.

Figures 8.4a and 8.4b, respectively, show WAXS data from the Pd containing film prior to and after reduction. Peaks consistent with scattering from f.c.c. Pd crystals are present

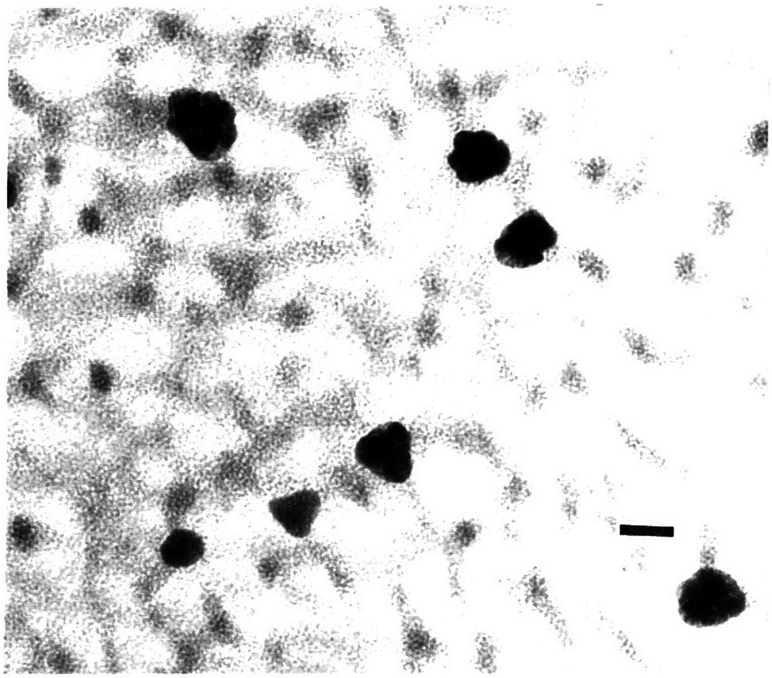

Figure 8.3: Electron micrograph of $[MTD]_{400}[NORCOOH]_{50}$ film after soaking in 0.1 M $Na_2PdCl_4x3H_2O$ (water/THF) solution (bar = 300 Å)

at 40.1° ([111]) and 46.7° ([200]).[5] A mean Pd crystal diameter of 78 Å was estimated by applying the Scherrer equation (3-1) and equation (3-2), to the Pd [111] peak in Figure 8.4a. The mean estimated Pd crystal diameter of 78 Å is consistent with the electron micrograph shown in Figure 8.3.

The verified presence of Pd clusters within the film, prior to reduction, leads us to conclude that THF can facilitate the reduction of metal ions with large positive electrochemical reduction potentials. No Pd clusters were observed, prior to reduction, in similar films soaked for two weeks at 25 °C in 0.1 M aqueous $Na_2PdCl_4x3H_2O$ solutions (See Chapter 3). The overall reaction, oxidation products of THF, and role of molecular oxygen are unknown. However, THF is known to undergo oxidation to both α-hydroxytetrahydrofuran and γ-butyrolacetone in solution with several metal oxide compounds.[6,7]

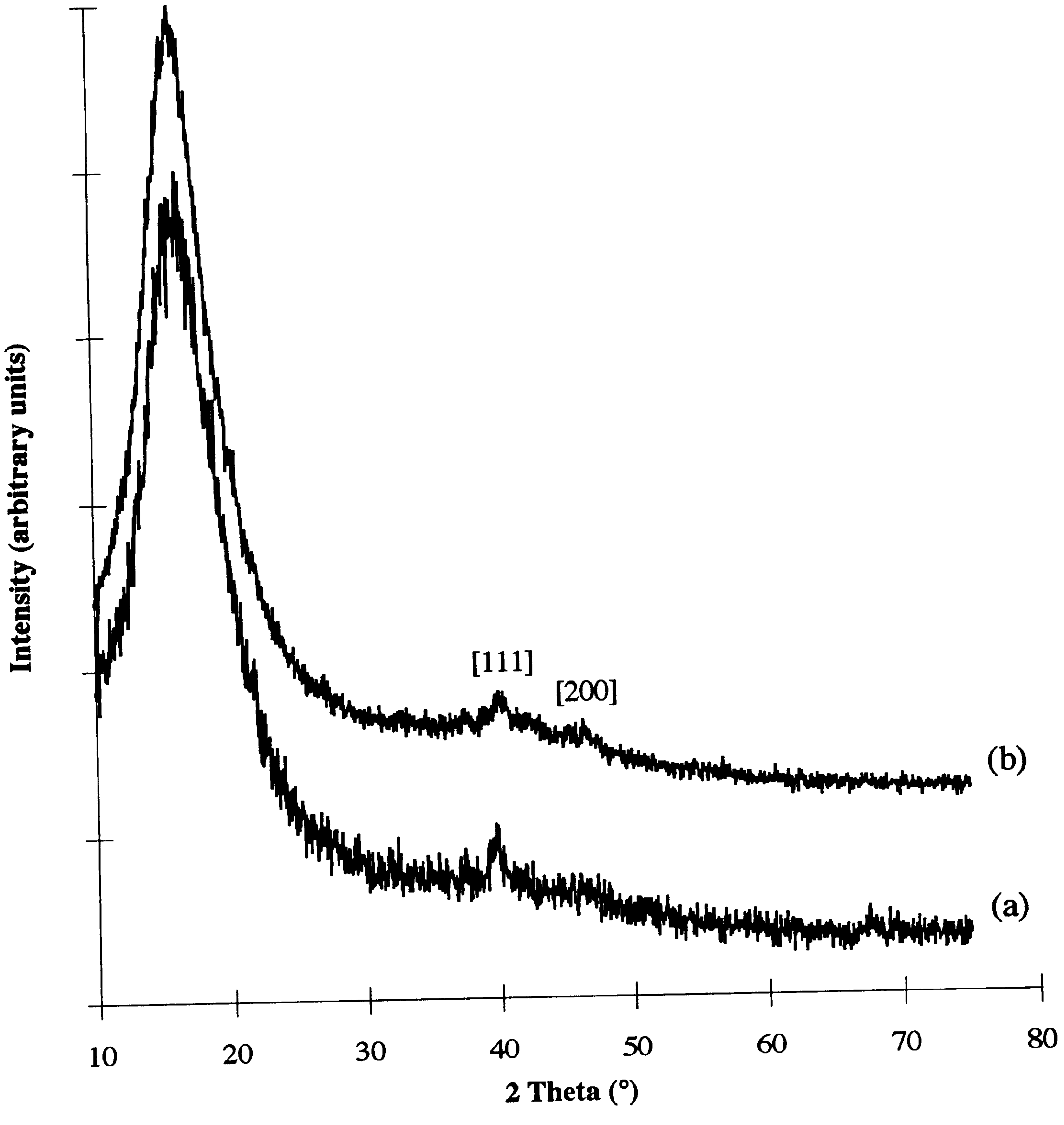

Figure 8.4: WAXS data from $[MTD]_{400}[NORCOOH]_{50}$ film after soaking in 0.1 M $Na_2PdCl_4x3H_2O$ (water/THF) solution: (a) prior to hydrogen reduction; (b) after hydrogen reduction

TEM observation showed the presence of 30-100 Å Pd nanoclusters, within the polyNORCOOH domains, after evaporation of THF from the 0.05 and 0.25 moles $Na_2PdCl_4x3H_2O$/mole COOH polymers. In addition, 200-400 Å Pd particles covered approximately 1 % of the 400 Å thick polymer slice observed with TEM. Following evaporation of THF from the 0.5 and 1.0 moles $Na_2PdCl_4x3H_2O$/mole COOH polymers, TEM observation showed very few domain confined 30-100 Å Pd clusters; but, a much higher concentration of 200-400 Å Pd particles (3-5 % coverage). TEM observation revealed little change in the Pd cluster size distributions following reduction (2 atm hydrogen, 115 °C, 6 days).

Figures 8.5 and 8.6, respectively, show electron micrographs of the 0.05 and 0.5 moles $Na_2PdCl_4x3H_2O$/mole COOH polymers after reduction. Several 30-100 Å domain confined Pd clusters are visible in Figure 8.5, while a large number of 200-400 Å Pd particles are present in Figure 8.6.

Figures 8.7 and 8.8, respectively, show WAXS data from the Pd loaded films before and after reduction. Figures 8.7a, 8.7b, and 8.7c correspond to the 0.05, 0.25 and 1.0 moles $Na_2PdCl_4x3H_2O$/mole COOH polymers, respectively. Figures 8.8a, 8.8b, 8.8c, and 8.8d, correspond to the 0.05, 0.25, 0.50, and 1.0 moles $Na_2PdCl_4x3H_2O$/mole COOH polymers, respectively. Peaks consistent with scattering from f.c.c. Pd crystals are present at 40.1° ([111]) and 46.7° ([200]),[5] in both Figures 8.7 and 8.8 for all loadings greater than 0.05 moles $Na_2PdCl_4x3H_2O$/mole COOH. Mean Pd crystal diameters of 100 Å were estimated by applying the Scherrer equation (3-1) and equation (3-2), to the Pd [111] peak in Figures 8.7c and 8.8d.

The mean estimated Pd crystal diameter of 100 Å for the 1.0 mole $Na_2PdCl_4x3H_2O$/mole COOH polymer seems to indicate that many of the 200-400 Å Pd particles are polycrystalline, since few smaller particles were observed with TEM. The observation of metallic Pd prior to reduction is consistent with the hypothesis that THF facilitates the reduction of metal ions with large positive electrochemical reduction potentials.

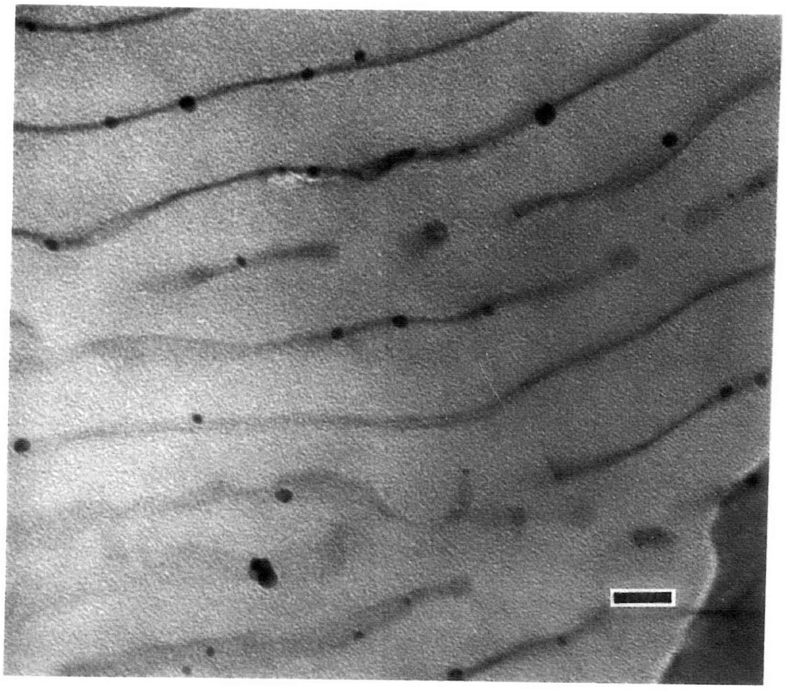

Figure 8.5: Electron micrograph of solution phase loaded $[MTD]_{400}[NORCOOH]_{50}$ (0.05 moles $Na_2PdCl_4x3H_2O$/mole COOH) after hydrogen reduction (bar = 300 Å)

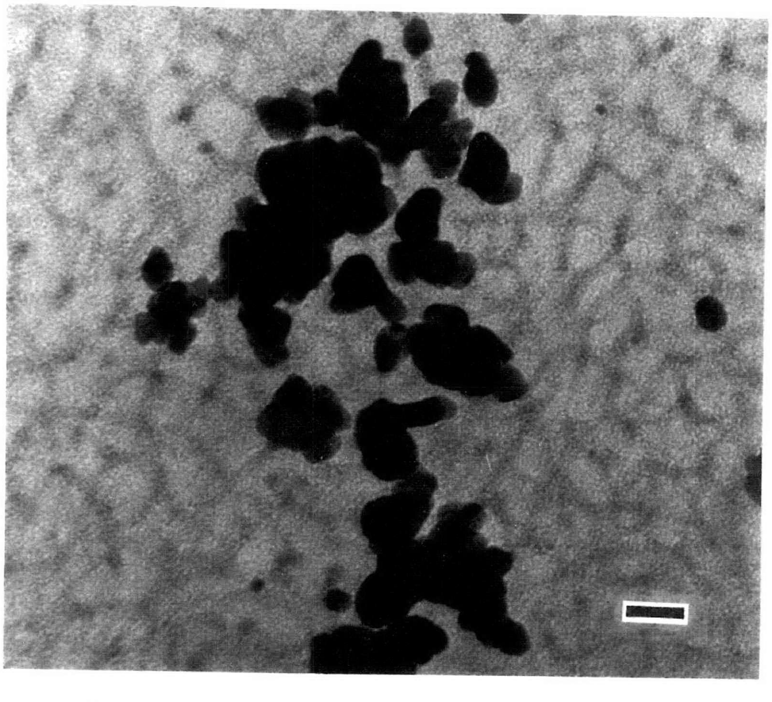

Figure 8.6: Electron micrograph of solution phase loaded $[MTD]_{400}[NORCOOH]_{50}$ (0.5 moles $Na_2PdCl_4x3H_2O$/mole COOH) after hydrogen reduction (bar = 300 Å)

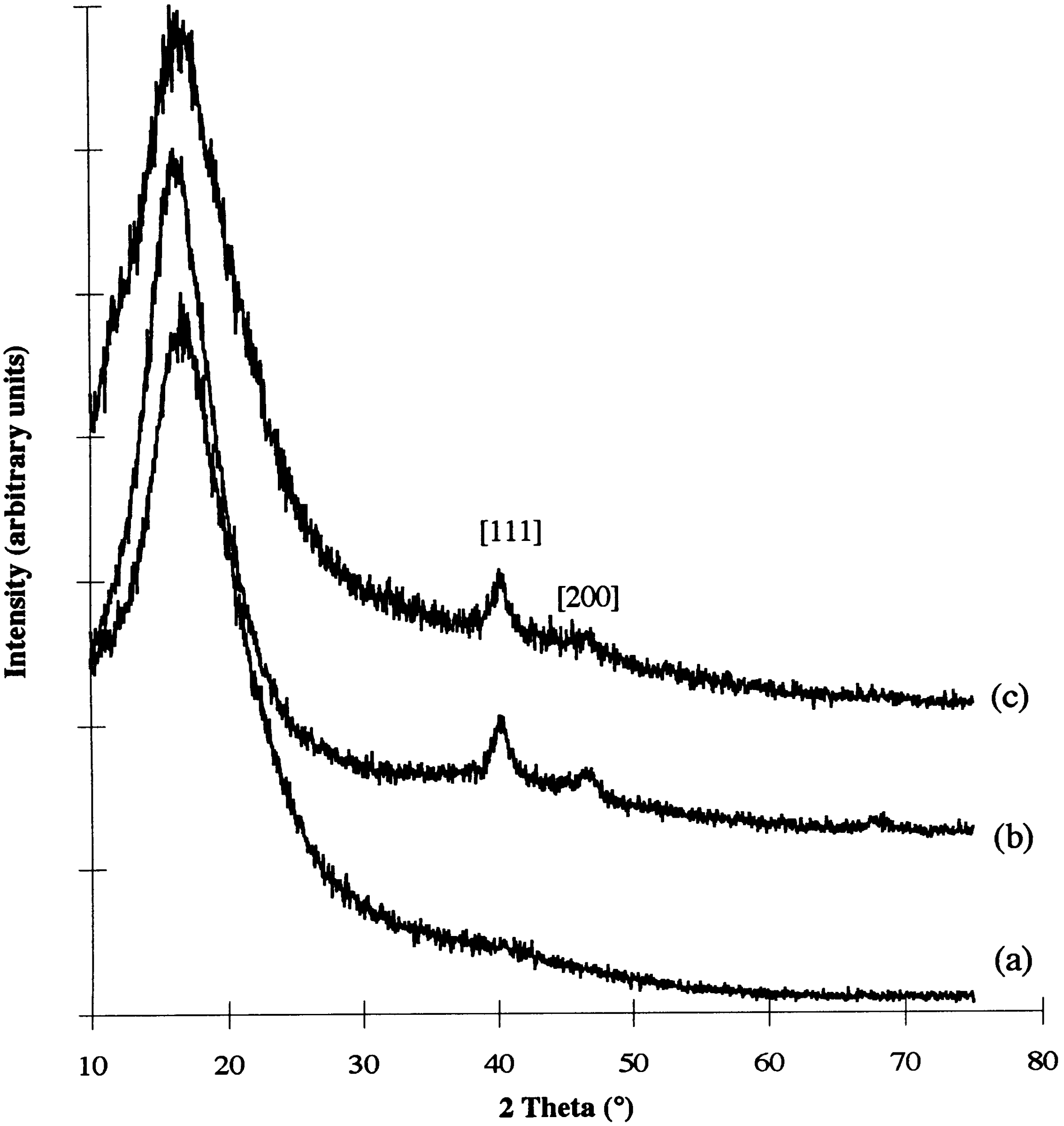

Figure 8.7: WAXS data from solution phase loaded $[MTD]_{400}[NORCOOH]_{50}$ prior to hydrogen reduction: (a) 0.05 moles $Na_2PdCl_4x3H_2O$/mole COOH; (b) 0.25 moles $Na_2PdCl_4x3H_2O$/mole COOH; (c) 1.0 moles $Na_2PdCl_4x3H_2O$/mole COOH

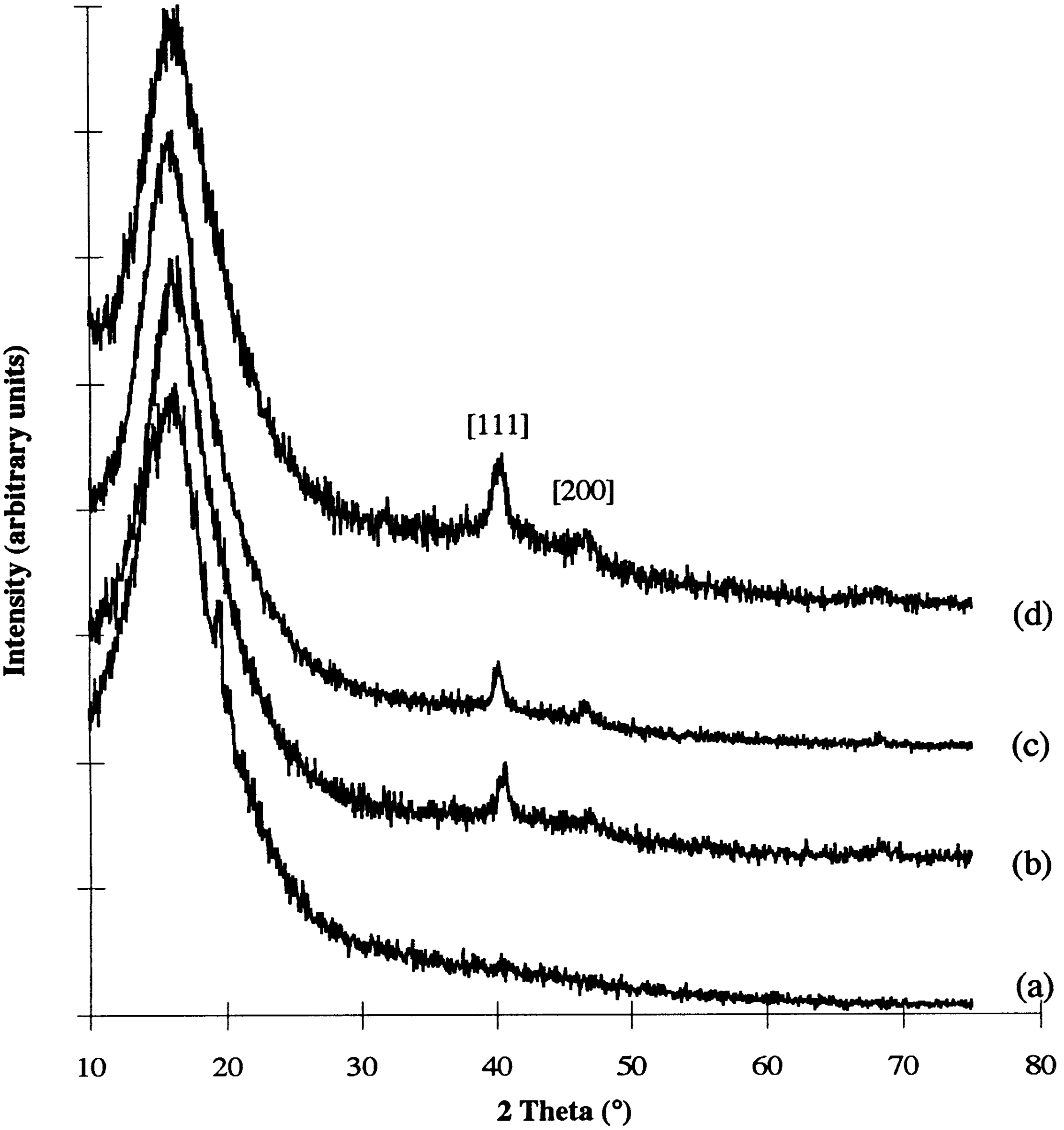

Figure 8.8: WAXS data from solution phase loaded $[MTD]_{400}[NORCOOH]_{50}$ after hydrogen reduction: (a) 0.05 moles $Na_2PdCl_4x3H_2O$/mole COOH; (b) 0.25 moles $Na_2PdCl_4x3H_2O$/mole COOH; (c) 0.50 moles $Na_2PdCl_4x3H_2O$/mole COOH; (d) 1.0 moles $Na_2PdCl_4x3H_2O$/mole COOH

8.4. Conclusions

Four hundred angstrom thick $[MTD]_{400}[NORCOH]_{50}$ films exhibited little Ag^+ ($Ag(OOCCH_3)$) or Pb^{+2} ($PbCl_2$) uptake from 0.005 M aqueous solutions. However, uniformly sized, homogeneously dispersed, Pd clusters (ca. 100 Å diameter) were observed, prior to hydrogen reduction, throughout the 400 Å thick films after floating on 0.005 M aqueous $Na_2PdCl_4x3H_2O$. Further cluster synthesis experiments with $[MTD]_x[NORCOH]_y$ are recommended, because $[MTD]_{400}[NORCOH]_{50}$ seems to offer the possibility of one-step loading and reduction, in the case of $Na_2PdCl_4x3H_2O$. Further ICP-AES experiments should be conducted to determine whether $Na_2PdCl_4x3H_2O$ loads into 10 μm thick films with verified interconnected morphologies. If so, such films should be examined with IR-spectroscopy to determine whether aldehyde groups (oxidation product of alcohols) appear following $Na_2PdCl_4x3H_2O$ loading.

Many 200-300 Å f.c.c. Pd particles were observed within a 0.5 mm thick $[MTD]_{400}[NORCOOH]_{50}$ film, prior to hydrogen reduction, after soaking in a 0.1 M $Na_2PdCl_4x3H_2O$ (4 ml de-ionized water/1 ml THF) solution. The presence of metallic Pd in the film, prior to hydrogen reduction, indicates that THF can facilitate the reduction of metal ions with large positive electrochemical reduction potentials. However, the overall reaction, oxidation products of THF, and role of oxygen are unknown.

Pd particles (30-100 Å and 200-400 Å) were also observed, prior to hydrogen reduction, within $[MTD]_{400}[NORCOOH]_{50}$ recovered from mixtures of 2 wt. % $[MTD]_{400}[NORCOOH]_{50}$ in THF and 0.125 M aqueous $Na_2PdCl_4x3H_2O$. Most clusters observed within the 0.05 and 0.25 moles $Na_2PdCl_4x3H_2O$/mole COOH polymers were from 30 to 100 Å in size and confined to the polyNORCOOH domains. Most clusters observed within the 0.50 and 1.0 moles $Na_2PdCl_4x3H_2O$/mole COOH polymers were from 200 to 400 Å in size and extended beyond the polyNORCOOH domains. The mean estimated Pd crystal diameter of 100 Å, for the 1.0 mole $Na_2PdCl_4x3H_2O$/mole COOH polymer, seems to indicate that many of the 200-400 Å Pd particles are polycrystalline, since few smaller particles were observed with TEM.

Storage under 2 atm of hydrogen for 6 days at 115 °C did not have a significant effect on the cluster size distribution in any of the cases studied.

Palladium loading of $[MTD]_{400}[NORCOOH]_{50}$ from $Na_2PdCl_4x3H_2O$, in the presence of THF, is a one-step method for the synthesis of polymer/palladium nanocluster composites. No additional reduction step is necessary because the THF acts as a reducing agent. Based on relative palladium WAXS peak heights in Figures 8.4, 8.7, and 3.18, this approach appears to allow higher palladium loadings than the procedure described in Chapter 3 (bulk film), which involves palladium loading from aqueous solutions followed by hydrogen reduction. Palladium loading in the presence of THF also leads to significantly larger clusters than the aqueous route described in Chapter 3: 0.1 M $Na_2PdCl_4x3H_2O$ (4 ml de-ionized water/1 ml THF) solution (200-300 Å particles), 0.05 and 0.25 moles $Na_2PdCl_4x3H_2O$/mole COOH in THF solution (30-100 Å nanoclusters), 0.1 M aqueous $Na_2PdCl_4x3H_2O$ followed by hydrogen reduction (10-20 Å nanoclusters).

The synthesis of palladium nanoclusters in the presence of THF does, however, have several disadvantages. Reduction of palladium ions begins rapidly in the presence of THF, whereas pure aqueous $Na_2PdCl_4x3H_2O$ solutions are stable for several months or more. It is also difficult to characterize the extent of palladium uptake in the presence of THF, since most ICPs are configured for aqueous solutions. The synthesis of palladium nanoclusters from 0.5 and 1.0 moles $Na_2PdCl_4x3H_2O$/mole COOH in THF solution is not recommended due to the large number of aggregated 200-400 Å palladium particles observed in those cases (Figure 8.6).

8.5. References for Chapter 8

(1) Spatz, J.P., Roescher, A., and Moller, M. *ACS Polymer Preprints* **1996**, 37, 409.

(2) Hirai, H., Nakao, Y., and Toshima, N. *J. Macromol. Sci. Chem.* **1978**, A12, 1117.

(3) Yen, C. and Chang, T. *J. Apply. Polym. Sci.* **1990**, 40, 53.

(4) Hojo, N., Shirai, H., and Hayashi, S. *J. Polym. Sci.* **1974**, 47, 299.

(5) Swanson, H.E. and Tatge, E. 'U.S. National Bureau of Standards Standard X-Ray Diffraction Patterns', NBS Circular 539, Volume I, U.S. Government Printing Office, Washington D.C., June 15, 1953.

(6) Denisov, E.T., Mitskevich, N.I., and Agabekov, V.E. 'Liquid-Phase Oxidation of Oxygen-Containing Compounds', Consultants Bureau, New York, 1975, p.173.

(7) Hudlicky, M. 'Oxidations in Organic Chemistry', ACS Monograph 186, American Chemical Society, Washington D.C., 1990, p. 169.

Chapter 9
Conclusions and Future Work

9.1. Conclusions

Polymer/metal nanocluster composites are a subject of great interest because of their wide range of potential applications as high selectivity catalysts, self-resetting polymeric fuses, non-fading dyes, nano-wire arrays, and magnetic security coatings.

We developed a fundamentally new, versatile, and broadly applicable method for synthesizing relatively uniformly sized and homogeneously dispersed metal nanoclusters within polymer films. Our technique offers a compromise between two previous methods of synthesizing polymer/metal cluster composites: deposition of metal vapor into polymer solutions (or liquid monomer)[1] and use of organometallic monomers[2]. Our metal nanoclusters are more evenly distributed and more uniformly sized than those made by depositing metal vapor into liquid monomer followed by polymerization, and our technique does not require the expensive and complicated synthesis of organometallic monomers.

In our strategy, outlined in Figure 1.9, metal ions (Ag^{+}, Au^{+3}, Cu^{+2}, Fe^{+2}, Fe^{+3}, Ni^{+2}, Pb^{+2}) or complexes ($[PdCl_4]^{-2}$, $[PtCl_6]^{-2}$) are coordinated to carboxylic acid groups within the water soluble polyNORCOOH domains of a $[MTD]_{400}[NORCOOH]_{50}$ block copolymer (MTD = methyltetracyclododecene and NORCOOH = 2-norbornene-5,6,-dicarboxylic acid) by immersion of the polymer in aqueous metal salt solutions. The metal ions and complexes are subsequently reduced by heating the metal loaded polymer under hydrogen or by immersion in an aqueous sodium borohydride solution. For several transition metals, the resulting nanoclusters are uniformly sized and homogeneously dispersed within the polyNORCOOH domains. Our "universal" metal cluster synthesis scheme uses the microphase-separated morphology of a block copolymer as a kinetic barrier to both cluster aggregation and cluster migration from the polyNORCOOH domains to the polyMTD matrix. This technique is potentially useful because it allows simple in-situ synthesis of several types of metal nanoclusters within a matrix whose morphology can be controlled by varying polymer block lengths. This technique allows for the possibility of cluster size control and the synthesis of shell-and-core clusters through multiple metal loading and reduction cycles.

We discovered that interconnectedness between the carboxylic acid functionalized domains (cylindrical or lamellar morphology) is necessary for metal ion uptake from aqueous solutions, because ion transport ($D_{eff} \sim 3.5 \times 10^{-11}$ cm^2/s, Ag^+) occurs primarily through the carboxylic acid functionalized domains rather than through the polyMTD matrix. This fact is in contrast to metal uptake from organometallic compounds which can be loaded into similar polymers, with isolated spherical polyNORCOOH domains, from dimethyl cadmium or diethyl zinc vapors.[3] Futhermore, we verified through inductively coupled plasma atomic emission spectroscopy (ICP-AES) and IR-spectroscopy, that ion exchange between acid protons and metal ions was the primary binding mechanism.[4,5]

UV-visible spectroscopy showed that 10 µm thick Ag, Au, and Cu cluster containing films were brightly colored due to the surface plasmon absorptions of the embedded clusters. Both UV-visible spectra and the theory of Clippe et al.[6] indicated our silver nanoclusters were electronically isolated within the 10 µm thick films following a single loading and reduction sequence (LARS, 535 mg Ag^+/g polyNORCOOH, 1.52×10^{18} clusters cm^{-3} within the polyNORCOOH domains).

A combination of WAXS and TEM showed that cluster size (ca. 30 Å) was relatively independent of the extent of Ag^+ loading during a single LARS (40 mg Ag^+/ g polyNORCOOH to 500 mg Ag^+/g polyNORCOOH). This indicates that nucleation is fast relative to growth. Metal loading is more efficient from metal acetates than from metal chlorides, because protons have a high affinity for free carboxylate ions. Protons liberated from -COOH during metal loading from MCl_2 form the strong acid, HCl, and are free to displace loaded metal ions. Protons liberated from -COOH during metal loading from $M(OOCCH_3)_2$ form weak, acetic acid, and are not as free to displace loaded metal ions.

IR-spectroscopy and ICP-AES showed that most carboxylic acid groups are regenerated during hydrogen reduction, and may participate in further metal loading. A 10 μm thick film was subjected to a series of four Ag^+ LARS, corresponding to a cumulative Ag^+ loading of 26 wt. % Ag in the overall polymer/Ag composite. The mean cluster size increased from 37 Å, after the first LARS, to 65 Å, after the fourth LARS. Therefore, pre-existing Ag clusters appear to act as nucleation sites for additional cluster growth during subsequent LARS. However, some smaller clusters were also observed following multiple LARS, indicating that the nucleation of new clusters also occurs, leading to an increase in the cluster size distribution.

Conversion of carboxylic acid groups, within $[MTD]_{400}[NORCOOH]_{50}$, to the sodium carboxylate form, $[MTD]_{400}[NORCOONa]_{50}$, results in large increases in both the rate and extent of transition metal and rare earth ion uptake from metal acetates, chlorides, nitrates, and sulfates. In the cases of Co, Eu, and Gd, containing compounds, significant loading can often be achieved from 0.005 M aqueous metal salt solutions into 10 μm thick $[MTD]_{400}[NORCOONa]_{50}$ films within hours; whereas, no loading was observed into $[MTD]_{400}[NORCOOH]_{50}$ films. The improvement in loading is due largely to the acetate ion's much lower stability constant with Na^+, $K_1 \sim 0.7$ (mole/l)$^{-1}$, than with H^+, $K_1 \sim 6.3\text{x}10^4$ (mole/l)$^{-1}$, which allows transition metal and rare earth ions, $K_1 \sim 3\text{-}1600$ (mole/l)$^{-1}$, to more easily exchange with the weakly bound Na^+ ions than with the much more strongly bound H^+ ions.

Our technique represents a significant advancement in the area of polymer/metal cluster composite synthesis; however, it has several noteworthy limitations, and will not necessarily be the best method for making a particular composite. At present, the maximum Pd ($Na_2PdCl_4\text{x}3H_2O$) and Pt ($H_2PtCl_6\text{x}6H_20$) loadings achievable in 10 μm thick $[MTD]_{400}[NORCOOH]_{50}$ films are 0.038 g Pd/g composite and 0.02 g Pt/g composite, respectively, during the first LARS. Similar block copolymers made with palladium, [Pd], and platinum, [Pt], containing organometallic monomers[2] rather than NORCOOH, contain 0.064 g Pd/g composite and 0.11 g Pt/g composite respectively. Pd and Pt are particularly difficult to load using our technique, because most acetate and chloride salts containing palladium or platinum have very low water solubilities. Neither $Na_2PdCl_4x3H_2O$ nor $H_2PtCl_6x6H_20$ are good candidates for metal loading, because the Pd and Pt are present in solution as complex anions ($[PdCl_4]^{-2}$ and $[PtCl_6]^{-2}$) rather than as cations.

Although our technique allows the loading of most transition metal and rare earth ions from aqueous acetate or chloride solutions into sodium carboxylate form films, efficient reduction of ions with negative electrochemical reduction potentials remains a challenge. Powerful gas phase reducing agents such as hydrazine vapor are highly toxic, and aqueous sodium borohydride reduction of Co^{+2} and Ni^{+2} appears to form amorphous metal borides.

Furthermore, our polymer films appear to provide little oxidative protection to the embedded clusters. Both Co and Cu nanoclusters were observed to oxidize completely over a period of time on the order of a month. When attempting the synthesis of shell-and-core particles, via multiple LARS with different metals, the most easily reducible metal must be loaded first; otherwise, clusters of the less easily reducible metal will be oxidized by ions of the more easily reducible metal during the second loading.

9.2. Future Work

During the past several years our group has learned a great deal about the science and art of metal cluster synthesis within block copolymer films. We examined different casting solvents and film casting techniques. We also explored all three basic block copolymer morphologies (spherical, cylindrical, and lamellar) and several polymer systems. We studied the variables affecting the extent of loading, cluster size, and cluster density, and experimented with several reduction techniques. However, much remains unknown.

We suspect an increase in the reduction temperature will lead to an increase in the cluster size, by increasing the mobility of small metal nuclei; but we have little experimental data to support this hypothesis. I also believe it would be interesting to measure the electrical conductivity of a silver containing film as a function of the extent of silver loading. Such an experiment would be even more interesting if it involved a polymer with a lamellar morphology. In which case, anisotropic (parallel vs. perpendicular to lamellae) behavior may be observed. Several metal nanoclusters exhibit characteristic colors within polymer films, due to the surface plasmon absorptions of the embedded clusters. It may be possible to shift the colors of cluster containing films by exposing them to coordinating solvents, which may alter the dielectric constant of the embedded clusters.

I recommend further exploration of magnetic cluster containing films. It may be possible to synthesize ferromagnetic EuS, by treating a Eu^{+2} loaded film with hydrogen sulfide. Lastly, the development of an electrically conductive, coordinating polymer may eliminate the difficulty of reducing ions with negative reduction potentials. It is possible, in theory, to reduce such ions by applying a positive potential, greater in magnitude than the ion's reduction potential.[7]

9.3. References for Chapter 9

(1) Klabunde, K.J., Habdas, J. and Cardenas-Trivino, G. *Chem. Mater.* **1989**, 1, 481.

(2) Chan, Y.N.C., Craig, G.S.W., Schrock, R.R. and Cohen, R.E. *Chem. Mater.* **1992**, 4, 885.

(3) Yue, J. and Cohen, R.E. *Supramolecular Science* **1994**, 1, 117.

(4) Helfferich, F.G. 'Ion Exchange', McGraw-Hill, Inc.New York, 1962, p. 279

(5) Calmon, C. in 'Adsorption and Ion Exchange'; AIChE Symp. Ser. 1984, 80, No. 233.

(6) Clippe, P., Evrard, R., and Lucas, A. *Phys. Rev. B.* **1976**, 14, 1715.

(7) Zumdahl, S.S. 'Chemistry', D.C. Heath and Company, Lexington, 1986, p. 739.

Appendix A
Materials

MTD monomer was donated by BFGoodrich (Contact Brian Goodall: 216-447-5389), and then de-oxygenated prior to use. NORCOOTMS (2-norbornene-5,6,-dicarboxylic acid-bis trimethylsilyl ester) and $Mo(CHCMe_2Ph)(NAr)(O\text{-}t\text{-}Bu)_2$ (Ar = 2,6-C_6H_3-i-Pr_2) were prepared according to literature procedures. Anhydrous toluene, from Aldrich, was stored over sodium prior to use. Benzaldehyde, from Aldrich, was distilled (take middle fraction) and de-oxygenated with Ar prior to use. Metal salts from Aldrich: cobalt (II) acetate hexahydrate (98%), cobalt (II) chloride hexahydrate (98%), cobalt (II) nitrate hexahydrate (98%), iron (II) chloride (98%), iron (III) chloride (97%), lead (II) chloride (98%), nickel (II) chloride (98%), nickel (II) nitrate hexahydrate (98%), nickel (II) sulfate hexahydrate (99%), silver (I) acetate (99.999%), sodium hydroxide (97%), and Strem: chloroplatinic acid hexahydrate (99.9%, $H_2PtCl_6x6H_2O$), copper (II) acetate (99%), copper (II) chloride (98%), europium (III) acetate hydrate (99.9%), europium (II) chloride (99.9%), europium (III) chloride hexahydrate (99.9%), gadolinium (III) acetate tetrahydrate (99.9%), gadolinium (III) chloride (99.9%), gold (III) chloride (99%), iron (II) acetate (97%), palladium (II) acetate (98%), palladium (II) chloride (99.9%), platinum (IV) chloride (99.9%), sodium tetrachloropalladate (II) trihydrate (99%, $Na_2PdCl_4x3H_2O$), sodium tetrachloroplatinate (II) hydrate (99%, $Na_2PtCl_4xH_2O$) were used without further purification. Aldrich 1000 μg/ml atomic absorption standard solutions were used to prepare all ICP-AES standards. All aqueous metal salt solutions were prepared using de-ionized water.

Appendix B
Equipment

Gel permeation chromatographic (GPC) analysis was carried out using a series of three Waters Ultrastyrogel™ columns (10^5 Å, 10^4 Å, and 10^3 Å) connected to a Waters Differential Refractometer R401. The mobile phase was toluene at a flow rate of 1 ml/min. The GPC columns were calibrated with commercially available polystyrene standards (Polysciences, Inc.). Samples were filtered using 0.5 μm Millipore Millex-LCR® syringe mounted filter units, and injected at a concentration of 4 mg polymer per ml of solution.

Spin-cast films were made using a Headway Research, Inc. Photo-Spinner. The thicknesses of spin-cast films were measured with a DEKTAK 8000 proflometer. Polymer glass transition temperatures were measured using a Perkin-Elmer DSC7, and a Mettler FP82 hot stage with a Mettler FP80 central processor. Hydrogen reductions were conducted in an Ace Glass #25 Ace-Thred, 200 ml hydrogenation/gas apparatus I.

The morphology of the microphase-separated block copolymers was determined using a JEOL 200 CX TEM operated at 200 kV. Ultra-thin (400-500 Å) samples for TEM observation were microtomed at room temperature with glass knives using a Sorvall Ultra Microtome MT 5000. Gold, 400 mesh grids were used to support all microtomed samples. Gold was chosen because it has the highest electrochemical reduction potential of all the metals studied, and therefore will not undergo electrochemical oxidation with metal ions in solution. The composition of metal and bimetallic nanoclusters was studied using both VG-HB603 (Chapter 3) and VG-HB501 (Chapter 6) scanning transmission electron microscopes (STEM, electron microprobe analysis mode), operated at 250 kV and 100 kV respectively. Aqueous metal ion concentrations were measured with a Perkin-Elmer Plasma 40 inductively coupled plasma atomic emission spectrophotometer. Approximate pH values were determined using EM-Reagents colorpHast® pH paper (pH 0-6). IR spectra were recorded on a Nicolet Magna-IR 550 spectrophotometer, in transmission mode, with a DTGS/KBr detector. UV-Visible spectra were recorded on a Cary 5E UV-Vis-NIR spectrophotometer, in transmission mode, with a R928 photomultiplier tube detector.

The crystal structure of the metal nanoclusters was determined using wide-angle X-ray scattering (WAXS), performed with a Rigaku rotating Cu anode X-ray source (λ = 1.54 Å). The Cu Kα line generated at 50 kV and 60 mA was filtered with a thin nickel plate. The 2θ diffraction data were collected in both reflection (Chapters 3 and 4) and transmission (Chapter 5 and beyond) modes with a collection time of 2-10 s for each 0.05° step. Transmission mode is preferred; the ratio of metal scattering peak height to polymer scattering peak height was observed to be strongly dependent on sample area for data taken in reflection mode.

The magnetic propeties of Co containing films were investigated using a Quantum Design Model MPMS, superconducting quantum interference device (SQUID).

Appendix C

Monomer Synthesis

C.1. Dicyclopentadiene "Cracking"

Cyclopentadiene monomer is not stable. It undergoes a Diels-Alder addition with itself at 25 °C. Dicyclopentadiene must be thermally cracked to cyclopentadiene just prior to NORCOOH synthesis. Charge dicyclopentadiene to a distillation (reservoir) flask below a short Vigreaux column. Attach a condenser outlet to the top of the distillation column, and attach another (ice cooled) receiver flask to the end of the condenser arm.

Begin heating the reservoir flask (150-190 °C). When the temperature at the top of the column reaches 39 °C, cyclopentadiene vapor will begin to condense and run through the condenser into the receiver flask. Run the process such that the flow rate into the receiver flask is 2-3 drops/sec (or slower), until 80 % of the dicyclopentadiene is collected as cyclopentadiene.

Rinse all glassware with acetone several times in the hood.

C.2. NORCOOH (2-norbornene-5,6-dicarboxylic acid)

NORCOOH was synthesized according to the following procedure: Stir fumaric acid (60g, 0.517 mol) in a slurry with 700 ml methanol, and freshly cracked cyclopentadiene (68.37 g, 1.034 mol, excess). Add both fumaric acid and cyclopentadiene rapidly to the methanol and stir overnight at room temperature. The reaction mixture will appear cloudy the next morning. Pour the solution into a large Petri dish and allow the methanol to evaporate.

Wash the crude NORCOOH 3-4 times with pentane (stirring vigorously). Dry the NORCOOH several days in air, and overnight under vacuum. Modify the quantities to suit your needs. 30 g of NORCOOH should last several years.

C.3. NORCOOTMS (2-norbornene-5,6-dicarboxylic acid-bis trimethylsilyl ester)

Perform entire synthesis in an inert atmosphere drybox. Stir NORCOOH (10 g, 0.055 mol) in 400 ml anhydrous diethyl ether at room temperature. Use a 1000 ml flask. Add additional diethyl ether as necessary to completely dissolve all NORCOOH. To the solution, add anhydrous pyridine (8.68 g, 0.110 mol) in one shot. Add de-oxygenated chlorotrimethylsilane (12 g, 0.110 mol) slowly to the rapidly stirred solution. A white pyridine hydrochloride precipitate forms immediately. Stir for 3 hr. For best results, add 10 % more pyridine and chlorotrimethylsilane than called for above. Any uncapped NORCOOH will deactivate the polymerization catalyst. See Randall Saunders' thesis (p. 200) for additional details.

Vacuum filter solution through a bed of celite to remove pyridine hydrochloride. Rotovap filtrate to dryness (fine white NORCOOTMS crystals remain). Dissolve crude NORCOOTMS in dry pentane and stir for 10 minutes (~200 ml). A sticky yellow PPT may form on the bottom of the flask. Vacuum filter solution through a bed of silica gel. Rotovap filtrate to dryness (fine white NORCOOTMS crystals remain). Dissolve NORCOOTMS in dry pentane (~400 ml). A cloudy white PPT may remain, it's not NORCOOTMS. Vacuum filter solution through a bed of alumina. The filtrate should be clear. Rotovap filtrate until NORCOOTMS crystallization begins to occur (~100 ml pentane remaining). Stopper flask and place in -30 °C freezer overnight. Decant excess pentane from NORCOOTMS crystals. Dissolve NORCOOTMS in diethyl ether (~80 ml). Rotovap filtrate until NORCOOTMS crystallization begins to occur (~30-40 ml ether remaining). Pour contents of flask into a wide-mouth jar, cap, and place in -30 °C freezer overnight. Decant excess diethyl ether and dry NORCOOTMS crystals inside box overnight. Break crystal lumps into a fine powder, and dry in drybox antechamber under vacuum overnight. I found the above described batch size convenient. Expect to recover 30-50 % of the theoretical NORCOOTMS yield.

Seal NORCOOTMS crystals in a vial and tape around lid. Store under nitrogen at -30 °C. Moisture in the drybox will convert enough NORCOOTMS to NORCOOH, to hinder ROMP reactions, over 4-8 months. Recrysallize old NORCOOTMS from pentane to allow continued use. I'm not quite sure why this works, but I've done it.

C.4. NORCOTMS (2-norbornene-5-methanol trimethylsilyl ester)

In an inert atmosphere drybox, stir de-oxygenated (freeze-pump-thaw cycled) NORCOH (20 g, 0.161 mol) and anhydrous pyridine (14.6 g used, 12.75 g = 0.161 mol) with 300 ml anhydrous diethyl ether. Slowly add chlorotrimethylsilane (20 g used, 17.5 g = 0.322 mol). White pyridine hydrochloride precipitates immediately. Stir 48 hr. Vacuum filter solution through celite to remove pyridine hydrochloride. The filtrate is a clear yellowish liquid. Rotovap off diethyl ether for 24 hr, until ~ 30 ml of NORCOTMS (yellowish oil) remains. Stir NORCOTMS over sodium spheres for 48 hr. Distill NORCOTMS from the sodium spheres in the drybox, using a short-path distillation column, under vacuum. Heat the NORCOOTMS slowly to avoid explosive boiling. The pure NORCOTMS distillate is amber (final yield ~ 20 g), while the liquid remaining in the reservoir flask is dark brown.

Seal NORCOTMS in a vial and tape around lid. Store under nitrogen at -30 °C.

Appendix D
Film Casting

During the course of this research $[MTD]_{400}[NORCOOH]_{50}$ films were cast from THF in three different thickness regimes: 1000 Å, 10 µm, and > 0.1 mm. The film casting techniques described below also apply to homopolymers and other block copolymers. Important film samples should be stored in an oxygen-free environment. Although films of 1000 Å or more in thickness appear to be air stable for several years, I have observed yellowing and decomposition of polymer "flake" (precipitated from pentane, but not yet cast into films) after three to six months of storage in air. This yellowing was observed in both polyMTD and $[MTD]_{400}[NORCOOH]_{50}$ films, indicating that c=c bond oxidation is the likely cause.

D.1. 1000 Å Thick Films

$[MTD]_{400}[NORCOOH]_{50}$ films of ca 1000 Å in thickness can be prepared by the spin-casting technique. Begin by cutting a square section from a glass microscope slide. Then, clean the slide with ethanol, and place the slide on the spin-caster. Using a Pasteur pipette, evenly coat the entire slide with a 50 wt. % solution of Ivory Clear® dish detergent in de-ionized water. Spin the slide dry (3000 RPM, 1 min.). Place 2-3 drops of a 3 wt. % polymer solution in THF, at the center of the soap film covered grid. Spin the polymer solution dry (3000 RPM, 1 min.). Remove the slide from the spin-caster, and scratch away the ends of the polymer film with a razor, leaving a square, sharp edged, center section. Score a grid of 1 mm by 1 mm polymer squares in the film using a razor or needle. **Slowly** immerse the slide in a dish of de-ionized water at a **45** ° angle. The soap film will dissolve, and the polymer squares should float off the slide onto the surface of the water. Capture the ca 1000 Å thick polymer sections on gold, 400 mesh grids. Try practicing with a 3 wt. % solution of polystyrene in toluene.

Films produced using this technique are thin enough to detect contrast with TEM, but too thick for observation of detailed morphology. Film thicknesses were measured using a DEKTAK proflometer.

D.2. 10 μm Thick Films

10 μm thick $[MTD]_{400}[NORCOOH]_{50}$ films can be cast using the following procedure when the relative humidity is 50 % or less (October-April). Prepare a 0.5 wt. % polymer solution in solvent grade THF. Add a sufficient mass of polymer solution to a glass, ultra-flat bottomed petre dish, to yield an average film thickness of 10 μm (assuming a polymer density of 1 g/cm^3). Cover the dish tightly with aluminum foil and allow the THF to evaporate over two days. After the THF has completely evaporated, place a nick in the film near the wall of the dish. Place several drops of de-ionized water on the film, over the nick. Allow the water to wet the glass surface under the polymer film. Remove and dry the polymer film with paper towel. The film should appear transparent and colorless. Vacuum dry for 2 hours at room temperature. Massing of the polymer both before and after film casting indicates that 7-8 wt. % residual THF remains in the film even after 24 hours of drying under vacuum. The mass of the residual THF was taken into account during subsequent ion loading experiments.

During the summer months, high humidity (> 50 %) will increase the water content of solvent grade THF and cause $[MTD]_{400}[NORCOOH]_{50}$ to precipitate. When this occurs the resulting films will be white, opaque, porous, and brittle. During periods of high humidity, prepare 1 wt. % solutions of polymer in anhydrous THF in the drybox. Add a sufficient mass of polymer solution to a glass, ultra-flat bottomed petre dish, to yield an average film thickness of 10 μm (assuming a polymer density of 1 g/cm^3). Cover the dish tightly with aluminum foil. Remove the covered dish from the drybox, and place in a sealed Rubbermaid® container. Purge with argon immediately, and twice daily for 15 minutes until THF evaporates (~10 days).

I used PYREX Petri Culture dishes (95 mm O.D. x 22 mm Ht., Corning 3162-BO) available through VWR, and cast 12 films at a time.

D.3. > 0.1 mm Thick Films

$[MTD]_{400}[NORCOOH]_{50}$ films, greater than 0.1 mm thick, were cast from 3 wt. % polymer solutions in solvent grade THF. Pour the desired amount of polymer solution into a rectangular casting cup, folded from Teflon coated aluminum foil, and supported on a glass microscope slide. Place the casting cup in a sealed glass jar. Poke a small hole in the lid, and allow the THF to evaporate over a week. The casting of thick films is not adversely affected by high humidity.